Experimental study and modeling of the quasi-static mechanical behavior of Ti6Al4V at room temperature

Thesis submitted to the University of Liège

for the degree of 'Docteur en Sciences de l'Ingénieur'

by Gaëtan Gilles

March 2015

Author's coordinates

Gaëtan GILLES

Université de Liège

Département ArGEnCo (Architecture, Géologie, Environnement et Constructions)

Secteur MS²F (Mécanique des Solides, des Fluides et des Structures)

Building B52/3, Office +1/448

Chemin des Chevreuils 1

4000 Liège

Belgium

Phone: +32 (0) 4 366 93 32

e-mail: ggilles@ulg.ac.be

Jury members

Mr. J.P. JASPART, president
Professor
ArGEnCo Department – MS²F Division (Mechanics of Solids, Fluids and Structures)
University of Liège, Belgium
Jean-Pierre.Jaspart@ulg.ac.be

Mrs. A.M. HABRAKEN, supervisor
Research Director FNRS
ArGEnCo Department – MS²F Division (Mechanics of Solids, Fluids and Structures)
University of Liège, Belgium
Anne.Habraken@ulg.ac.be

Mr. L. DUCHÊNE, co-supervisor
Lecturer
ArGEnCo Department – MS²F Division (Mechanics of Solids, Fluids and Structures)
University of Liège, Belgium
L.Duchene@ulg.ac.be

Mr. J.P. PONTHOT
Professor
LTAS Department – MN2L Division (Non Linear Computational Mechanics)
University of Liège, Belgium
JP.Ponthot@ulg.ac.be

Mrs. O. CAZACU
Professor
Department of Mechanical and Aerospace Engineering
Research Engineering and Education Facility (REEF)
University of Florida, USA
cazacu@reef.ufl.edu

Mr. T. BALAN
Associate Professor
M2P Department (Mechanics, Materials, Processes)
Laboratory of Microstructures and Mechanics of Materials (LEM3)
Arts et Métiers ParisTech – Metz Campus, France
tudor.balan@ensam.eu

Mr. T. KUWABARA
Professor
Department of Mechanical Systems Engineering
Tokyo University of Agriculture and Technology, Japan
kuwabara@cc.tuat.ac.jp

Mrs. P. VERLEYSEN
Professor
Department of Materials Science and Engineering
Ghent University, Belgium
Patricia.Verleysen@UGent.be

Acknowledgments

First, I would like to express my grateful thanks to Anne Marie Habraken and Laurent Duchêne from the ArGEnCo Department who supervised my work, for their attention and for all the time they awarded to me.

I would like to acknowledge Dr. Oana Cazacu for her valuable support and her advices in this research, as well as her warm welcome during my stage at REEF (University of Florida, USA) between January and April 2010.

All my thanks also go to Prof. Toshihiko Kuwabara (Tokyo University of Agriculture and Technology, Japan), Prof. Sandrine Thuillier (LIMATB, Université de Bretagne-Sud, France), Prof. Gérard Ferron (LPMM, Université Paul Verlaine-Metz, France), Prof. Tudor Balan (LEM3, Arts et Métiers ParisTech, France) as well as the current and former team members from the Materials and Structures Mechanics Laboratory (especially Carl Vroomen, Etienne Rondia, Olivier Milis and Pierre Gonry) for their help in the achievement of the experimental tests.

I am very grateful to the current and former workmates of the "Lagateam" for their friendship during all my work: Christophe Henrard, Renée Schwartz, Anne-Françoise Gerday, Frédéric Pascon, Cédric Lequesne, Chantal Bouffioux, Mohamed Ben Bettaïeb, Walid Hammami, Clément Keller, Paulo Florès, Víctor Tuninetti, Carlos Guzmán, Ingrid Neira and everyone I have not cited.

I would also like to express a special thank to the secretaries, especially Laurence Defrère and Chantal Marquet, for their kindness and their moral support.

Finally, the Belgian Fund for Scientific Research F.R.S.-FNRS (FRIA grant) and the Belgian Federal Science Policy Office are greatly acknowledged for their financial support.

Vita

2015……..	PhD Engineering Sciences, University of Liège, Belgium
2007……..	Civil Physical Engineer, University of Liège, Belgium
2004……..	Bachelor of Engineering Sciences, University of Liège, Belgium

Publications related to Ti6Al4V

Tuninetti V., Gilles G., Pardoen T. and Habraken A.M. (2015). *Anisotropy and tension-compression asymmetry modeling of the room temperature plastic response of Ti-6Al-4V*. International Journal of Plasticity, 67:53-68.

Gilles G., Habraken A.M. and Duchêne L. (2014). *Experimental investigation and phenomenological modeling of the quasi-static mechanical behavior of TA6V titanium alloy*. Key Engineering Materials, 622-623:1200-1206.

Gilles G., Habraken A.M., Cazacu O., Balan T. and Duchêne L. (2013). *Experimental and numerical study of TA6V mechanical behavior under different quasi-static strain paths at room temperature*. AIP Conference Proceedings, 1532:651-656.

Gilles G., Cazacu O., Hammami W., Habraken A.M. and Duchêne L. (2012). *Experimental and numerical study of TA-6V mechanical behavior in different monotonic loading conditions at room temperature*. Procedia IUTAM, 3:100-114.

Tuninetti V., Gilles G., Milis O., Lecarme L. and Habraken A.M. (2012). *Compression test for plastic anisotropy characterization using optical full-field displacement measurement technique*. Steel Research International.

Tuninetti V., Gilles G., Milis O., Neira Torres I. and Habraken A.M. (2013). *Quasi-static mechanical behaviour of Ti-6Al-4V alloy at room temperature*. In: Proceedings of 12th International Conference on Computational Plasticity, Fundamentals and Applications (COMPLAS XII), Barcelona, Spain, 51-62.

Tuninetti V., Gilles G., Péron-Lührs V. and Habraken A.M. (2012). *Compression test for metal characterization using digital image correlation and inverse modeling*. Procedia IUTAM, 4:206-214.

Gilles G., Hammami W., Libertiaux V., Cazacu O., Yoon J.H., Habraken A.M. and Duchêne L. (2011). *Experimental characterization and elasto-plastic modeling of the quasi-static mechanical response of TA-6V at room temperature*. International Journal of Solids and Structures, 48:1277-1289.

Gilles G., Tuninetti V., Ben Bettaïeb M., Cazacu O., Habraken A.M. and Duchêne L. (2011). *Experimental characterization and constitutive modeling of TA6V mechanical behavior in plane strain state at room temperature*. AIP Conference Proceedings, 1383:78-85.

Hammami W., Gilles G., Habraken A.M. and Duchêne L. (2011). *Phenomenological and crystal plasticity approaches to describe the mechanical behaviour of Ti6Al4V titanium alloy*. International Journal of Material Forming, 4:205-215.

Gilles G., Habraken A.M. and Duchêne L. (2010). *Material parameter identification of Cazacu's model for Ti6Al4V using the simulated annealing algorithm*. Materials Science Forum, 636-637:1125-1130.

Publications related to thermo-mechanical-metallurgical simulations

Gilles G., Neira Torres I., Tchuindjang J.T., Sinnaeve M., Florès P., Lecomte-Beckers J. and Habraken A.M. (2015). *Modelling of stress field evolution in bimetallic rolling mill rolls during the manufacturing process*. Paper submitted to Rolls 5 conference (Birmingham, UK).

Neira Torres I., Gilles G., Tchuindjang J.T., Lecomte-Beckers J., Sinnaeve M. and Habraken A.M. (2014). *Study of residual stresses in bimetallic work rolls*. Advanced Materials Research, 996:580-585.

Neira Torres I., Gilles G., Tchuindjang J.T., Lecomte-Beckers J., Sinnaeve M. and Habraken A.M. (2013). *Prediction of residual stresses by FE simulations on bimetallic work rolls during cooling*. Computer Methods in Materials Science, 13:84-91.

Other publications

Florès P., Tuninetti V., Gilles G., Gonry P., Duchêne L. and Habraken A.M. (2010). *Accurate stress computation in plane strain tensile tests for sheet metal using experimental data*. Journal of Materials Processing Technology, 210:1772-1779.

Attended conferences

- Materiais 2009, Lisbon, Portugal
- SolMech 2010, Warsaw, Poland
- Numisheet 2011, Seoul, Korea
- Numiform 2013, Shenyang, China
- Metal Forming 2014, Palermo, Italy

Summary

The work aims to characterize the quasi-static mechanical behavior of the Ti6Al4V titanium alloy at room temperature and to describe it by a phenomenological model.

The thesis is divided in four parts. The first one presents a literature review of the basic properties of titanium and its alloys (crystal structure, classification, deformation mechanisms), then it focuses on the specific mechanical features of Ti6Al4V. It also proposes a state of art in the field of the phenomenological constitutive laws used to model the mechanical behaviors of metals.

The second part deals with the experimental campaign conducted on a 0.6 mm thick Ti6Al4V sheet. The devices and the tests are first described before giving the test results. The campaign includes experiments with monotonic and complex strain paths (tension, compression, simple shear, plane strain, Bauschinger tests, deep-drawing processes, layer compression tests). The experimental results show that the material displays anisotropy in yield stress, *r*-ratios and hardening, as well as a strength differential effect between tension and compression.

The third part describes the implementation of the yield criteria CPB06ex*n* in the non-linear finite element code LAGAMINE developed in MSM team. These criteria are selected to model the yield locus of Ti6Al4V since they are able to take into account both the anisotropy and the tension-compression asymmetry exhibited by the alloy. Several parameter identifications are performed using the classical simulated annealing algorithm. They determine that CPB06ex2 is required to represent the yield surface. The criterion is next associated to different hardening formulations: (1) Voce isotropic law; (2) mixed Voce isotropic – Armstrong-Frederick kinematic law; (3) model taking into account the evolution of the yield locus shape with the deformation. The identification of the hardening parameters is achieved from the monotonic and Bauschinger tests either by inverse method, or by the simulated annealing method.

The last part of the thesis proposed a validation of the different modelings in the case of the layer compression tests and the deep-drawing processes.

Table of contents

Acronyms & abbreviations

2D	two-dimensional
3D	three-dimensional
AF	Armstrong-Frederick
ArGEnCo	Architecture, Geology, Environment and Constructions
bcc	body-centered cubic
CP	Commercially Pure
CRSS	Critical Resolved Shear Stress
CSA	Classical Simulated Annealing
DIC	Digital Image Correlation
DP	Dual Phase
EBSD	Electron BackScatter Diffraction
fcc	face-centered cubic
FE	Finite Element
FEM	Finite Element Method
hcp	hexagonal close-packed
HSLA	High-Strength Low-Alloy
IAP	Interuniversity Attraction Poles
IF	Interstitial Free
JC	Johnson-Cook
LEM3	Laboratoire d'Etude des Microstructures et de Mécanique des Matériaux
LCT	Layer Compression Test

m.r.d.	multiple random density
MS²F	Mechanics of Solids, Fluids and Structures
ND	Normal Direction
RD	Rolling Direction
SD	Strength Differential
TD	Transverse Direction
TRIP	Transformation Induced Plasticity
TUAT	Tokyo University of Agriculture and Technology
ULg	University of Liège
VPSC	ViscoPlastic Self-Consistent
WEDM	Wire Electrical Discharge Machining
XRD	X-Ray Diffraction
ZA	Zerilli-Armstrong

Symbols

Mathematical operators

$:$	Double contracted product
$\lvert\ \rvert$	Absolute value
$\lVert\ \rVert$	Norm of a tensor
∂	Partial derivative
$\int$	Integral symbol
d	Derivative
e	Exponential
$\exp(\ )$	Exponential
$\ln(\ )$	Natural logarithm
$\sup(\ )$	Least upper bound
$\mathrm{tr}(\ )$	Trace of a tensor

Latin characters

a	Parameter in Hosford (1972) yield criterion
	Degree of homogeneity

	Semi-major axis of an ellipse
a_1, a_2, a_3	Intersections of a lattice plane with the coordinate axes
a_i, $i=1\ldots6$	Parameters in the expression of J_2^0
b	Degree of homogeneity
	Material constant in the Lou *et al.* (2013) approach
	Semi-minor axis of an ellipse
$\mathbf{b}$	External volumetric loads
b_i, $i=1\ldots11$	Parameters in the expression of J_3^0
c	Parameter in Drucker yield criterion
	Parameter in Karafillis and Boyce (1993) yield criterion
	Parameter in Cazacu and Barlat (2001) yield criterion
	Parameter in Cazacu and Barlat (2004) yield criterion
	Parameter in Prager law
c_d	Parameter in the Noman *et al.* (2010) approach
c_i, $i=1\ldots6$	Parameters in Barlat *et al.* (1991) yield criterion
c_l	Parameter in the Noman *et al.* (2010) approach
c_P	Parameter in Teodosiu-Hu model
c_R	Parameter in Voce law
c_{SD}	Parameter in Teodosiu-Hu model
c_{SL}	Parameter in Teodosiu-Hu model
c_X	Parameter in Armstrong-Frederick law
d	Smallest common denominator of the integers a_1, a_2, a_3
e	Relative error
f	Parameter in Teodosiu-Hu model
g	Function used in Teodosiu-Hu model
h	Miller index
	Function used in Teodosiu-Hu model

	Height
h_d^{sat} , h_l^{sat}	Parameters in the Noman *et al.* (2010) approach
h_x , h_y	Material constants in the Lou *et al.* (2013) approach
i	Miller index
	Index
j	Index
k	Miller index
	Index
	Parameter in Drucker yield criterion
	Strength-differential parameter in CPB06 and SRP09 yield criteria
l	Miller index
	Current length
l_0	Initial length
$\underline{m}$	Slip direction
$\tilde{m}$	Scaling factor
n	Parameter in Swift law
	Parameter in Johnson-Cook model
	Parameter in Zerilli-Armstrong model
$\underline{n}$	Normal to slip plane
n_L	Parameter in Teodosiu-Hu model
n_P	Parameter in Teodosiu-Hu model
p	Probability
p_i	Parameter
$\mathbf{q}$	Vector of nodal values
r	Parameter in Teodosiu-Hu model
	r-ratio (Lankford coefficient)
	Radius

$\mathbf{s}$	Deviator of the Cauchy stress tensor
$s_1,\ s_2,\ s_3$	Principal values of the stress deviator
s_R	Parameter in Voce law
s_X	Parameter in Armstrong-Frederick law
t	Current thickness
	Time
$\mathbf{t}$	External surface loads
t_0	Initial thickness
t_H	Thickness of the homogeneous zone
$\mathbf{u}$	Displacement field
u,v,w	Components of a lattice direction
w	Current width
w_0	Initial width
$\mathbf{x}$	Nodal position vector
$x_1,\ x_2,\ x_3$	Coordinates in the local axes
z	Displacement
A	Parameter in Johnson-Cook model
	Current area of a cross-section
A_H	Area of the homogeneous zone
B	Material constant in the Lou *et al.* (2013) approach
	Parameter in Johnson-Cook model
$\mathbf{B}$	Transformed strain rate tensor
	Strain-displacement tensor
$B_1,\ B_2,\ B_3$	Principal values of the transformed strain rate tensor $\mathbf{B}$
C	Parameter in Johnson-Cook model
$\mathbf{C}$	Fourth-order tensor used in CPB06 yield criterion
$C_0,\ C_1,\ C_3,\ C_4,\ C_5$	Parameters in Zerilli-Armstrong model

$\mathbf{C}^e$	Fourth-order elasticity tensor
$\mathbf{D}^p$	Plastic strain rate tensor
E	Error function
F	Parameter in Hill (1948) yield criterion
	Force
$\mathbf{F}$	Deformation gradient tensor
$\mathbf{F}^{\text{ext}}$	Nodal external force vector
F_H	Force acting on the homogeneous zone
$\mathbf{F}^{\text{int}}$	Nodal internal force vector
$\mathbf{F}^{\text{OOB}}$	Out-of-balance force vector
F_T	Total force
G	Parameter in Hill (1948) yield criterion
H	Parameter in Hill (1948) yield criterion
$\mathbf{H}$	Fourth-order tensor used in SRP09 yield criterion
	Shape function matrix
$\mathcal{H}$	Fourth-order tensor used in the Noman *et al.* (2010) approach
$\mathcal{H}_d$	Fourth-order tensor used in the Noman *et al.* (2010) approach
$\mathcal{H}_l$	Fourth-order tensor used in the Noman *et al.* (2010) approach
$\mathbf{I}$	Second-order identity tensor
I_1	First invariant of the Cauchy stress tensor
J_2	Second invariant of the stress deviator
J_2^0	Extension of the second invariant J_2
J_3	Third invariant of the stress deviator
J_3^0	Extension of the second invariant J_3
K	Parameter in Swift law
$\mathbf{K}$	Fourth-order symmetric deviatoric unit tensor
	Tangent stiffness tensor

L	Parameter in Hill (1948) yield criterion
$\mathbf{L}$	Fourth-order tensor used in Barlat *et al.* (1991) yield criterion
M	Parameter in Hill (1948) yield criterion
$\mathbf{M}$	Mandel stress tensor
N	Parameter in Hill (1948) yield criterion
$\mathbf{N}$	Current direction of the plastic strain rate tensor
$\mathbf{P}$	Internal variable (second-order tensor) used in Teodosiu-Hu model
P_D	Variable used in Teodosiu-Hu model
$\mathbf{Q}$	Stress potential gradient
R	Internal variable in Voce law
	Radius
$\mathbf{R}$	Rotation tensor
	Reaction
R_0	Initial yield stress
S	Surface
	Sensitivity
$\mathfrak{S}$	Internal variable (fourth-order tensor) used in Teodosiu-Hu model
S_D	Variable used in Tedosiu-Hu model
$\mathfrak{S}_L$	Variable (fourth-order tensor) used in Teodosiu-Hu model
S_{sat}	Parameter in Teodosiu-Hu model
T	Temperature
$\mathbf{T}$	Second-order tensor
T_{melt}	Melting temperature
T_{room}	Room temperature
$\mathbf{U}$	Stretch tensor
V	Volume
W_E	External work

W_H	Homogeneous strain field width
W_I	Internal work
W_p , W^p	Plastic work per unit of volume
W_T	Total width
$\mathbf{X}$	Back-stress tensor
$\mathbf{X}'$	Deviator of the back-stress tensor
X_0	Parameter in Teodosiu-Hu model
X_1, X_2, X_3	Coordinates in the material axes
X_{sat}	Parameter in Teodosiu-Hu model
Y	Threshold function

Greek characters

α	Orientation of the loading direction with respect to RD during a test
	Coefficient
	Temperature reduction rate
α_i	Constant
β_i	Constant
γ	Shear strain
γ_i	Constant
δ_{ij}	Components of the Kronecker delta
ε	True strain
$\dot{\bar{\varepsilon}}$	Equivalent strain rate
ε_0	Parameter in Swift law
$\dot{\bar{\varepsilon}}_0$	Reference plastic strain rate (Johnson-Cook model)
ε_{ave}	Average strain

$\boldsymbol{\varepsilon}^B$	Biot strain tensor
ε^e	Elastic strain
$\dot{\boldsymbol{\varepsilon}}^e$	Elastic strain rate tensor
$\boldsymbol{\varepsilon}^G$	Green-Lagrange strain tensor
$\boldsymbol{\varepsilon}^N$	Hencky/logarithmic/natural/true strain tensor
ε^p	Plastic strain
$\boldsymbol{\varepsilon}^p$	Plastic strain tensor
$\dot{\varepsilon}^p$	Plastic strain rate
$\dot{\boldsymbol{\varepsilon}}^p$	Plastic strain rate tensor
$\bar{\varepsilon}^p$	Equivalent plastic strain
$\dot{\bar{\varepsilon}}^p$	Equivalent plastic strain rate
η	Weighting factor
θ	Loading direction
λ	Angle between the loading direction and a slip direction
$\dot{\lambda}$, $\dot{\lambda}'$	Plastic multiplier
μ	Proportional scalar determined by the consistency condition (Ziegler law)
	Friction coefficient
ν	Poisson ratio
ξ	Boundary
ρ	Density
σ	Normal stress
$\bar{\sigma}$	Equivalent yield stress associated to a yield criterion
$\bar{\sigma}_s$	Equivalent yield stress associated to a symmetric yield criterion
$\boldsymbol{\sigma}$	Cauchy stress tensor
σ_0, σ_0'	Reference stress
σ_1, σ_2, σ_3	Principal values of the Cauchy stress tensor

σ_F	Yield stress under uniaxial tension in a reference direction
σ^C	Yield stress under uniaxial compression
$\bar{\sigma}_s$	Equivalent yield stress associated to a symmetric yield function
σ^T	Yield stress under uniaxial tension
τ	Shear stress
τ_C	Critical resolved shear stress
τ_Y	Yield stress in pure shear
ϕ	Angle between the loading direction and the normal to a slip plane
ϕ_1, ϕ_2	Functions in Karafillis and Boyce (1993) yield criterion
φ	Yield function
χ	Weighting factor
ψ	Strain rate potential
Θ	Hardening rate
$\mathbf{\Sigma}$	Transformed stress tensor
Σ_1, Σ_2, Σ_3	Principal values of the transformed stress tensor $\mathbf{\Sigma}$
Φ	Plastic potential function

Part I General introduction

Chapter 1 Introduction

1.1. General context of the thesis

Nowadays, Ti6Al4V titanium alloy is widely used in various industrial sectors (Figure 1-1) for its high strength-to-weight ratio, its good corrosion resistance and its biocompatibility. Many applications can be found in aerospace (turbine engine, airframe applications), medical (surgical implants), luxury automotive (valves, valve springs, connecting rods, rocker arms) and petrochemical industries (heat exchangers, reactors), see Boyer *et al.* (1994), Lütjering and Williams (2007). For example, recent investigations have been conducted to replace steel in aircraft engine parts by Ti6Al4V and to reduce by 10% the mass of the structure (Wallon Region project Winnomat 2 Fabulous, see Tuninetti (2014)).

a

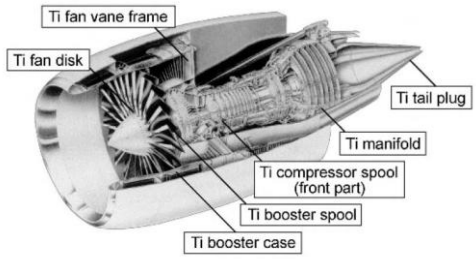

b

c

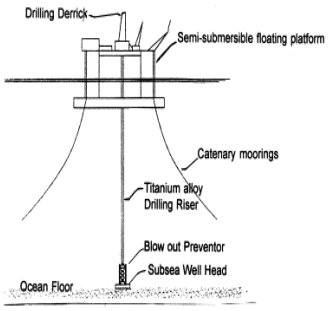

d

Figure 1-1 Examples of applications using Ti6Al4V titanium alloy in (a) aerospace, (b) defense, (c) petrochemical industry, (d) medical industry.

The alloy consists of an α-phase which is hexagonal closed-packed (hcp) and a β-phase which is body centered cubic (bcc). The volume fractions may be different, depending on heat treatment and interstitial content. The microstructure is also affected by the mechanical treatment and can show different geometrical arrangements of both phases (see Chapter 2). The material exhibits a pronounced anisotropy and a strength asymmetry between tension and compression.

Several studies have been performed to understand the mechanical behavior of Ti6Al4V and to model it, in moderate as well as in high strain rates and temperatures (see for instance Khan *et al.* (2004), Khan *et al.* (2007), Peirs (2012), Picu and Majorell (2002), Salem and Semiatin (2009)). However the development of phenomenological yield criteria for hcp metals is not very significant. Indeed anisotropic formulations developed for materials with cubic structure (Hill (1948), Karafillis and Boyce (1993), Ferron *et al.* (1994), Cazacu and Barlat (2003), Rabahallah *et al.* (2009)) are still used in FEM simulations involving hcp metals. However studies such as Kuwabara *et al.* (2001) show that classic plasticity models (J_2-flow theory, Hill (1948)) are not able to capture the observed response. In order to overcome this lack of phenomenological formulations adapted to hcp metals, new criteria which are able to take into account both plastic anisotropy and tension-compression asymmetry have recently been developed (Cazacu *et al.* (2006), Plunkett *et al.* (2008), Nixon *et al.* (2010)).

Based on this context, the present thesis which has been performed at the MS^{2}F division from the ArGEnCo department of the University of Liège proposes a comprehensive experimental and theoretical investigation of the quasi-static mechanical behavior of Ti6Al4V at room temperature. In order to complete this work successfully, several collaborations were led with different scientific teams:

- Prof. O. Cazacu (University of Florida – REEF, USA) who helped in the development and the implementation of the phenomenological constitutive law used into the finite element code LAGAMINE to model hcp materials;
- Prof. T. Kuwabara (Tokyo University of Agriculture and Technology, Japan), Prof. S. Thuillier (Université de Bretagne-Sud – LIMATB, France), Prof. G. Ferron (Université Paul Verlaine-Metz – LPMM, France) and Prof. T. Balan (Arts et Métiers ParisTech – LEM3, France) who helped in the achievement of some experimental tests.

The thesis was also incorporated within the framework of the IAP project P6/24 (Physics based multilevel mechanics of metals) which lasted from 2007 to 2011. Further interactions held in the on-going IAP project P7/21 (INTEMATE – Multiscale mechanics of interface dominated materials, 2012-2017).

1.2. Objectives of the thesis

The main objectives of the thesis are the following ones:

1. The achievement of a large experimental campaign in order to characterize the mechanical behavior of Ti6Al4V under monotonic and complex strain paths;

2. The implementation of a phenomenological model adapted to describe the mechanical behavior of Ti6Al4V into the finite element code LAGAMINE;

3. The identification of the parameters included in the proposed phenomenological modeling based on the experimental tests conducted on the material;

4. The validation of the phenomenological model by comparing the finite element results with the experimental data obtained from the tests under complex strain paths.

1.3. Contributions of the thesis

Three main original contributions provided by this thesis can be highlighted:

1. Generation of a large data base on the mechanical behavior of a 0.6 mm thick Ti6Al4V sheet. This set of experimental data allowed a better understanding and a quantification of the plastic anisotropy and the tension-compression asymmetry displayed by the material. In addition the results from layer compression tests (developed from the works of Tuninetti (2014)) and deep-drawing processes were used to study the ability of the modeling to predict the response of Ti6Al4V. It has to be noted that, in order to acquire skills in the practice of laboratory work, I conducted the tensile, plane strain, simple shear, Bauschinger and layer compression tests at the Materials and Structures Mechanics Laboratory, and I participated in the achievement of the deep-drawing tests by Prof. T. Balan at LEM3.

2. Implementation of the CPB06ex*n* yield criteria family associated to a hardening formulation taking into account the evolution of the yield locus shape into LAGAMINE code. Since the experimental tests conducted on Ti6Al4V revealed anisotropy in hardening, a model considering a dependence of the parameters with the plastic deformation was developed with the help of Prof. O. Cazacu.

3. Development of a procedure to identify the material parameters based on the simulated annealing method. The formulation of the yield criteria CPB06ex*n* does not enable to easily determine the parameters from the experimental data (yield stresses and tensile *r*-ratios). For this reason, the classical simulated annealing algorithm was selected and adapted to fit the theoretical yield locus using the experimental one.

1.4. Content of the thesis

The thesis is divided into eight chapters. The first one is the present introduction which describes the context, the objectives and the contributions of the thesis.

Chapter 2 reviews some physical and metallurgical properties of titanium alloys, then focuses on the specific features of Ti6Al4V.

Chapter 3 presents a state of the art in the field of the phenomenological yield criteria and the hardening laws used to model the mechanical behavior of materials. A particular attention is given to the yield criteria adapted to metals with a hcp crystal structure and to hardening formulations taking into account the evolution of the yield locus shape with the plastic deformation.

Chapter 4 lists the different devices which enabled the achievement of the experiments conducted on Ti6Al4V sheet. The methodology used to analyse the results is then described for the different tests (tension, compression, plane strain, simple shear, compression of a layer stack, deep-drawing).

Chapter 5 deals with the results of the experimental campaign. The material characterization reveals the anisotropy in yield stresses, *r*-ratios and hardening exhibited by the studied Ti6Al4V sheet, as well as the strength differential effect between tension and compression.

Chapter 6 describes the implementation of the CPB06 yield criterion and its extensions (CPB06ex*n* family) into the finite element code LAGAMINE. These criteria are associated to two hardening formulations. The first one considers Voce isotropic hardening law combined to Armstrong-Fredericks kinematic law, while the second model takes into account the evolution of the parameters included in the yield criteria with the plastic work.

Chapter 7 presents the parameter identification. The principle of different optimization methods is first explained. The identification of the initial and subsequent yield loci is then performed using the classical simulated annealing algorithm, while the hardening parameters involved in Voce and Armstrong-Frederick laws are determined by inverse method.

In Chapter 8, the validation of the different models proposed in this work is investigated in the case of the layer compression tests and the deep-drawing processes by comparing the finite element predictions with the experimental results.

Finally, Chapter 9 proposes conclusions about the thesis and suggests further studies.

Five appendices can be found after Chapter 9. Three of these appendices concern the CPB06 yield criterion and particularly its convexity (appendix A), its insensitivity to hydrostatic pressure (appendix B) and the computation of the associated stress potential gradient (appendix E). The appendices C and D detail the determination of the stress-strain curves relative to the plane strain tests and the computation of the yield stresses for different strain paths, respectively.

The references are listed at the end of the manuscript.

Chapter 2 Titanium and titanium based alloys

A large part of this study concerns the experimental characterization of the quasi-static mechanical response displayed by Ti6Al4V titanium alloy under different loading conditions. For any material, the observed behavior is intimately related to the physical properties and the deformation mechanisms which can be activated. Thereby it seemed interesting to review some basic characteristics of titanium and its alloys firstly, then to describe the specific features of Ti6Al4V. This chapter provides physical and metallurgical data from literature which enable to understand the macroscopic mechanical behavior of titanium alloys, especially the investigated material.

2.1. Crystal structure

In Table 2-1 are shown some basic properties of titanium (Lütjering and Williams (2007)). Pure titanium displays a hexagonal close-packed structure (α-phase) below 882°C (see Figure 2-1 and Figure 2-2). At temperatures higher than this limit called the β-transus, an allotropic phase transformation occurs, changing the hexagonal structure to a body-centered cubic structure (β-phase). Titanium enters the liquid phase when reaching the melting temperature at 1670°C.

Melting temperature [°C]	1670
Allotropic transformation $\beta \rightarrow \alpha$ [°C]	882
Young modulus at room temperature [GPa]	115
Yield stress level [MPa]	1000
Density [kg/m³]	4500

Table 2-1 Important properties of titanium

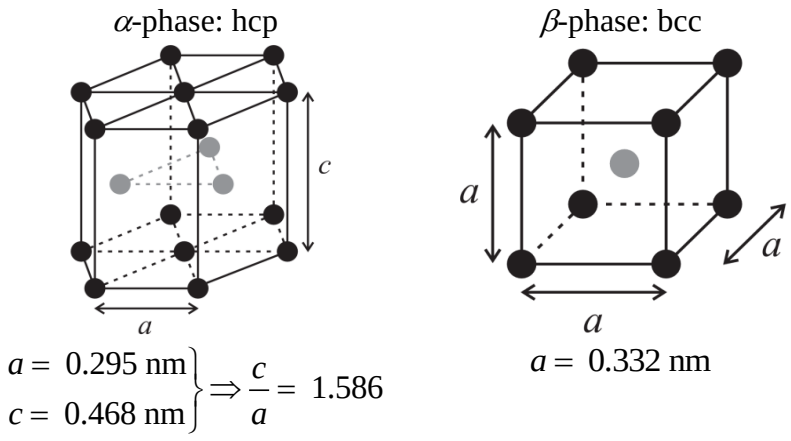

Figure 2-1 Unit cell and lattice parameters of the α-phase at room temperature and the β-phase at 900°C

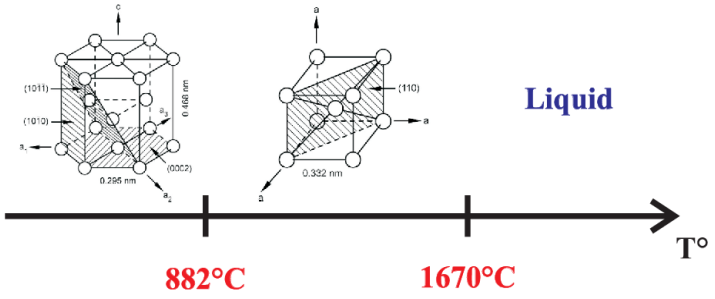

Figure 2-2 Allotropic transformation of titanium

Alloying elements can influence the β-transus of pure titanium and are usually classified into three different types:

- The **α-stabilizing elements** increase the β-transus with increasing solute content (see Figure 2-3). Aluminum is the most widely used alloying element in titanium alloys owing to its large solubility in both the α- and β-phases. Oxygen (used to modify the strength level), carbon and nitrogen are other examples of α-stabilizers.
- The **β-stabilizing elements** decreases the β-transus with increasing solute content (see Figure 2-3). They are divided into two categories:
    - β-isomorphous elements (V, Mo, Nb, …) which make possible the stabilization of the β-phase to room temperature when used in sufficient concentrations.
    - β-eutectoid elements (Cr, Fe, Si, …) which can lead to the formation of intermetallic compounds Ti_xA_y.
- The **neutral elements** (Zr, Sn) which have no or a weak influence on the β-transus.

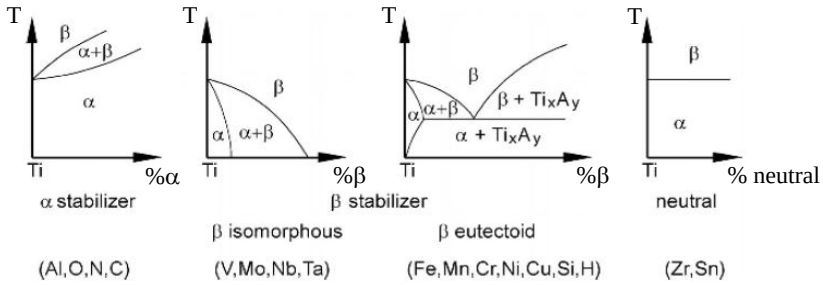

Figure 2-3 Schematic phase diagrams showing the effect of alloying elements (Lütjering and Williams (2007))

Several binary phase diagrams, as illustrated in Figure 2-4, can be found in Boyer *et al.* (1994) and Lütjering and Williams (2007). Generally, it is to be noted that most commercial titanium alloys include more than two elements. In principle, ternary or quaternary phase diagrams (see Figure 2-5) should be used. In practice, only binary diagrams are used as a qualitative guideline.

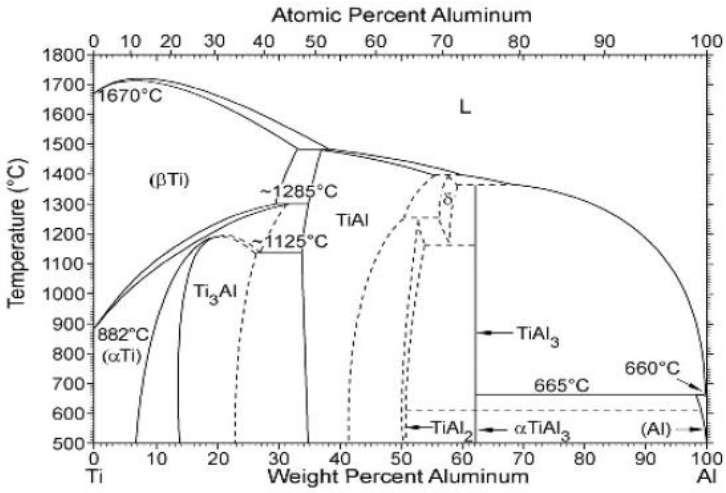

Figure 2-4 Ti-Al phase diagram (Lütjering and Williams (2007))

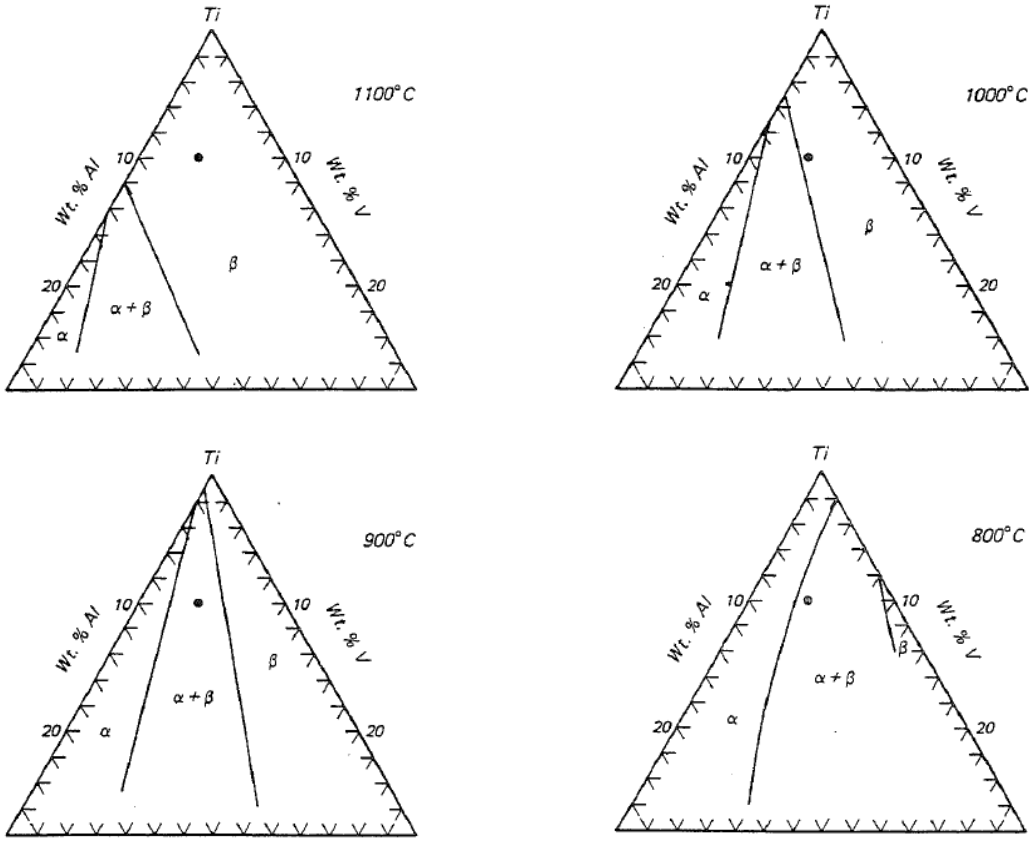

Figure 2-5 Isothermal sections of the ternary Ti-Al-V phase diagram at different temperatures (Boyer et al. (1994)); the black dot corresponds to Ti6Al4V titanium alloy

2.2. Alloy classification

According to their position in a pseudo-binary section through a β-isomorphous phase diagram (Figure 2-6), commercial titanium alloys are generally classified as follows:

- **α-alloys** are characterized by satisfactory strength, toughness, creep resistance and weldability. They are suitable for cryogenic applications owing to the absence of a ductile-brittle transformation. The β-phase volume fraction is low (2-5%).
- **α+β-alloys** are widely used. They generally display high strength at room and moderate temperatures. Their properties can be controlled by heat treatments. The group of α+β-alloys has a range from the α/α+β phase boundary up to the intersection of the M_S-line with room temperature happens. The M_S-line represents the boundary from which a martensitic transformation occurs when fast cooling from the β-phase domain to room temperature. The β-phase volume fraction may vary from 10 to 50% at room temperature.
- **β-alloys** are actually metastable β-alloys owing to their location in the equilibrium α+β phase region[1]. They are interesting for their extreme formability, but are unsuitable for low temperature applications. A characteristic feature of these alloys is that they do not transform martensitically upon fast cooling from the β-phase domain.

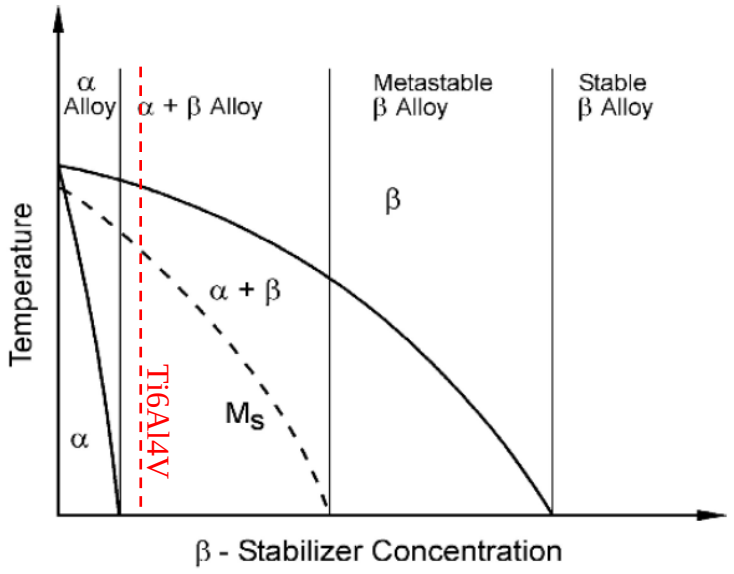

Figure 2-6 Schematic pseudo-binary section through a β-isomorphous phase diagram (Lütjering and Williams (2007))

[1] Actually the stable β-alloys do not exist as commercial materials. This is the reason why the expression "β-alloys" is commonly used to refer to metastable β-alloys.

2.3. Deformation mechanisms

The plastic deformation of crystalline materials is related to the slip of some crystallographic planes which is due to the motion of dislocations. Usually, the slip planes and the slip directions are those with the highest packing density. In the case of single crystals, slip systems are activated when the applied stress σ reaches a critical value depending on the critical resolved shear stress (CRSS) τ_C, the angle ϕ between the loading direction and the normal to the slip plane $\underline{n}$, and the angle λ between the loading direction and the slip direction $\underline{m}$ (see Figure 2-7). This condition is given by Schmid's law for each slip system characterized by $\underline{m}$ and $\underline{n}$:

$$\sigma = \frac{\tau_c}{\cos\phi.\cos\lambda} \tag{2.1}$$

where $\cos\phi.\cos\lambda$ is called the Schmid factor and ranges from 0 to 0.5.

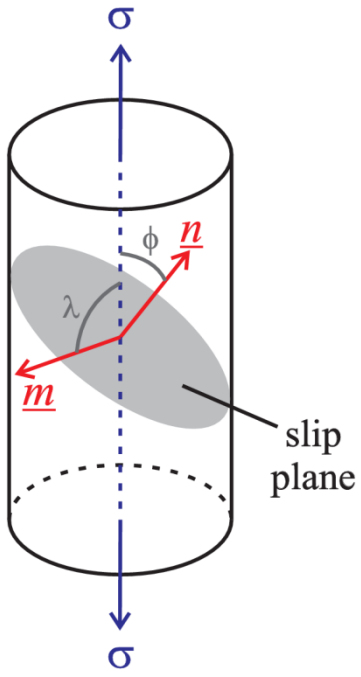

Figure 2-7 Determination of the CRSS

In the case of polycrystals, the conventional dislocation glide on slip systems remains the main source of plastic deformation, but the behavior significantly differs from the one of single crystals. Indeed, polycrystalline materials include numerous crystals with different orientations and having common boundaries. In order to satisfy the stress and strain continuity across the grain boundaries, several slip systems are activated and the geometrically necessary dislocations appear due to strain gradient.

In the following sections, the main slip systems which can be activated in titanium and its alloys are introduced. In addition, some details are given about *twinning* which may play an important role in the response of these materials.

2.3.1. Slip systems

Before detailing the different slip systems in titanium, it is advisable to give a brief summary of the Miller index notation.

In crystallography, the lattice planes are defined by their *Miller indices*, *i.e.* three integers related to the intersections between the plane and the coordinate axes (Figure 2-8). If a_1, a_2, a_3 denote these intersections, the Miller indices h, k, l are respectively given by:

$$h = \frac{d}{a_1}, k = \frac{d}{a_2}, l = \frac{d}{a_3} \tag{2.2}$$

where d is the smallest common denominator of a_1, a_2, a_3. A lattice plane is designated by $(h\,k\,l)$ while the notation $\{h\,k\,l\}$ denotes the set of the equivalent planes.

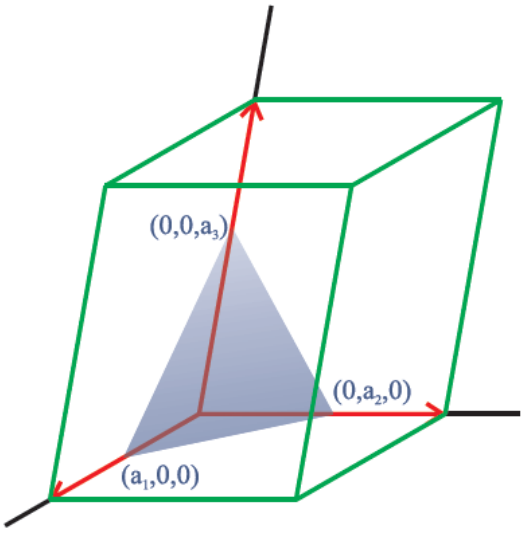

Figure 2-8 Miller indices

In a similar way, the lattice directions are expressed by three integers u, v, w proportional to the components of the directional unit vector. A lattice direction is expressed by $[u\,v\,w]$ while the set of the equivalent directions is denoted by $\langle u\,v\,w\rangle$.

In the case of a hexagonal system, it is convenient to use four coordinate axes, as shown in Figure 2-9. Thereby it is possible to use a four-digit set of Miller-Bravais indices (h, k, i, l) where i is a redundant index defined by:

$$i = -h - k \tag{2.3}$$

The advantage of this notation for labeling planes and directions in a hexagonal lattice is to make the permutation symmetries apparent.

The main slip directions observed in the hexagonal α-phase of titanium and titanium alloys are those of the type $\langle 11\bar{2}0 \rangle$[2], also named $\langle a \rangle$-direction. Three different categories of slip planes are associated to this direction:

- The **basal** planes (0002)
- The **prismatic** planes $\{10\bar{1}0\}$
- The **pyramidal** planes $\{10\bar{1}1\}$

It is also observed the presence of $\langle c+a \rangle$ dislocations ($\langle 11\bar{2}3 \rangle$ direction) which is explained by the fact that, when the *c*-axis of a grain is oriented along the direction of the applied stress, $\langle a \rangle$ dislocations cannot be activated owing to the null value of their Schmid factor. From the possible slip planes, $\{10\bar{1}1\}\langle 11\bar{2}3 \rangle$ and $\{11\bar{2}2\}\langle 11\bar{2}3 \rangle$ slip systems are feasible. The second one is more likely to be activated because of its high Schmid factor when the loading direction coincides with the *c*-axis. A schematic view of the different slip planes and slip directions is given in Figure 2-9. Table 2-2 lists the main slip systems and their number.

Concerning the bcc β-phase, the main slip systems are $\{110\}\langle 111 \rangle$ and $\{112\}\langle 111 \rangle$ (see Table 2-2). Some studies (e.g. Gil Sevillano *et al.* (1980), Turkmen *et al.* (2002)) include other slip systems such as $\{123\}\langle 111 \rangle$.

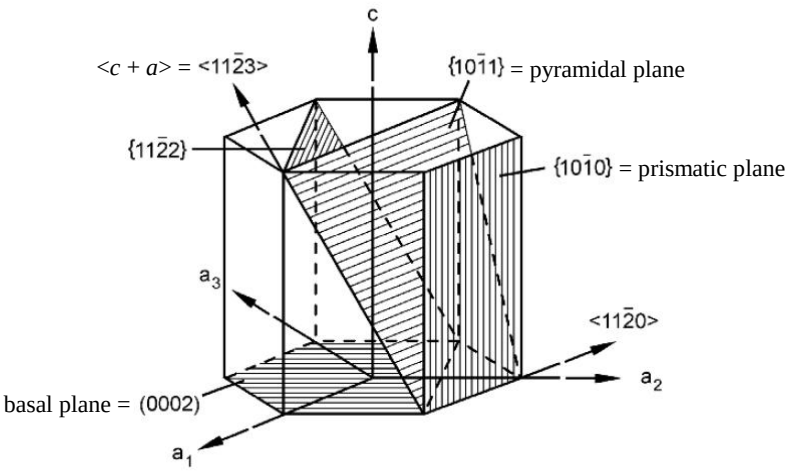

Figure 2-9 Representation of the different slip planes and slip directions in the hexagonal α-phase (Lütjering and Williams (2007))

[2] In Miller notation, a negative index is written with a bar above the corresponding integer.

	Slip direction	Slip plane	Number of slip systems	
			Total	Independent
hcp α-phase	$\langle 11\bar{2}0 \rangle$	(0002)	3	2
	$\langle 11\bar{2}0 \rangle$	$\{10\bar{1}0\}$	3	2
	$\langle 11\bar{2}0 \rangle$	$\{10\bar{1}1\}$	6	4
	$\langle 11\bar{2}3 \rangle$	$\{11\bar{2}2\}$	6	5
bcc β-phase	$\langle 111 \rangle$	$\{110\}$	12	
	$\langle 111 \rangle$	$\{112\}$	12	

Table 2-2 Main slip systems in the hcp α-phase and bcc β-phase

2.3.2. Twinning

Twinning is a deformation mechanism characterized by a re-orientation of the crystal lattice (Figure 2-10). The atoms move in such a way that the initial lattice and the twinned part are symmetric with respect to a plane called *twin plane*. This mechanism has the effect of changing the orientation of the crystal lattice and consequently the possible slip planes with respect to the external loading. Therefore, owing to this re-orientation, some dislocations can be activated in the twinned part.

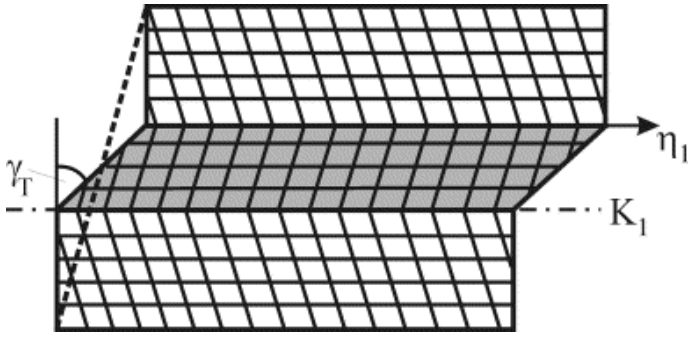

Figure 2-10 Re-orientation of the crystal lattice owing to twinning (Marketz et al. (2003)): K_1 and η_1 are the twinning plane and shear direction, respectively

Twinning is a significant deformation mechanism in commercially pure (CP) titanium and some α titanium alloys, but is almost inhibited in α+β alloys due to the small phase dimensions (see Section 2.4.2), high solute content and presence of Ti_3Al precipitates.

The main twinning systems observed in pure α titanium are $\{10\bar{1}2\}\langle 10\bar{1}\bar{1} \rangle$, $\{11\bar{2}1\}\langle 11\bar{2}\bar{6} \rangle$ and $\{11\bar{2}2\}\langle 11\bar{2}\bar{3} \rangle$. Under tension loading parallel to the *c*-axis, the first two modes are activated, the most frequent being $\{10\bar{1}2\}\langle 10\bar{1}\bar{1} \rangle$ twin mode. In the case of a compression along the *c*-axis, $\{11\bar{2}2\}\langle 11\bar{2}\bar{3} \rangle$ twins are activated. As said previously, twinning plays a major role in pure titanium or CP titanium with low oxygen concentrations. Indeed, the occurrence of twins decreases when increasing the solute atom concentrations in α titanium, such as oxygen or aluminum.

2.4. Features of Ti6Al4V titanium alloy

Ti6Al4V, also named TA6V or Ti64, is the most widely used titanium alloy. One of its usages is found in the aerospace industry. The following list gives several applications in this field (Boyer *et al.* (1994)):

- engine components (blades, discs, wheels) ;
- complex housings ;
- airframe components (cargo-handling equipment, flow diverters, torque tubes for brakes, helicopter rotor hubs);
- missile and space components (wings, missile bodies, optical sensor housings, ordnance).

This work focusing on the mechanical characterization of Ti6Al4V, specific features of the alloy are given in the next sections.

2.4.1. Chemical composition

As suggested by the designation of the alloy, Ti6Al4V contains about 6% of aluminum and 4% of vanadium. The other important alloying elements are oxygen, nitrogen and iron. These elements, in particular oxygen and nitrogen, increase the strength when increasing their content. Conversely, it is possible to improve the ductility thanks to lower additions of oxygen, nitrogen and aluminum. Table 2-3 lists the chemical composition of this alloy in different studies.

Elements	Ti [%]	Al [%]	V [%]	O [%]	N [ppm]	C [ppm]	H [ppm]	Fe [%]
Follansbee and Gray (1989)	Bal.	6.4	4.0	0.18	10	650	-	0.13
Philippe *et al.* (1995)	Bal.	6.08	3.87	0.1474	71	231	-	0.15
Medina Perilla and Gil Sevillano (1995)	Bal.	6.03-6.11	3.83-3.90	0.10-0.11	40-50	30-80	<5	0.13-0.16
Fundenberger *et al.* (1997)	Bal.	6.08	3.87	0.147	71	230	11	0.15
Nemat-Nasser *et al.* (2001)	Bal.	6.21-6.33	3.61-4.13	0.19-0.2	80-100	100-200	6-20	0.19-0.21
Majorell *et al.* (2002)	Bal.	6.31	4.06	0.18	80	160	9-14	1.16
Khan *et al.* (2004)	Bal.	5.97	4.09	0.174	80	430	41	0.15
Gilles *et al.* (2011)	Bal.	6.22-6.27	3.93-4.00	0.19-0.20	60.0	80.0-90.0	86.0-100.0	0.16

Table 2-3 Chemical composition of Ti6Al4V found in the literature

2.4.2. Microstructure

As shown in Figure 2-5 and Figure 2-11, Ti6Al4V is an $\alpha+\beta$ alloy at room and higher temperatures (the β-transus is ~995°C or 1268 K). The volume fractions of both α and β-phases and their geometrical arrangements may be different, depending on the thermomechanical treatment (Figure 2-11) and the interstitial content (mainly oxygen). Usually, the β-phase volume fraction does not exceed 10% (see Philippe *et al.* (1995), Medina Perilla and Gil Sevillano (1995), Fundenberger *et al.* (1997), Bridier *et al.* (2005)).

In general, three different microstructures can be distinguished (Boyer *et al.* (1994)):

- **Lamellar structures** are readily obtained by slow cooling into the two-phase domain from above the β-transus. The nucleation and the growth of the α-phase in plate form starting from β-grain boundaries mainly depend on the cooling rate.
- **Equiaxed microstructures** can be produced by extensive mechanical working in the $\alpha+\beta$ domain. This process causes the breakup of lamellar α-grains into equiaxed α-grains. The so-called *mill-annealed* microstructure is obtained by subsequent annealing at about 700°C. Another technique to produce equiaxed microstructures involves a recrystallization annealing of 4h at 925°C followed by slow cooling, which results in coarse α-grains.
- **Bimodal type microstructures** consist of isolated primary α-grains in a transformed β-matrix. They can be produced by a 1h annealing at 955°C followed by water quenching or air cooling, and aging at 600°C.

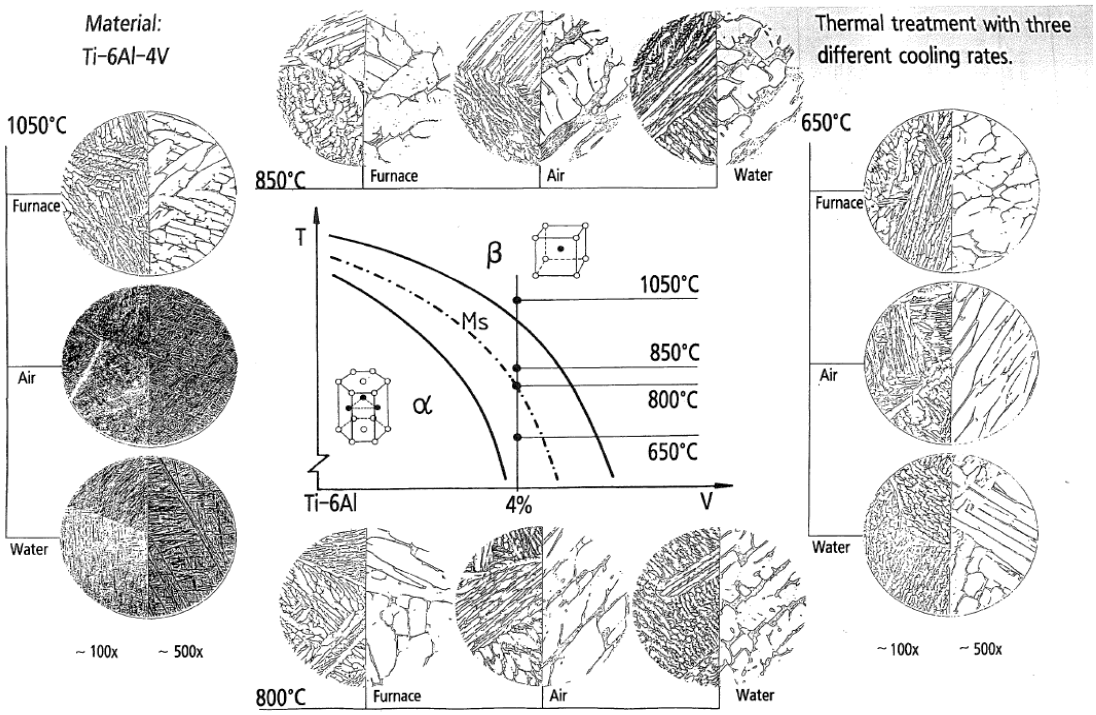

Figure 2-11 Influence of thermal treatment and cooling rate on the microstructure of Ti6Al4V (Boyer et al. (1994))

2.4.3. Mechanical properties

2.4.3.1. Elastic properties

According to the literature, Young modulus of Ti6Al4V varies from 100 to 130 GPa while Poisson ratio ranges from 0.26 to 0.36 at room temperature (Boyer *et al.* (1994); Fukuhara and Sanpei (1993); Bruno and Dunn (1997)). The elastic coefficients are influenced by:

- the volume fraction of the phases and thus the thermomechanical treatment
- the specimen orientation in textured rolled sheet
- the interstitial and substitutional elements
- ageing

2.4.3.2. Slip systems and twinning

Owing to the reduced number of available slip systems compared to bcc and fcc crystal lattices, hcp metals generally display a pronounced anisotropic behavior. This anisotropy is also influenced by the initial texture of the material, as observed in Lowden and Hutchinson (1975) in the case of Ti6Al4V (Figure 2-12). In general, the experimental analysis of active slip systems by EBSD or TEM reveals the following decreasing order of contribution (Philippe *et al.* (1995); Fundenberger *et al.* (1997); Bridier *et al.* (2005)):

- Prismatic slip $\{10\bar{1}0\}\langle 11\bar{2}0\rangle$
- Basal slip $(0002)\langle 11\bar{2}0\rangle$
- Pyramidal slip $\{10\bar{1}1\}\langle 11\bar{2}3\rangle$

Another specific feature exhibited by hcp materials is the strength asymmetry between tension and compression as shown in Figure 2-13 (Graff *et al.* (2007); Lee *et al.* (2008); Kim *et al.* (2008); Medina Perilla and Gil Sevillano (1995); Fundenberger *et al.* (1997)). For most of them, this strength differential (SD) effect is due to the directionality of twinning. However, because of its high aluminum content, Ti6Al4V displays few twins (Lowden and Hutchinson (1975); Philippe *et al.* (1995); Medina Perilla and Gil Sevillano (1995); Fundenberger *et al.* (1997)). Recently, Tirry *et al.* (2010) have shown that only the $\{10\bar{1}2\}$ twin mode seems to be activated for monotonic deformations, moderate strains and strain rates, but a very low volume fraction is measured (less than 1%). Later Coghe *et al.* (2012) have investigated the importance of twinning in a Ti6Al4V titanium alloy subjected to static and dynamic compression tests. Depending on the orientation of the loading direction with respect to the initial texture, the twin fraction can reach a value of 4.8% in the static case and 8.9% in the dynamic case. Lowden and Hutchinson (1975) suggested that the $\langle c+a\rangle$ dislocations play a significant role in plasticity of Ti6Al4V at room temperature and can explain the SD effect. It was observed that their motion is asymmetric, *i.e.* the CRSS is different in the forward and backward directions, and unusually sensitive to hydrostatic pressure. Later, Jones and Hutchinson (1981) showed the occurrence of cross-slip when the $\langle c+a\rangle$ dislocations move on $\{10\bar{1}1\}$ planes in uniaxial compression along the *c*-axis, while cross-slip is not active in uniaxial tension. This results in asymmetry in the CRSS of $\langle c+a\rangle$ slip systems and thus also contributes to the occurrence of SD effects.

a

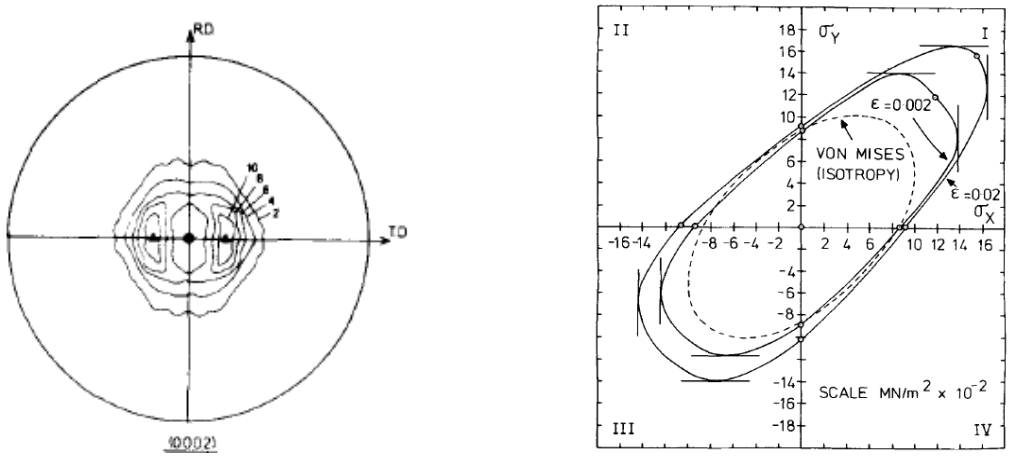

b

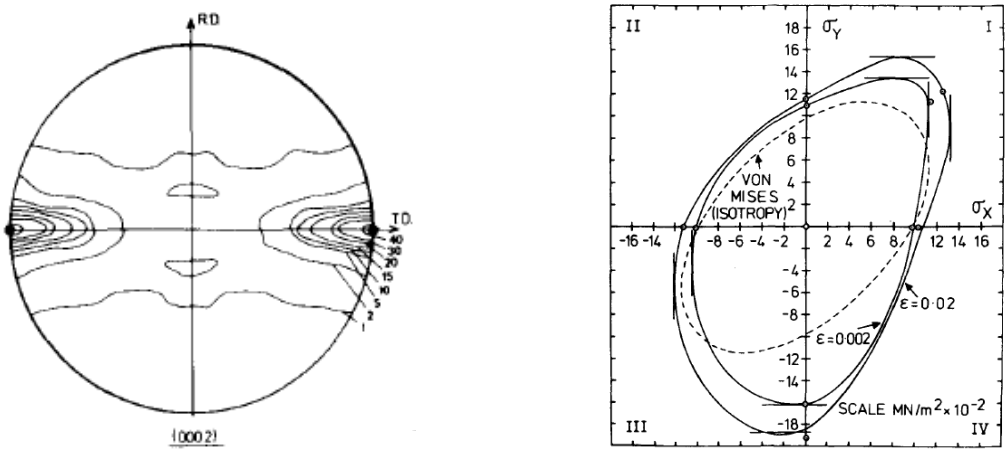

Figure 2-12 Initial texture ((0002) pole figure) and yield loci at different equivalent strains of two batches of Ti6Al4V in sheet form: (a) material with high density of basal poles along ND; (b) material with strong maximum along TD (Lowden and Hutchinson (1975)). The theoretical yiel loci are determined using the method in Lee and Backofen (1966).

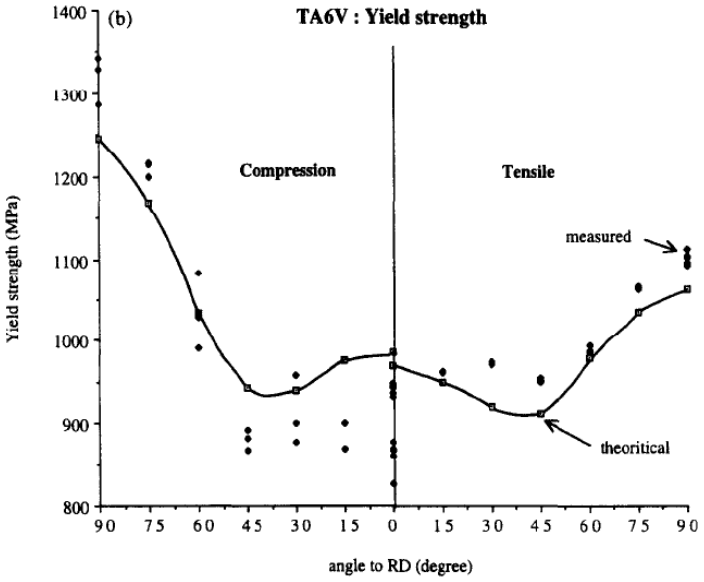

Figure 2-13 Anisotropy in tensile and compressive yield stresses for Ti6Al4V after Fundenberger et al. (1997): a significant tension-compression asymmetry in yielding is observed along TD

2.4.3.3. Effect of temperature and strain rate

Although this subject is not developed in this work, it has to be noted that Ti6Al4V is very sensitive to temperature and strain rate (see Figure 2-14). Several studies have been devoted to understand and model its mechanical behavior at high strain rates and high temperatures (Khan *et al.* (2004); Khan *et al.* (2007); Macdougall and Harding (1999); Majorell *et al.* (2002); Picu and Majorell (2002); etc.). In Figure 2-14, it can be noticed that:

- the yield stress and the work-hardening respectively increases and decreases when increasing the strain rate;
- the flow stress decreases when increasing the temperature.

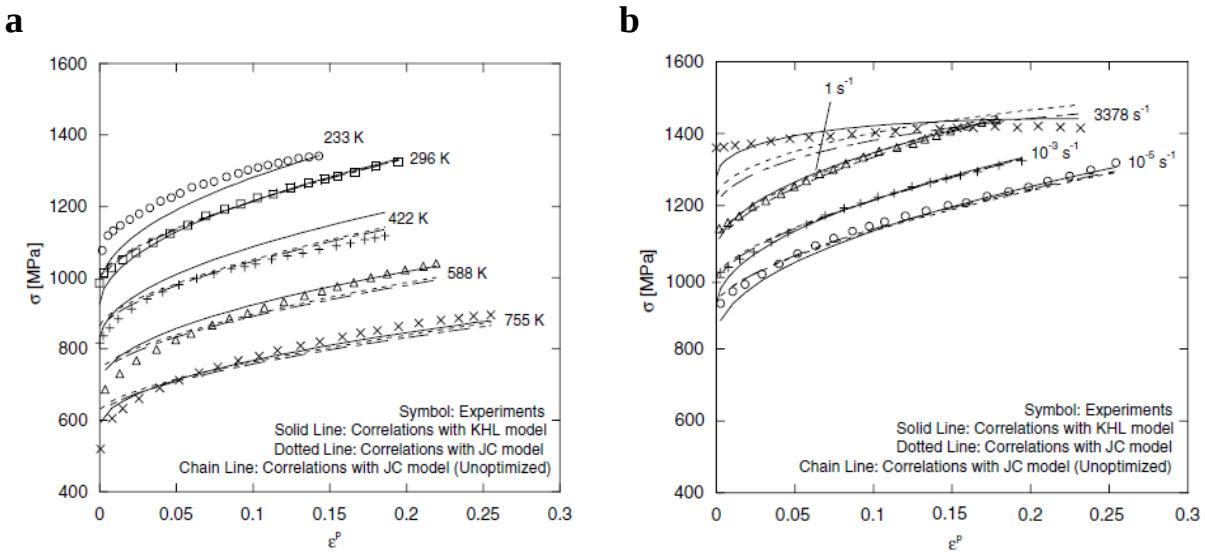

Figure 2-14 Influence of the temperature and the strain rate on the mechanical behavior of Ti6Al4V and correlations with Khan-Huang-Liang (KHL) and Johnson-Cook (JC) models: (a) compression tests at different temperatures and 10^{-3} s^{-1}; (b) compression tests at room temperature and different strain rates (Khan et al. (2004))

In addition, Majorell *et al.* (2002) showed that the decrease in flow stress with temperature is significant up to 1255 K. Above this value, the flow stress becomes almost insensitive to temperature. This marked difference in the mechanical behavior is due to the change in microstructure. Indeed, the β-phase volume fraction increases above 950 K until the β-transus. At 1230 K, the amount of β-phase is larger than 50% and begins to play a sizeable role on the material response.

2.5. Conclusion

This chapter defines the main physical and metallurgical properties of titanium alloys and especially Ti6Al4V. The microstructure and its evolution during the deformation of the material allow understanding and predicting the mechanical behavior at the macroscale. For instance, they can explain the dependence of the hardening with the strain path. However, in this work, it is proposed to use a phenomenological analysis which has to be able to model the macroscopic behavior of the material without modeling the microstructure evolution.

Chapter 3 Constitutive modeling of sheet metal mechanical behavior

The plastic behavior at macroscopic level exhibited by materials can be described by different approaches. In the industrial simulations, elastic-plastic models developed in the framework of the mathematical theory of plasticity (e.g. Hill (1948), Barlat *et al.* (1991), Karafillis and Boyce (1993)) are often used owing to their simplicity to be implemented in a finite element code, their reasonable accuracy and moderate CPU time. On the other hand, crystal plasticity based models (e.g. Sachs (1928), Taylor (1938), Delannay *et al.* (2002), Van Houtte *et al.* (2005)) include phenomenological elastic/plastic models at the single-crystal level and different homogenization techniques to obtain the response of the polycrystal. This explains their enhanced predictability of the mechanical behavior. Nevertheless, as the microscopic models are not the subject of this work, they will not be discussed since they are not the subject of the thesis.

All models are based on experimental observations concerning the onset of plastic deformation and its subsequent evolution under applied load. The onset of plasticity is described by an analytical yield function while the hardening is characterized by a flow rule. Both the yield function and the hardening law allow the subsequent plastic deformations to be computed for any loading and geometry. Depending on the specific mechanical properties which can be displayed by materials, phenomenological yield criterions can be sorted in different ways: isotropic or anisotropic formulations; symmetric or asymmetric functions; pressure sensitive or insensitive criteria; …

This chapter is divided into 3 sections. The first one introduces the notion of stress and strain rate potentials, while the second section deals with formulations for the description of the hardening. The last section gives some conclusions concerning the constitutive models.

3.1. Stress and strain rate potentials

The onset of plastic flow is generally described by a continuous yield function $\varphi\left(\sigma_{ij}\right)$, also called stress potential and depending on the components σ_{ij} of the Cauchy stress tensor. The yield locus is defined by the following relationship:

$$\varphi\left(\sigma_{ij}\right)=\sigma_0 \tag{3.1}$$

where σ_0 is a reference stress (for instance the uniaxial yield stress in tension along a specific direction). Based on the postulate stated by Drucker (1950) which gives a general definition of the stable work-hardening materials, it can be shown that this function must be convex in the space of the stress components. Another consequence is the normality of the strain rate vector to the yield surface, which induces that the flow rule is associated:

$$\dot{\varepsilon}_{ij}^{p}=\dot{\lambda}\frac{\partial\varphi}{\partial\sigma_{ij}} \tag{3.2}$$

$\dot{\lambda}$ is a positive scalar factor called plastic multiplier while $\dot{\varepsilon}_{ij}^{p}$ are the components of the plastic strain rate tensor. In most materials, the associated flow rule is a valid assumption. However, it can be violated, especially in soil mechanics. In this case, a plastic potential function Φ, different from the yield surface, must be defined. The non-associated flow rule is then expressed as:

$$\dot{\varepsilon}_{ij}^{p}=\dot{\lambda}\frac{\partial\Phi}{\partial\sigma_{ij}} \tag{3.3}$$

Another feature of most yield criterions, mainly for metals with low porosity, is the hydrostatic pressure insensitivity. Mathematically, it means that the yield function φ is independent of the first invariant of the stress tensor $I_1=\mathrm{tr}\left(\boldsymbol{\sigma}\right)=\sigma_{ii}$.

Based on the plastic work equivalence principle, Ziegler (1983) and Hill (1987) proved that it is possible to associate a strain rate potential $\psi\left(\dot{\varepsilon}_{ij}^{p}\right)$ with any convex stress potential $\varphi\left(\sigma_{ij}\right)$. This strain rate potential is defined by:

$$\psi\left(\dot{\varepsilon}_{ij}^{p}\right)=\dot{\lambda}' \tag{3.4}$$

with the following associated flow rule:

$$\sigma_{ij}=\sigma_0'\frac{\partial\psi}{\partial\dot{\varepsilon}_{ij}^{p}} \tag{3.5}$$

It has to be noted that $\sigma_0=\sigma_0'$ and $\dot{\lambda}=\dot{\lambda}'$ when the stress potential φ and the dual strain rate potential ψ are homogeneous of degree 1. In this section, some isotropic formulations are first presented. Next, a review of few anisotropic formulations, defined in the material

orthotropy axes, is proposed by choosing the following convention: direction 1 = rolling direction (RD), direction 2 = transverse direction (TD), direction 3 = normal direction (ND). It is worth noting that a particular attention is given to criterions adapted to describe the yield locus of hexagonal closed-packed materials (e.g. Cazacu *et al.* (2006); Plunkett *et al.* (2008); …).

3.1.1. Isotropic formulations

The two best-known isotropic yield criterions were developed by Von Mises and Tresca. The first one assumes that the yield limit is independent of the third invariant of the stress deviator $J_3 = \frac{1}{3}\mathrm{tr}\left(\mathbf{s}^3\right)$. The Von Mises criterion is of the form:

$$\varphi = \sqrt{\frac{1}{2}\left[\left(\sigma_{11}-\sigma_{22}\right)^2+\left(\sigma_{22}-\sigma_{33}\right)^2+\left(\sigma_{33}-\sigma_{11}\right)^2+6\left(\sigma_{12}^2+\sigma_{13}^2+\sigma_{23}^2\right)\right]} = \sigma^T \tag{3.6}$$

σ^T being the yield stress under uniaxial tension. It can be formulated in the following way:

$$\varphi = \sqrt{3J_2} = \sigma^T \tag{3.7}$$

where $J_2 = \frac{1}{2}\mathrm{tr}\left(\mathbf{s}^2\right)$ is the second invariant of the stress deviator $\mathbf{s} = \boldsymbol{\sigma} - \frac{1}{3}\mathrm{tr}\left(\boldsymbol{\sigma}\right)\mathbf{I}$, $\mathbf{I}$ denoting the second-order identity tensor. It can be defined a dual potential which is written as:

$$\psi = \sqrt{\frac{2}{3}\left[\left(\dot{\varepsilon}_{11}^p\right)^2+\left(\dot{\varepsilon}_{22}^p\right)^2+\left(\dot{\varepsilon}_{33}^p\right)^2+2\left(\dot{\varepsilon}_{12}^p\right)^2+2\left(\dot{\varepsilon}_{13}^p\right)^2+2\left(\dot{\varepsilon}_{23}^p\right)^2\right]} = \sqrt{\frac{2}{3}\dot{\varepsilon}_{ij}^p\dot{\varepsilon}_{ij}^p} \tag{3.8}$$

which is the definition of the Von Mises equivalent plastic strain rate.

In the Tresca yield criterion, the yield limit is linked to the maximal shear stress:

$$\varphi = \sup_{i\neq j}\left(\left|\sigma_i-\sigma_j\right|\right) = 2\tau_Y \tag{3.9}$$

where σ_i is the *i*-th eigenvalue of the stress tensor ($i = 1,2,3$) and τ_Y is the yield stress in pure shear . It can also be written as:

$$\varphi = 4J_2^3 - 27J_3^2 - 36\tau_Y^2J_2^2 + 96\tau_Y^4J_2 = 64\tau_Y^6 \tag{3.10}$$

where $J_3 = \frac{1}{3}\mathrm{tr}\left(\mathbf{s}^3\right)$ is the third invariant of the stress deviator.

The shape of the Von Mises yield locus in the section $\sigma_3 = 0$ is an ellipse centered in the origin whose major axis is inclined at 45° to the σ_1 axis. The Tresca yield locus is a hexagon inscribed in this ellipse (Figure 3-1).

Drucker (1949) proposed the following yield criterion:

$$\varphi = J_2^3 - cJ_3^2 = k^2 \tag{3.11}$$

where c is a constant and $k^2 = 27\left(\frac{\sigma^T}{3}\right)^6$. The convexity of the yield surface is ensured when $-\frac{27}{8} \le c \le 2.25$.

Later, Hosford (1972) suggested the following formulation:

$$\varphi = |\sigma_2 - \sigma_3|^a + |\sigma_3 - \sigma_1|^a + |\sigma_1 - \sigma_2|^a = 2\left(\sigma^T\right)^a \tag{3.12}$$

where a is an integer ≥ 1 and σ_1, σ_2, σ_3 are the principal stresses. This criterion is reduced to the Von Mises criterion for $a = 2$ and to the Tresca criterion for $a \to \infty$. The yield locus for any intermediate value of a is located between the first two surfaces introduced previously (see some examples in Figure 3-1).

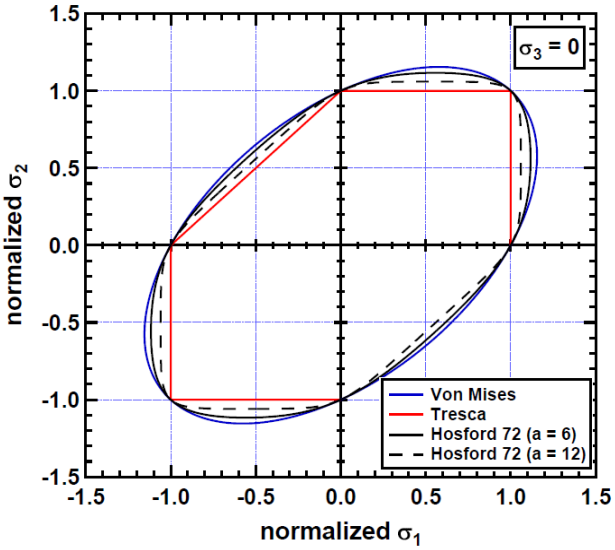

Figure 3-1 Comparison between Von Mises, Tresca and Hosford (1972) yield loci in the biaxial plane $\sigma_3 = 0$

The yield loci described by the Von Mises, Tresca and Hosford (1972) criteria are symmetric, *i.e.* the uniaxial yield stresses in tension and compression along a same direction are identical. Nevertheless some materials such as hcp metals display an asymmetry between tension and compression due to deformation mechanisms such as twinning or directional slip (Hosford (1993)). In order to take into account this strength differential effect, Cazacu and Barlat (2004) proposed the following criterion:

$$\varphi = \left(J_2\right)^{3/2} - cJ_3 = \tau_Y^3 \tag{3.13}$$

where c is a material parameter which depends on the uniaxial yield stresses in tension (σ^T) and compression (σ^C):

$$c = \frac{3\sqrt{3}\left[\left(\sigma^T\right)^3 - \left(\sigma^C\right)^3\right]}{2\left[\left(\sigma^T\right)^3 + \left(\sigma^C\right)^3\right]} \tag{3.14}$$

It is worth noting that the Von Mises yield criterion is recovered when $c = 0$, *i.e.* $\sigma^T = \sigma^C$. In order to ensure the convexity of the function, the range of c must be $\left[-3\sqrt{3}/2, 3\sqrt{3}/4\right]$.

Cazacu *et al.* (2006) introduced another criterion of the form:

$$\varphi = \left(|s_1| - ks_1\right)^a + \left(|s_2| - ks_2\right)^a + \left(|s_3| - ks_3\right)^a \tag{3.15}$$

where s_1, s_2, s_3 are the eigenvalues of the stress deviator while a is the degree of homogeneity and k is the strength differential parameter. Similarly to the constant c defined previously, k can be expressed in terms of the uniaxial yield stresses in tension and compression:

$$k = \frac{1 - h\left(\frac{\sigma^T}{\sigma^C}\right)}{1 + h\left(\frac{\sigma^T}{\sigma^C}\right)} \tag{3.16}$$

with

$$h\left(\frac{\sigma^T}{\sigma^C}\right) = \left[\frac{2^a - 2\left(\frac{\sigma^T}{\sigma^C}\right)^a}{\left(2\frac{\sigma^T}{\sigma^C}\right)^a - 2}\right]^{\frac{1}{a}} \tag{3.17}$$

It can be shown that the convexity is ensured when $a \geq 1$ and $k \in \left[-1.0, 1.0\right]$ (see Appendix A for the proof). The Von Mises yield criterion is recovered when $k = 0$ ($\sigma^T = \sigma^C$, *i.e.* no tension-compression asymmetry) and $a = 2$. Figure 3-2 shows the shape of the yield locus in the biaxial plane ($\sigma_3 = 0$) for different values of the parameter k (a is fixed to 2). It can actually be noticed that, higher k is in absolute value, higher the strength asymmetry is. Moreover, it can be observed that, for the upper and lower bound values of k, the yield function (3.15) corresponds to a triangle with rounded vertices.

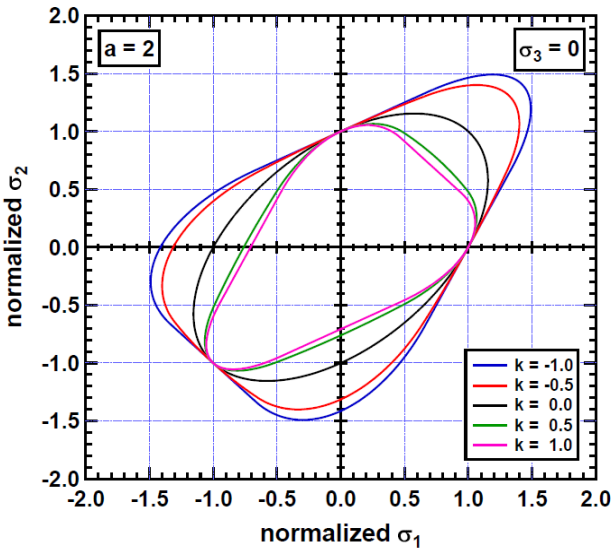

Figure 3-2 Influence of the parameter k on the yield locus shape (section $\sigma_3 = 0$ in the biaxial plane)

3.1.2. Anisotropic formulations

Generally, sheet metals display anisotropy owing to the texture developed in the rolling processes. Two ways can be used to take into account the plastic anisotropy:

- the generalized invariants approach which consists in constructing generalizations of the invariants to anisotropic conditions;
- the linear transformation approach which consists in applying a fourth-order symmetric and orthotropic tensor on the stress tensor (or its deviator) or on the plastic strain rate tensor.

The most famous anisotropic yield criterion was developed by Hill (1948). It is used in many finite element codes due to its simplicity to implement. This criterion is an extension of the Von Mises criterion to anisotropy. The yield function is of the form:

$$\varphi = \sqrt{\frac{1}{2}\left[F\left(\sigma_{22}-\sigma_{33}\right)^2 + G\left(\sigma_{33}-\sigma_{11}\right)^2 + H\left(\sigma_{11}-\sigma_{22}\right)^2 + 2L\sigma_{23}^2 + 2M\sigma_{13}^2 + 2N\sigma_{12}^2 \right]} = \sigma_F \quad (3.18)$$

where F, G, H, L, M, N are material parameters while σ_F is the yield stress under uniaxial tension in a reference direction (in general the rolling direction). In the case of a sheet, the identification of the parameters can readily be achieved with three experimental tensile tests along RD, TD and 45° from RD. It can be shown that the exact dual potential is given by:

$$\psi = \sqrt{\frac{2F}{\Delta}\left(\dot{\varepsilon}_{11}^p\right)^2 + \frac{2G}{\Delta}\left(\dot{\varepsilon}_{22}^p\right)^2 + \frac{2H}{\Delta}\left(\dot{\varepsilon}_{33}^p\right)^2 + \frac{4}{L}\left(\dot{\varepsilon}_{23}^p\right)^2 + \frac{4}{M}\left(\dot{\varepsilon}_{13}^p\right)^2 + \frac{4}{N}\left(\dot{\varepsilon}_{12}^p\right)^2} \quad (3.19)$$

where $\Delta = FH + FG + HG$.

Barlat *et al.* (1991) proposed an anisotropic extension of the Hosford (1972) isotropic yield criterion to a general stress state. The anisotropy is introduced by applying a fourth-order symmetric and orthotropic tensor $\mathbf{L}$ on the stress tensor:

$$\mathbf{s} = \mathbf{L} : \boldsymbol{\sigma} \tag{3.20}$$

where ":" denotes the double contracted product between a fourth-order tensor and a second-order tensor:

$$\left(\mathbf{L} : \boldsymbol{\sigma}\right)_{ij} = L_{ijkl}\sigma_{kl} \tag{3.21}$$

In (3.12), the principal stresses are substituted by the eigenvalues s_1, s_2, s_3 of the transformed tensor $\mathbf{s}$:

$$\varphi = \left|s_2 - s_3\right|^a + \left|s_3 - s_1\right|^a + \left|s_1 - s_2\right|^a = 2\left(\sigma^T\right)^a \tag{3.22}$$

Relative to the orthotropy axes (RD,TD,ND), the tensor $\mathbf{L}$ is represented by:

$$\mathbf{L} = \begin{bmatrix} \frac{c_2 + c_3}{3} & -\frac{c_3}{3} & -\frac{c_2}{3} & 0 & 0 & 0 \\ -\frac{c_3}{3} & \frac{c_3 + c_1}{3} & -\frac{c_1}{3} & 0 & 0 & 0 \\ -\frac{c_2}{3} & -\frac{c_1}{3} & \frac{c_1 + c_2}{3} & 0 & 0 & 0 \\ 0 & 0 & 0 & c_4 & 0 & 0 \\ 0 & 0 & 0 & 0 & c_5 & 0 \\ 0 & 0 & 0 & 0 & 0 & c_6 \end{bmatrix} \tag{3.23}$$

where c_i $(i = 1, 2, \ldots, 6)$ are material parameters.

Karafillis and Boyce (1993) used the same principle as Barlat *et al.* (1991) to suggest the following yield function:

$$\varphi = (1-c)\phi_1 + c\phi_2 = 2\left(\sigma^T\right)^b \tag{3.24}$$

where b is the degree of homogeneity while ϕ_1 and ϕ_2 are given by:

$$\phi_1 = \left|s_1 - s_2\right|^b + \left|s_2 - s_3\right|^b + \left|s_3 - s_1\right|^b \tag{3.25}$$

$$\phi_2 = \frac{3^b}{2^{b-1}+1}\left(\left|s_1\right|^b + \left|s_2\right|^b + \left|s_3\right|^b\right) \tag{3.26}$$

Cazacu and Barlat (2001) extended Drucker (1949) yield criterion to orthotropy by replacing the invariants J_2 and J_3 by the generalized invariants J_2^0 and J_3^0, respectively:

$$\varphi = \left(J_2^0\right)^3 - c\left(J_3^0\right)^2 = 27\left(\frac{\sigma^T}{3}\right)^6 \tag{3.27}$$

where:

$$\begin{aligned} J_2^0 &= \frac{a_1}{6}\left(\sigma_{11}-\sigma_{22}\right)^2+\frac{a_2}{6}\left(\sigma_{22}-\sigma_{33}\right)^2+\frac{a_3}{6}\left(\sigma_{11}-\sigma_{33}\right)^2 \\ &+ a_4\sigma_{12}^2+a_5\sigma_{13}^2+a_6\sigma_{23}^2 \end{aligned} \tag{3.28}$$

$$\begin{aligned} J_3^0 &= \frac{1}{27}\left(b_1+b_2\right)\sigma_{11}^3+\frac{1}{27}\left(b_3+b_4\right)\sigma_{22}^3+\frac{1}{27}\left[2\left(b_1+b_4\right)-b_2-b_3\right]\sigma_{33}^3 \\ &- \frac{1}{9}\left(b_1\sigma_{22}+b_2\sigma_{33}\right)\sigma_{11}^2-\frac{1}{9}\left(b_3\sigma_{33}+b_4\sigma_{11}\right)\sigma_{22}^2 \\ &- \frac{1}{9}\left[\left(b_1-b_2+b_4\right)\sigma_{11}+\left(b_1-b_3+b_4\right)\sigma_{22}\right]\sigma_{33}^2 \\ &+ \frac{2}{9}\left(b_1+b_4\right)\sigma_{11}\sigma_{22}\sigma_{33}-\frac{\sigma_{13}^2}{3}\left[2b_9\sigma_{22}-b_8\sigma_{33}-\left(2b_9-b_8\right)\sigma_{11}\right] \\ &- \frac{\sigma_{12}^2}{3}\left[2b_{10}\sigma_{33}-b_5\sigma_{22}-\left(2b_{10}-b_5\right)\sigma_{11}\right]-\frac{\sigma_{23}^2}{3}\left[\left(b_6+b_7\right)\sigma_{11}-b_6\sigma_{22}-b_7\sigma_{33}\right] \\ &+ 2b_{11}\sigma_{12}\sigma_{13}\sigma_{23} \end{aligned} \tag{3.29}$$

This criterion involves 18 material parameters in 3D analysis (6 for J_2^0 and 11 for J_3^0). It has to be noted that the generalized invariants are developed based on rigorous mathematical theorems (see Cazacu and Barlat (2003)).

As explained in Chapter 2 and the previous section, hcp materials exhibit both anisotropy and asymmetry in yielding. In order to take into account these features, Cazacu and Barlat (2004) proposed to extend the yield function (3.13) as follows:

$$\varphi=\left(J_2^0\right)^{3/2}-cJ_3^0=\tau_Y^3 \tag{3.30}$$

with J_2^0 and J_3^0 defined hereabove by Equations (3.28) and (3.29), respectively.

In Cazacu *et al.* (2006), the isotropic yield criterion (3.15) is extended to orthotropy by applying a fourth-order symmetric and orthotropic tensor $\mathbf{C}$ on the stress deviator, *i.e.* s_1, s_2, s_3 are substituted by the principal values Σ_1, Σ_2, Σ_3 of a transformed tensor $\boldsymbol{\Sigma}$ defined as:

$$\boldsymbol{\Sigma}=\mathbf{C}:\mathbf{s} \tag{3.31}$$

In the orthotropy axes, $\mathbf{C}$ is represented in Voigt notation by:

$$\mathbf{C}=\begin{bmatrix} C_{11} & C_{12} & C_{13} & 0 & 0 & 0 \\ C_{12} & C_{22} & C_{23} & 0 & 0 & 0 \\ C_{13} & C_{23} & C_{33} & 0 & 0 & 0 \\ 0 & 0 & 0 & C_{44} & 0 & 0 \\ 0 & 0 & 0 & 0 & C_{55} & 0 \\ 0 & 0 & 0 & 0 & 0 & C_{66} \end{bmatrix} \tag{3.32}$$

The resulting anisotropic yield criterion, called CPB06, is of the form:

$$\varphi = \left(|\Sigma_1| - k\Sigma_1\right)^a + \left(|\Sigma_2| - k\Sigma_2\right)^a + \left(|\Sigma_3| - k\Sigma_3\right)^a \tag{3.33}$$

As the isotropic formulation (Equation (3.15)), CPB06 yield function is convex when $-1 \le k \le 1$ and $a \ge 1$ (see Appendix A).

Cazacu *et al.* (2010) developed an anisotropic strain rate potential for hcp metals which is the exact dual of CPB06 yield criterion with $a = 2$. This potential is called SRP09 and is written as ($\tilde{m}$ denotes a scaling factor defined by the uniaxial tensile curve in RD chosen as reference):

$$\tilde{m}\,\psi = \begin{cases} \dfrac{1}{1-k}\sqrt{B_1^2 + B_2^2 + \left[\dfrac{3k^2-10k+3}{3k^2+2k+3}\right]B_3^2} & \text{if} \quad \dfrac{B_3}{\sqrt{B_1^2+B_2^2+B_3^2}} \le \dfrac{-\left(3k^2+2k+3\right)}{\sqrt{6\left(k^2+3\right)\left(3k^2+1\right)}} \\ \dfrac{1}{1+k}\sqrt{B_1^2 + B_2^2 + \left[\dfrac{3k^2+10k+3}{3k^2-2k+3}\right]B_3^2} & \text{if} \quad \dfrac{B_3}{\sqrt{B_1^2+B_2^2+B_3^2}} \ge \dfrac{\left(3k^2-2k+3\right)}{\sqrt{6\left(k^2+3\right)\left(3k^2+1\right)}} \\ \dfrac{1}{1-k}\sqrt{B_2^2 + B_3^2 + \left[\dfrac{3k^2-10k+3}{3k^2+2k+3}\right]B_1^2} & \text{if} \quad \dfrac{B_1}{\sqrt{B_1^2+B_2^2+B_3^2}} \le \dfrac{-\left(3k^2+2k+3\right)}{\sqrt{6\left(k^2+3\right)\left(3k^2+1\right)}} \\ \dfrac{1}{1+k}\sqrt{B_2^2 + B_3^2 + \left[\dfrac{3k^2+10k+3}{3k^2-2k+3}\right]B_1^2} & \text{if} \quad \dfrac{B_1}{\sqrt{B_1^2+B_2^2+B_3^2}} \ge \dfrac{\left(3k^2-2k+3\right)}{\sqrt{6\left(k^2+3\right)\left(3k^2+1\right)}} \\ \dfrac{1}{1-k}\sqrt{B_3^2 + B_1^2 + \left[\dfrac{3k^2-10k+3}{3k^2+2k+3}\right]B_2^2} & \text{if} \quad \dfrac{B_2}{\sqrt{B_1^2+B_2^2+B_3^2}} \le \dfrac{-\left(3k^2+2k+3\right)}{\sqrt{6\left(k^2+3\right)\left(3k^2+1\right)}} \\ \dfrac{1}{1+k}\sqrt{B_3^2 + B_1^2 + \left[\dfrac{3k^2+10k+3}{3k^2-2k+3}\right]B_2^2} & \text{if} \quad \dfrac{B_2}{\sqrt{B_1^2+B_2^2+B_3^2}} \ge \dfrac{\left(3k^2-2k+3\right)}{\sqrt{6\left(k^2+3\right)\left(3k^2+1\right)}} \end{cases} \tag{3.34}$$

where B_1, B_2, B_3 are the principal values of the transformed strain rate tensor $\mathbf{B} = \mathbf{H} : \dot{\boldsymbol{\varepsilon}}^p$. $\mathbf{H}$ is a fourth-order orthotropic tensor associated with plastic anisotropy tensor $\mathbf{C}$ involved in Equation (3.32). Denoting $\mathbf{K}$ the fourth-order symmetric deviatoric unit tensor defined by:

$$K_{ijkl} = \frac{\delta_{ik}\delta_{jl} + \delta_{il}\delta_{jk}}{2} - \frac{\delta_{ij}\delta_{kl}}{3} \tag{3.35}$$

it can be proved that $\mathbf{H}$ is the inverse of the tensor $\mathbf{L} = \mathbf{CK}$.

Plunkett *et al.* (2008) have shown that by incorporating into the isotropic criterion given by (3.15) additional linear transformations, an improved representation of the anisotropy can be obtained. If n linear transformations operating on the stress deviator are considered, the general form of the anisotropic criterion, called CPB06ex*n*, is:

$$\varphi = \sum_{i=1}^{n} f\left(\Sigma_1^{(i)}, \Sigma_2^{(i)}, \Sigma_3^{(i)}, k^{(i)}, a\right) \tag{3.36}$$

where

$$f\left(\Sigma_1^{(i)},\Sigma_2^{(i)},\Sigma_3^{(i)},k^{(i)},a\right)=\left(\left|\Sigma_1^{(i)}\right|-k^{(i)}\Sigma_1^{(i)}\right)^a+\left(\left|\Sigma_2^{(i)}\right|-k^{(i)}\Sigma_2^{(i)}\right)^a+\left(\left|\Sigma_3^{(i)}\right|-k^{(i)}\Sigma_3^{(i)}\right)^a \quad (3.37)$$

In (3.36) and (3.37), $k^{(i)}$ ($i=1,2,\ldots,n$) are material parameters that allow for the description of strength differential effects, a is the degree of homogeneity, while $\left(\Sigma_1^{(i)},\Sigma_2^{(i)},\Sigma_3^{(i)}\right)$ are the principal values of the *i*-th transformed tensor:

$$\boldsymbol{\Sigma}^{(i)}=\mathbf{C}^{(i)}:\mathbf{s} \quad (3.38)$$

It is worth noting that, although the transformed stress tensors defined in (3.31) or (3.38) are not deviatoric, the yield function is pressure insensitive (see Appendix B for the proof).

Recently, Lou *et al.* (2013) suggested a simple approach to take into account the strength differential effect into symmetric yield functions by adding a weighted pressure term for incompressible sheet metals in plane stress state. The yield criterion is of the form:

$$\varphi=B\left(bI_1+\bar{\sigma}_s\right) \quad (3.39)$$

where $\bar{\sigma}_s$ is the equivalent yield stress associated to a symmetric yield function while b and B are two material constants: the former modulates the strength differential effect and the latter is a scaling factor determined by the reference stress-strain curve. The convexity of Equation (3.39) is satisfied if the symmetric yield function $\bar{\sigma}_s$ is convex since the Hessian matrix of φ is identical to the one of $\bar{\sigma}_s$. It can be shown that the range of b is $\left[-1,1\right]$, corresponding to a wide range of the ratio σ^T/σ^C ($0<\sigma^T/\sigma^C<\infty$).

Equation (3.39) can be extended to take into account an anisotropic sensitivity to pressure. The parameter b is replaced by two constants h_x and h_y as follows:

$$\varphi=B\left(h_x\sigma_{11}+h_y\sigma_{22}+\bar{\sigma}_s\right) \quad (3.40)$$

The effect of these two parameters is to modulate the ratios of the tensile flow stress to the compressive flow stress in RD and TD, respectively.

3.2. Hardening models

Hardening is related to the evolution of the yield surface in the stress space with the plastic deformation. From a phenomenological point of view, the two classical ways of dealing with hardening are isotropic and kinematic hardening models. Isotropic hardening models assume a uniform size evolution of the yield locus without displacement of its center in the stress space (Figure 3-3 (a)). Conversely, kinematic hardening models describe the translation of the yield locus without taking into account its expansion (Figure 3-3 (b)). They are adapted to depict the Bauschinger effect, *i.e.* the decreasing of the flow stress after a strain reversal. In both cases, the shape of the yield surface remains unchanged. Mixed hardening models, consisting in a combination of both isotropic and kinematic formulations, also exist and are very often used in practice.

In this work, it is assumed that yielding is described as follows:

$$\varphi\left(\boldsymbol{\sigma}-\mathbf{X},\bar{\varepsilon}^{p},\dot{\bar{\varepsilon}}^{p}\right)=\bar{\sigma}\left(\boldsymbol{\sigma}-\mathbf{X},\bar{\varepsilon}^{p},\dot{\bar{\varepsilon}}^{p}\right)-Y\left(\bar{\varepsilon}^{p},\dot{\bar{\varepsilon}}^{p}\right) \tag{3.41}$$

where:

- $\bar{\sigma}$ is the effective stress according to the given yield criterion (see Section 3.1);
- $\bar{\varepsilon}^{p}$ and $\dot{\bar{\varepsilon}}^{p}$ are respectively the effective strain and strain rate associated to $\bar{\sigma}$ using the work-equivalence principle (Hill (1987)):

$$dW_{p}=\sigma_{ij}d\varepsilon_{ij}^{p}=\bar{\sigma}d\bar{\varepsilon}^{p} \tag{3.42}$$

The kinematic hardening is introduced through the back-stress tensor $\mathbf{X}$ and Y denotes a threshold function whose evolution describes the size of the yield surface during the plastic deformation (isotropic hardening). The next sections introduce some examples of hardening plasticity and viscoplasticity models, respectively.

a

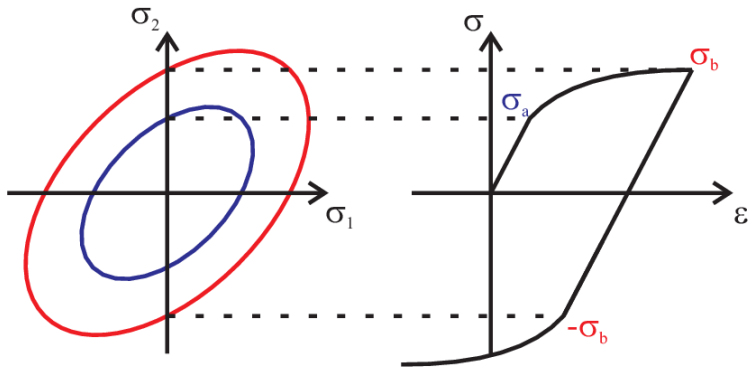

b

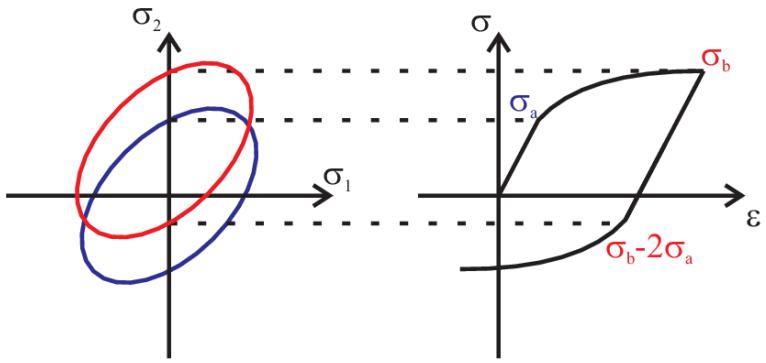

Figure 3-3 Schematic of the yield locus evolution and the associated stress-strain curve under a tension-compression loading sequence when considering (a) an isotropic hardening and (b) a kinematic hardening, respectively.

3.2.1. Hardening plasticity laws

3.2.1.1. Isotropic hardening formulations

Swift

Swift (Swift (1952)) proposed a power law which is suitable for describing the mechanical response of materials whose behavior does not display saturation:

$$Y\left(\bar{\varepsilon}^{p}\right) = K\left(\varepsilon_0 + \bar{\varepsilon}^{p}\right)^{n} \tag{3.43}$$

K, ε_0 and n are material parameters which must be determined for each material.

Voce

Voce law (Voce (1948)) is expressed as:

$$Y\left(\bar{\varepsilon}^{p}\right) = R_0 + R \tag{3.44}$$

where:

$$dR = c_R\left(s_R - R\right)d\bar{\varepsilon}^{p} \tag{3.45}$$

R_0 is the initial yield stress while c_R and s_R are respectively the isotropic hardening saturation rate and value.

Other isotropic hardening formulations exist and can be found in the literature (see for instance Lemaitre *et al.* (2009)). Depending on the scope of application, one or another of these laws is more suitable to describe the hardening behavior.

3.2.1.2. Kinematic hardening formulations

Prager

Prager (Prager (1955)) proposed a formulation assuming that the yield surface moves in the direction of the plastic strain rates:

$$d\mathbf{X} = c\, d\boldsymbol{\varepsilon}^{p} \tag{3.46}$$

where c is a material constant.

Prager hardening law is very simple to implement into a finite element code and make the computational algorithms more stable and less time-consuming. However, although the Bauschinger effect is qualitatively represented, the model is unable to fit the experimental behavior, especially the ratcheting effects.

Ziegler

According to Ziegler (Ziegler (1959)), one shortcoming of Prager linear kinematic law is that it provides results which are not consistent for 2D and 3D cases. Indeed, if the yield locus in a 3D space moves in the direction of its normal at the loading point, it can be shown that the

movement of the yield surface in a 2D space takes place in another direction. In addition, in the case of a uniaxial tension, Prager law predicts that the yield locus moves towards the positive direction of loading causing kinematic hardening of the material, but also towards the other directions causing a transverse softening, which is not observed in the experiments.

Ziegler suggested to modify Prager model as follows:

$$d\mathbf{X} = \left(\boldsymbol{\sigma} - \mathbf{X}\right) d\mu \tag{3.47}$$

This formulation implies that the yield locus is translated along the $\left(\boldsymbol{\sigma} - \mathbf{X}\right)$ direction. μ is a proportional scalar determined by the consistency condition.

Armstrong-Frederick

Armstrong-Frederick law (Armstrong and Frederick (1966)) is a non-linear formulation defined as follows:

$$d\mathbf{X} = c_X \left(s_X \; d\boldsymbol{\varepsilon}^p - \mathbf{X} \, d\bar{\varepsilon}^p \right) \tag{3.48}$$

where c_X and s_X are the kinematic hardening saturation rate and value, respectively. The first term in Equation (3.48) expresses a linear evolution of the back-stress with the plastic strain rates, as in Prager model, while the second one is a recall term called dynamic recovery.

Depending on the applications, kinematic hardening can be described by other formulations, such as the approach proposed by Chaboche (Lemaitre *et al.* (2009)) which consists in introducing different back-stress terms with different saturation values and rates. Nevertheless the three laws presented hereabove are sufficient in this study.

3.2.1.3. Mixed and distortional hardening formulations

In order to take into account both the expansion of the yield surface in the stress space and the Bauschinger effect, isotropic and kinematic hardening laws are very often coupled (e.g. Swift and Ziegler, Voce and Armstrong-Frederick, …). This coupling is denoted as "mixed hardening model". Nevertheless, these formulations may be inappropriate to describe other macroscopic effects such as the work-hardening stagnation and the work-softening exhibited by some polycrystalline metals under strain-path change. This section introduces some examples of distortional hardening laws.

Based on transmission electron microscopy observations, Teodosiu and Hu (1995) proposed a model in the framework of continuum mechanics able to capture the strain-path dependent hardening. This model was first developed for bcc monocrystals (Hu (1992)). Later it was successfully applied to IF steel sheets (Hoferlin (2001), Li *et al.* (2003)), dual phase steels and aluminum (Bouvier *et al.* (2002)).

The model is based on a set of four internal variables:

- R : isotropic contribution to hardening, described by Swift or Voce laws (see Section 3.2.1.1);
- $\mathbf{X}$: kinematic contribution to hardening (back-stress tensor);
- $\mathfrak{S}$: fourth-order tensor which accounts for the directional strength of planar persistent dislocation structures

- **P** : second-order tensor which takes into account the polarity.

Denoting by $\bar{\sigma}$ the equivalent effective stress associated to a stress potential, the yield criterion is written as:

$$\varphi = \bar{\sigma} - R_0 - R - f\left\|\mathfrak{S}\right\| = 0 \tag{3.49}$$

where f is a material parameter such that $0 \le f \le 1$.

The term $f\left\|\mathfrak{S}\right\|$ represents the contribution of the persistent dislocation structures to the isotropic hardening while R_0 is the initial yield stress. The evolution law for the polarity tensor $\mathbf{P}$ is written as:

$$d\mathbf{P} = c_P\left(\mathbf{N} - \mathbf{P}\right)d\bar{\varepsilon}^p \tag{3.50}$$

c_P characterizes the polarization rate of the persistent dislocation structures while $\mathbf{N}$ is the current direction of the plastic strain rate tensor:

$$\mathbf{N} = \frac{\mathbf{D}^p}{\left\|\mathbf{D}^p\right\|} \tag{3.51}$$

The back-stress tensor evolves as follows:

$$d\mathbf{X}' = c_X\left[X_{\text{sat}}\frac{\mathbf{s} - \mathbf{X}'}{\bar{\sigma}} - \mathbf{X}'\right]d\bar{\varepsilon}^p \tag{3.52}$$

where c_X represents the saturation rate of the back-stress deviator $\mathbf{X}'$ and X_{sat} is a material parameter characterizing the saturation value of $\left\|\mathbf{X}'\right\|$. This latter parameter is given by:

$$X_{\text{sat}} = X_0 + \left(1 - f\right)\sqrt{r\left\|\mathfrak{S}\right\|^2 + \left(1 - r\right)S_D^2} \tag{3.53}$$

where X_0 is the initial value of X_{sat} while r is a material parameter. $S_D = \mathbf{N}:\mathfrak{S}:\mathbf{N}$ represents the strength of the dislocation structures associated with the currently active slip systems. When a strong path-change occurs, dislocation structures associated with the subsequent strain-rate direction can significantly evolve from the rest of the persistent structures. In order to describe such processes, $\mathfrak{S}$ is split as follows:

$$\mathfrak{S} = S_D\mathbf{N}:\mathbf{N} + \mathfrak{S}_L \tag{3.54}$$

with $\mathfrak{S}_L$ being the part of $\mathfrak{S}$ associated with the latent part of the persistent dislocation structures. S_D and $\mathfrak{S}_L$ are ruled by the following equations:

$$\begin{cases} d\mathfrak{S}_L = -c_{SL}\left(\dfrac{\left\|\mathfrak{S}_L\right\|}{S_{\text{sat}}}\right)^{n_L}\mathfrak{S}_L d\bar{\varepsilon}^p \\ dS_D = c_{SD}\left[g\left(S_{\text{sat}} - S_D\right) - hS_D\right]d\bar{\varepsilon}^p \end{cases} \tag{3.55}$$

where c_{SD} and c_{SL} represent the saturation rate of S_D and $\mathfrak{S}_L$, respectively, while S_{sat} denotes the saturation value of S_D. h describes the slight loss of S_D at the beginning of a reversed deformation. Its value is significant only during a microplastic stage and is determined by:

$$h = \frac{1}{2}\left(1 - \frac{\mathbf{X}' : \mathbf{N}}{X_{\text{sat}}\left(\mathbf{s} - \mathbf{X}'\right) : \mathbf{N}}\bar{\sigma}\right) \tag{3.56}$$

The function g describes the work-hardening stagnation and the resumption of work-hardening after a reversed deformation. Using the projection $P_D = \mathbf{P} : \mathbf{N}$ of the polarity tensor on $\mathbf{N}$, it is defined by:

$$g = \begin{cases} 1 - \dfrac{c_P}{c_{SD} + c_P}\left|\dfrac{S_D}{S_{\text{sat}}} - P_D\right| & \text{if} \quad P_D \geq 0 \\ \left(1 + P_D\right)^{n_P}\left(1 - \dfrac{c_P}{c_{SD} + c_P}\dfrac{S_D}{S_{\text{sat}}}\right) & \text{otherwise} \end{cases} \tag{3.57}$$

where n_P is a positive material parameter.

From Equation (3.49) to Equation (3.57), it can be noticed that Teodosiu-Hu hardening model involves 13 material parameters, *i.e.* R_0, $\left(c_R, s_R\right)$ or $\left(\varepsilon_0, n\right)$, f, c_X, X_0, c_P, c_{SD}, S_{sat}, n_P, c_{SL}, r and n_L. The model has already proved its ability to describe the behavior of a large diversity of polycrystalline materials, e.g. aluminum alloys, ferritic steels, DP steels, TRIP steels, HSLA steels, etc. (see for instance Florès (2005), Haddadi *et al.* (2006), Florès *et al.* (2007))

Based on Teodosiu-Hu model, Wang *et al.* (2008) proposed an alternative formulation for cross-hardening. It is assumed that the dislocation structures developing during loading can also result in latent hardening during continuous strain-path changes. The evolution of the fourth-order tensor $\mathfrak{S}$ is described as follows:

$$d\mathfrak{S} = c_{SD}\left\{g\left(S_{\text{sat}} - S_D\right) - hS_D\right\} d\bar{\varepsilon}^p \, \mathbf{N} : \mathbf{N} - c_{SL}\left(\frac{\left\|\mathfrak{S}_L\right\|}{S_{\text{sat}}}\right)^{n_L} \mathfrak{S}_L \, d\bar{\varepsilon}^p \tag{3.58}$$

Using Equations (3.55) and (3.58), it can be shown that:

$$d\mathfrak{S}^T - d\mathfrak{S}^W = S_D\left(d\mathbf{N} : \mathbf{N} + \mathbf{N} : d\mathbf{N}\right) \tag{3.59}$$

where $\mathfrak{S}^T$ and $\mathfrak{S}^W$ are the tensor $\mathfrak{S}$ associated to Teodosiu-Hu and Wang models, respectively. The result of Equation (3.59) means that both models agree only for loading histories in which the current direction $\mathbf{N}$ is constant.

Noman *et al.* (2010) introduced another approach based on an evolution relation able to capture the effects of an evolving dislocation microstructure on the hardening behavior and the shape of the yield surface. The yield function is of the form:

$$\varphi = \sqrt{(\mathbf{M}-\mathbf{X})\mathcal{K}(\mathbf{M}-\mathbf{X})} - R_0 - R = \bar{\sigma} - R_0 - R \tag{3.60}$$

where $\mathbf{M}$ denotes the Mandel stress tensor. The effective stress $\bar{\sigma}$ depends on a fourth-order tensor $\mathcal{K}$ evolving as follows:

$$d\mathcal{K} = c_d \left\{ h_d^{\text{sat}} \mathbf{N}:\mathbf{N} - \mathcal{K}_d \right\} d\bar{\varepsilon}^p + c_l \left\{ h_l^{\text{sat}} \left(\mathbf{K} - \mathbf{N}:\mathbf{N} \right) - \mathcal{K}_l \right\} d\bar{\varepsilon}^p \tag{3.61}$$

with:

$$\mathcal{K}_d = \left(\mathbf{N}\mathcal{K}\mathbf{N}\right)\mathbf{N}:\mathbf{N} = h_d\, \mathbf{N}:\mathbf{N} \tag{3.62}$$

and

$$\mathcal{K}_l = \mathcal{K} - h_d\, \mathbf{N}:\mathbf{N} \tag{3.63}$$

where $\mathbf{K}$ is the deviatoric part of the fourth-order identity tensor (see Equation (3.35)). $\mathcal{K}_d$ and $\mathcal{K}_l$ represent the "dynamic" and "latent" parts of the tensor $\mathcal{K}$, respectively. The parameters h_d^{sat} and c_d (resp. h_l^{sat} and c_l) are respectively the saturation value and the saturation rate associated to $\mathcal{K}_d$ (resp. $\mathcal{K}_l$). It can be noticed that Equation (3.61) is analogous to Equation (3.58). This model, unlike those of Teodosiu-Hu and Wang, allows the shape of the yield surface to change with cross-hardening. However the additional effects such as the hardening stagnation after a reversed strain-path are not taken into account.

The yield locus of most hcp materials does not uniformly evolve. Indeed the hardening response is very dependent on the strain path, as it will be shown in the case of Ti6Al4V in Chapter 5. Nevertheless the distortional hardening formulations introduced above are not convenient for physically describing the mechanical behavior of hcp materials since these models were developed on the basis of the intragranular deformation mechanisms involved in bcc and fcc metals. In addition the latter are less prone to twinning than hcp metals. A first approach to take into account the distortion of the yield surface shape with plastic deformation consists in assuming that the parameters p_i ($i = 1 \ldots N$, N being the total number of parameters) associated to the yield criterion are functions of the accumulated equivalent strain $\bar{\varepsilon}^p$, for instance as follows:

$$p_i = \alpha_i + \beta_i \left(1 - e^{-\gamma_i \bar{\varepsilon}^p}\right) \tag{3.64}$$

where α_i, β_i and γ_i are constants. This approach was applied by Nebebe *et al.* (2009) using the yield criterion (3.30), then by Yoon *et al.* (2013) and later by Ghaffari Tari *et al.* (2014) (see Figure 3-4) using the CPB06 yield criterion and its extensions (Equations (3.33) and (3.36)).

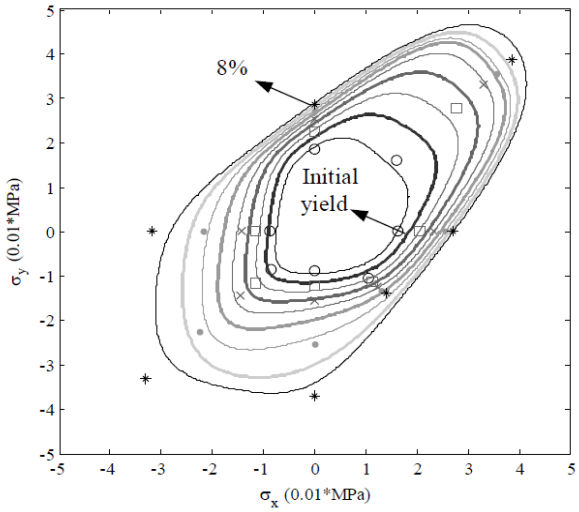

Figure 3-4 Yield surface evolution of AZ31B magnesium alloy with accumulated plastic strain up to 8% (Ghaffari Tari et al. (2014))

Another modeling is proposed by Plunkett *et al.* (2006) in order to describe the anisotropic hardening behavior exhibited by hcp metals. The parameters are considered to evolve as a function of the equivalent plastic strain $\bar{\varepsilon}^p$. They are determined for several levels of $\bar{\varepsilon}^p$, namely $\bar{\varepsilon}^{p,(1)} < \ldots < \bar{\varepsilon}^{p,(k)} < \ldots < \bar{\varepsilon}^{p,(m)}$, $k = 1 \ldots m$, where $\bar{\varepsilon}^{p,(1)}$ corresponds to initial yielding and $\bar{\varepsilon}^{p,(m)}$ corresponds to the highest level of equivalent plastic strain attainable in all mechanical tests. Next, for each of the individual level $\bar{\varepsilon}^{p,(k)}$, the equivalent stress $\bar{\sigma}$ associated to the yield criterion used for the modeling is computed. To determine the yield surface corresponding to an intermediate level $\left(\bar{\varepsilon}^{p,(k)} \le \bar{\varepsilon}^p \le \bar{\varepsilon}^{p,(k+1)}\right)$, a linear interpolation is used:

$$\bar{\sigma} = \eta\left(\bar{\varepsilon}^p\right)\bar{\sigma}^{(k)} + \left(1 - \eta\left(\bar{\varepsilon}^p\right)\right)\bar{\sigma}^{(k+1)} \tag{3.65}$$

where η is a weighting factor defined as:

$$\eta\left(\bar{\varepsilon}^p\right) = \frac{\bar{\varepsilon}^{p,(k+1)} - \bar{\varepsilon}^p}{\bar{\varepsilon}^{p,(k+1)} - \bar{\varepsilon}^{p,(k)}} \tag{3.66}$$

such that $\eta\left(\bar{\varepsilon}^{p,(k)}\right) = 1$ and $\eta\left(\bar{\varepsilon}^{p,(k+1)}\right) = 0$.

Based on the studies of Hill and Hutchinson (1992) and Hill *et al.* (1994), the plastic work per unit volume W_p can be used to define the different levels instead of the equivalent plastic strain (see e.g. Gilles *et al.* (2011)). The equivalent stress is then determined by:

$$\bar{\sigma} = \eta\left(W_p\right)\bar{\sigma}^{(k)} + \left(1 - \eta\left(W_p\right)\right)\bar{\sigma}^{(k+1)} \tag{3.67}$$

with

$$\eta\left(W_p\right) = \frac{W_p^{(k+1)} - W_p}{W_p^{(k+1)} - W_p^{(k)}} \tag{3.68}$$

Yoon *et al.* (2011) proposed to apply the linear interpolation to calculate the anisotropy coefficients involved in the CPB06 yield criterion or its extensions:

$$C_{ij} = \eta\left(W_p\right)C_{ij}^{(k)} + \left(1-\eta\left(W_p\right)\right)C_{ij}^{(k+1)} \tag{3.69}$$

If only one mechanism exists to account for the evolution of the yield locus shape, Equation (3.64) is likely enough to describe the distortional hardening. If several mechanisms take place simultaneously, Equations (3.65)-(3.66) or (3.67)-(3.68) are more adapted. Nevertheless the identification of these models is based on monotonic tests. Actually, the evolution of the texture depends on the strain path, which means that the experimental results obtained from different mechanical tests correspond to different states of the material. It could be interesting to use a reliable microscopic model able to perform texture updates and to rebuild the yield locus during finite element simulations (see for instance Van Houtte *et al.* (2011)). However such a model is difficult to develop in the case of hcp metals. VPSC could maybe serve this purpose if twinning is well modeled.

3.2.2. Rate-dependent hardening laws

3.2.2.1. Johnson-Cook

Johnson-Cook (JC) model (Johnson and Cook (1983)) is an empirical law which is written as follows:

$$Y\left(\bar{\varepsilon}^p, \dot{\bar{\varepsilon}}^p\right) = \left[A + B\left(\bar{\varepsilon}^p\right)^n\right]\left(1 + C\ln\frac{\dot{\bar{\varepsilon}}^p}{\dot{\bar{\varepsilon}}_0}\right)\left[1-\left(\frac{T-T_{\text{room}}}{T_{\text{melt}}-T_{\text{room}}}\right)^m\right] \tag{3.70}$$

where A, B, C, m and n are material parameters. T, T_{room} and T_{melt} are respectively the current, room and melting temperatures, while $\dot{\bar{\varepsilon}}_0$ is an arbitrary reference plastic strain rate. In Equation (3.70), the flow stress is described as the product of three factors:

- $A + B\left(\bar{\varepsilon}^p\right)^n$ represents the link with the plastic strain (hardening);
- $1 + C\ln\frac{\dot{\bar{\varepsilon}}^p}{\dot{\bar{\varepsilon}}_0}$ is linked to the strain rate sensitivity;
- $1-\left(\frac{T-T_{\text{room}}}{T_{\text{melt}}-T_{\text{room}}}\right)^m$ takes into account the thermal effects.

It has to be noted that the law as expressed in Equation (3.70) presents two drawbacks:

1. if $\dot{\bar{\varepsilon}}^p < \dot{\bar{\varepsilon}}_0$, the viscosity term induces a reduction of the yield stress ;
2. if $T < T_{\text{room}}$, a numerical error will occur when the exponent m is lower than 1.

In order to avoid these problems, it is required to rewrite JC model as:

$$Y\left(\bar{\varepsilon}^p, \dot{\bar{\varepsilon}}^p\right) = \left[A + B\left(\bar{\varepsilon}^p\right)^n\right]\left(1 + C\ln\dot{\bar{\varepsilon}}^{*p}\right)\left[1-T^{*m}\right] \tag{3.71}$$

with the following conditions:

$$\dot{\bar{\varepsilon}}^{*p} = \begin{cases} \dfrac{\dot{\bar{\varepsilon}}^{p}}{\dot{\bar{\varepsilon}}_0} & \text{if} \quad \dot{\bar{\varepsilon}}^{p} \geq \dot{\bar{\varepsilon}}_0^{p} \\ 1 & \text{if} \quad \dot{\bar{\varepsilon}}^{p} < \dot{\bar{\varepsilon}}_0^{p} \end{cases} \tag{3.72}$$

$$T^{*} = \begin{cases} \dfrac{T - T_{\text{room}}}{T_{\text{melt}} - T_{\text{room}}} & \text{if} \quad T \geq T_{\text{room}} \\ 0 & \text{if} \quad T < T_{\text{room}} \end{cases} \tag{3.73}$$

Since it is numerically robust and easy to incorporate into finite element codes, JC model was used in many studies to describe the plastic behavior of hcp materials such as magnesium (Altenhof *et al.* (2004); Duc-Toan *et al.* (2010); Ulacia *et al.* (2011)) or titanium (Jeunechamps (2008); Khan *et al.* (2004); Lee and Lin (1998b); Meyer Jr and Kleponis (2001); Milani *et al.* (2009); Peirs (2012); Seo *et al.* (2005)).

3.2.2.2. Zerilli-Armstrong

Zerilli-Armstrong (ZA) model (Zerilli and Armstrong (1987)) is expressed in two forms:

1. the first one is addressed to fcc materials:

$$Y\left(\bar{\varepsilon}^{p}, \dot{\bar{\varepsilon}}^{p}\right) = C_0 + C_1 \left(\bar{\varepsilon}^{p}\right)^{n} e^{\left(-C_3 T + C_4 T \ln \dot{\bar{\varepsilon}}^{p}\right)} \tag{3.74}$$

2. the second one is addressed to bcc materials:

$$Y\left(\bar{\varepsilon}^{p}, \dot{\bar{\varepsilon}}^{p}\right) = C_0 + C_1 e^{\left(-C_3 T + C_4 T \ln \dot{\bar{\varepsilon}}^{p}\right)} + C_5 \left(\bar{\varepsilon}^{p}\right)^{n} \tag{3.75}$$

where C_0, C_1, C_3, C_4, C_5 and n are constant parameters. Unlike JC model, this law has a physical sense because it is based on dislocation mechanics.

According to Meyer Jr and Kleponis (2001), ZA model used as empirical model since it does not explicitly include hcp crystal structures can be better to describe the strain rate hardening behavior of Ti6Al4V than JC model. However, it is not recommended for temperatures above about one-half of the absolute melting temperature.

3.3. Conclusions

In this chapter, some phenomenological yield functions as well as hardening laws used to describe the mechanical behavior of materials were introduced. In the framework of this thesis, CPB06 yield function and its extensions will be used to model the yield locus of Ti6Al4V owing to their ability to take into account both the anisotropy and the tension-compression asymmetry displayed by the alloy. Concerning the hardening behavior, it will be shown in the experimental characterization of Ti6Al4V (Chapter 5) that the material response is sensitive to the strain path and then the yield surface shape evolves with the plastic deformation. The degree of anisotropy in hardening will be studied by comparing the experimental curves with

FE results obtained when an isotropic hardening is used. Next the evolution of the yield locus shape will be modeled with the approach previously described by Equations (3.67) and (3.68). The models proposed in this work to describe the mechanical behavior of Ti6Al4V have been implemented into the non-linear finite element code LAGAMINE developed by the department ArGEnCo of ULg.

It has to be noted that, as Ti6Al4V is very sensitive to temperature and strain rate, it is also essential to consider its viscous behavior in the modeling. However it was decided to focus this thesis on the anisotropy and the tension-compression asymmetry exhibited by the material since viscoplastic investigations would increase a lot the number of tests in the experimental campaign. In addition, research conducted by Tuninetti and Habraken (2014) confirmed that, at low strain rates (10^{-3} s^{-1} to 10^{-1} s^{-1}) and medium temperatures (room temperature, 150°C and 400°C), the anisotropy effects are dominant.

Part II Experimental investigation

Chapter 4 Description of the experimental devices and the mechanical tests

---

The characterization of a material needs to carry out some experimental tests depending on the number and the nature of the parameters involved in the model used to describe its mechanical behavior. This chapter introduces all the devices which enabled the achievement of the experiments on the studied Ti6Al4V titanium alloy. The methodology followed for the different tests as well as the geometry of the specimens are described in the next sections. The experimental results and their analysis will be given in Chapter 5.

4.1. Equipment

4.1.1. Testing machines

4.1.1.1. Zwick 100 kN

A very simple way to characterize the mechanical behavior of a material is to carry out uniaxial tensile or compressive tests. In the case of compression, care must be taken in the choice and the design of the specimens as well as in the experimental procedure. Indeed, flat specimens have to be avoided unless solid plates are used in order to prevent buckling (see for instance Section 4.1.1.2). A cylinder shape is usually preferred but it requires lubrication between the tools and the samples to reduce barreling.

A Zwick 100 kN machine (see Figure 4-1 (a)), available at the Materials and Structures Mechanics Laboratory, was used to perform uniaxial tensile tests on Ti6Al4V. The main features of the machine are listed in Table 4-1. The device is provided with a mechanical extensometer (Zwick Multisens Light model – see Figure 4-1 (b)) which measures the current length of the

specimen. In addition, the acquisition system is able to record the applied force, the crosshead displacement and the standard stroke.

a **b**

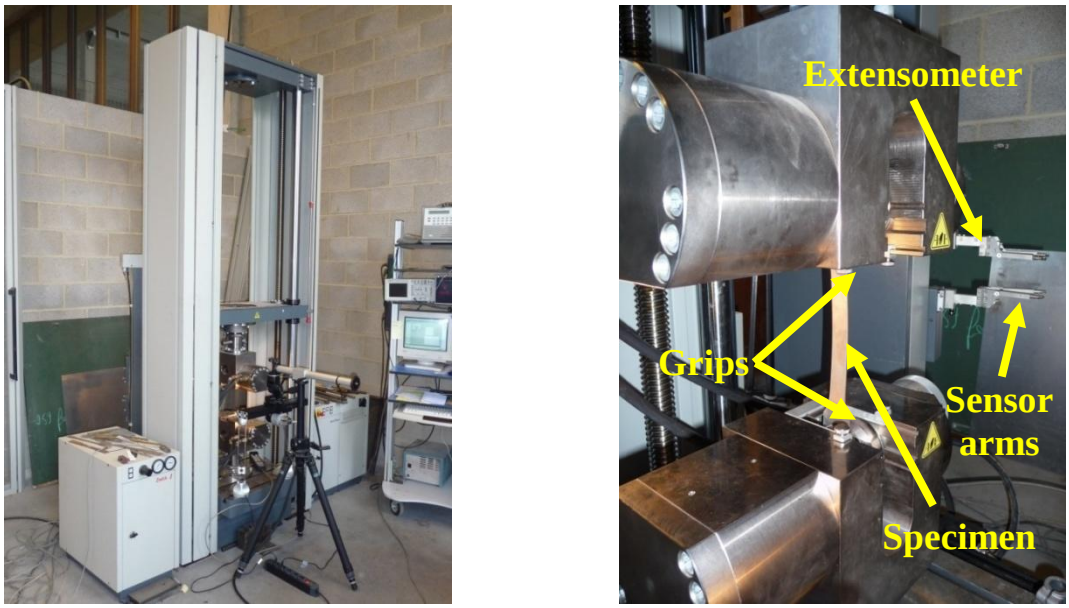

Figure 4-1 Experimental device used for tensile tests: (a) Zwick 100kN machine, (b) detailed view of the grips and the extensometer

Nominal load capacity		+/- 100 kN
Nominal stroke	Compression (between supports)	0 to 1500 mm
	Tension	0 to 1700 mm
Crosshead velocity		0.1 to 400 mm/min
100 kN hydraulic grips		

Table 4-1 Features of the Zwick 100kN machine

4.1.1.2. Comb-shaped dies apparatus

As specified in Section 2.4.3.2, hcp metals display a strength asymmetry between tension and compression. In order to quantify this asymmetry in the case of Ti6Al4V, compression tests were required. Since the Materials and Structures Mechanics Laboratory has no device adapted to perform in-plane compression on sheet specimens, the tests were conducted at TUAT (Japan) using the method and the comb-shaped dies apparatus developed by Pr. T. Kuwabara (Kuwabara *et al.* (2009)). Additional tensile tests were also performed and compared with the results obtained in compression.

A schematic of the recently developed tension/compression testing device is depicted in Figure 4-2. The lower die 1 is fixed and the lower die 2 is on a slide rail that enables it to move smoothly in a horizontal direction. The sheet specimen is set on the lower dies and attached by chucking plates. The upper dies are placed on the specimen in such a way that the four holes are aligned with the pins fixed to the lower dies, which enables a synchronized movement. The lower die 2 is actuated in the horizontal direction by a servo-controlled hydraulic cylinder A. The hydraulic cylinder B applies a constant blank-holding force on the specimen

in order to prevent buckling. The blank-holding pressure is about 12 MPa. The specimen is lubricated on both sides with Vaseline and Teflon sheets (0.05 mm thickness), thus reducing the friction coefficient to 0.02. The longitudinal strain was recorded using a strain gauge (Tokyo Sokki Co., FCA-1-11-1L) glued on the specimen. The compression force applied to the specimen is measured using a load cell connected to the right part of the lower die 2. The outputs of the measured force and strain are monitored every second using A/D data acquisition and a personal computer.

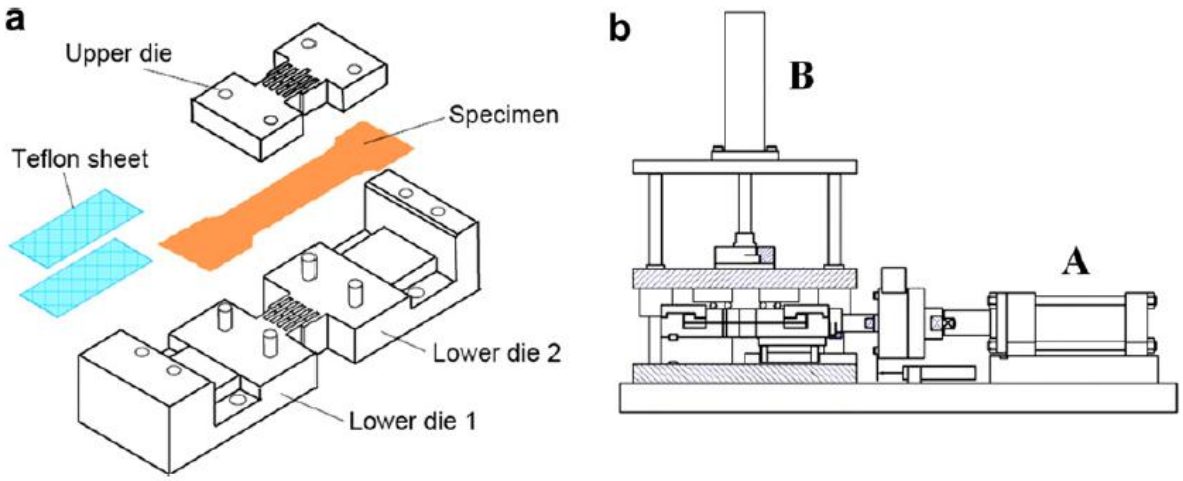

Figure 4-2 Schematic diagram of the comb-shaped apparatus: (a) configuration of the dies, (b) overview of the apparatus (after Kuwabara et al. (2009))

4.1.1.3. Biaxial machine

The mechanical behavior of a material can be better characterized by testing it under multiaxial and non-proportional loads. A series of experiments were carried out with a biaxial machine designed by P. Florès (Florès (2003); Florès (2005)) at the Materials and Structures Mechanics Laboratory (Figure 4-3). This machine uses a vertical (A1) and a horizontal (A2) actuators which enable the displacement of the grips (G). These actuators are controlled by a computer either in force or in displacement.

Different tests can be performed with the biaxial machine:

- plane strain tests;
- simple shear tests;
- Bauschinger tests (simple shear in one direction, followed by simple shear in the reversed direction);
- orthogonal test (plane strain in the vertical direction, followed by simple shear in the horizontal direction);
- simultaneous plane strain and simple shear tests.

The current mechanical features of the system control are listed in Table 4-2. These characteristics are essential in the design of the samples, in particular in the choice of the specimen thickness.

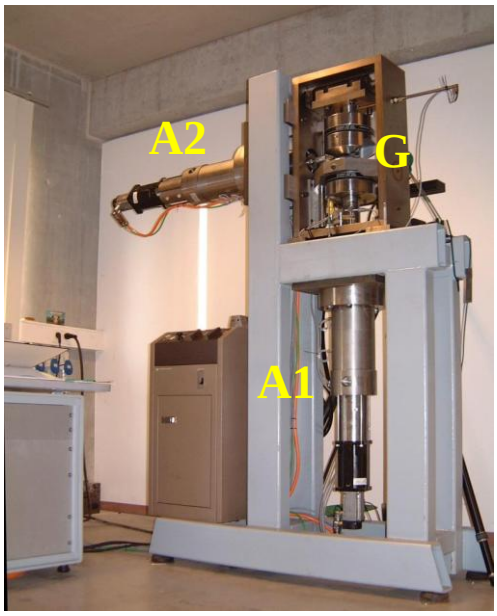

Figure 4-3 Overview of the biaxial machine

	Max/min force [kN]	Max/min displacement (sensor 1) [mm]	Max/min displacement (sensor 2) [mm]	Max/min speed [mm/s]
Vertical motion	+/- 100	+/- 10	+/- 25	$5\times10^{-3}/5\times10^{-2}$
Horizontal motion	+/- 100	+/- 25	---	$5\times10^{-3}/5\times10^{-2}$

Table 4-2 Main features of the system control

4.1.1.4. SCHENK Hydropuls 400 kN press

The study of the mechanical behavior under a biaxial state can be carried out using other testing techniques and specimen geometries (Kuwabara (2007)):

1. **Hydraulic bulge test:** a circular blank is bulged by applying a pressurized fluid with an electric pump (see Figure 4-4). This technique is used in several investigations, e.g. Lăzărescu *et al.* (2011), Lemoine *et al.* (2011), Li *et al.* (2003), Thuillier (2008).

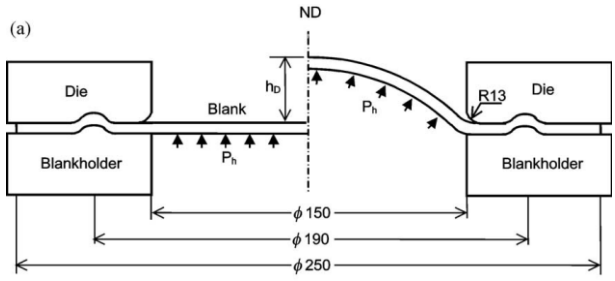

Figure 4-4 Schematic view of a bulge test (example from Li et al. (2003))

2. **Biaxial tension test using cruciform specimens:** different geometries are proposed in the literature. A review of them can be found in Kuwabara (2007).
3. **Uniaxial/biaxial compression test** using a stack of sheets.

This last technique enables to study the behavior of the material under different stress states (see Figure 4-5). Biaxial compression tests require an experimental device which is not very common, while uniaxial compression can be performed with any press. However two difficulties can be encountered when compressing along RD and TD: (1) failure can occur by delamination of the stack; (2) owing to the low thickness of the layers, delamination can also arise by buckling. For these reasons, uniaxial compression is usually carried out along ND. It has to be noted that, if the friction between the specimen and the dies of the machine is low and if it is assumed that the material response is insensitive to the hydrostatic pressure, the layer compression test is similar to a balanced biaxial tensile test (Coppieters (2012)).

In order to determine the behavior of Ti6Al4V alloy under a biaxial stress state, a SCHENCK Hydropuls 400 kN press (Figure 4-6) was used to compress stacks composed of several Ti6Al4V sheet layers. The machine can be controlled in force, in displacement or in constant strain rate. Its mechanical features are given in Table 4-3.

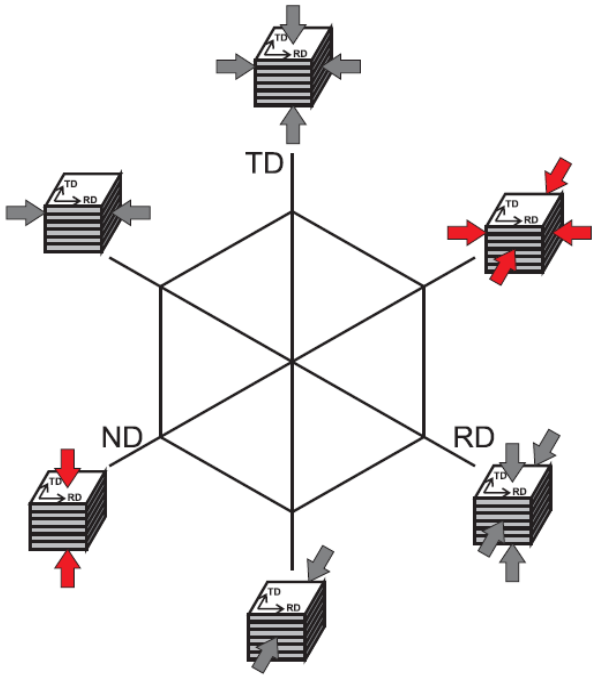

Figure 4-5 Stress directions on the π-plane in the (RD,TD,ND) reference frame

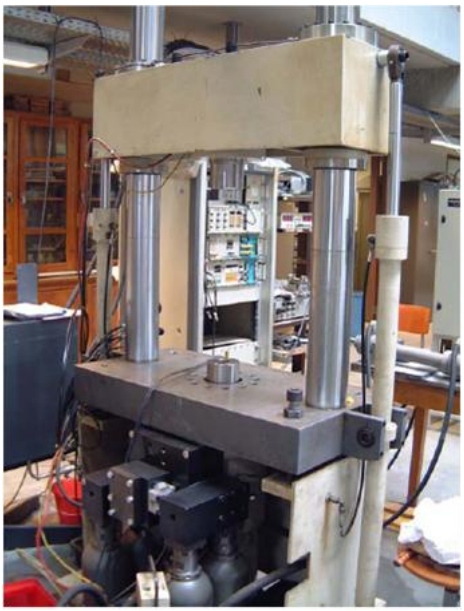

Figure 4-6 Overview of the uniaxial SCHENK Hydropuls 400 kN machine

Maximum capacity of the dynamometer	+/- 400 kN
Maximum displacement of the punch	+/- 125 mm
Machine deflection	1.4 mm to 350 kN
Speed	0.001 mm/s … 2 m/s
Strain rate range	0.0001/s to 0.1/s

Table 4-3 Characteristics of the SCHENCK Hydropuls 400 kN press

4.1.1.5. Zwick-Roell 1200 kN

When trying to validate a constitutive modeling, it is interesting to simulate a forming process in which different stress states are encountered and to compare the numerical predictions with the experiment. In this context, cup deep-drawing tests were conducted on Ti6Al4V at LEM3 (Arts et Métiers ParisTech, Metz, France). The deep-drawing process was carried out using a Zwick-Roell 1200 kN machine (Figure 4-7 (a)) and the experimental setup shown in Figure 4-7 (b). The characteristics of the device are listed in Table 4-4.

Maximum crosshead speed	400 mm/min
Crosshead position resolution	1 µm
Displacement sensor resolution	0.5 µm

Table 4-4 Characteristics of the experimental device used in the deep-drawing process

a **b**

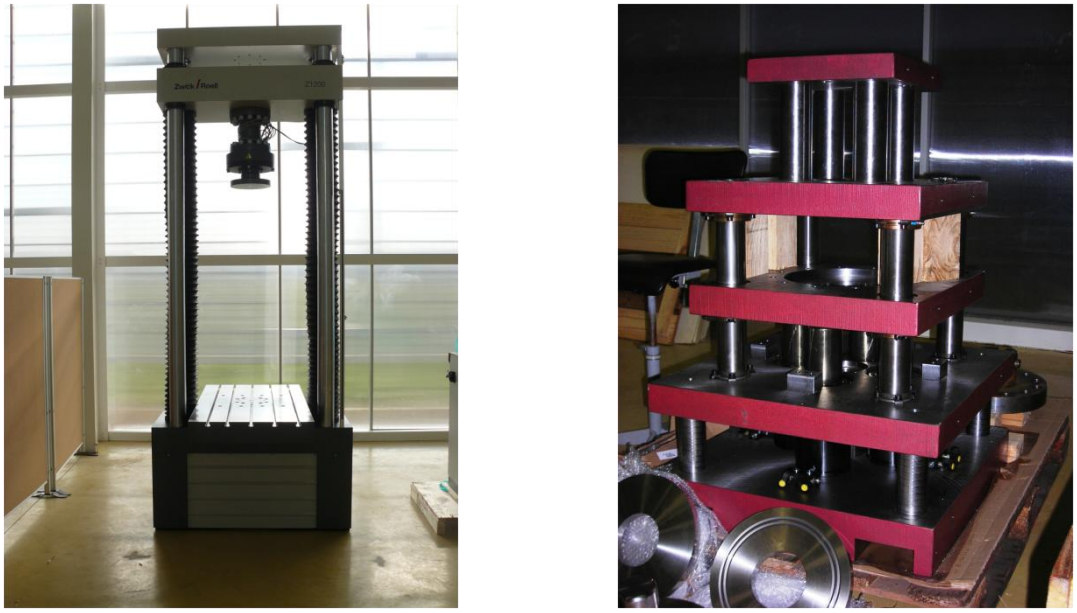

Figure 4-7 Experimental device used for deep-drawing tests: (a) Zwick-Roell 1200kN machine, (b) test setup

4.1.2. Optical measurement systems

For some experimental tests, an optical measurement system was used in addition to sensors in order to determine the displacement and strain fields by DIC. This technique is a full-field image analysis method which offers several benefits:

- It affords to visualize the strain gradients and hot spots which can occur when testing non-homogeneous and anisotropic materials.
- Some measurements, unrealizable with other techniques (strain gauges, extensometer, etc.) are made possible.
- As it is a non-contact system, some measurement errors (e.g. deflection of the testing machine, slip of the specimen under the grips, …) are prevented.

Owing to the increasing development of high resolution digital cameras, compact mechanical design and computer technology, DIC has widely expanded in industry applications (development and design tools, production inspection) and proved its efficiency in numerous investigations on material characterization (Knockaert (2001), Florès (2005), Duflou *et al.* (2008), Thuillier (2008), Hogström *et al.* (2009), Merklein and Kuppert (2009), Florès *et al.* (2010), Libertiaux *et al.* (2011), Tuninetti *et al.* (2012)).

4.1.2.1. Principles of DIC

DIC requires two digital cameras to locate a point in 3D space by triangulation (Figure 4-8). One camera can be enough in the case of a 2D analysis, but it is then required to maintain the tracked surface planar and at a constant distance from the camera. In 3D analysis, the determination of the object point position needs to know the orientations of the cameras with respect to each other (distance and angle) and some additional parameters relative to systematic image errors (translation of the principal point, lens distortions).

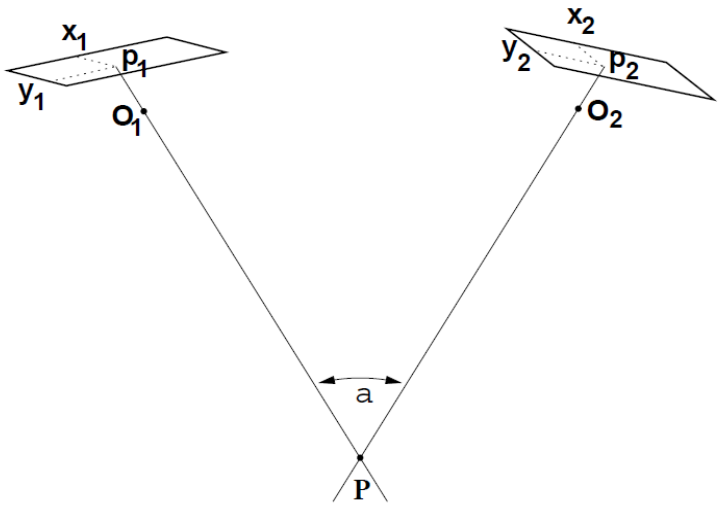

Figure 4-8 Principle of a 3D measuring arrangement: the rectangular planes represent the cameras' chips, O_1 and O_2 are the perspectives centers while x_1 and y_1 (respectively x_2 and y_2) are the coordinates of the point P relative to the first (respectively second) camera (GOM (2001)).

In order to track the displacement of points, a stochastic pattern with good contrast, as shown in Figure 4-9, is painted on the surface of the test object. Different methods exist to apply the stochastic pattern: colored spray paint, airbrush, printing, etc. It is worth noting that the speckle size distribution is very important since it affects the accuracy on the displacement field measurements (Lecompte *et al.* (2006)).

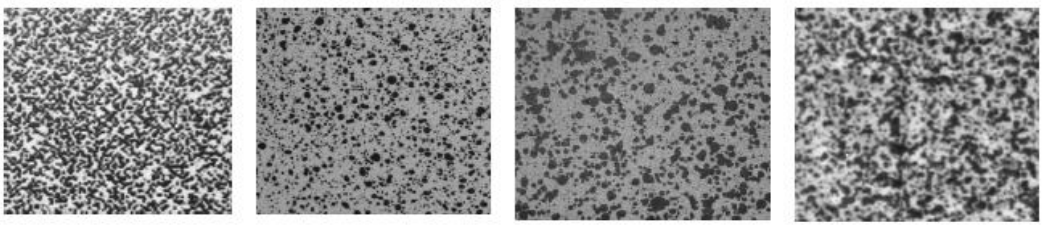

Figure 4-9 Examples of stochastic patterns

Before carrying out an experimental test, a picture (or more) of the undeformed state is taken in order to define a reference and to divide the specimen's surface into *facets* characterized by their grey level distribution. Then the optical system tries to track these facets on the images corresponding to every deformed configuration. The correlation is performed by applying a transformation consisting in a combination of a translation, a rotation and a distortion. The dimensions of the facets in the deformed configuration can be determined by several methods, e.g. Gaussian least squares adjustment, tangential model, spline-model, etc. Once the deformed configuration is known, the deformation gradient tensor $\mathbf{F}$ and therefore the strain field can be computed. Depending on the post-processing software, different definitions of the strain tensor for large deformations are proposed. All these definitions are based on the decomposition of the deformation gradient tensor into an orthogonal rotation tensor $\mathbf{R}$ and a symmetric stretch tensor $\mathbf{U}$ (*polar decomposition*):

$$\mathbf{F} = \mathbf{RU} \tag{4.1}$$

If $\mathbf{I}$ denotes the second-order identity tensor, the main strain tensors are defined as follows:

- *Biot* or *engineering* strain tensor: $\boldsymbol{\varepsilon}^B = \mathbf{U} - \mathbf{I}$
- *Green(-Lagrange)* strain tensor: $\boldsymbol{\varepsilon}^G = \frac{1}{2}\left(\mathbf{U}^2 - \mathbf{I}\right) = \frac{1}{2}\left(\mathbf{F}^T\mathbf{F} - \mathbf{I}\right)$
- *Hencky* or *logarithmic* or *natural* or *true* strain tensor: $\boldsymbol{\varepsilon}^N = \ln \mathbf{U}$

4.1.2.2. Systems used for the experimental tests

The biaxial machine (see Section 4.1.1.3) was equipped with the Aramis® optical measurement system developed by GOM (Figure 4-10). One camera was used to determine the displacement and strain fields evolving on the surface of the samples since the latter are flat. Aramis® has already proved its efficiency as measurement system in previous works (see Knockaert (2001), Florès (2003) and Florès (2005)) and especially in experiments carried out on the biaxial machine.

a **b**

Figure 4-10 Aramis® system: (a) camera, (b) computer hardware for the post-processing

During the layer compression tests performed on the SCHENK press (see Section 4.1.1.4), the displacements and the strains of the specimens were determined with the LIMESS optical system (Figure 4-11) and the VIC-3D software. The setting up, pointing, focusing and calibration of the cameras were previously achieved by Víctor Tuninetti in the framework of the FABULOUS project (the details can be found in Tuninetti and Habraken (2011)).

Figure 4-11 Cameras of the system LIMESS

4.2. Mechanical experiments

4.2.1. Definition of the reference systems

As the studied material is in sheet form (see Chapter 5), two reference frames are generally considered:

- *orthotropy* or *material* axes (X_1, X_2, X_3) which coincide with RD, TD and ND respectively;
- *local* axes (x_1, x_2, x_3).

x_1 and x_2 are chosen in the plane of the sheet depending on the specimen and the loading conditions (see next sections) while x_3 coincides with ND. The angle α defines the orientation of x_1 with respect to RD (see Figure 4-12).

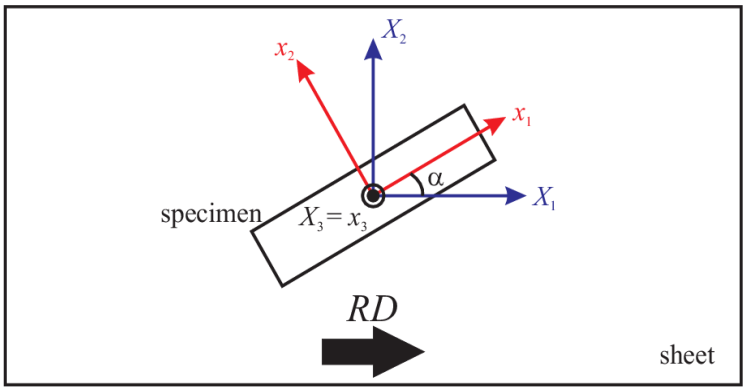

Figure 4-12 Definition of the global and material axes

If $\mathbf{T}$ is a 2nd order tensor, its components in the orthotropic and local frames are linked in the following way:

$$\mathbf{T}\big|_{(X_1,X_2,X_3)} = \mathbf{R}\,\mathbf{T}\big|_{(x_1,x_2,x_3)}\,\mathbf{R}^T \tag{4.2}$$

where $\mathbf{R}$ is a rotation matrix defined as:

$$\mathbf{R} = \begin{bmatrix} \cos\alpha & -\sin\alpha & 0 \\ \sin\alpha & \cos\alpha & 0 \\ 0 & 0 & 1 \end{bmatrix} \tag{4.3}$$

4.2.2. Uniaxial tests

4.2.2.1. Tension

Introduction

Tensile tests are the most simple to perform and widely used to study the material mechanical behavior (anisotropy, hardening, …). If the loading direction is chosen along the x_1-axis, the general stress state in the local frame is expressed by:

$$\boldsymbol{\sigma}\big|_{(x_1,x_2,x_3)} = \begin{bmatrix} \sigma & 0 & 0 \\ 0 & 0 & 0 \\ 0 & 0 & 0 \end{bmatrix} \tag{4.4}$$

with $\sigma = \dfrac{F}{A} > 0$. F is the force applied to the specimen while A is the current area of the cross section. The latter can be deduced from the strain state:

$$\boldsymbol{\varepsilon}\big|_{(x_1,x_2,x_3)} = \begin{bmatrix} \varepsilon_1 & 0 & 0 \\ 0 & \varepsilon_2 & 0 \\ 0 & 0 & \varepsilon_3 \end{bmatrix} \tag{4.5}$$

ε_1, ε_2, ε_3 are respectively the axial, width and thickness logarithmic or true strains, *i.e.*:

$$\varepsilon_1 = \ln\frac{l}{l_0} \tag{4.6}$$

$$\varepsilon_2 = \ln\frac{w}{w_0} \tag{4.7}$$

$$\varepsilon_3 = \ln\frac{t}{t_0} \tag{4.8}$$

where l, w and t are respectively the gage length, the width and the thickness of the sample (the subscript "0" refers to the initial values). As long as there is no necking, the current area of the cross section (Figure 4-13) is given by:

$$A = wt = w_0 t_0 \exp\left(\varepsilon_2 + \varepsilon_3\right) \tag{4.9}$$

Assuming an elasto-plastic regime, isotropic elasticity and volume conservation during plastic deformation, it leads to:

$$A = w_0 t_0 \exp(\varepsilon_2^e + \varepsilon_3^e)\exp(\varepsilon_2^p + \varepsilon_3^p) = w_0 t_0 \exp(-2\nu\varepsilon_1^e - \varepsilon_1^p) \tag{4.10}$$

where ν is the Poisson ratio.

It can be noticed that this relationship requires the knowledge of the elastic constants. An approximation can be made by considering volume conservation during all the deformation, *i.e.* $\varepsilon_1+\varepsilon_2+\varepsilon_3=0$. The current area is then assessed as follows:

$$A^* = w_0 t_0 \exp\left(-\varepsilon_1\right) \tag{4.11}$$

The ratio between the exact and estimated areas is:

$$\rho = \frac{A}{A^*} = \frac{\sigma^*}{\sigma} = \exp\left(\left(1-2\nu\right)\varepsilon_1^e\right) \tag{4.12}$$

with $\sigma^* = \dfrac{F}{A^*}$. For $\varepsilon_1^e = 1\%$ (the elastic strain hardly exceeds this value in Ti6Al4V titanium alloy) and $0.28 \le \nu \le 0.35$, ρ ranges from 1.003 to 1.0044, *i.e.* a relative error lower than 1%, which proves the validity of the approximation.

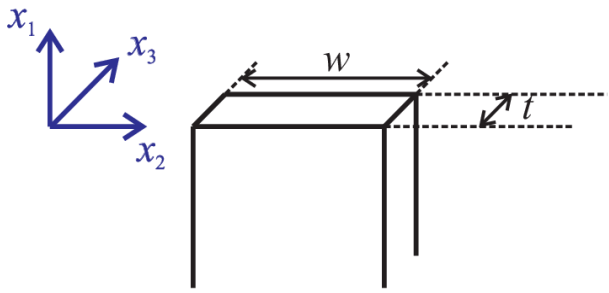

Figure 4-13 Cross section of the specimen: w is the width while t is the thickness

In the material frame, the stress and strain tensors are expressed as follows:

$$\boldsymbol{\sigma}_{\left(X_1,X_2,X_3\right)}\Big| = \begin{bmatrix} \sigma\cos^2\alpha & \sigma\sin\alpha\cos\alpha & 0 \\ \sigma\sin\alpha\cos\alpha & \sigma\sin^2\alpha & 0 \\ 0 & 0 & 0 \end{bmatrix} \tag{4.13}$$

$$\boldsymbol{\varepsilon}_{\left(X_1,X_2,X_3\right)}\Big| = \begin{bmatrix} \varepsilon_1\cos^2\alpha+\varepsilon_2\sin^2\alpha & \left(\varepsilon_1-\varepsilon_2\right)\sin\alpha\cos\alpha & 0 \\ \left(\varepsilon_1-\varepsilon_2\right)\sin\alpha\cos\alpha & \varepsilon_1\sin^2\alpha+\varepsilon_2\cos^2\alpha & 0 \\ 0 & 0 & \varepsilon_3 \end{bmatrix} \tag{4.14}$$

In order to characterize the anisotropy of Ti6Al4V in tension, tests are performed on the Zwick 100kN machine (see Section 4.1.1.1) at room temperature and at a constant strain rate of 3×10^{-4} s^{-1} along eleven directions in the plane of the sheet (α ranging from 0° to 90° by steps of 10° and $\alpha = 45°$). The specimens are cut by milling and have an overall length of 299.6 mm, a gage length of 105 mm and a gage width of 15 mm (Figure 4-14).

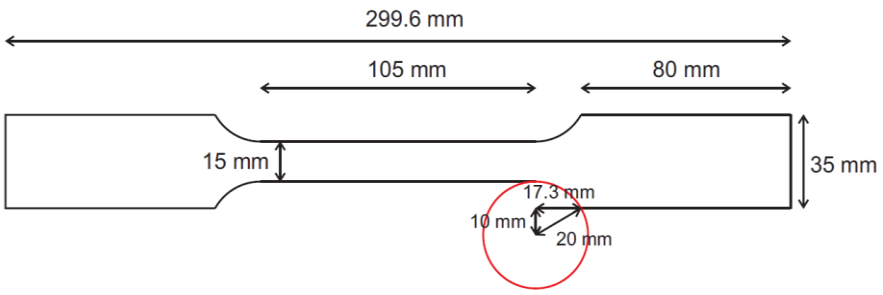

Figure 4-14 Geometry and dimensions of tensile specimens

For each loading direction, the tests are duplicated four times as follows:

- two tests up to failure;
- one test up to a strain of 5%;
- one test up to a strain of 10% (when failure occurs beyond this value).

The specimens deformed at 5% and 10% of strain level are used to achieve texture measurements.

The applied force is recorded by a load cell and the longitudinal strain ε_l is measured with the mechanical extensometer. The stress is then computed using:

$$\sigma \approx \frac{F}{A^*} \tag{4.15}$$

A^* is computed from Equation (4.11) with ε_1 being ε_l.

In addition to the measurements performed by the extensometer, the strain field in the gage zone is determined by the Aramis® system in order to assess the tensile Lankford coefficient or *r*-ratio. The latter is defined as the plastic width strain rate divided by the plastic thickness strain rate. Because the thickness change involves large relative measurement uncertainty, the axial strain (ε_l) and the width strain (ε_w) are used with assumed volume constancy to infer the thickness strain (ε_t). Thus, the Lankford coefficient is given by:

$$r \equiv \frac{\dot{\varepsilon}_w^p}{\dot{\varepsilon}_t^p} = -\frac{\dot{\varepsilon}_w^p}{\dot{\varepsilon}_l^p + \dot{\varepsilon}_w^p} \tag{4.16}$$

where the superscript p refers to plastic strain, and the subscripts l, w and t refer to length, width and thickness, respectively.

The effect of the strain rate on the mechanical behavior in tension is also investigated. Experiments are carried out along RD at 10^{-4} s^{-1}, 10^{-3} s^{-1}, 10^{-2} s^{-1} and 10^{-1} s^{-1}. In order to check the reproducibility, each test is reproduced at least two times.

Equipment validation

Before performing the tensile tests, it must be checked that:

- the strain rate is actually maintained constant;

- the data provided by Aramis® are in good agreement with the measurements of the extensometer.

Strain rate constancy

The (logarithmic) strain rate along the length direction is given by:

$$\dot{\varepsilon}_l = \frac{d}{dt}\left(\ln\frac{l}{l_0}\right) = \frac{dl/dt}{l} \tag{4.17}$$

This relationship can be written as follows:

$$\frac{dl}{l} = d\left(\ln l\right) = \dot{\varepsilon}dt \tag{4.18}$$

Since the machine is controlled in displacement, solving Equation (4.18) shows that a constant strain rate is obtained when the length evolves with time in an exponential way, namely:

$$l(t) = l_0 \exp(Ct) \tag{4.19}$$

where C is the value of the desired strain rate. In order to achieve this requirement, the current length of the specimen is regulated by a PID controller.

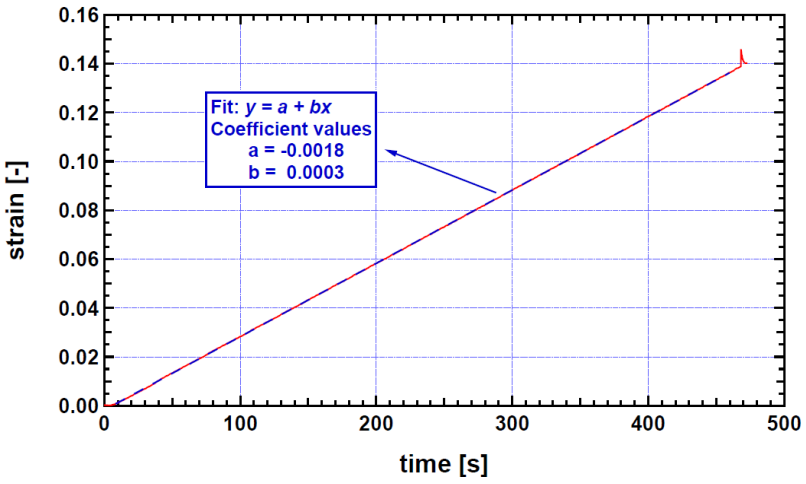

Figure 4-15 Evolution of the axial strain with time for a test at 3×10^{-4} s^{-1}

Figure 4-15 shows the axial strain as a function of time for a test at 3×10^{-4} s^{-1}. It can be observed that the evolution is linear and the slope of the line is in agreement with the prescribed strain rate.

Comparison of data recorded by the optical and mechanical measurement systems

As explained previously, images of the specimen are snapped by the camera and compared in order to compute the displacement and strain fields. Aramis® is able to export data along a section defined by the user. An example is given in Figure 4-16 which shows the axial and

transversal strain fields along the gage length of the sample and at different stages of the deformation. The strain peak is due to necking.

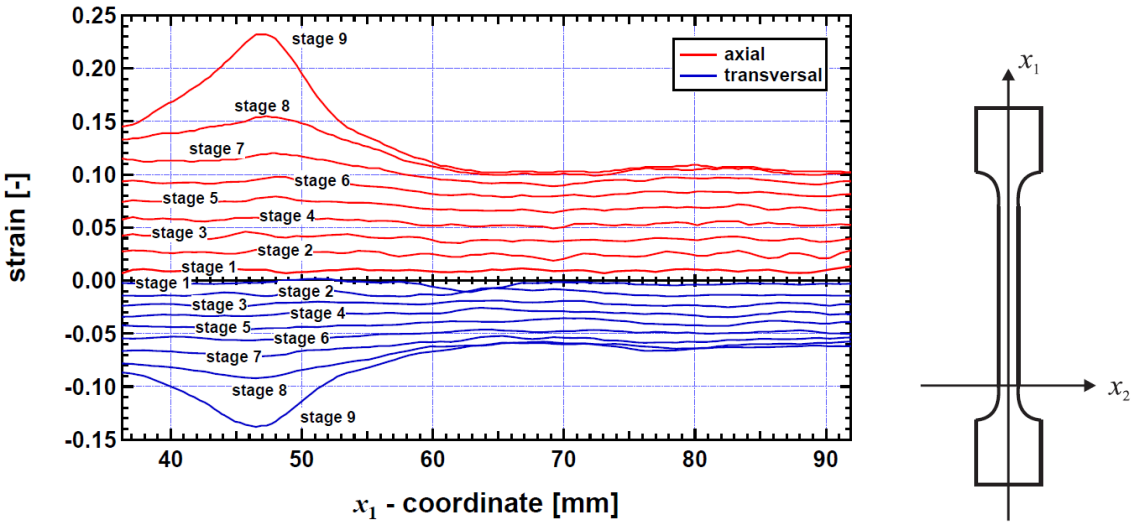

Figure 4-16 Axial and transversal strain fields along the gage length of the specimen (x_1-direction, x_2 = 0) at different stages

As the extensometer measures the length between the sensor arms (see Figure 4-17), the axial strain determined by Eq. (4.6) corresponds to an average value.

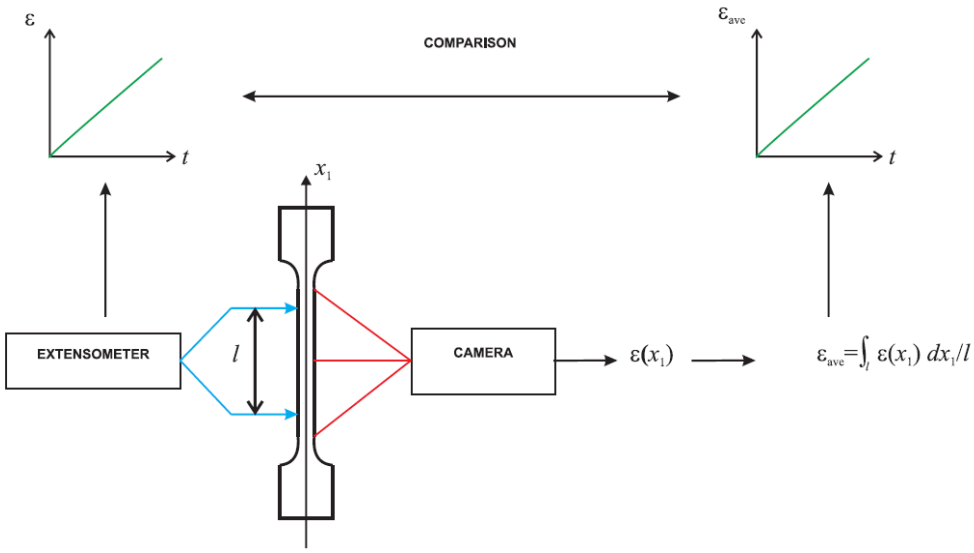

Figure 4-17 Comparison of the axial strains computed from the data of both measurement systems

Based on the axial strain field $\varepsilon(x_1)$ computed by Aramis® along the x_1-axis (loading direction), it is possible to assess the average strain ε_{ave} by:

$$\varepsilon_{ave} = \frac{\int_l \varepsilon(x_1)\,dx_1}{l} \tag{4.20}$$

and to compare the results obtained with the two measurement systems (Figure 4-17).

Figure 4-18 shows the evolution of the average strain with time according to the extensometer and Aramis®. It can be observed that both systems are in very good agreement.

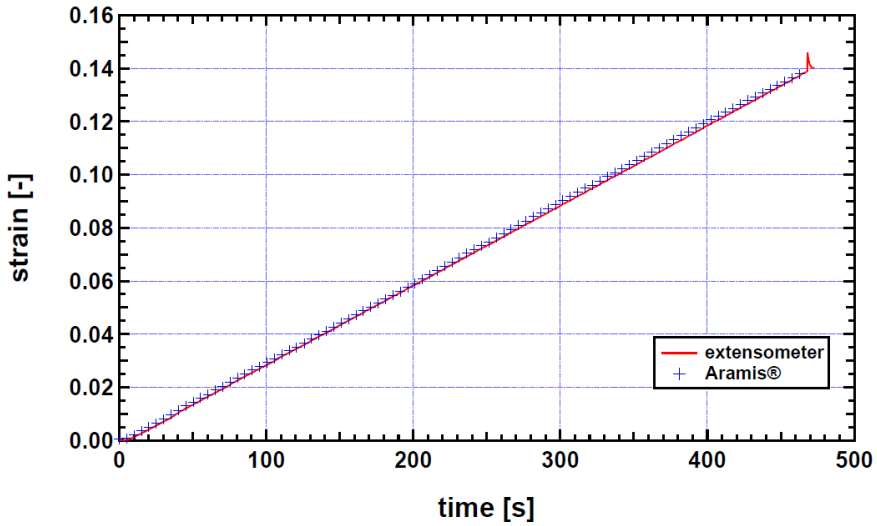

Figure 4-18 Evolution of the average axial strain according to the extensometer and the Aramis® optical system (test at $3\times10^{-4}\ s^{-1}$)

4.2.2.2. Compression

In order to investigate the effect of the loading orientation on the mechanical response and quantify the tension-compression asymmetry of Ti6Al4V, compression tests are required. Using the same local frame as for tensile tests, the general stress state is:

$$\boldsymbol{\sigma}\big|_{(x_1,x_2,x_3)} = \begin{bmatrix} -\sigma & 0 & 0 \\ 0 & 0 & 0 \\ 0 & 0 & 0 \end{bmatrix} \tag{4.21}$$

with $\sigma > 0$. In the material frame, the stress tensor is given by:

$$\boldsymbol{\sigma}\big|_{(X_1,X_2,X_3)} = \begin{bmatrix} -\sigma\cos^2\alpha & -\sigma\sin\alpha\cos\alpha & 0 \\ -\sigma\sin\alpha\cos\alpha & -\sigma\sin^2\alpha & 0 \\ 0 & 0 & 0 \end{bmatrix} \tag{4.22}$$

The axial, width and thickness strains are computed as previously (Equations (4.6), (4.7) and (4.8)).

The material uniaxial response in tension and compression in three in-plane orientations, namely in RD, 45° and TD, respectively, was measured by Pr T. Kuwabara and his team from TUAT. The tests were carried out on the comb-shaped dies apparatus described in Section 4.1.1.2 and repeated three times to check the experimental reproducibility. The sample dimensions are shown in Figure 4-19.

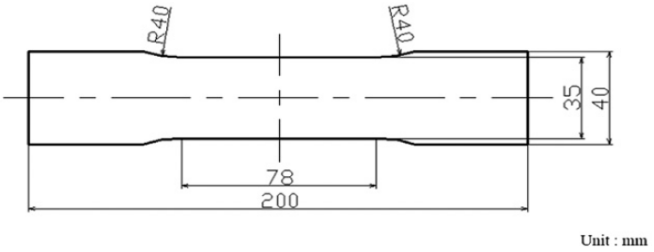

Figure 4-19 Geometry and dimensions of the specimens used at TUAT

It has to be specified that the experimental device used at TUAT does not allow the control of the strain rate. Nevertheless, it is possible to keep the mean strain rate nearly constant. The latter was fixed to 3×10^{-4} s^{-1}.

4.2.3. Biaxial tests

4.2.3.1. Tests carried out on the biaxial machine

Plane strain

Considering the configuration in Figure 4-13, the plane strain state assumes that:

$$\varepsilon_2 = 0 \tag{4.23}$$

and the strain tensor in the local frame is then of the form:

$$\boldsymbol{\varepsilon}\big|_{(x_1,x_2,x_3)} = \begin{bmatrix} \varepsilon_1 & 0 & 0 \\ 0 & 0 & 0 \\ 0 & 0 & \varepsilon_3 \end{bmatrix} \tag{4.24}$$

Consequently, the general stress state displays two non-zero components:

$$\boldsymbol{\sigma}\big|_{(x_1,x_2,x_3)} = \begin{bmatrix} \sigma_1 & 0 & 0 \\ 0 & \sigma_2 & 0 \\ 0 & 0 & 0 \end{bmatrix} \tag{4.25}$$

In the material frame, the stress and strain tensors are respectively given by:

$$\boldsymbol{\sigma}\big|_{(X_1,X_2,X_3)} = \begin{bmatrix} \sigma_1\cos^2\alpha + \sigma_2\sin^2\alpha & (\sigma_1-\sigma_2)\sin\alpha\cos\alpha & 0 \\ (\sigma_1-\sigma_2)\sin\alpha\cos\alpha & \sigma_1\sin^2\alpha + \sigma_2\cos^2\alpha & 0 \\ 0 & 0 & 0 \end{bmatrix} \tag{4.26}$$

$$\boldsymbol{\varepsilon}\big|_{(X_1,X_2,X_3)} = \begin{bmatrix} \varepsilon_1\cos^2\alpha & \varepsilon_1\sin\alpha\cos\alpha & 0 \\ \varepsilon_1\sin\alpha\cos\alpha & \varepsilon_1\sin^2\alpha & 0 \\ 0 & 0 & \varepsilon_3 \end{bmatrix} \tag{4.27}$$

In practice, plane strain tests are performed by applying tension to a piece of sheet metal with a high width to length ratio. The drawback of this simple technique is that the stress in the transverse direction σ_2 cannot be determined experimentally.

The tensile plane strain tests were carried out with the biaxial machine designed by P. Florès (see Section 4.1.1.3). Two computers are used during these tests. The first one (Figure 4-10 (b) at the left) enables the control of the actuators. The computation of the displacement and the strain fields is achieved thanks to the Aramis® measurement system which is installed on the second computer (Figure 4-10 (b) at the right). The latter is connected to the camera (Figure 4-10 (a)) used to snap pictures of the deformed sample.

The first plane strain tensile tests were performed with the specimen geometry used in Florès (2005) (Figure 4-20 (a)). The velocity of the vertical actuator was 5×10^{-3} mm/s while the horizontal actuator is maintained fixed. The samples are placed in the grips as shown in Figure 4-20 (b). In order to determine the strain field by image correlation, a stochastic pattern is beforehand painted on the gage zone located at mid-length (30 mm × 3 mm).

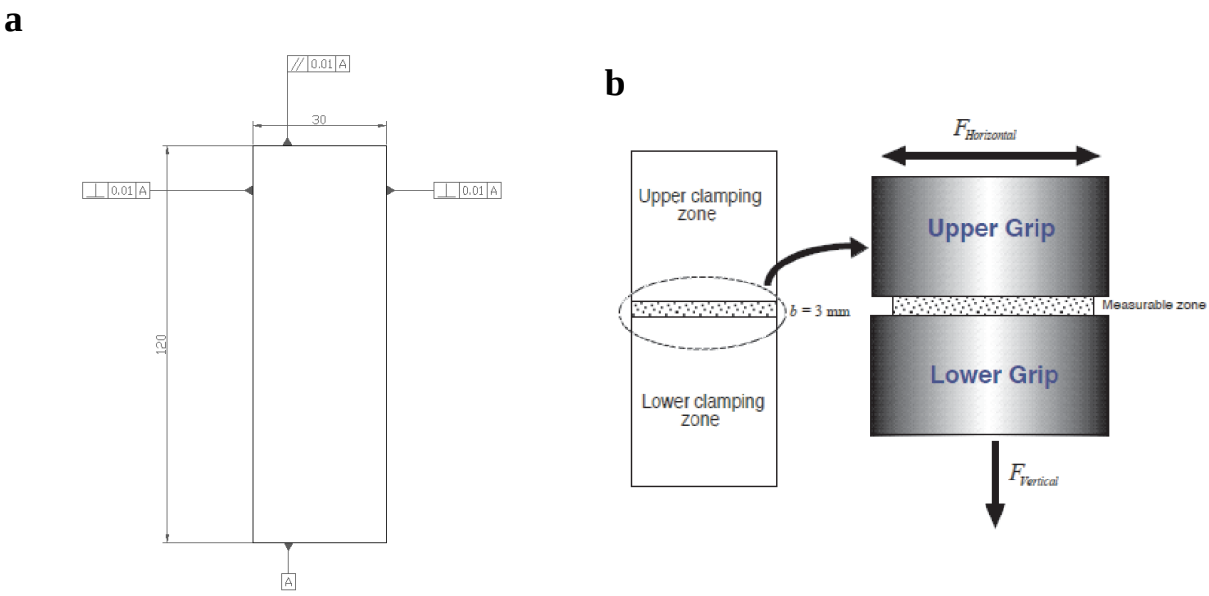

Figure 4-20 (a) Geometry and dimensions (in mm) of the specimens used for the first plane strain tests, (b) configuration of a specimen inside the grips

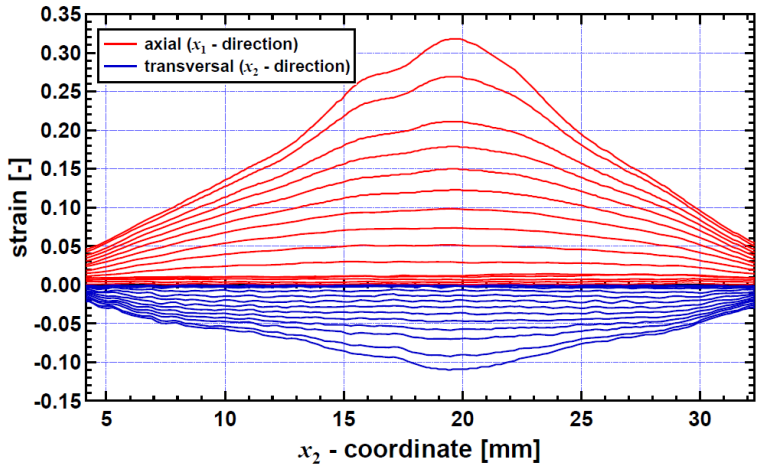

Figure 4-21 Axial and transversal strain distributions along the width of the gage zone at different stages of the deformation (rectangular shape specimen)

Before proceeding the stress computation, it is required to check the homogeneity of the strain distribution. Figure 4-21 depicts an example of the axial (x_1 -direction) and transversal (x_2 -direction) strain fields along the width of the gage zone. It is noticed that a significant strain concentration is present at the center of the specimen, making complex the analysis of the results. An observation of the frames at different stages of the deformation (Figure 4-22) shows that the specimen glides inside the grips, which explains the heterogeneity of the strain distribution. This gliding is due to the fact that the clamping force is not uniformly applied, its magnitude being slightly lower near to the gage zone than at the center of the clamping zone. Thereby, given this defect in the machine and the mechanical properties of titanium (high yield limit), it is very difficult to prevent the specimen from gliding.

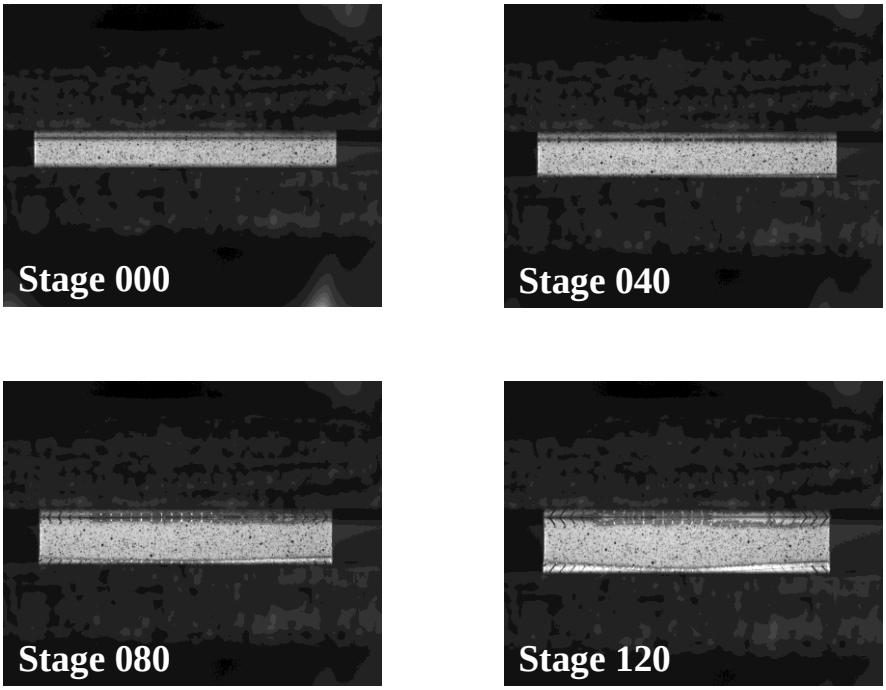

Figure 4-22 Images of the gage zone at different stages of a plane strain test with a rectangular shape specimen

Based on the work of Pijlman (2002) and Florès *et al.* (2010), a new geometry (Figure 4-23) was designed and experimented while controlling the occurrence of gliding. The specimens have a rectangular shape as previously, but with notches at mid-length. The gage zone is 25 mm wide and 3 mm high.

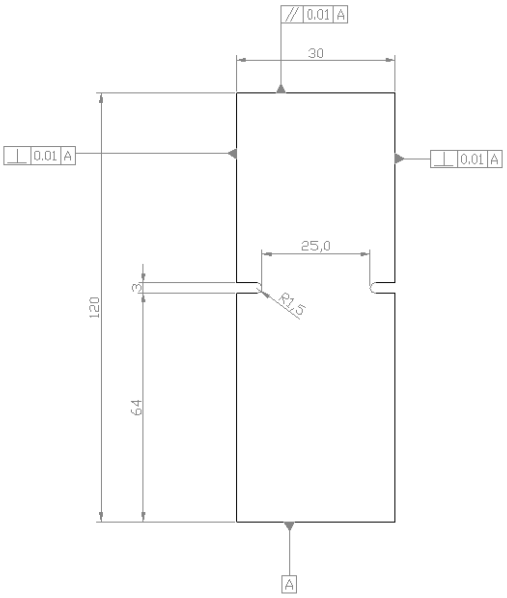

Figure 4-23 Geometry and dimensions (in mm) of the specimens used for the second plane strain tests

Tests were performed at a velocity of the actuators of 5×10^{-3} mm/s. The axial and transversal strain fields along the width of the gage zone were provided by Aramis®. Figure 4-24 shows a typical distribution where two different areas can be distinguished:

- a homogeneous central zone in plane strain state (the transversal strain is low compared to the axial strain) whose size decreases as long as the specimen is being deformed;
- a heterogeneous zone at the edges of the specimen where strains evolve faster than strains at the central zone.

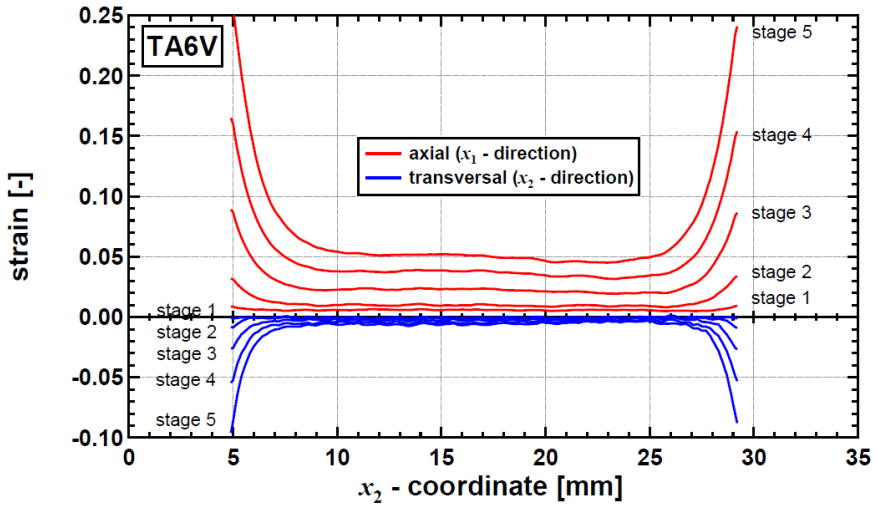

Figure 4-24 Axial and transversal strain distributions along the width of the gage zone at different stages of the deformation (specimen with notches)

Since the strain field is not uniform, the edge effects must be taken into account in the stress computation. A methodology similar to the one proposed by Florès *et al.* (2010) was used. It consists firstly in identifying the homogeneous strain field zone at the different stages of the deformation process. Theoretically the strain distribution is uniform when:

$$\frac{\partial \varepsilon_{11}}{\partial x_2} = 0 \tag{4.28}$$

where ε_{11} denotes the axial strain. In practice, a range $[-\xi\,;\xi]$ inside which the strain field is considered homogeneous is defined at each stage of the deformation. The condition (4.28) is then expressed as:

$$-\xi \le \frac{\partial \varepsilon_{11}}{\partial x_2} \le \xi \tag{4.29}$$

The boundary ξ is chosen as the average deviation of the strain gradient $\frac{\partial \varepsilon_{11}}{\partial x_2}$ from zero at a $d = 5$ mm wide central zone of the specimen, *i.e.*:

$$\xi = \sqrt{\frac{\int_d \left(\frac{\partial \varepsilon_{11}}{\partial x_2}\right)^2 dx_2}{d}} \tag{4.30}$$

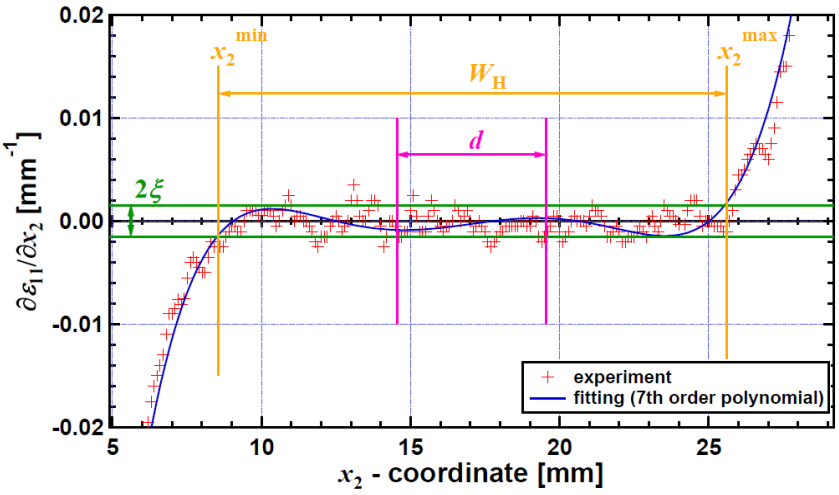

Figure 4-25 Determination of the homogeneous zone width W_H: the red symbols represent the experimental strain gradient which is fitted by a 7th order polynomial (blue curve), while d and 2ξ are respectively the central zone of the specimen and the domain inside which the strain field is assumed uniform

The strain gradient is then fitted by using a 7th order polynomial (Figure 4-25) and the homogeneous strain field width W_H is computed as follows:

$$W_H = x_2^{\max} - x_2^{\min} \tag{4.31}$$

with

$$x_2^{\min} = x_2\left(\left.\frac{\partial \varepsilon_{11}}{\partial x_2}\right|_{\text{fitted}} = -\xi\right) \;,\; x_2^{\max} = x_2\left(\left.\frac{\partial \varepsilon_{11}}{\partial x_2}\right|_{\text{fitted}} = \xi\right) \tag{4.32}$$

If W_T denotes the total width of the gage zone, the evolution of the ratio W_H / W_T can be drawn as a function of the average strain at the center of the specimen $\bar{\varepsilon}_{11}^c$ defined as follows:

$$\bar{\varepsilon}_{11}^c = \frac{1}{d}\int_d \varepsilon_{11}\, dx_2 \tag{4.33}$$

Figure 4-26 displays an example for a plane strain test along RD.

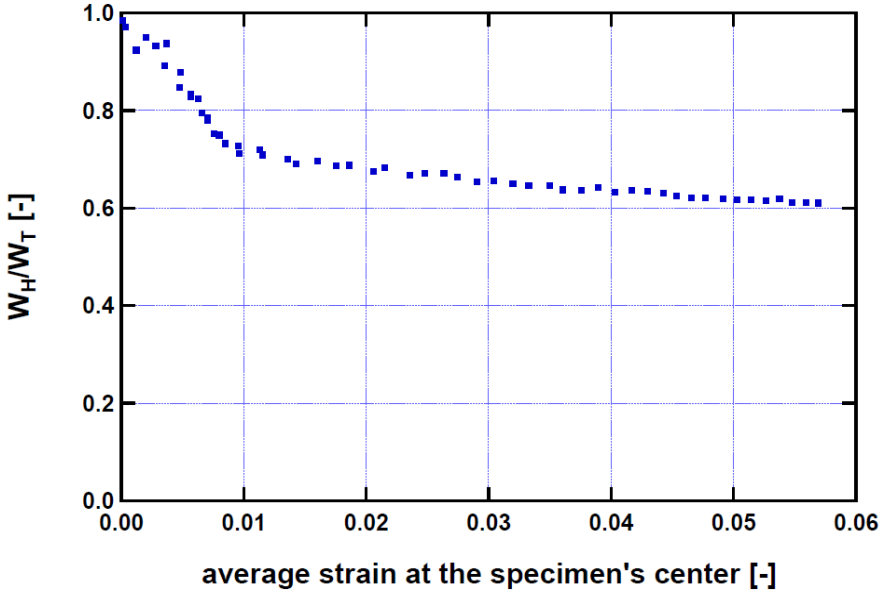

Figure 4-26 Evolution of the homogeneous zone width to total width ratio with the average strain at the center of the gage zone (plane strain test along RD)

With the previous results, the cross section A_H of the homogeneous zone can be determined as follows:

$$A_H = W_H t_H \tag{4.34}$$

where t_H is the actual thickness of the homogeneous zone. The latter is computed by:

$$t_H = t_0 \exp\left(-\bar{\varepsilon}_{11}^c\right) \tag{4.35}$$

In Equation (4.35), t_0 is the initial thickness of the specimen. In addition, the plane strain condition ($\varepsilon_{22} = 0$) and the volume conservation ($\varepsilon_{33} = -\varepsilon_{11} - \varepsilon_{22} = -\bar{\varepsilon}_{11}^c$) are assumed.

The computation of the normal stress σ_{11} under a plane strain state requires the determination of the actual force acting on the homogeneous zone F_H :

$$\sigma_{11} = \frac{F_H}{A_H} \tag{4.36}$$

Based on the study of An *et al.* (2004), Florès *et al.* (2010) suggests to express F_H in terms of the total force F_T applied to the specimen (measured experimentally by the biaxial machine) and the width of the homogeneous zone, *i.e.*:

$$F_H = F_H\left(F_T, W_H\right) \tag{4.37}$$

A numerical analysis, based on experimental data obtained for the studied Ti6Al4V alloy, was performed in order to study the evolution of F_H and define a relationship with the experimental data. It is shown in Appendix C that the force applied to the homogeneous zone can be expressed as follows:

$$\frac{F_H}{F_T} = \alpha \frac{W_H}{W_T} + \left(1-\alpha\right) \tag{4.38}$$

where α is a coefficient, and thus the stress component σ_{11} is given by:

$$\sigma_{11} = \frac{F_H}{A_H} = \alpha \frac{F_T}{W_T t_H} + \left(1-\alpha\right)\frac{F_T}{W_H t_H} \tag{4.39}$$

The coefficient α is determined by linear regression. The result of the numerical analysis is $\alpha = 1.0154$.

Equation (4.39) is then used to compute the stress-strain response of Ti6Al4V in plane strain in RD, 45°-direction and TD (see Figure 4-27).

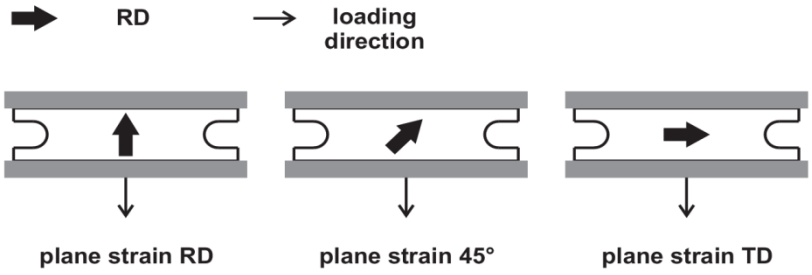

Figure 4-27 Schematic of the plane strain tests in RD, 45°-direction and TD

Simple shear and Bauschinger tests

Compared to uniaxial tension or compression, simple shear tests offer several advantages:

- the specimens do not require complex shapes (a rectangular one as shown in Figure 4-20 (a) can be suitable for materials less stiff than the studied Ti6Al4V);
- plastic instabilities existing in tension (localization, necking) or in compression (barreling) do not occur in simple shear;
- a large range of homogeneous strains can be achieved.

Nevertheless, some problems can be encountered during the experiments. Indeed, as it will be shown further, a part of the specimen clamped zones deforms, involving a sliding movement under the grips. The extent of this sliding depends on the material and the quality of the grips. Moreover, as depicted in Figure 4-28, two opposite corners of the gage zone are subjected to transverse tension or compression, causing premature failure and initiation of buckling respectively. More details about the advantages and drawbacks of simple shear tests can be found in Bouvier *et al.* (2006).

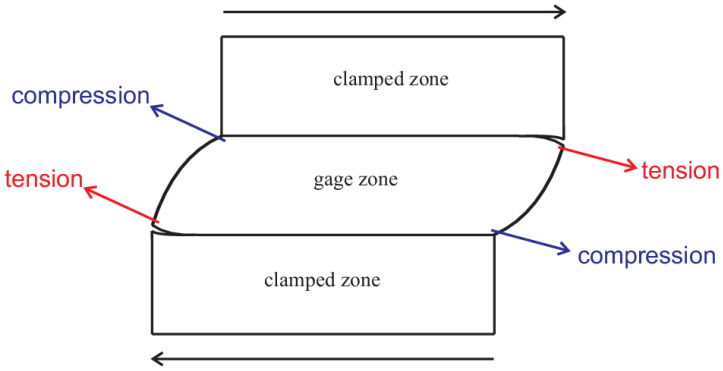

Figure 4-28 Area of the sample in transverse tension and compression during a simple shear test

Figure 4-29 shows the initial and deformed configurations of a facet in simple shear state. The deformation gradient tensor $\mathbf{F}$ is expressed by:

$$\mathbf{F} = \begin{bmatrix} 1 & \gamma & 0 \\ 0 & 1 & 0 \\ 0 & 0 & 1 \end{bmatrix} \tag{4.40}$$

where

$$\gamma = \tan\theta = \frac{d}{b} \tag{4.41}$$

d represents the relative displacement of the facet while b is its height which is maintained constant. It has to be noted that $\det \mathbf{F} = 1$ (see Equation (4.40)), which means that the volume is conserved.

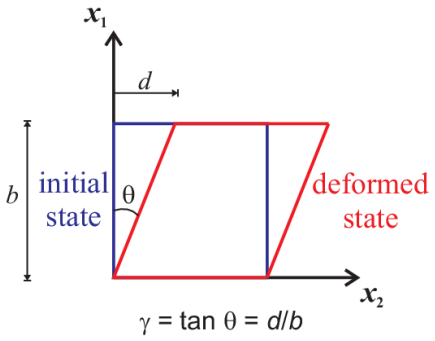

Figure 4-29 Schematic representation of simple shear

In the local frame, the general forms of the stress and strain tensors in simple shear are given by:

$$\boldsymbol{\sigma}\big|_{(x_1,x_2,x_3)} = \begin{bmatrix} \sigma_1 & \tau & 0 \\ \tau & \sigma_2 & 0 \\ 0 & 0 & 0 \end{bmatrix} \tag{4.42}$$

$$\boldsymbol{\varepsilon}\big|_{(x_1,x_2,x_3)} = \begin{bmatrix} \varepsilon_{11} & \varepsilon_{12} & 0 \\ \varepsilon_{12} & \varepsilon_{22} & 0 \\ 0 & 0 & 0 \end{bmatrix} \tag{4.43}$$

with $|\varepsilon_{11}| = |\varepsilon_{22}|$ (volume conservation).

In the material frame, Equation (4.2) yields to:

$$\boldsymbol{\sigma}\big|_{(X_1,X_2,X_3)} = \begin{bmatrix} \sigma_1\cos^2\alpha + \sigma_2\sin^2\alpha - \tau\sin 2\alpha & (\sigma_1-\sigma_2)\sin\alpha\cos\alpha + \tau\cos 2\alpha & 0 \\ (\sigma_1-\sigma_2)\sin\alpha\cos\alpha + \tau\cos 2\alpha & \sigma_1\sin^2\alpha + \sigma_2\cos^2\alpha + \tau\sin 2\alpha & 0 \\ 0 & 0 & 0 \end{bmatrix} \tag{4.44}$$

$$\boldsymbol{\varepsilon}_{(X_1,X_2,X_3)}\big| = \begin{bmatrix} \varepsilon_{11}\cos^2\alpha + \varepsilon_{22}\sin^2\alpha - \varepsilon_{12}\sin 2\alpha & (\varepsilon_{11}-\varepsilon_{22})\sin\alpha\cos\alpha + \varepsilon_{12}\cos 2\alpha & 0 \\ (\varepsilon_{11}-\varepsilon_{22})\sin\alpha\cos\alpha + \varepsilon_{12}\cos 2\alpha & \varepsilon_{11}\sin^2\alpha + \varepsilon_{22}\cos^2\alpha + \varepsilon_{12}\sin 2\alpha & 0 \\ 0 & 0 & \varepsilon_3 \end{bmatrix} \tag{4.45}$$

In the case of small strains (elastic domain), the stress state can be considered as pure shear:

$$\boldsymbol{\sigma}\big|_{(x_1,x_2,x_3)} = \begin{bmatrix} 0 & \tau & 0 \\ \tau & 0 & 0 \\ 0 & 0 & 0 \end{bmatrix} \tag{4.46}$$

The simple shear tests on Ti6Al4V were first carried out on specimens with a rectangular shape (Figure 4-20 (a)). The velocity of the horizontal actuator was 5×10^{-3} mm/s while the vertical actuator was fixed.

The homogeneity of the strain field along the width of the gage zone was studied before determining the stress-strain curves. An example of distribution, provided by Aramis®, is given in Figure 4-30. It can be noticed that the edge effect is very significant, making difficult the stress computation. As for plane strain tensile tests, the heterogeneity of the strain field is due to a significant sliding movement of the specimen inside the grips, as observed in Figure 4-31.

In order to prevent gliding, a new specimen geometry (Figure 4-32) was designed and tested. Compared to the previous ones, the length of the samples is shorter in order that the clamping force applies on a smaller surface, increasing in this way the indentation of the grips in the material. In addition, notches are machined at mid-length, decreasing the size of the gage zone.

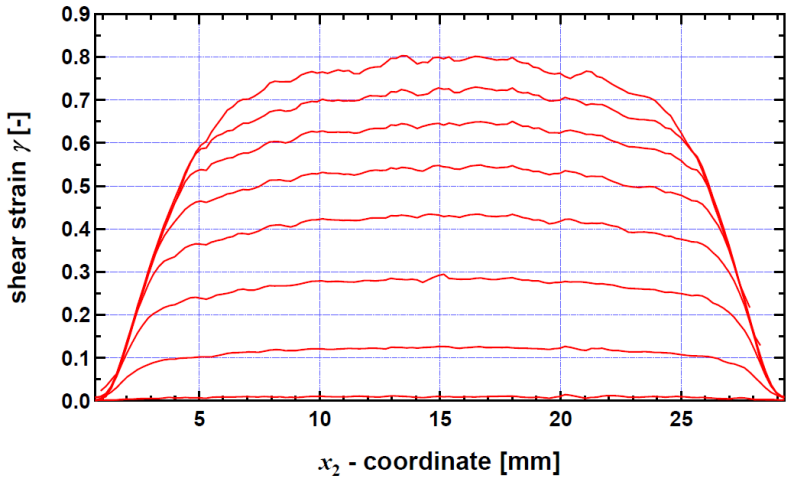

Figure 4-30 Shear strain γ distribution along the width of the gage zone at different stages of the deformation (rectangular shape specimen)

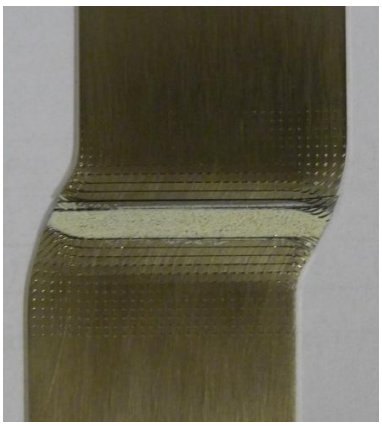

Figure 4-31 Gage zone of a specimen subjected to simple shear

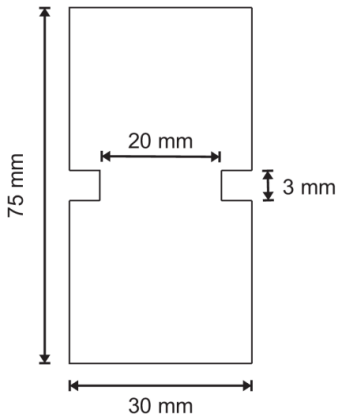

Figure 4-32 Geometry and dimensions of the specimens used for the second simple shear tests

Figure 4-33 shows the strain field at different stages of the deformation process when the new specimen geometry is used. It can be observed that a wide zone of homogeneous strain is obtained.

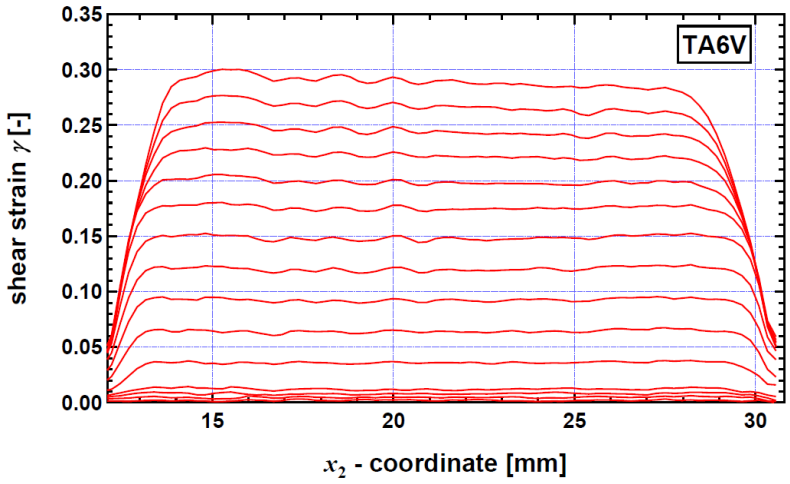

Figure 4-33 Shear strain γ distribution along the width of the gage zone at different stages of the deformation (specimen with notches)

In order to check that the specimen is actually in simple shear state, the different components of the deformation gradient tensor in the sheet plane were exported with Aramis® at the center of the gage zone and compared with the corresponding shear strain γ (Figure 4-34 (a)). For each stage of the deformation, the following results are obtained:

- the components F_{11} and F_{22} are equal to 1 while $F_{21} = 0$;
- $F_{12} = \gamma$ (see linear fitting in Figure 4-34(a)).

These observations are in good agreements with the theoretical form of the deformation gradient tensor given in Equation (4.40).

Figure 4-34 (b) compared the absolute values of the major and minor strains[3], respectively denoted ε_1 and ε_2, at the specimen's center. As specified previously, volume conservation is assumed in simple shear, which involves that:

$$|\varepsilon_1| = |\varepsilon_2| \tag{4.47}$$

The results in Figure 4-34 (b) show a good correlation with Equation (4.47).

It is worth noting that, although it is possible to reach large strains (Figure 4-33), the tests has to be stopped when premature failure occurs at the areas subjected to tension (see Figure 4-35). The initiation of cracks can be detected by observing the force-strain curve. Indeed, as shown in Figure 4-36, the force applied to the specimen progressively decreases when failure begins.

[3] The major and minor strains are defined as the maximal and minimal eigenvalues of the strain tensor in the sheet plane.

a

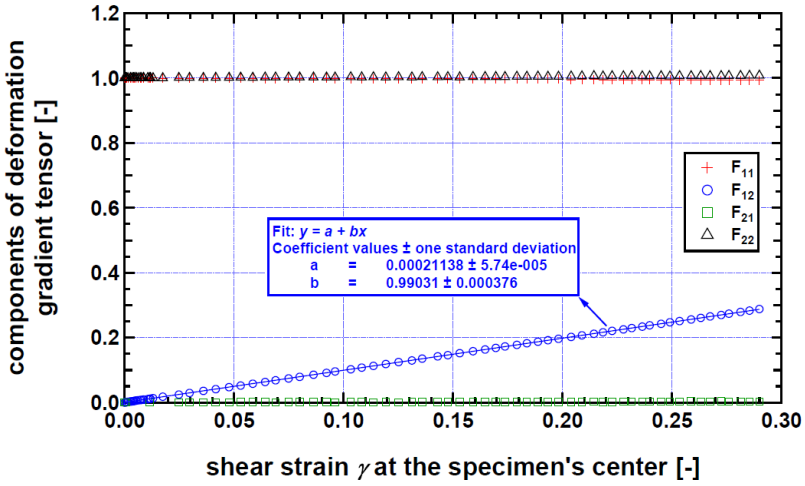

b

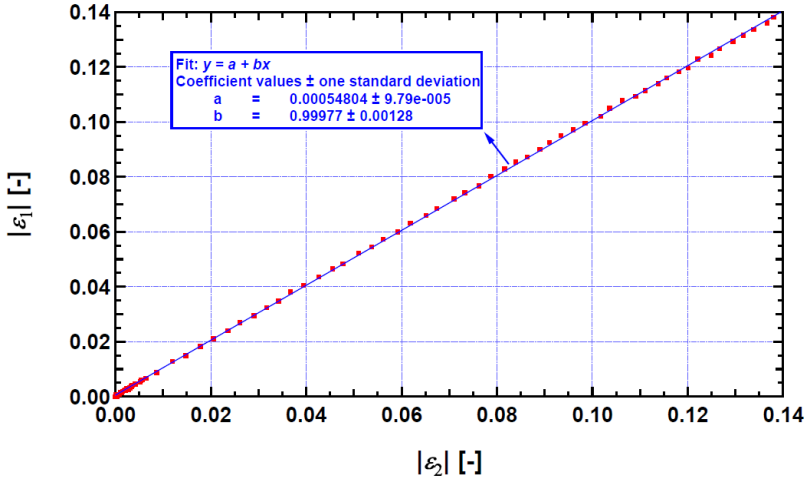

Figure 4-34 (a) Components of the deformation gradient tensor at the specimen's center compared with the corresponding shear strain γ ; (b) correlation between the major and minor strains (in absolute values) at the specimen's center

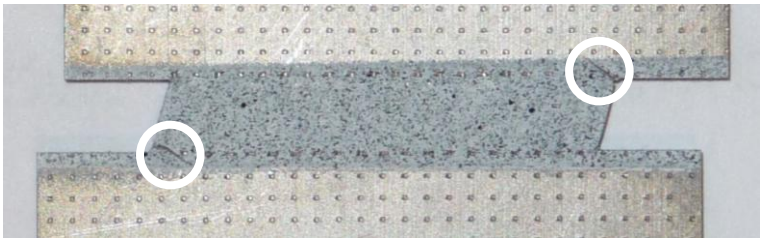

Figure 4-35 Cracks at the corners subjected to transverse tension

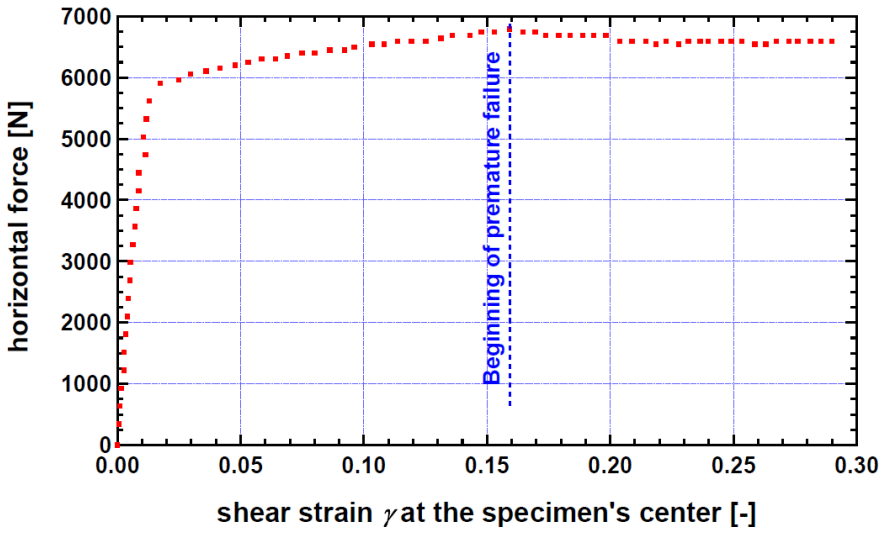

Figure 4-36 Evolution of the force applied to the specimen as a function of the strain at its center during a simple shear test: the force gradually decreases from 16% of strain, when failure starts at the areas in tension

Simple shear tests are performed in three in-plane orientations (see Figure 4-37). For each loading direction, the tests are repeated four times in order to check the experimental reproducibility. It has to be noted that the experiments in the 45°-orientation are carried out in both the forward and backward directions in order to observe a possible asymmetry in the mechanical response. The shear stress τ is computed by assuming the homogeneity of the strain field over the whole gage zone width and the volume conservation:

$$\tau = \frac{F_T}{A_0} \tag{4.48}$$

where F_T is the total force measured by the load cell of the horizontal actuator and A_0 is the initial area of the cross section. The shear strain γ is determined by calculating the average of the strain field distribution at the center of the gage zone.

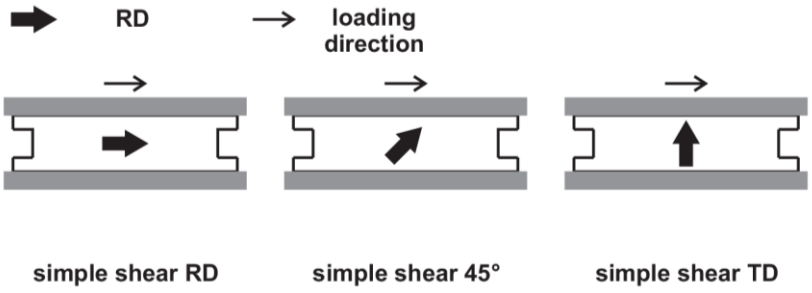

Figure 4-37 Schematic of the simple shear tests in RD, 45°-direction and TD

In addition to simple shear, Bauschinger tests were carried out on Ti6Al4V in order to study the influence of a strain path change on the material behavior. Bauschinger tests are obtained by reversing the loading direction during a simple shear test after the specimen has reached a certain amount of shear strain in the forward direction. These tests were performed with a horizontal actuator speed of 5×10^{-3} mm/s in RD with 10% pre-strain. The specimens have the same geometry and dimensions as those used in simple shear experiments (Figure 4-32).

4.2.3.2. Layer compression tests

In order to assess the mechanical behavior of Ti6Al4V under a biaxial state, layer compression tests were performed using the SCHENK Hydropuls 400 kN press described in Section 4.1.1.4. The specimens were composed with 23 elliptic layers which were stacked in order to form a cylinder (see Figure 4-38 (a)). The elliptic shape was chosen in order that the material axes (*i.e.* RD and TD) are not randomly oriented when assembling the layers. Indeed the latter were cut in such a way that the major and minor axes of the ellipses, respectively denoted 2*a* and 2*b* (Figure 4-38 (b)), coincide with RD and TD, respectively. The cutting of the layers was performed by WEDM which consists in using a thin metal wire constantly fed from a spool. During the process, the sheet is being watered by a dielectric fluid which flushes the cut debris away. WEDM enables a good surface roughness and does not alter the properties of the material, excepted in fatigue.

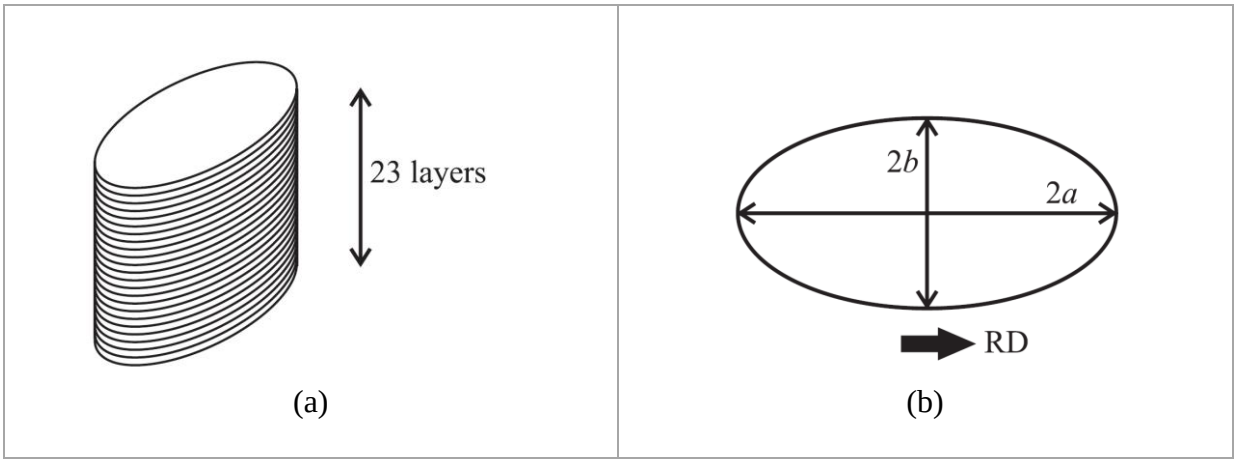

Figure 4-38 (a) shape of the specimens; (b) geometry of the cross-section: 2a and 2b denote the major and minor axes of the ellipse, respectively

During the compression of a stack, the out-of-plane displacement and strain fields were determined using three systems of two cameras placed around the specimen (see Figure 4-39). A stochastic pattern was painted on the free surface of the stack (Figure 4-40) in order to track the displacement of different points and to compute the strains by DIC.

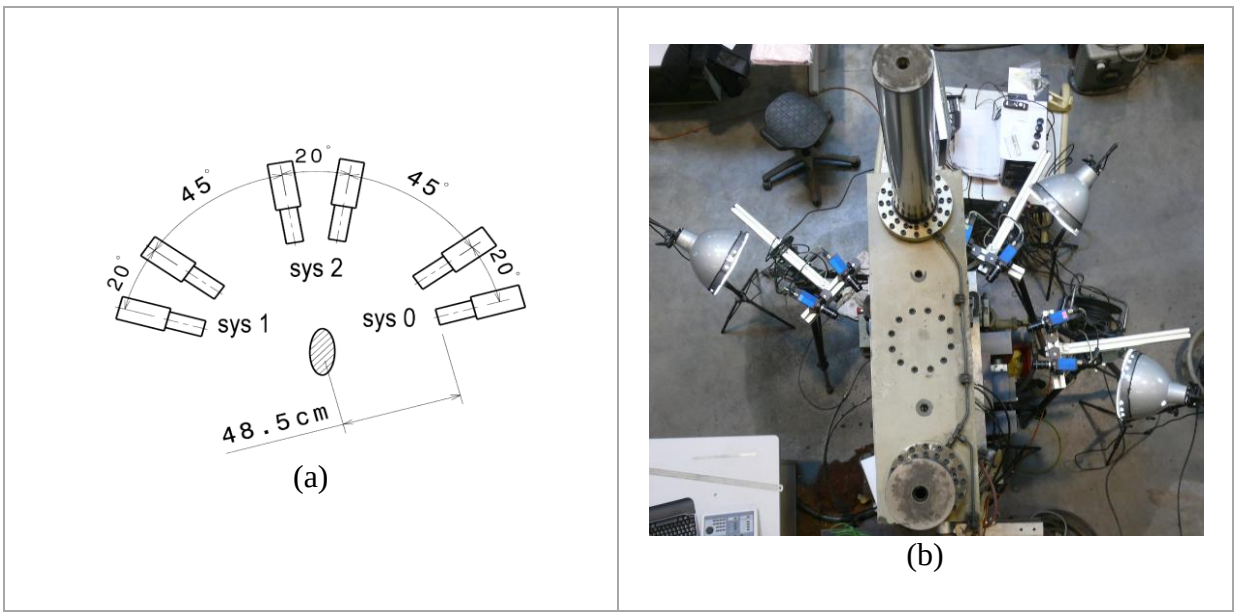

Figure 4-39 Experimental setup: (a) schematic view; (b) actual configuration

Figure 4-40 Specimen with a stochastic pattern on the lateral free surface

In order to maintain a constant strain rate during the deformation of the specimen, a procedure developed by Tuninetti *et al.* (2011) and taking into account the deflection of the machine was used. The average true compression strain $\overline{\varepsilon}_c$ is given by:

$$\overline{\varepsilon}_c = \ln\left(\frac{h}{h_0}\right) \tag{4.49}$$

where h_0 and h are respectively the initial and current height of the specimen. The strain rate is then written as:

$$\dot{\overline{\varepsilon}}_c = \frac{\dot{h}}{h} \tag{4.50}$$

A constant strain rate is obtained when the height evolves with time in an exponential way, *i.e.*:

$$h(t) = h_0\, e^{Ct} \tag{4.51}$$

where C denotes the value of the constant. Theoretically, if the dies are assumed rigid, the reduction in height of the specimen is given by the displacement z of the punch, which leads to:

$$z = h_0\left(1 - e^{Ct}\right) \tag{4.52}$$

In practice, z includes two terms:

- the reduction in height of the stack (z_{sp}), as previously mentioned;
- the deflection of the machine since the dies are actually deformable pieces.

It results that the strain rate applied to the specimen is different in the elastic domain. Indeed, during the elastic regime, the load increases at a high rate, producing high deflections of the machine. However, at larger strains, the strain rate is close to the targeted one since the increase rate of the force applied to the specimen is lower, inducing less deflections.

Figure 4-41 shows an example of the average axial strain evolution with time. The computation of the average axial strain is based on the data determined along the middle cross-section of the specimen, *i.e.* at mid-height of the stack. It can be observed that the strain rate is kept quasi-constant (~9.10^{-4} s^{-1} on average) during all the deformation.

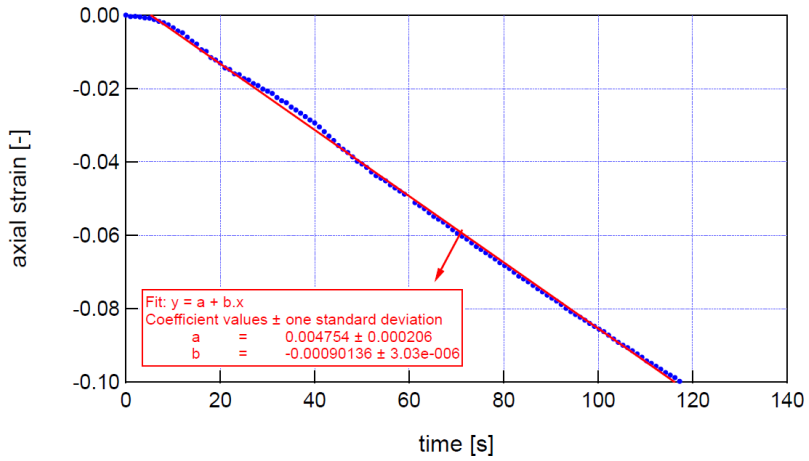

Figure 4-41 Evolution of the average axial strain with time during a layer compression test

Table 4-5 lists some features of the different layer compression tests performed on Ti6Al4V, namely:

- the identification number of the test and the specimen;
- the main dimensions of the specimen measured before and after the test (major and minor axes of the middle cross-section, height of the stack);
- the thickness of the paint layer placed on the lateral surface of the specimen and used for DIC.

In addition, it is specified if the test was performed or not at a constant strain rate.

The initial and final lengths of the major and minor axes were measured with a microscope (in the case of the final dimensions, the central layer of the stack was used since the geometry of the middle cross-section is studied) while the initial and final heights of the specimens were determined with the help of a micrometer. Regarding the thickness of the paint layer, the latter was also assessed using the micrometer as follows:

- after painting the stochastic pattern on the lateral surface of the stack, the dimensions of the cross-section were again measured three times in RD (major axis) and TD (minor axis);
- if the indices 0 and p denote the measurements without and with taking into account the paint layer respectively, the average thickness of the latter can be assessed by $t_a = a_p - a_0$ in RD and $t_b = b_p - b_0$ in TD;
- the average thickness around the cross-section, given in Table 4-5, is then calculated by $t = \frac{t_a + t_b}{2}$.

Finally, it has to be noted that the first five experiments only helped to adjust the displacement of the punch in order to obtain a constant strain rate and to check that the optical measurement system was in good working order.

Test number	1	2	3	4	5	6	7	8	9	10
Specimen number	2	3	5	7	8	4	6	9	10	11
Constant strain rate	no	no	yes	yes	no	yes	yes	yes	yes	yes
Initial height [mm]	13.85	13.83	13.81	13.81	13.92	14.07	14.10	13.55	14.16	14.16
Initial length of the major axis [mm]	20.0	20.0	20.0	20.0	20.0	20.0	20.0	20.0	20.0	20.0
Initial length of the minor axis [mm]	10.0	10.0	10.0	10.0	10.0	10.0	10.0	10.0	10.0	10.0
Final height [mm]	-	12.65	12.80	12.80	-	13.00	12.93	12.43	12.99	12.99
Final length of the major axis [mm]	-	-	20.67	20.65	20.67	20.67	20.64	20.65	20.63	20.72
Final length of the minor axis [mm]	-	-	10.66	10.65	10.66	10.69	10.75	10.70	10.69	10.77
Paint layer thickness [mm]	0.15	0.125	0.20	0.17	0.17	0.125	0.15	0.14	0.125	0.18

Table 4-5 Features of the different layer compression tests

4.2.4. Deep-drawing tests

Figure 4-42 shows a schematic view of the device which is used in LEM3 (Arts et Métiers ParisTech – Metz Campus, France) during a deep-drawing process. The latter consists in drawing a sheet metal into a forming die with a punch. A blank-holder is used to maintain the sheet during the process in order to prevent wrinkling which can occur near the edges of the blank if the blank-holder force is non-existent or too low. On the other hand, a too high force can cause a failure of the sheet. Finally a lubricant is placed between the specimen and the tools in order to reduce friction ($\mu \sim 0.04$).

Deep-drawing was performed by Prof. T. Balan and his team on five Ti6Al4V circular blanks with a diameter of 180 mm, *i.e.* a radius $R_B = 90$ mm. Table 4-6 provides the geometries of the tools and the lubricant used for each experimental test. It can be noticed that just the internal and profile radii of the matrix, as well as the lubricant, were changed from one experiment to another. The speed of the punch was fixed to 1 mm/s. During each drawing, the force and the displacement of the punch were measured. Then the earing profile of the deformed cup was manually determined (see Figure 4-43). Since failure occurs before the complete drawn of the sheet for all the tests, the earing profile corresponds to the radius of the cup as a function of the orientation with respect to RD.

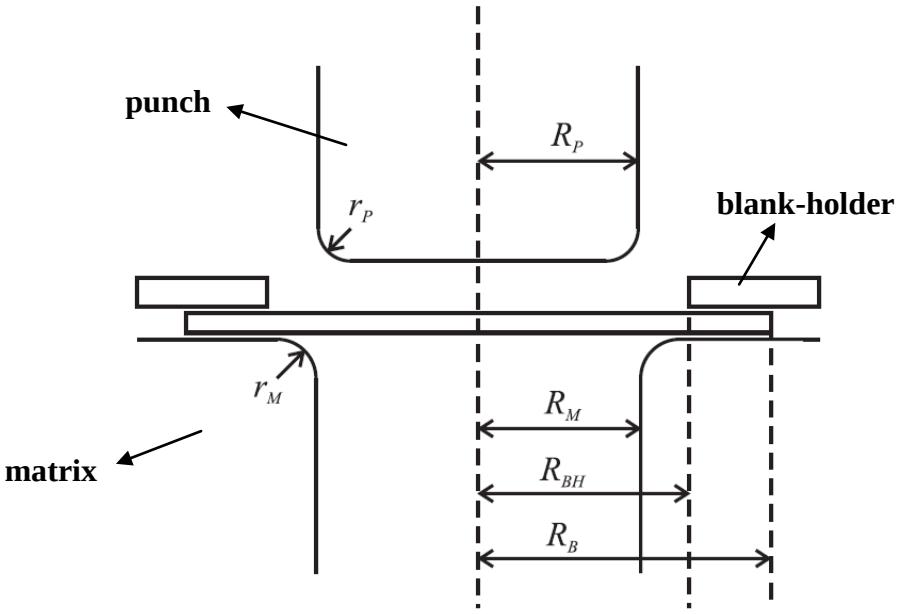

Figure 4-42 Schematic view of the experimental device used for deep-drawing

	Test 1	Test 2	Test 3	Test 4	Test 5
Radius of the punch R_P [mm]	49.25	49.25	49.25	49.25	49.25
Profile radius of the punch r_P [mm]	10	10	10	10	10
Internal radius of the blank-holder R_{BH} [mm]	50	50	50	50	50
Internal radius of the matrix R_M [mm]	55	55	50	50	50
Profile radius of the matrix r_M [mm]	10	10	8	8	12
Lubricant	Oil	Oil + Teflon	Oil	Oil + Teflon	Oil + Teflon
Blank-holder force [kN]	75	75	75	75	75

Table 4-6 Features of the different deep-drawing tests: dimensions of the tools and lubricant

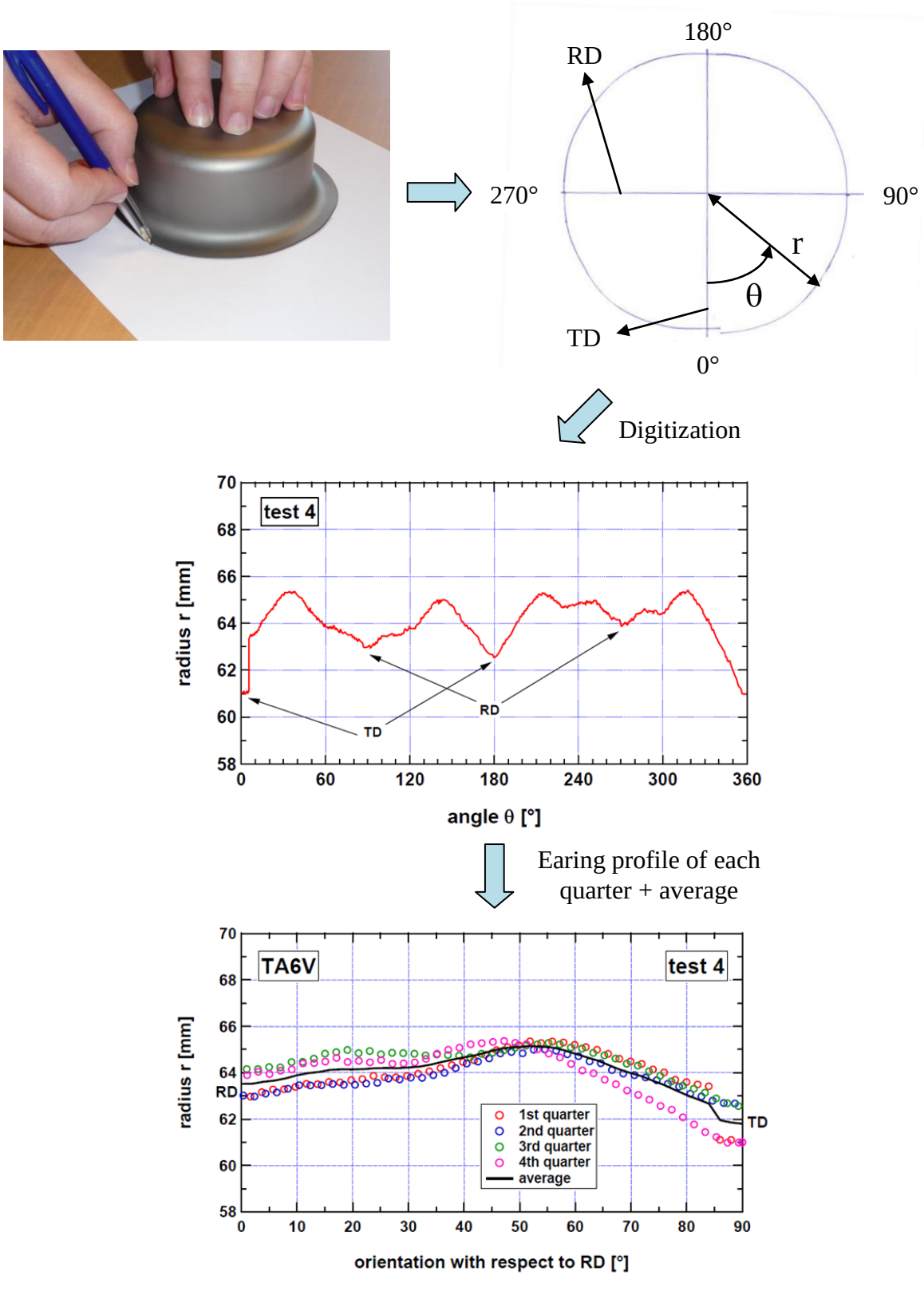

Figure 4-43 Determination of the earing profile (test 4)

Chapter 5 Experimental campaign

In order to understand the mechanical behavior of Ti6Al4V titanium alloy, several studies have been conducted as well in moderate than in high strain rates and temperatures. Here is given a non exhaustive list of these investigations: Lowden and Hutchinson (1975) performed tensile, compression and plane strain compression tests on six batches of material with different textures and observed a large strength differential effect for conditions where the *c*-axis deformation is involved; Follansbee and Gray (1989) carried out compression tests at temperatures between 76 and 495 K, and strain rates between 0.001 and 3000 s^{-1}; Fukuhara and Sanpei (1993) studied the evolution of the elastic moduli (Young modulus, shear modulus, Poisson ratio, …) with the temperature; Medina Perilla and Gil Sevillano (1995) tested the material under different quasi-static stress states (tension, compression, simple shear); Bruno and Dunn (1997) measured the elastic constants for Ti6Al4V by means of neutron diffraction; Lee and Lin (1998b) and Lee and Lin (1998a) studied the effects of the strain rate (500 $s^{-1} \leq \dot{\varepsilon} \leq$ 3000 s^{-1}) and the temperature ($T_{room} \leq T \leq$ 1100 °C) on the plastic deformation behavior; Macdougall and Harding (1999) carried out torsional tests over a wide range of strain rates (between 300 and 1000 s^{-1}) on thin-walled tubular specimens; Majorell *et al.* (2002) investigated the mechanical response under low and moderate strain rates (0.001 – 10 s^{-1}) as well as various temperature conditions (650 – 1340 K); Khan *et al.* (2004) and later Khan *et al.* (2007) studied the quasi-static, dynamic, multiaxial and non-proportional loading responses of Ti6Al4V at different strain rates and temperatures; Peirs (2012) characterized the impact dynamic behavior of the material (strain rates between 100 and 1000 s^{-1}) under tension, shear and torsion; …

In this chapter, a comprehensive experimental investigation of the mechanical response of Ti6Al4V is presented. The studied material is first introduced. Next the anisotropy exhibited by the alloy at room temperature is examined under different quasi-static strain loading conditions and then for different strain rates in tension.

5.1. Description of the material

The Ti6Al4V titanium alloy studied in this work is in 0.6 mm thick sheet form designated as "TIMETAL® 6-4 Titanium Tôle Aéro SQ" and produced by TIMET. The chemical composition is listed in Table 5-1. The sheet was mill annealed one hour at 760°C.

	Ti [%]	Al [%]	V [%]	O [%]	N [ppm]	C[ppm]	H [ppm]	Fe [%]
TOP	Bal.	6.22	3.93	0.19	60	80	100	0.16
BOTTOM	Bal.	6.27	4.00	0.20	60	90	86	0.16

Table 5-1 Chemical composition of the Ti6Al4V alloy investigated (data provided by TIMET)

The microstructure and the initial texture of the as-received material were determined by EBSD and XRD. It is observed that the α-phase and β-phase volume fractions are respectively of ~90% and ~10% (Figure 5-1). The average grain size is of ~7.5 µm for the α-phase (see grain size distribution in Figure 5-2) while it is of ~1 µm for the β-phase. The analysis of the (0002) pole figure shows that the material is initially anisotropic (see Figure 5-3). Indeed, the texture displays two density peaks (between 5 and 6 m.r.d.) at +/- 13° from the plate normal direction (ND) as well as a peak along TD (~3 m.r.d.).

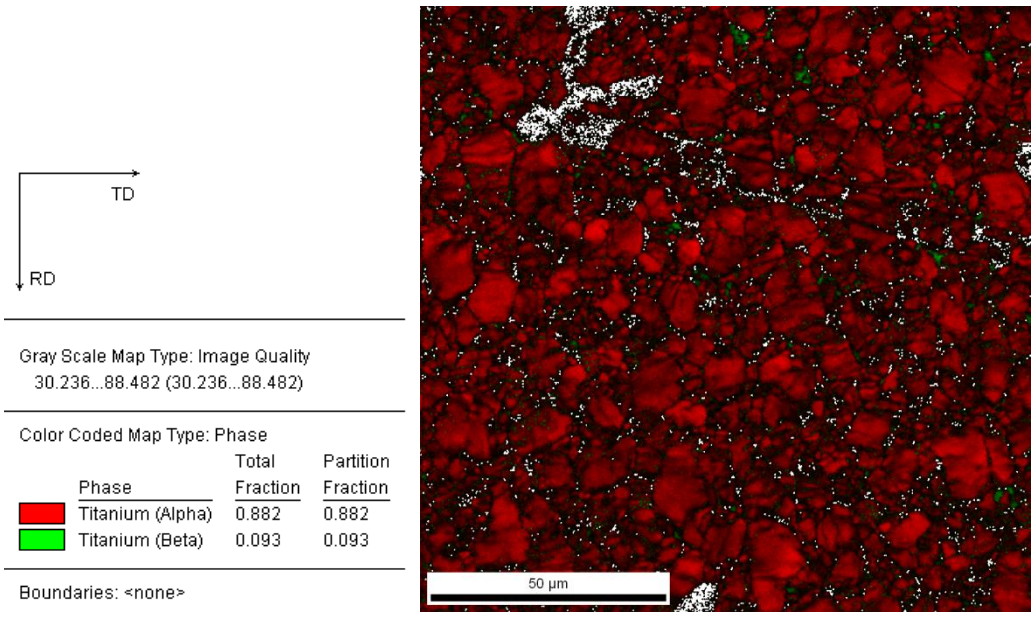

Figure 5-1 Initial microstructure of Ti6Al4V (EBSD scan): the α-grains and β-grains are respectively colored in red and in green

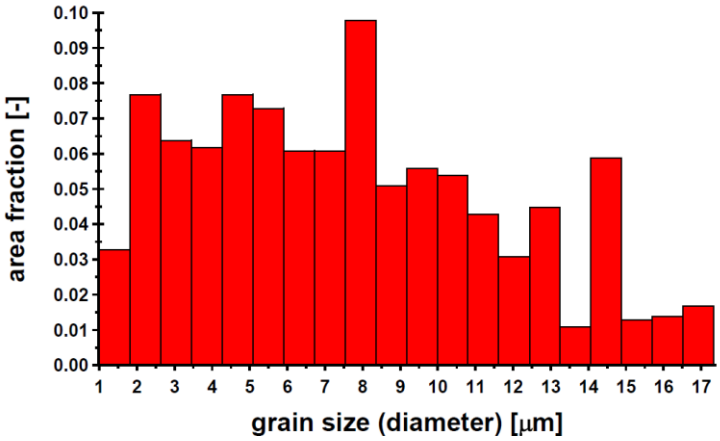

Figure 5-2 Grain size distribution of the α-phase

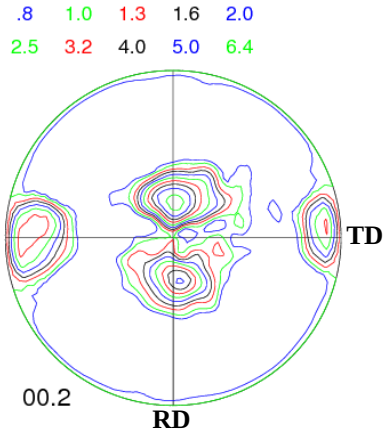

Figure 5-3 Initial texture of Ti6Al4V ((0002) pole figure) measured by XRD; the scale is given in m.r.d.

5.2. Study of the anisotropy

5.2.1. Anisotropy in tension

Figure 5-4 shows the axial force – longitudinal displacement curves obtained in uniaxial tension for eleven loading directions with respect to RD, *i.e.* from 0° to 90° by steps of 10° and 45°. The force is measured by the load cell while the displacement is given by the mechanical extensometer. It can already be noticed that the material displays an anisotropic behavior.

It has to be noted the small oscillations which are due to the regulation parameter adjustment. In order to maintain a constant strain rate, the machine crosshead undergoes a series of accelerations and decelerations, causing fluctuations which may be significant when choosing a wrong set of regulation parameters. Table 5-2 lists the values used to inhibit as much as possible the amplitude of these oscillations.

Elongation control	0.005
Force control	0.2
Position control	0
Deceleration	10

Table 5-2 Regulation parameters used in tensile tests

Each curve plotted in Figure 5-4 corresponds to an average of the four tests performed for each loading direction. An example showing the experimental and average curves for the 30°-loading direction is given in Figure 5-5. The standard deviation is also computed in order to assess the experimental errors (Figure 5-6).

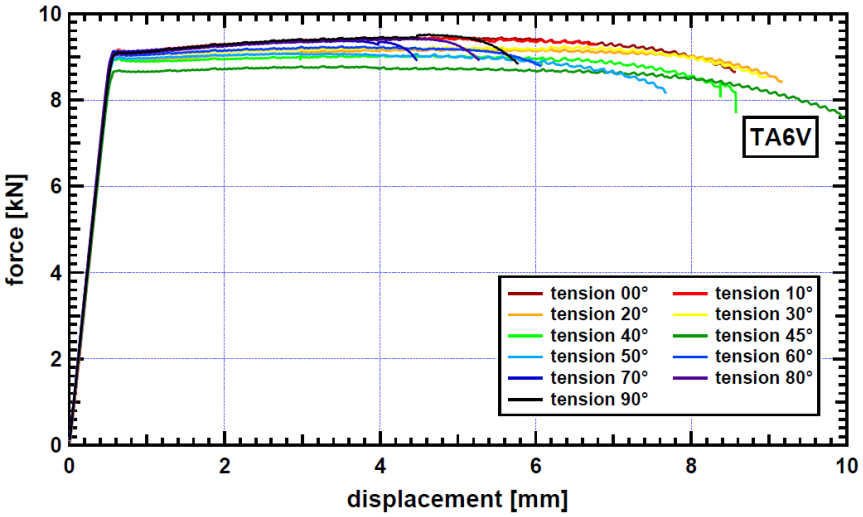

Figure 5-4 Force-displacement curves in uniaxial tension along eleven loading directions in the plane of the sheet

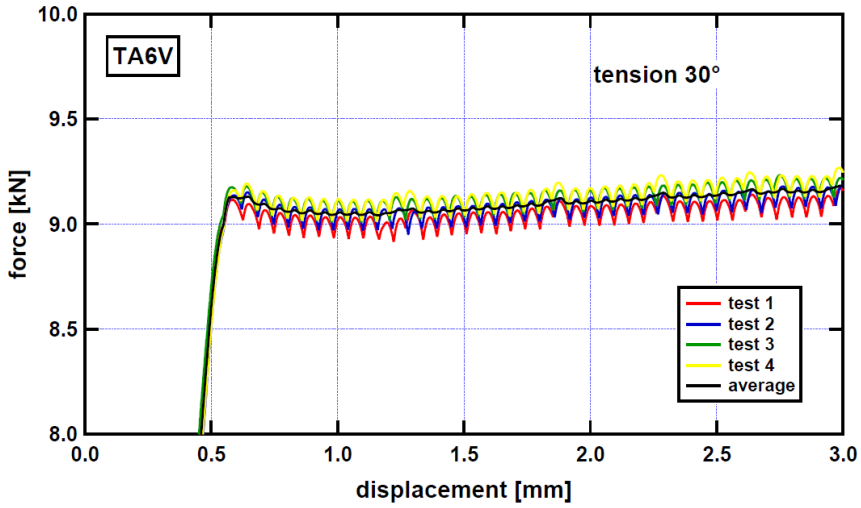

Figure 5-5 Experimental and average force-displacement curves in tension along the 30°-direction

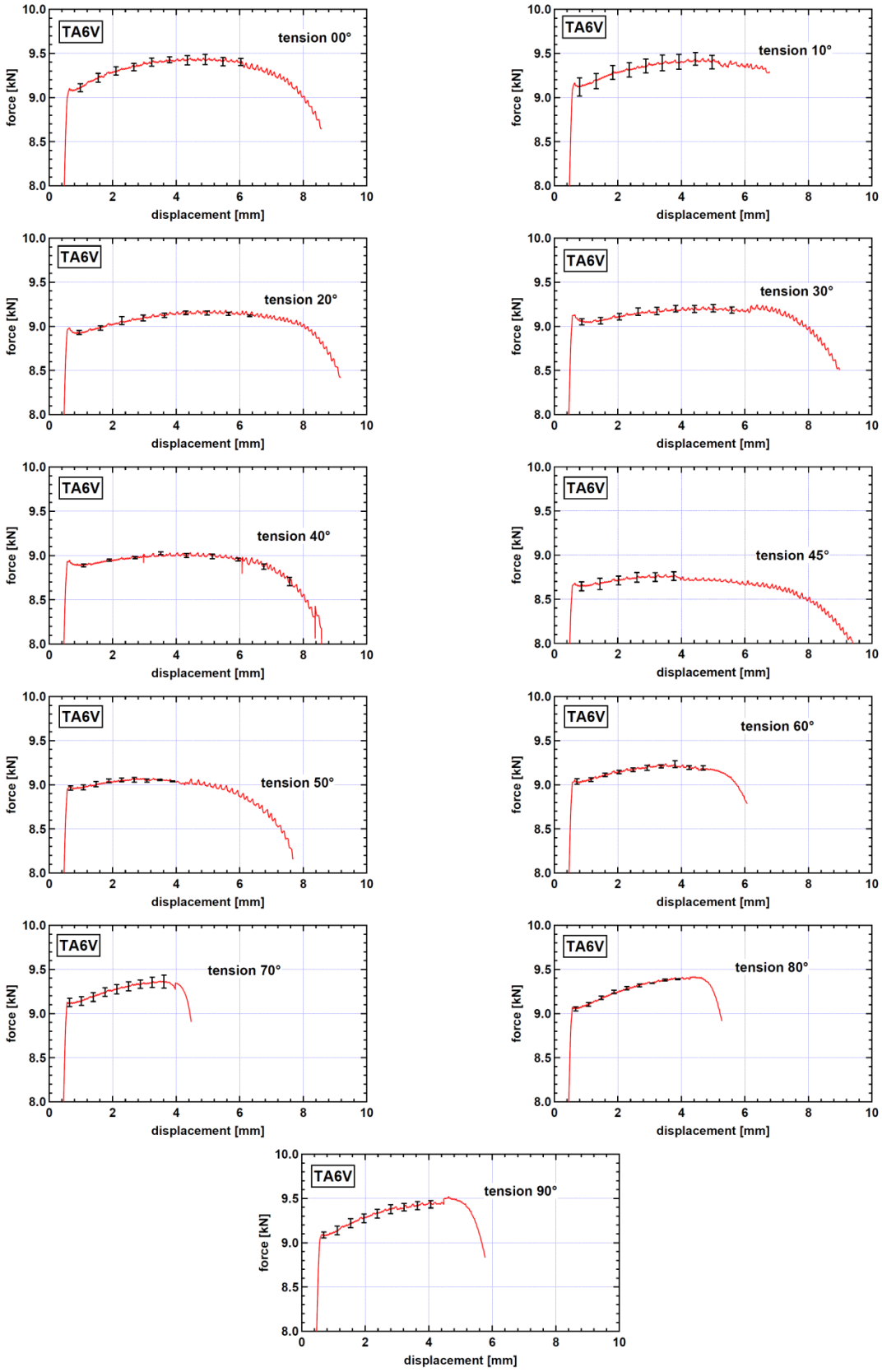

Figure 5-6 Average force-displacement curves with error bars for each loading direction

Based on the measured force and displacement, the true stress and the logarithmic strain are determined by using Eq. (4.15) and (4.6) respectively. The average stress-strain curves for each loading direction are depicted in Figure 5-7. The same experimental results with error bars are given in Figure 5-9. The stress-strain curves exhibit the standard concave-down appearance (*i.e.* steadily decreasing hardening rate). In all tests, shear type fracture is observed (see Figure 5-8).

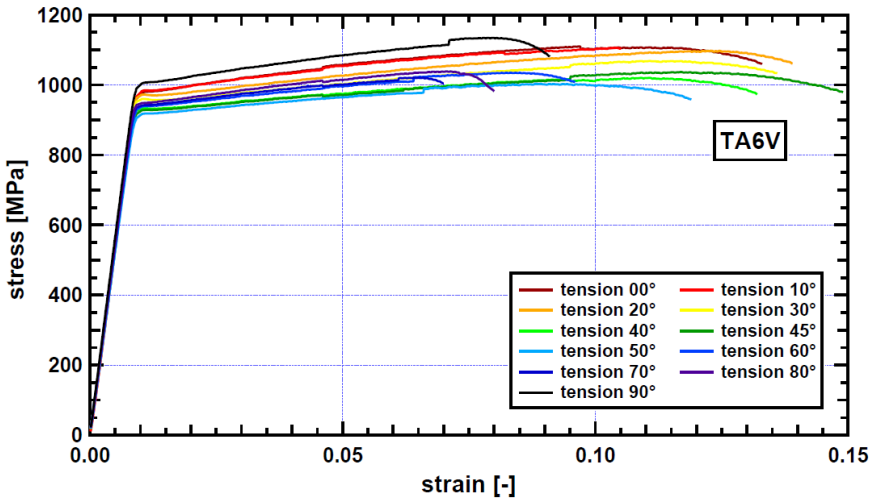

Figure 5-7 Stress-strain curves in uniaxial tension along eleven loading directions

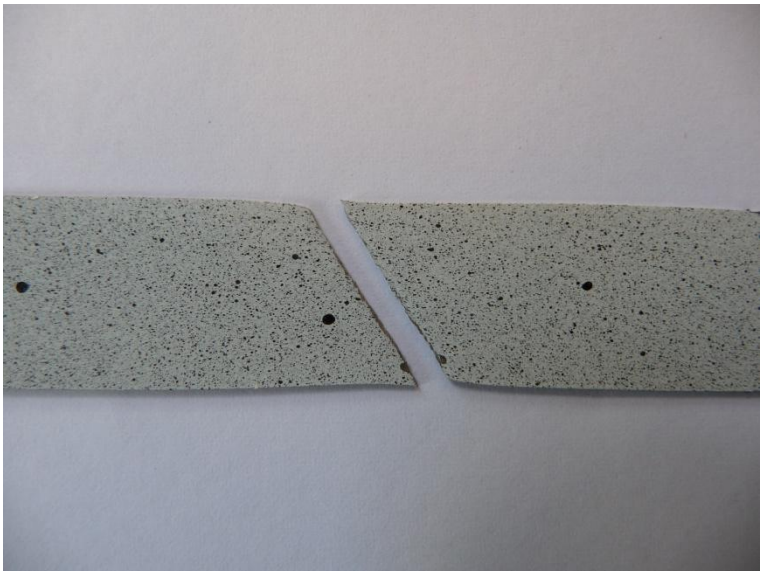

Figure 5-8 Fracture of a tensile specimen

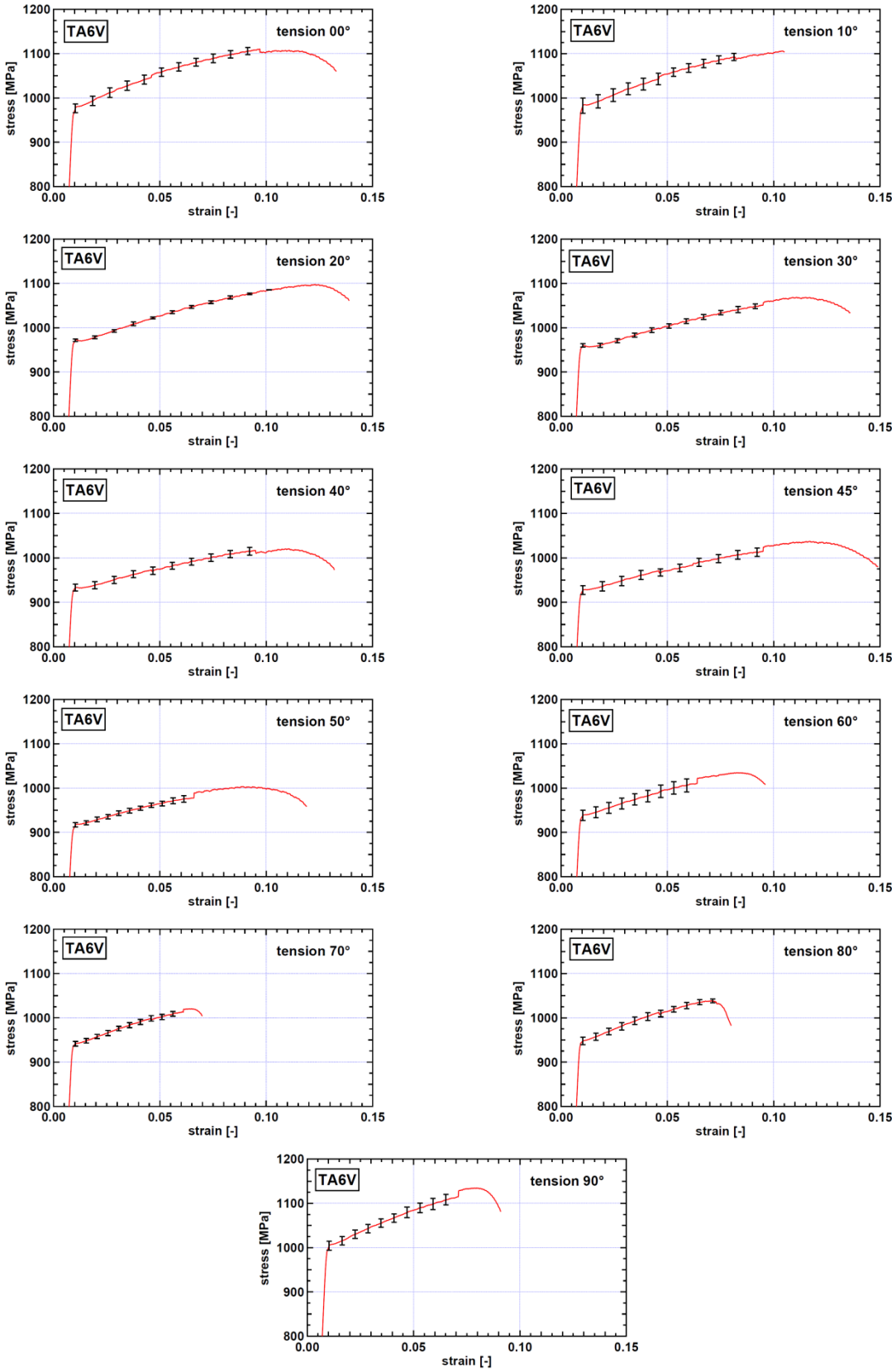

Figure 5-9 Average stress-strain curves with error bars for each loading direction

Elastic anisotropy

Young modulus is determined by linear regression on the elastic part of each tensile stress-strain curve. Figure 5-10 shows the average values as well as the standard deviations computed for each loading direction. It can be noticed a low anisotropy, the largest and smallest moduli (respectively 113 GPa and 105 GPa) being observed in the transverse direction and the 50°-direction. Nevertheless, it will be assumed in this study that the material is isotropic elastic with a Young modulus $\bar{E}$ given by the average over all the tested directions, *i.e.*:

$$\bar{E} = \frac{E_0 + 2E_{10} + 2E_{20} + 2E_{30} + 2E_{40} + 2E_{45} + 2E_{50} + 2E_{60} + 2E_{70} + 2E_{80} + E_{90}}{20} \tag{5.1}$$

which leads to $\bar{E} = 109$ GPa.

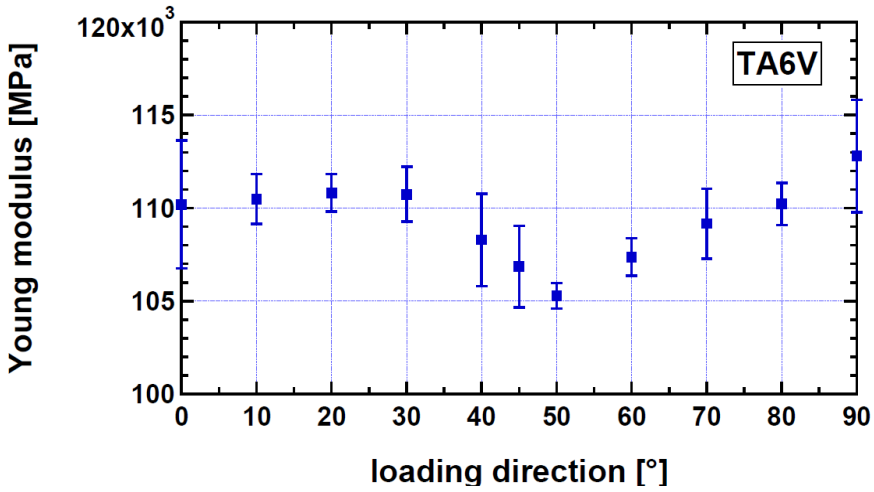

Figure 5-10 Young modulus as a function of the specimen orientation: the bold symbols are the average values while the bars represent the standard deviation

Plastic anisotropy

The observation of the tensile stress – strain curves shows the plastic anisotropy displayed by Ti6Al4V. In order to characterize this anisotropy, the uniaxial tensile yield stress σ_α^T in each direction α with respect to RD is assessed. The rolling direction yield stress is defined by the offset method (see Figure 5-11). The choice of the offset is fixed to a plastic strain value ε_0^p, usually 0.2%, corresponding to a plastic work W_0^p given by:

$$W_0^p = \int_0^{\varepsilon_0^p} \sigma_{ij} d\varepsilon_{ij}^p = \int_0^{\varepsilon_0^p} \sigma \, d\varepsilon^p \tag{5.2}$$

where σ and ε^p are the axial stress and plastic strain, respectively.

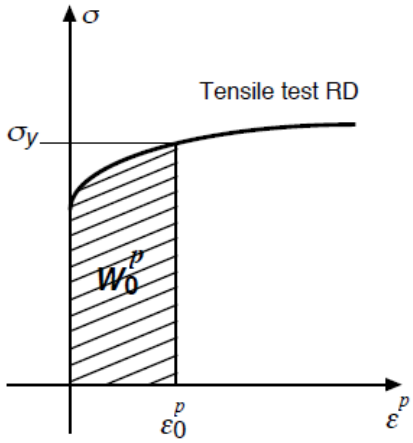

Figure 5-11 Determination of the tensile yield stress along RD ($\sigma_y = \sigma_0^T$) by the offset method (Florès (2005))

For the other orientations, the work-equivalence principle (Hill (1987)) is used to determine the yield stress (see Appendix D). It has to be noted that this technique will next be applied to define the initial yield limit for other stress states (see Figure 5-12).

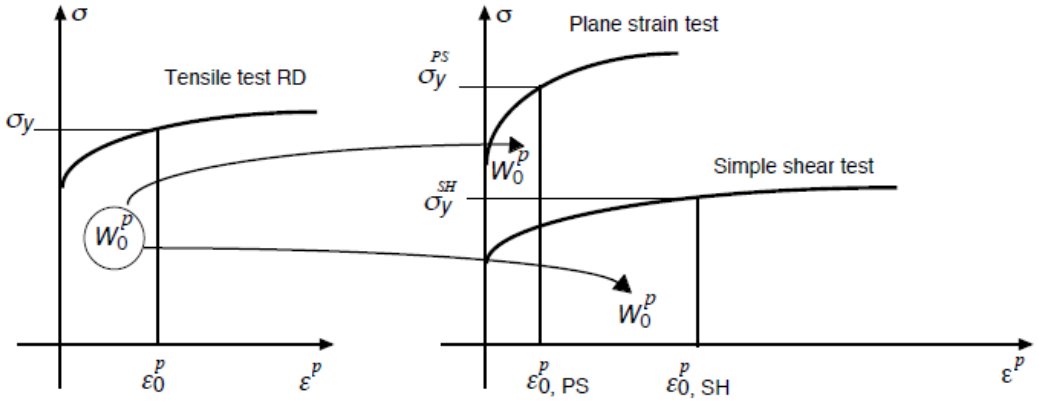

Figure 5-12 Determination of the yield stress for different stress states using the work-equivalence principle (Florès (2005))

The material anisotropy can also be characterized by the *r*-ratios. The average axial and transversal plastic strains along the gage length are determined by using the data provided by Aramis®. In all the tests, it is observed that the evolution of the plastic strains with time is almost linear as long as necking does not occur (see example on Figure 5-13). The *r*-ratio can thereby be considered as being constant. For each test, the following procedure is performed:

- a trend line is fitted on the linear part of each plastic strain-time curve;
- the axial and transversal plastic strain rates are given by the slope of the trend lines;
- the *r*-ratio is computed by using Eq. (4.16).

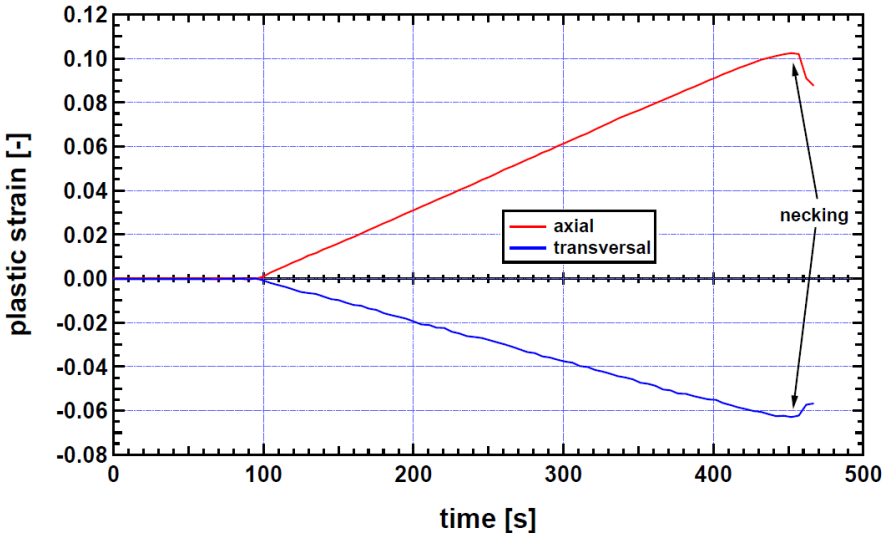

Figure 5-13 Evolution of the axial and transversal plastic strains with time (test along 20°-direction)

Figure 5-14 and Figure 5-15 respectively show the anisotropy of the tensile yield stresses and *r*-ratios as a function of the loading direction. It can be noticed that the in-plane anisotropy in initial yield stresses is moderate. An anisotropy ratio for the tensile yield stresses defined by the ratio of the yield stress in the transverse direction (the largest one measured) to that in the 50°-direction (the smallest one measured) is 1.094. However, the anisotropy in *r*-values is very strong, the *r*-ratio in the 60°-direction (the largest one) being more than double the *r*-ratio in the 10°-direction (the lowest one).

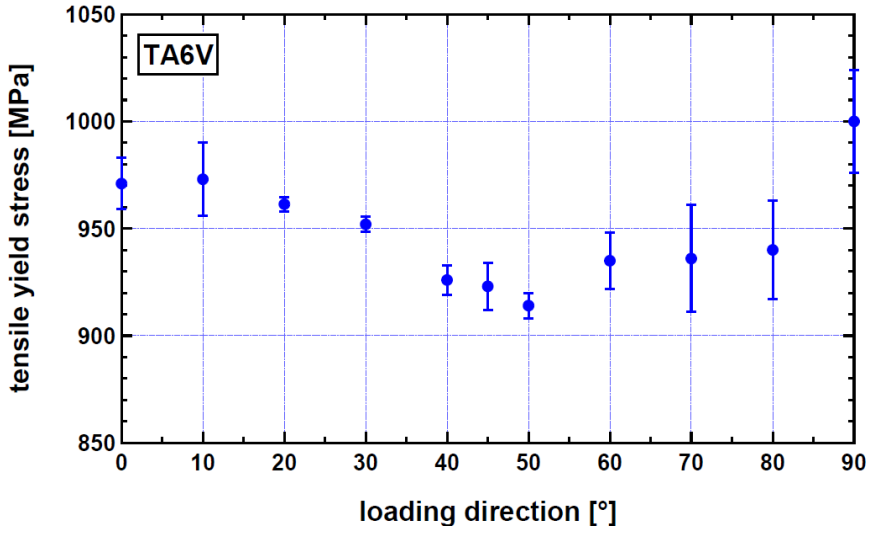

Figure 5-14 Anisotropy in tensile yield stresses: the bold symbols are the average values while the bars represent the standard deviation

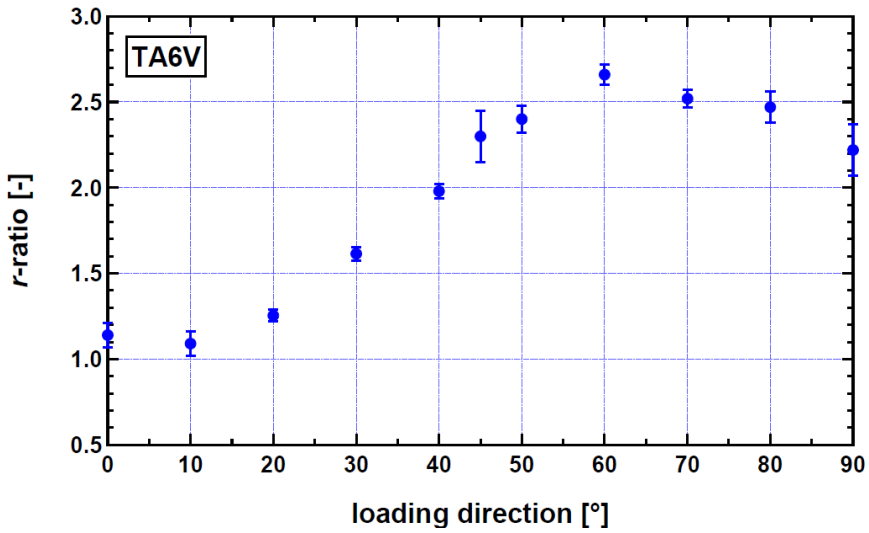

Figure 5-15 Anisotropy in r-ratios: the bold symbols are the average values while the bars represent the standard deviation

The results of Figure 5-15 are compared with the data from Fundenberger *et al.* (1997) and Medina Perilla and Gil Sevillano (1995) on Ti6Al4V, see Figure 5-16. The *r*-values determined in this work are higher than those of both studies, likely due to a different thermomechanical treatment in the production of the sheets. However, it has to be noted a very similar trend between the three sets of data.

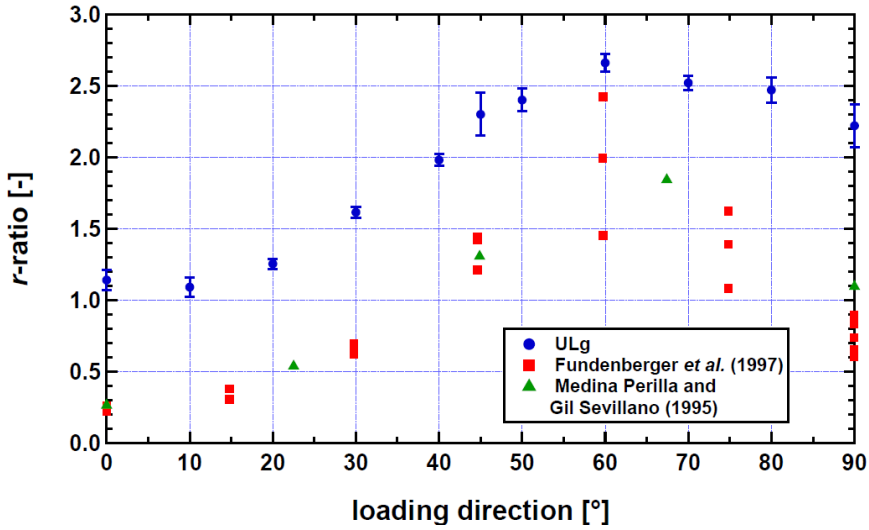

Figure 5-16 Comparison of the measured r-ratios with the data from Fundenberger et al. (1997) and Medina Perilla and Gil Sevillano (1995)

From Figure 5-7, it can be observed that the hardening rate $\Theta = \partial\sigma/\partial\varepsilon$ is different from one loading direction to another. However the oscillations exhibited in the stress-strain curves make its computation rather difficult. Although different smoothing techniques were used with the software IGOR Pro, it was not possible to determine with sufficient accuracy the

evolution of Θ during the deformation and then the different hardening stages. Nevertheless, in order to assess the influence of the loading direction on the hardening rate, a simple procedure was performed and consisted in fitting a trend line on each stress-strain curve in a delimited strain range, namely between 1% and 6% in the present case (see Figure 5-17). The average hardening rate $\bar{\Theta}$ is then provided by the slope of the line. The results (see Figure 5-18) show that, when uniaxial tension is applied, $\bar{\Theta}$ is maximal along RD and TD while it is minimal along the 45°-direction, pointing out again the anisotropic behavior of Ti6Al4V.

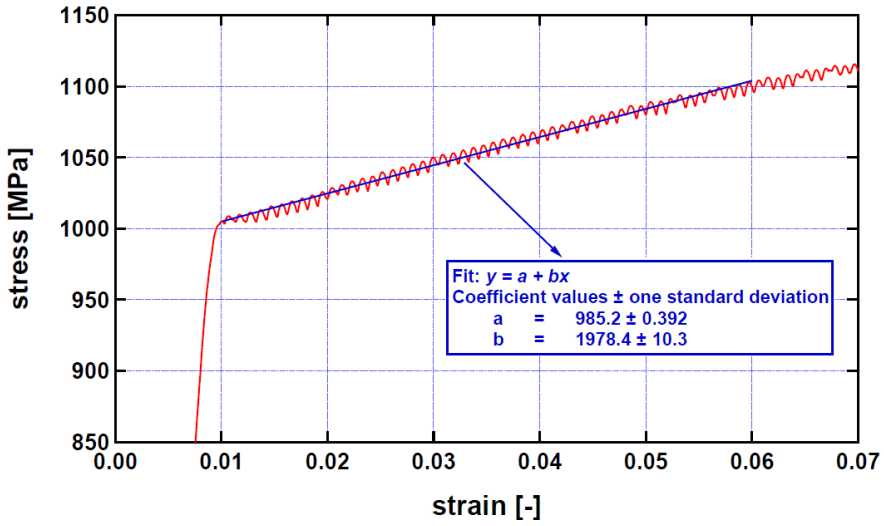

Figure 5-17 Example of linear fitting on a stress-strain curve in the strain range between 1% and 6% (test along TD)

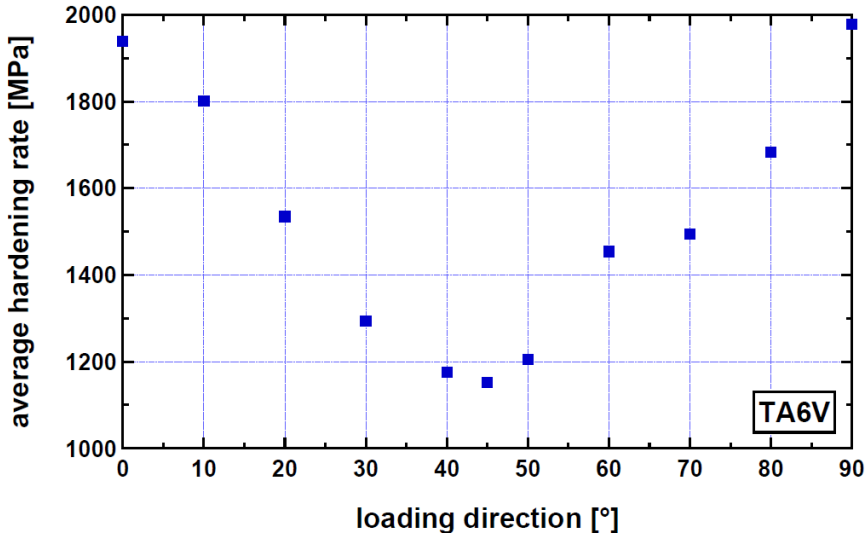

Figure 5-18 Influence of the loading direction on the hardening rate when Ti6Al4V is subjected to uniaxial tension

5.2.2. Anisotropy in compression

The average experimental curves in compression obtained by TUAT along RD, 45°-direction and TD are shown in Figure 5-19 and Figure 5-20 while the yield stresses in each direction, determined by the work-equivalence principle, are given in Figure 5-21 (a). As previously, the average hardening rate was also computed by fitting a straight line on each experimental curve in the strain range from 1% to 6% for tensile tests and from 1% to 9% for compression tests. The results are given in Figure 5-21 (b). Regardless of the loading orientation, the material is strongest in TD (see Figure 5-19), the material anisotropy in tension being more pronounced than in compression. Comparison between the tensile and compressive responses along each of these loading directions show that the material displays tension-compression asymmetry in yielding and hardening (Figure 5-20 and Figure 5-21).

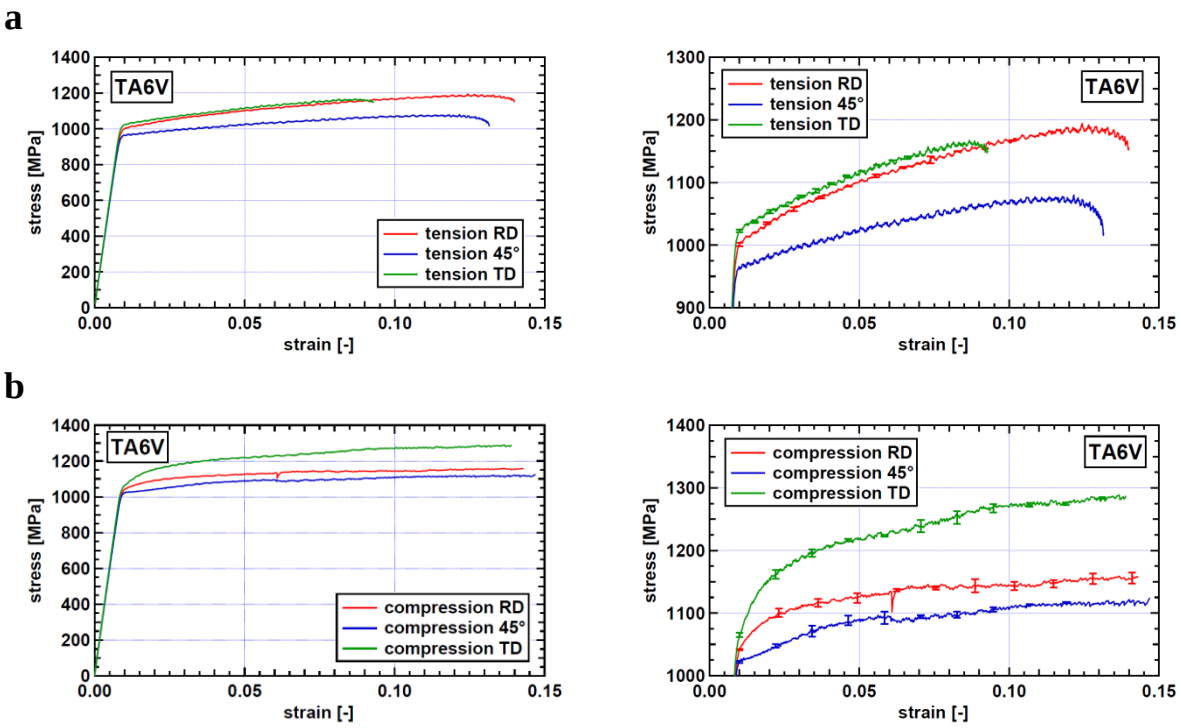

Figure 5-19 Uniaxial test results (left panel: average curves; right panel: average curves with error bars) in three in-plane orientations showing the material's anisotropy in (a) tension and (b) compression, respectively (tests performed at TUAT)

a

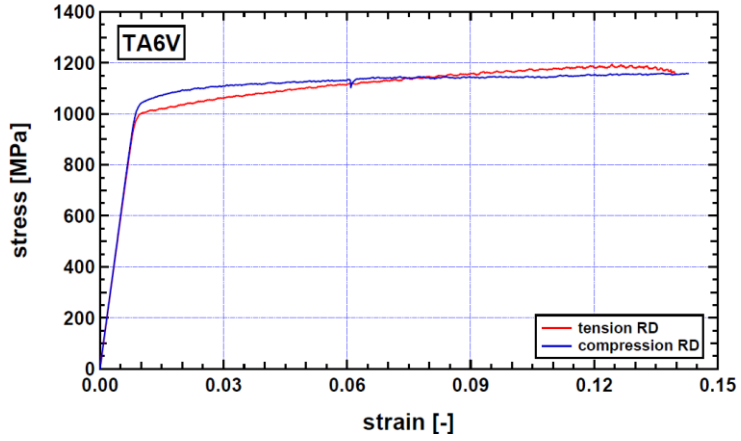

b

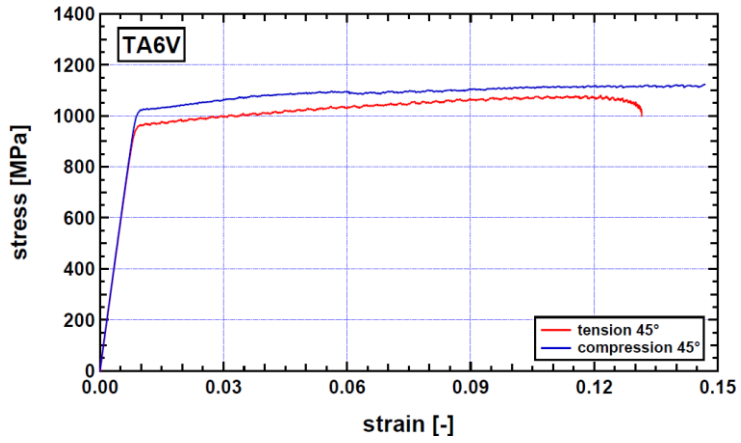

c

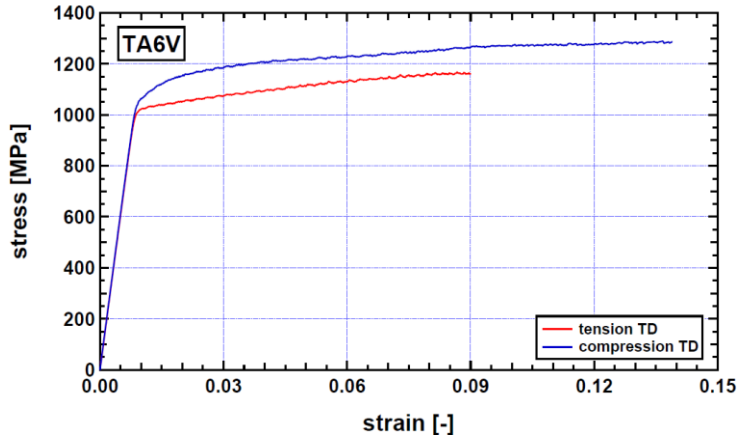

Figure 5-20 Comparison between the tension and compression response in (a) RD, (b) 45°-direction, (c) TD, respectively

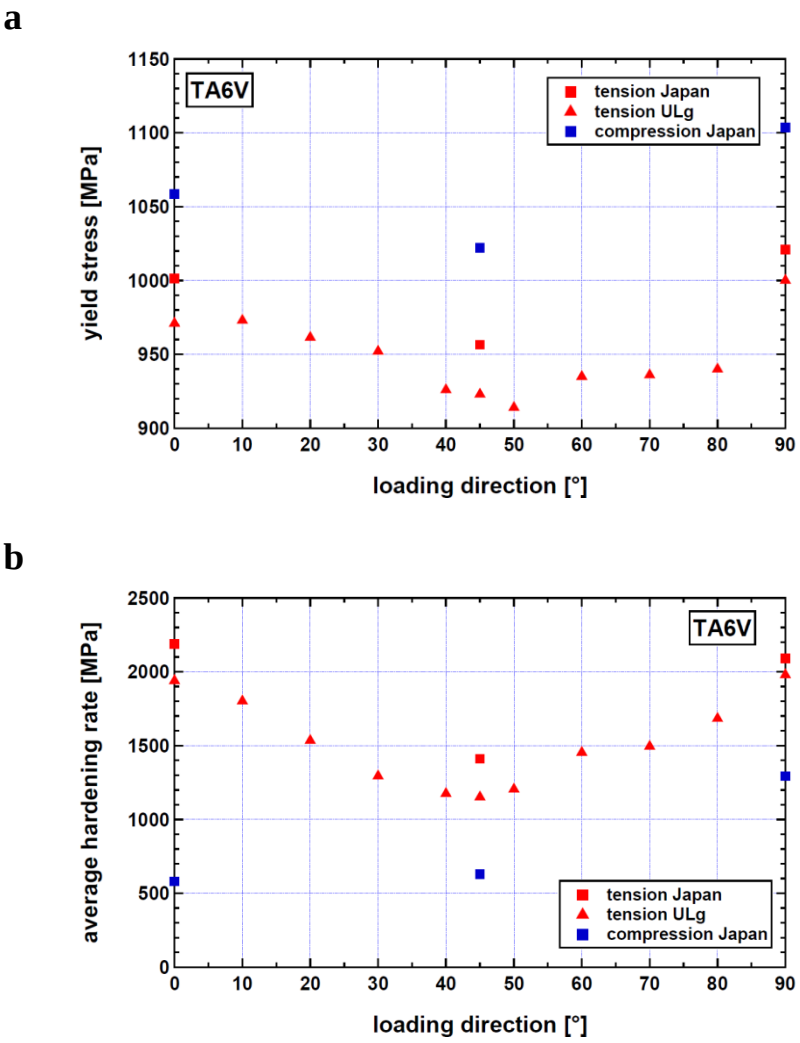

Figure 5-21 Anisotropy in (a) yield stresses and (b) hardening rates in tension and compression for Ti6Al4V based on the tests conducted at TUAT and ULg

Comparison of the results in tension from ULg and TUAT

By comparing the tensile yield stresses based on the tests conducted at TUAT with those measured at ULg (see Figure 5-21), it can be noticed that the values are different. Nevertheless if the yield stresses are normalized as follows:

$$s_\alpha^T = \frac{\sigma_\alpha^T}{\sigma_0^T} \tag{5.3}$$

where σ_α^T and σ_0^T represent respectively the tensile yield stress in the α-direction and RD, the results (see Figure 5-22 (a)) show a good agreement between the measurements of both laboratories. In the same way, the average hardening rates are compared in Figure 5-22 (b), showing a similar trend.

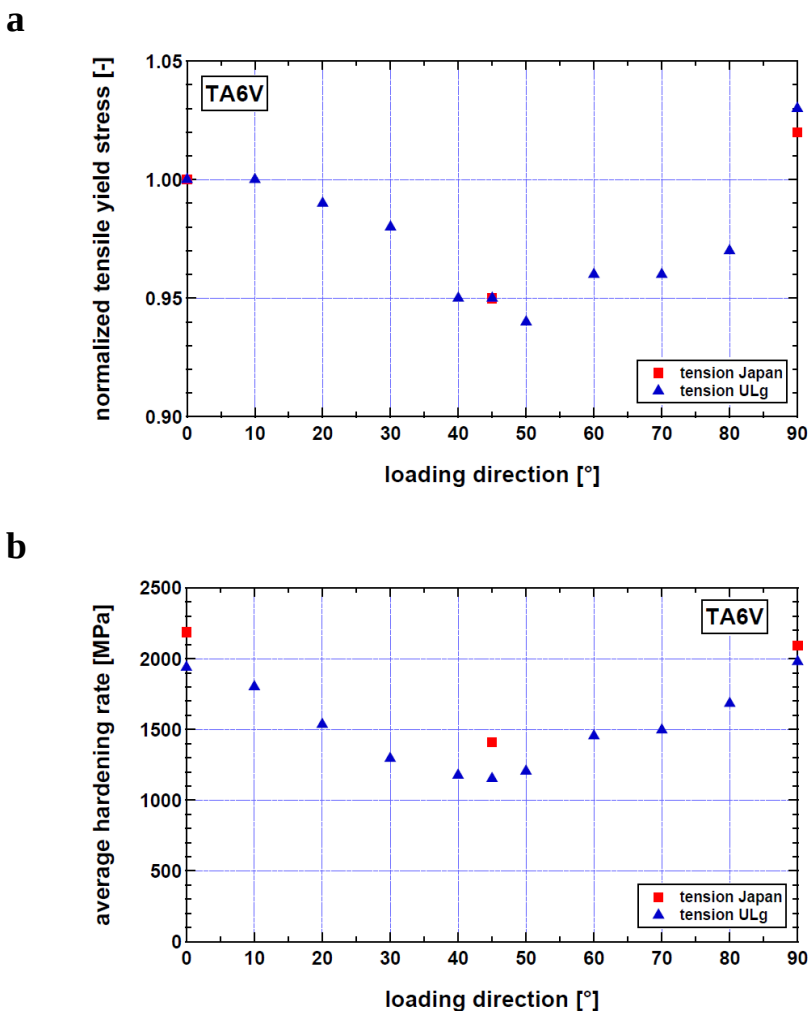

Figure 5-22 Comparison of (a) the tensile yield stresses and (b) the average hardening rates based on the tests carried out at ULg (blue symbols) and TUAT (red symbols)

The discrepancy between tensile test results obtained at ULg and TUAT could be attributed to the strain rate sensitivity of the material, since the strain rate cannot be maintained constant with the experimental device used at TUAT. Nevertheless it will be shown in Section 5.3 that the effect of the strain rate in the range 10^{-4} – 10^{-3} s^{-1} is not significant. Other reasons could be related to ageing of the alloy, to the difference in experimental setup and specimen geometry, or to the position of the samples with respect to the width direction of the sheet.

5.2.3. Anisotropy in plane strain

The resulting stress-strain curves in plane strain along RD, 45° and TD are shown in Figure 5-23. The axial stress σ_{11} and the axial strain ε_{11} were determined using the methodology described in Section 4.2.3.1. It can be observed that the material exhibits moderate anisotropy in plane strain, the strongest behavior being in TD.

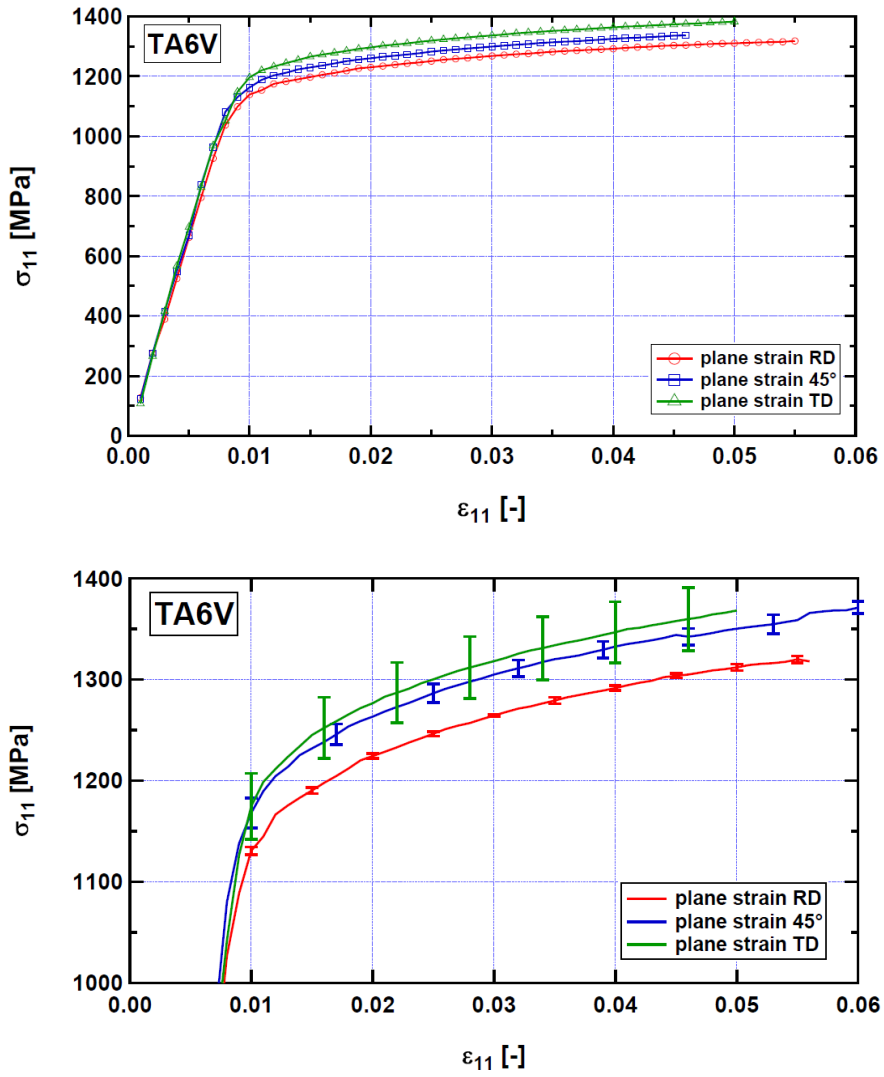

***Figure 5-23 Plane strain test results (Upper panel: average curves; lower panel: zoom and average curves with error bars) in three in-plane directions (RD, 45°, TD) determined using Equation* (4.39) *and* $\alpha = 1.0154$**

5.2.4. Anisotropy in simple shear

Figure 5-24 compares the stress-strain curves in simple shear along RD, 45° and TD. The stress component τ, denoted "shear stress", was computed using Equation (4.48) while γ, denoted "shear strain" was determined by Equation (4.41). It can be observed that the mechanical behavior is identical in RD and TD, while the flow stress is higher in the 45°-direction. Nevertheless the material displays a moderate anisotropy in yielding while the hardening behavior is almost the same in each loading orientation.

It has to be noted that no discrepancy has been observed in the material response depending on whether the simple shear tests in 45° with respect to RD are performed in the forward direction or the backward direction.

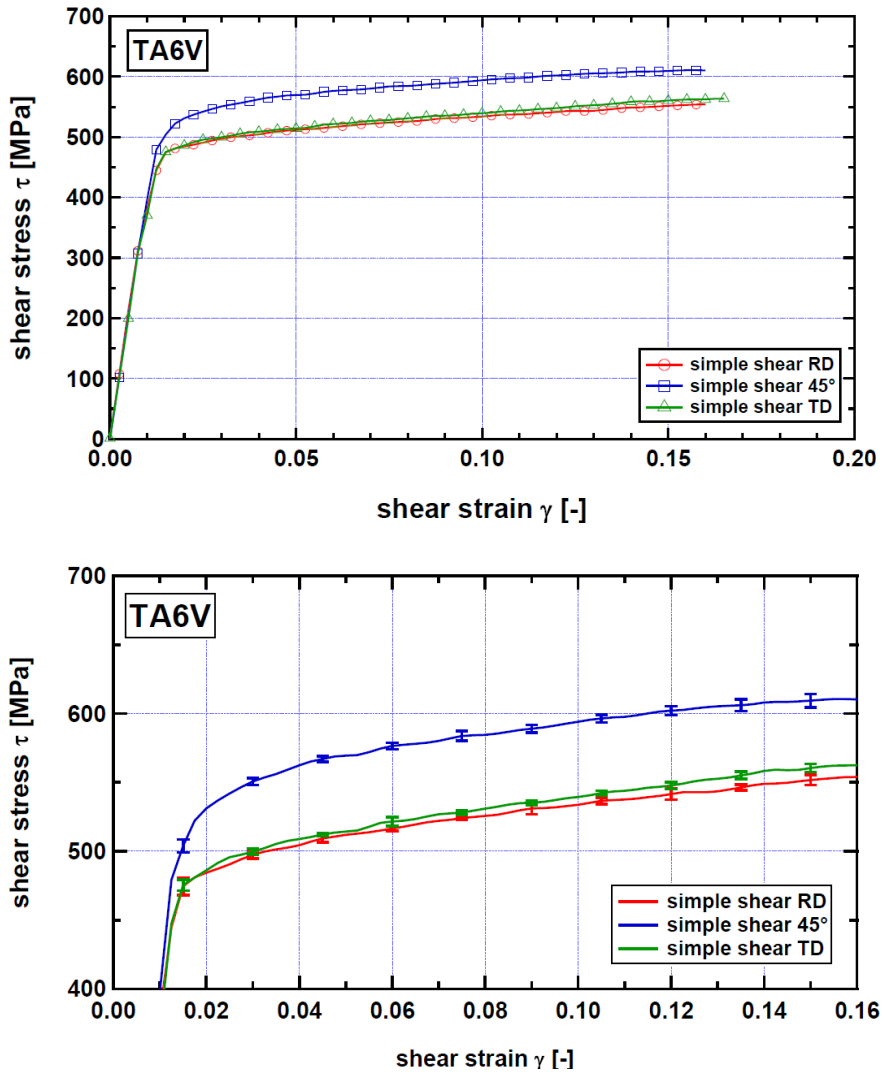

Figure 5-24 Simple shear test results in three in-plane directions (RD, 45°, TD)

Bauschinger tests in RD with 10% pre-strain were also carried out in order to study the effect of a strain path change on the mechanical behavior. The average stress-strain curve is given in Figure 5-25.

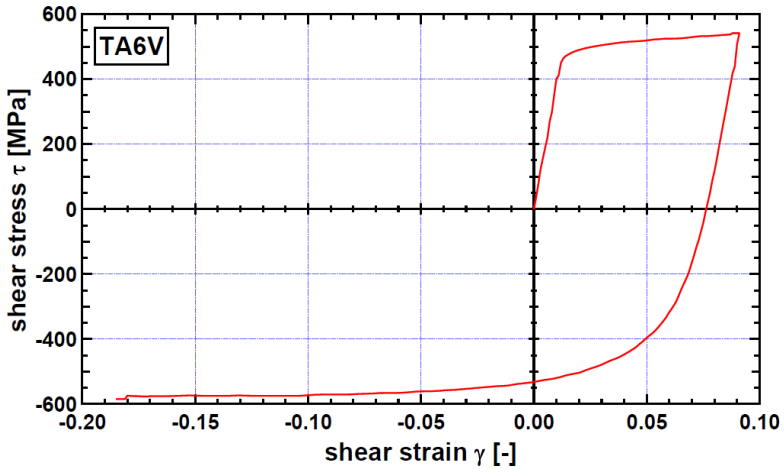

Figure 5-25 Bauschinger simple shear test result in RD with 10% pre-strain

In order to compare the material response with the one observed in monotonic shear, the experimental curve is plotted using the absolute value of the shear stress and the accumulated shear strain in Figure 5-26. It can immediately be noticed a significant Bauschinger effect, *i.e.* a decrease of the flow stress upon strain reversal.

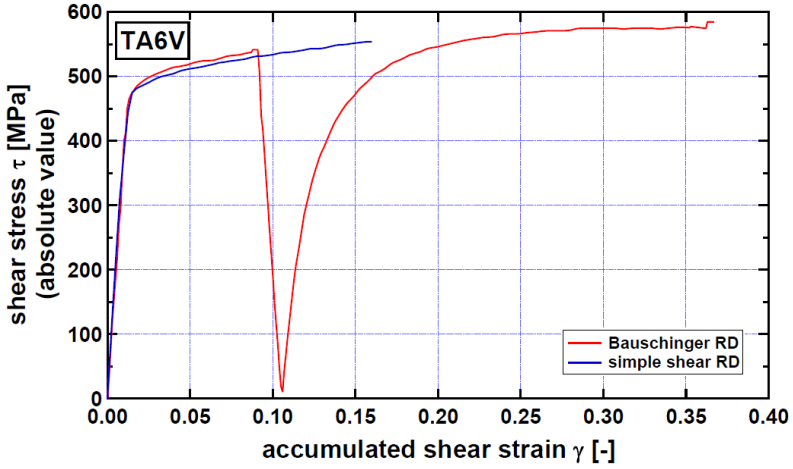

Figure 5-26 Comparison between simple shear and Bauschinger test results in RD

5.2.5. Observations about the yield locus and the hardening

Figure 5-27 compares in the biaxial plane ($\sigma_{12}=0$) the theoretical yield locus according to Von Mises criterion (Equation (3.6)) with the experimental data obtained for the monotonic tests (tension, compression, plane strain and simple shear) and determined at four levels of plastic work per unit of volume using the work-equivalence principle (see Figure 5-12). It has to be noted that the data are normalized, *i.e.* for a same level of plastic work, each value is divided by the corresponding stress in tension along RD. Two remarks must be reported concerning the data in plane strain and simple shear:

- The plane strain tests only allow the experimental determination of the stress component along the loading direction. For the first level of plastic work corresponding to the initial yield locus, the second component can approximately be determined using Hooke's law. Denoting by σ_{11} and σ_{22} the stress components along the loading and transverse directions respectively, and assuming that the elasticity of the material is isotropic, it can be determined that:

$$\sigma_{22}=\nu\sigma_{11} \tag{5.4}$$

  where ν is the Poisson ratio. For the higher levels of plastic work, only a straight line to which the yield locus must be tangent can be plotted to represent the plane strain state.

- In simple shear, the determination of the complete stress state is not possible. Indeed, as in the case of the plane strain tests, one stress component cannot be identified. Nevertheless, at the onset of plasticity, it can be assumed that the stress state is close to

pure shear. For this reason, only the shear data in the initial yield locus are shown in Figure 5-27.

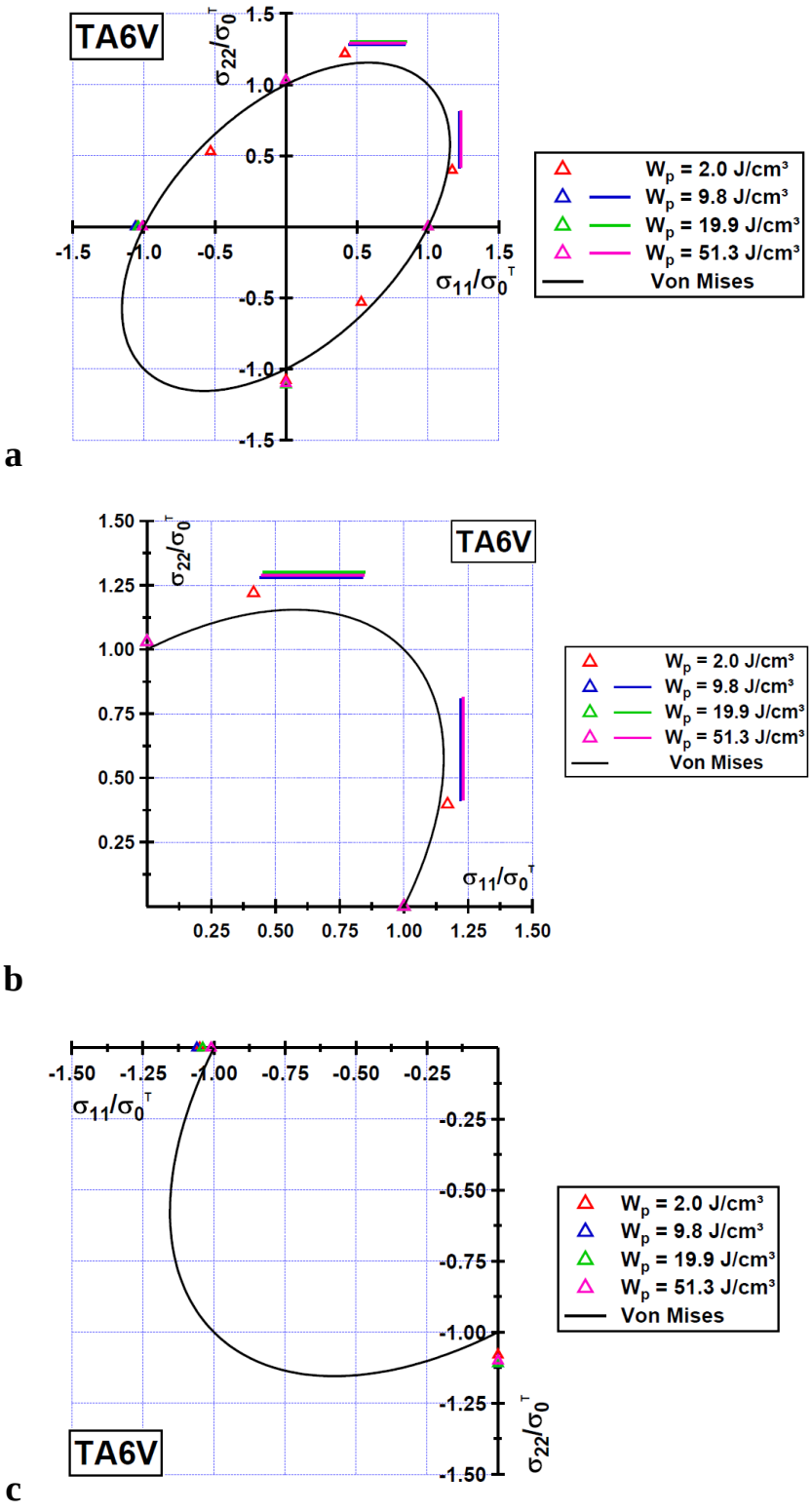

Figure 5-27 Comparison of the yield locus according to isotropic Von Mises criterion with the experimental data at different levels of plastic work per unit of volume: (a) biaxial plane, (b) first quadrant, (c) third quadrant

The comparison of the experimental results with the theoretical yield locus according to Von Mises criterion reveals the degree of anisotropy displayed by Ti6Al4V titanium alloy. Hereafter Figure 5-28, Figure 5-29 and Figure 5-30 show the distribution of the stress ratios $\sigma_\theta^T/\sigma_0^T$ and $\sigma_\theta^C/\sigma_0^T$ (where the subscript θ denotes the loading direction while the superscripts T and C identify the data in tension and in compression respectively) at different levels of plastic work. These levels correspond to the following plastic strains when tension is applied to the material along RD: 0.2% for the first level (onset of plasticity), 1% for the second level, 2% for the third level and 5% for the last one. The results show that the hardening behavior is not isotropic since it depends on the loading direction, which means that the shape of the yield locus evolves with the plastic deformation.

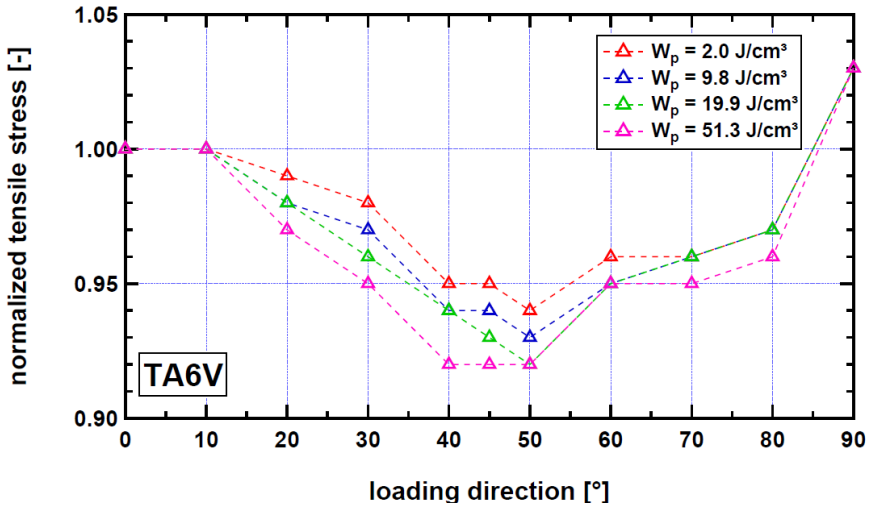

Figure 5-28 Evolution of the stress ratio distribution in tension with respect to the plastic work

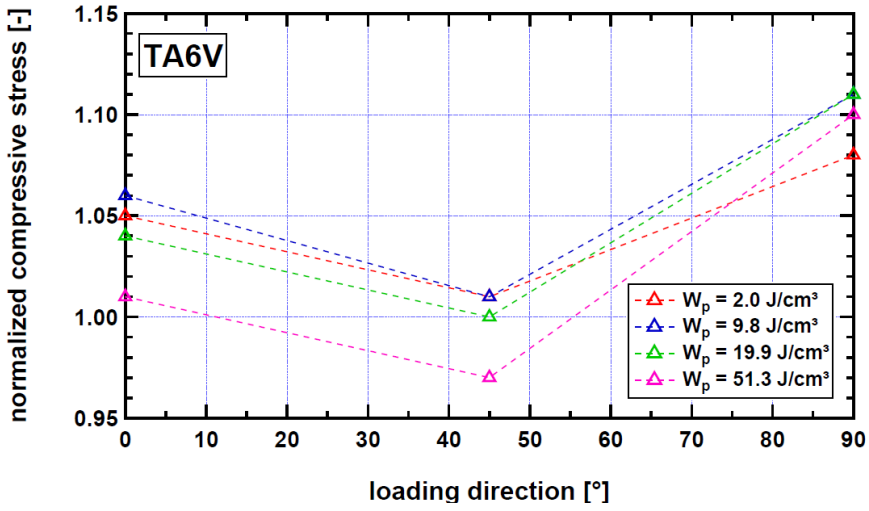

Figure 5-29 Evolution of the stress ratio distribution in compression with respect to the plastic work

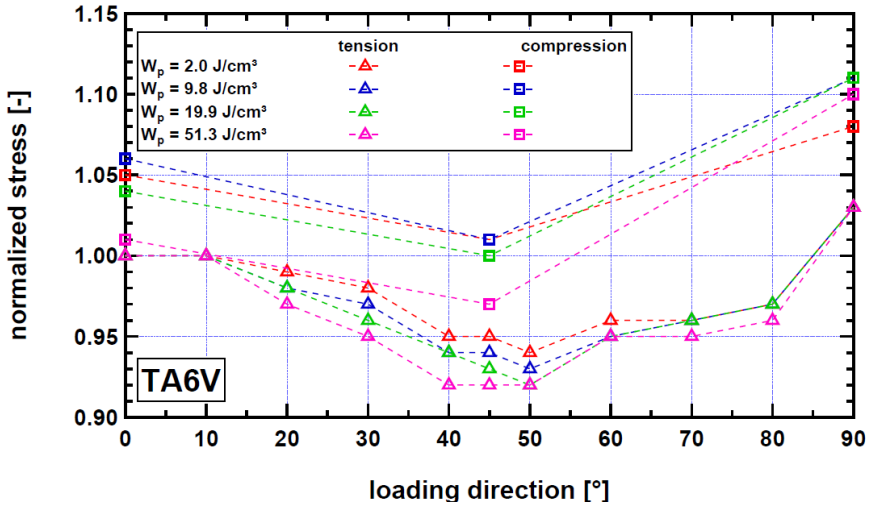

Figure 5-30 Comparison of the results in tension and compression given in Figure 5-28 and Figure 5-29

5.2.6. Results from layer compression tests

Evolution of the middle cross-section geometry

In order to compute the axial stress occuring in a layer compression test, it is required to determine the actual area of the middle cross-section during the deformation of the specimen. As explained in Section 4.2.3.2, with the help of DIC, it is possible to track the position of any point on the painted lateral surface. Thus the middle cross-section can be located and its shape can be determined at any stage of the deformation (see Figure 5-31). A subroutine developed by Halir and Flusser (1998) is then used to fit the experimental cross-section by an ellipse, enabling to assess its area. Nevertheless, it has to be noted that the measures are affected by some errors, as it can be observed in Figure 5-32 in which the area determined by DIC is compared with the initial and final actual area measured before and after each experiment with the help of a micrometer. A Matlab subroutine developed by V. Tuninetti (Tuninetti *et al.* (2011)) was used to correct the data provided by DIC (see for instance the results for the test 7 shown in Figure 5-32). This correction is performed as follows. If i ($i = 0 \ldots N$) denotes the stage of the deformation and if a_i^{DIC} and a_i^{ac} represent the length of the semi-major axis determined by DIC and its actual length respectively, the error Δa_i is defined by:

$$\Delta a_i = a_i^{\mathrm{DIC}} - a_i^{\mathrm{ac}} \tag{5.5}$$

However, only the errors before and after loading are known, *i.e.* Δa_0 and Δa_N. If the error is assumed to linearly evolve with the average axial strain ε, it can be written:

$$\Delta a_i = \Delta a_0 + \frac{\Delta a_N - \Delta a_0}{\varepsilon_N - \varepsilon_0}\left(\varepsilon_i - \varepsilon_0\right) \tag{5.6}$$

and so the "correct" length a_i^{corr} can be assessed:

$$a_i^{\mathrm{corr}} = a_i^{\mathrm{DIC}} - \Delta a_i \tag{5.7}$$

The same procedure is applied for the semi-minor axis and the "corrected" area A_i^{corr} is given by:

$$A_i^{corr} = \pi a_i^{corr} b_i^{corr} \tag{5.8}$$

where b denotes the semi-minor axis of the ellipse.

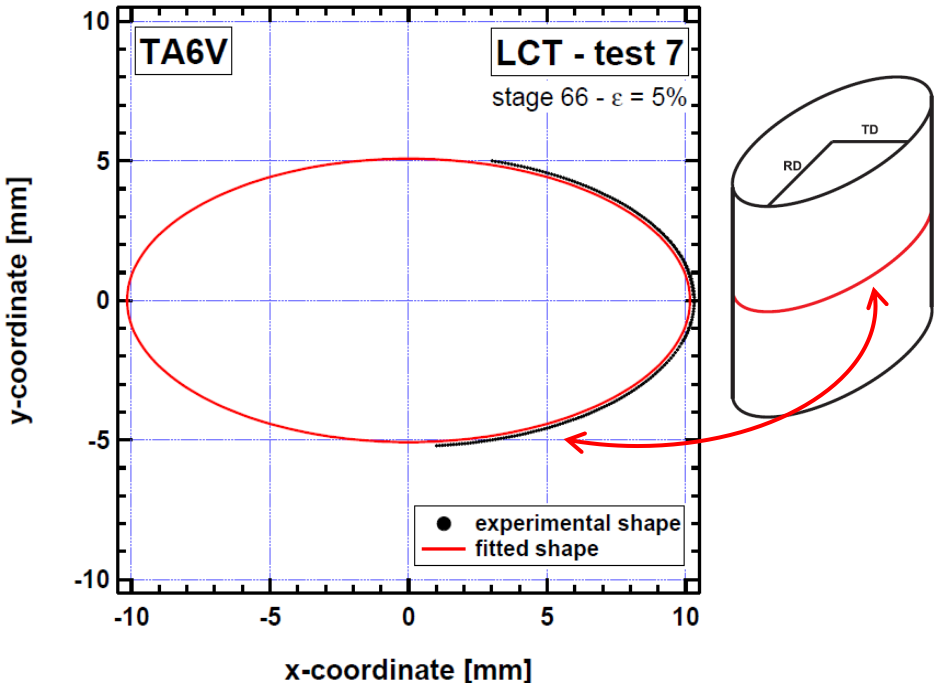

Figure 5-31 Shape of the middle cross-section at $\varepsilon = 5\%$ (stage 66 – test7): the black dots represent the experimental data (DIC) which are fitted by an ellipse (red curve) using the subroutine proposed by Halir and Flusser (1998)

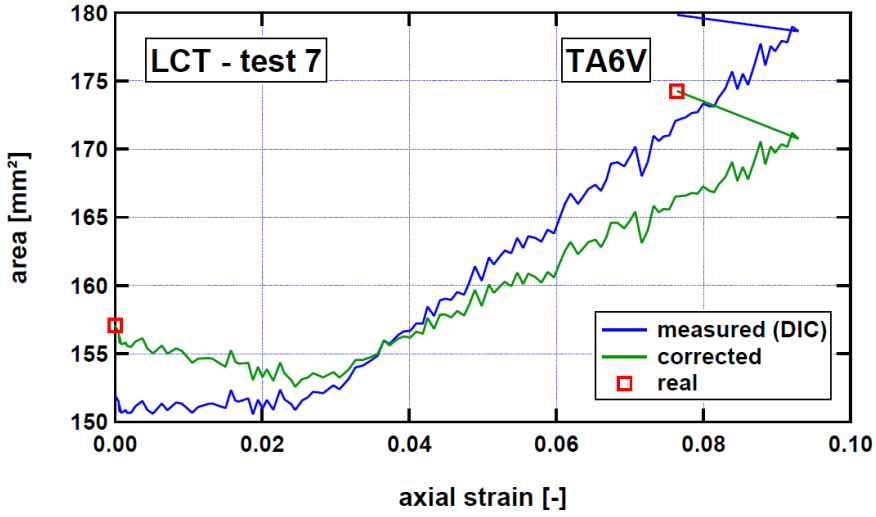

Figure 5-32 Area of the middle cross-section with respect to the average axial strain (test 7): the different data refer to the area determined by DIC (blue curve), the corrected area (green curve) and the area measured before and after the test (red symbols)

As the deformed cross-section is assumed to be an ellipse at each stage, it can be interesting to study the evolution of the semi-major axis and semi-minor axis, respectively denoted a and b, with the axial strain (see Figure 5-33) or else the evolution of their ratio (see Figure 5-34).

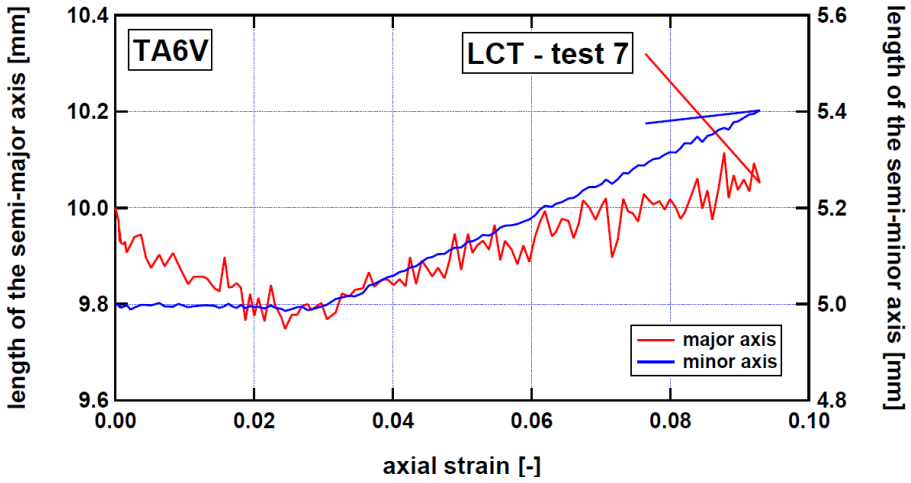

Figure 5-33 Evolution of the semi-major and semi-minor axes of the middle cross-section with the axial strain (test 7)

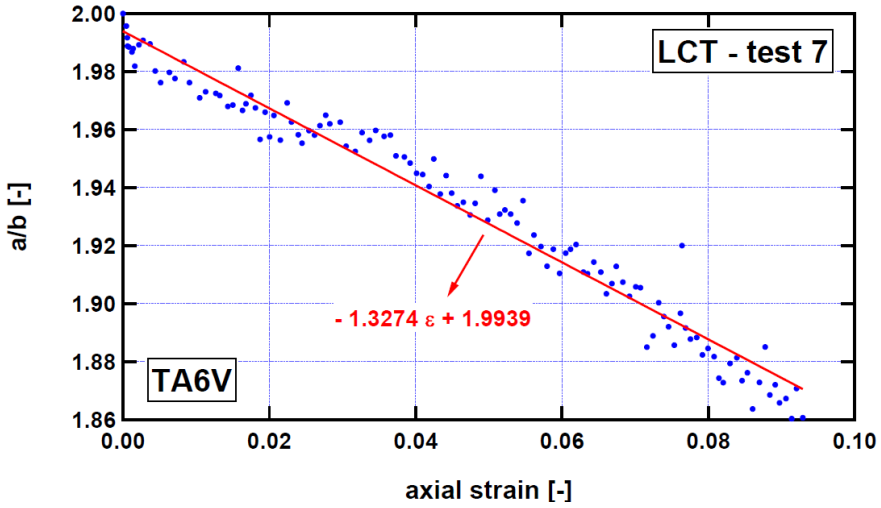

Figure 5-34 Evolution of the major to minor axes ratio with the axial strain (test 7)

For the tests 7, 8 and 9, it was observed that the ratio a/b decreases with increasing strain (in absolute value), which results into a growth of the cross-section more significant in TD than in RD. This can also be observed by plotting, for different stages of the deformation, the shape of the middle cross-section (Figure 5-35) or r with respect to θ (Figure 5-36), these two parameters being defined as follows:

- r is the distance between the center of the ellipse and a point on the free surface of the section;
- θ is the angle between the semi-major axis a (along RD) and r ($\theta = 0$ when $r = a$).

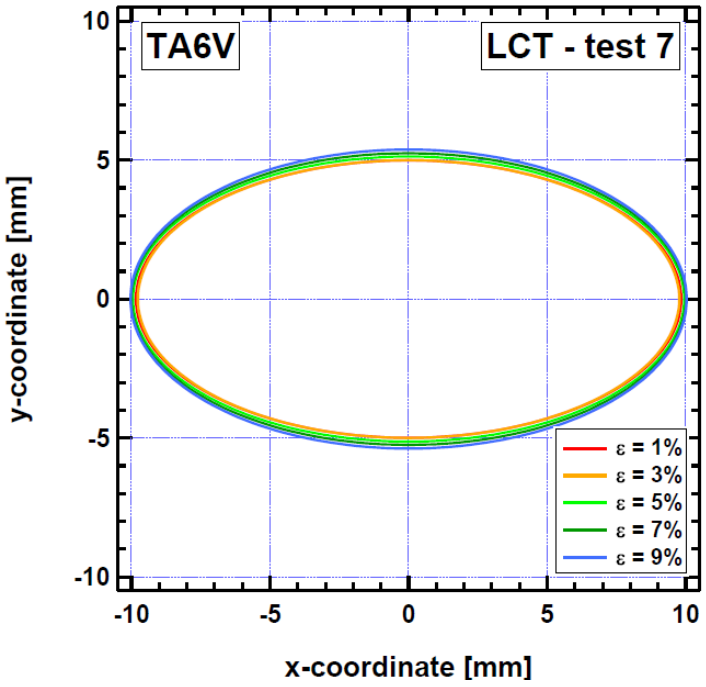

Figure 5-35 Shape of the middle cross-section at different average strain levels (test 7)

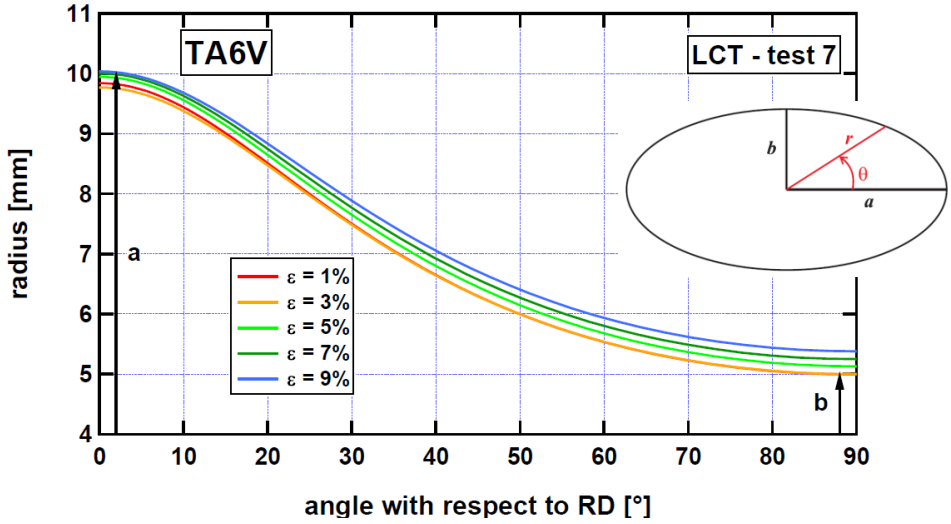

Figure 5-36 Distance r with respect to the angle θ at different average strain levels (test 7)

Concerning the tests 6 and 10, the conclusions differ from the above results as it can be seen in Figure 5-37 to Figure 5-40: the growth of the middle cross-section is larger in the RD than in the TD. It was observed that some images taken at the end of these tests were not correlated properly by the DIC process. In order to analyze the results, these images had to be neglected and some assumptions had to be made to perform the correction presented in Figure 5-32. An example is given in Figure 5-40 where the r-θ curves obtained for the tests 6 and 10 are different from those resulting from the tests 7, 8 and 9. However this does not prove that these experiments have to be rejected since no conclusion about compression in plane anisotropy can be deduced at this level as friction along the minor and major axis directions induce different constraints in the material flow. In addition it can be noticed different results in the

evolution of the ratio between the major and the minor axes of the cross-section depending on the test (Figure 5-41). Since the same procedure was followed during the experimental campaign, it is likely that friction played a sizeable influence in the shape evolution of the cross-section. An analysis of the friction effect through finite element simulations will be performed in Chapter 8.

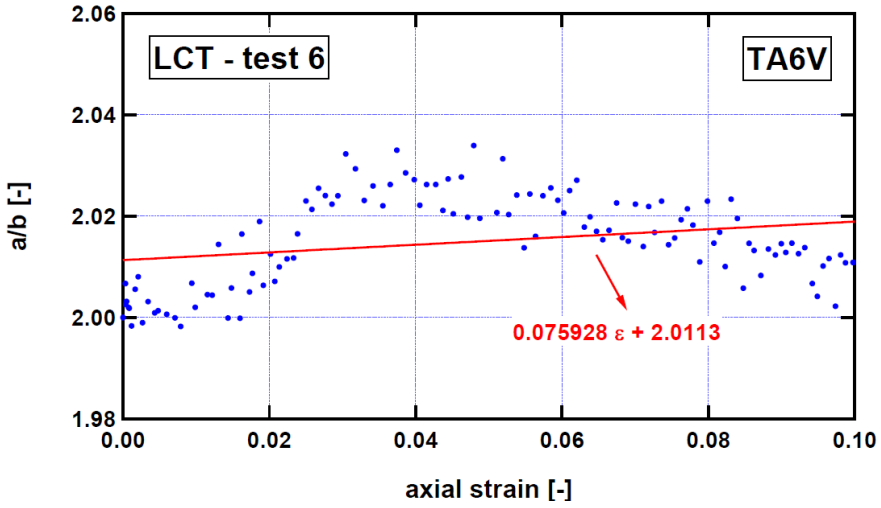

Figure 5-37 Evolution of the major to minor axes ratio with the axial strain (test 6)

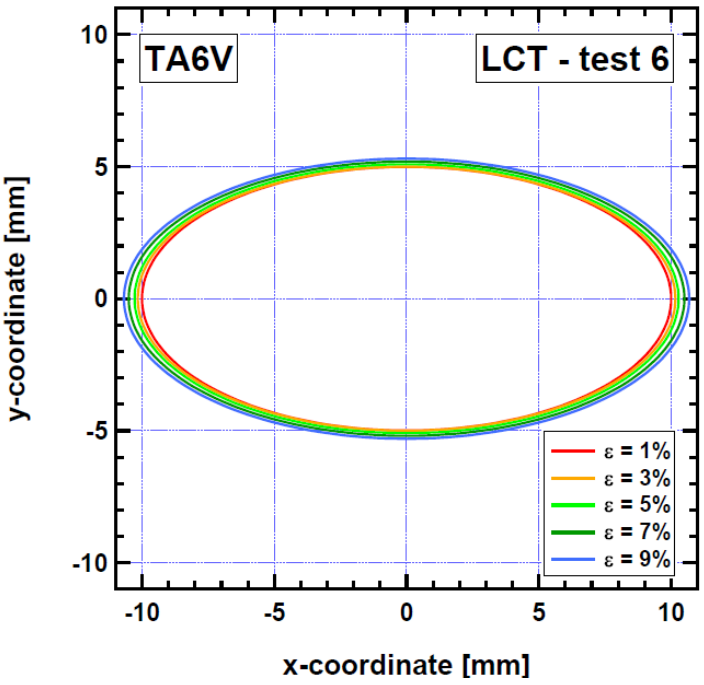

Figure 5-38 Shape of the middle cross-section at different average strain levels (test 6)

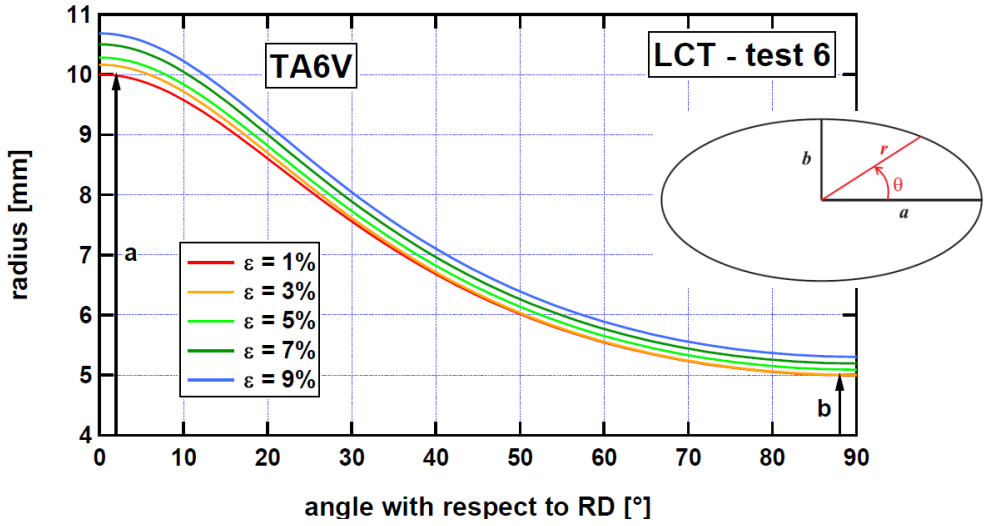

Figure 5-39 Distance r with respect to the angle θ at different average strain levels (test 7)

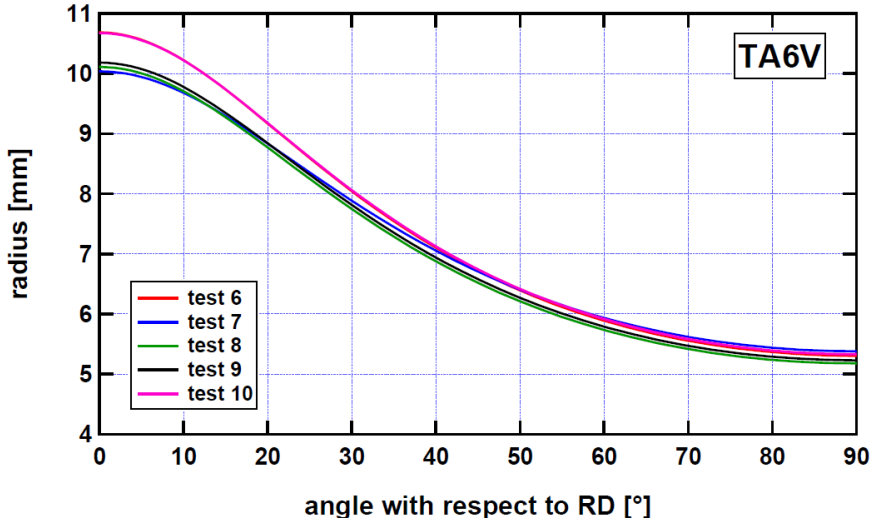

Figure 5-40 Distance r with respect to the angle θ for the different tests when the average axial strain reaches 9%

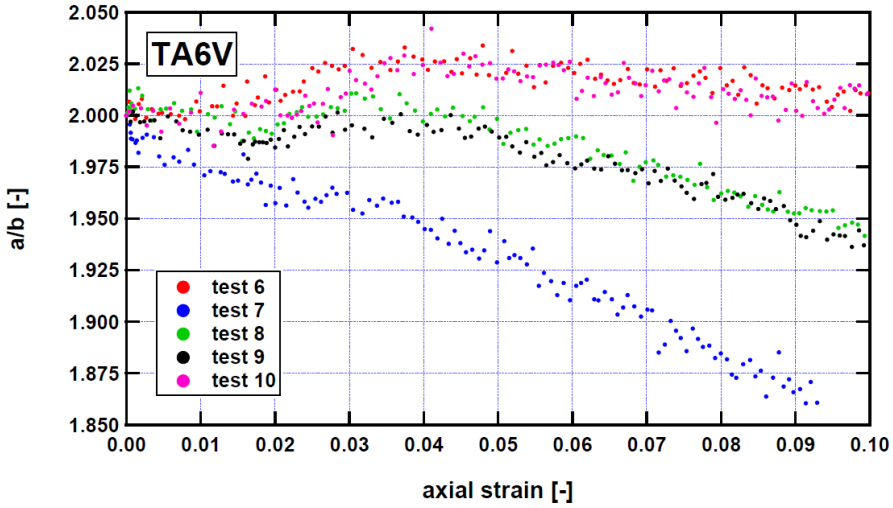

Figure 5-41 Evolution of the major to minor axes ratio with the axial strain for the different tests

In order to assess the effect of the friction coefficient with the help of finite element simulations, the experimental curvature of the specimen lateral surface in RD was determined for a strain level of 7%. The barreling effect can be observed in Figure 5-42.

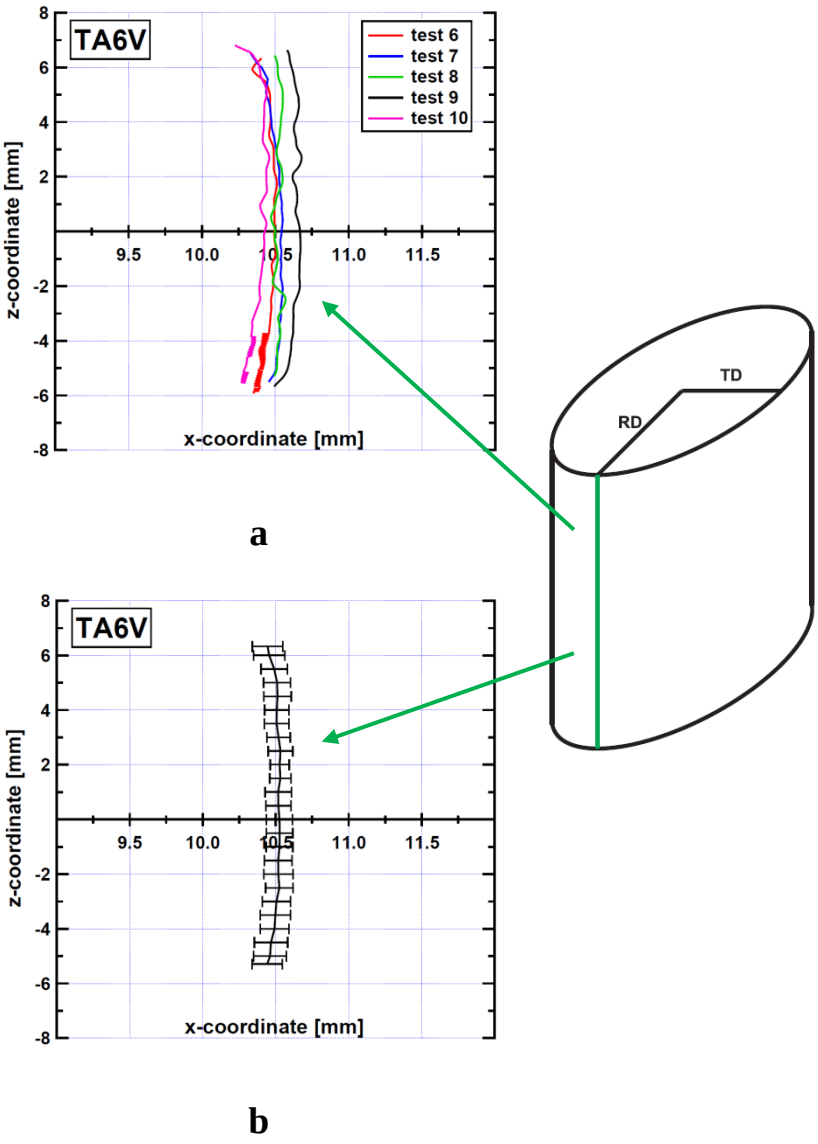

Figure 5-42 Curvature of the specimen lateral surface in RD at an average strain level of 7%: (a) results for the different tests; (b) average curve with error bars.

Strain field

DIC enables to determine the strain field at the lateral free surface. Figure 5-43 gives an example in which the evolution of the axial strain field along the middle cross-section of the specimen is plotted. The observation of the results obtained for the different tests shows that the material displays anisotropy. Nevertheless, each test reveals a strain field which is different of each other for a same level of the average axial strain (see Figure 5-44). This discrepancy of the results could be explained by the fact that the friction between the specimen and the experimental device as well as the parallelism defect of the punches can significantly affect the material response. Finite element simulations will be used in the third part of this work to determine the most reliable behavior.

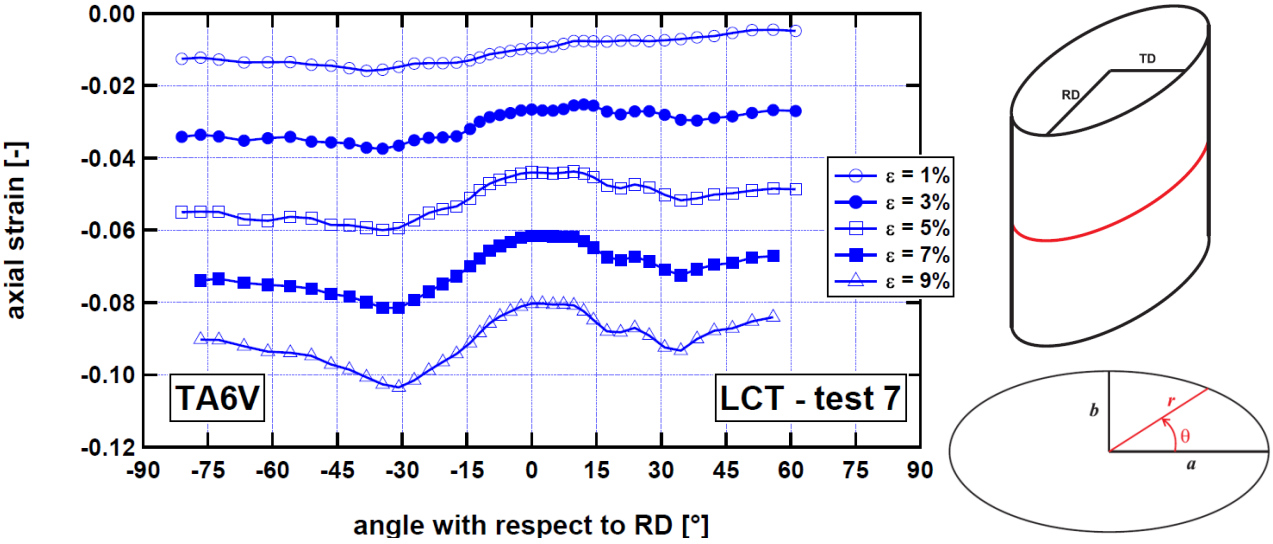

Figure 5-43 Distribution of the axial strain along the middle cross-section at different average strain levels (test 7)

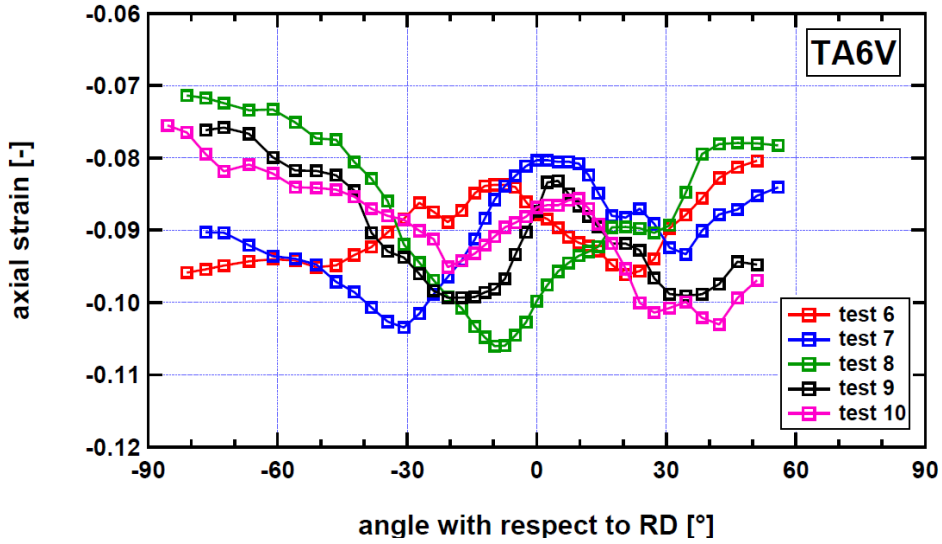

Figure 5-44 Distribution of the axial strain along the middle cross-section for the different tests when the average strain reaches 9%

Stress-strain curves

The axial stress is computed using three different approaches:

1. the force F measured by the load cell is divided by the cross-section area A^{DIC} determined by DIC:

$$\sigma^{\mathrm{DIC}} = \frac{F}{A^{\mathrm{DIC}}} \tag{5.9}$$

2. the force is divided by the cross-section area A^{vc} when assuming volume conservation:

$$\sigma^{vc} = \frac{F}{A^{vc}} \tag{5.10}$$

3. the force is divided by the corrected cross-section area A^{corr} (see Equations (5.5) to (5.8)):

$$\sigma^{corr} = \frac{F}{A^{corr}} \tag{5.11}$$

As it can be seen in Figure 5-45, these three approaches provide different results when the material is in plastic regime, which explains the interest to determine the actual area of the cross-section. It can also be noticed that a transition occurs before reaching the elastic regime due to the cavities which might exist between the different layers of the stack at the beginning of the test.

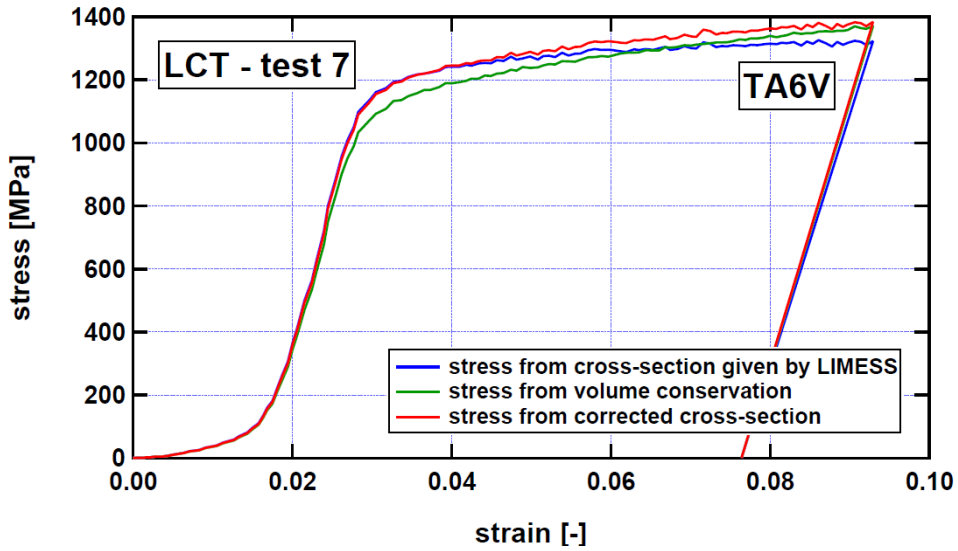

Figure 5-45 Comparison of the axial stress-axial strain curves respectively determined by three different approaches

In order to compare the stress-strain curves of the different tests, these are first shifted (see Figure 5-46) in such a way as to overlay the elastic part of each curve. An average curve is then determined. A relative good agreement can be observed considering the variation of the previous results (shape of the cross-section, strain field) from a test to another.

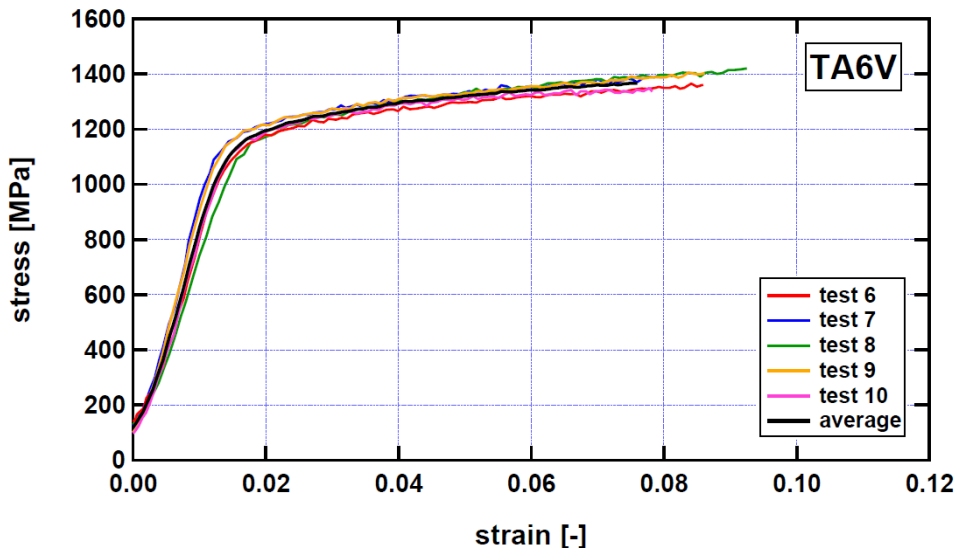

Figure 5-46 Comparison of the stress-strain curves obtained for each test and the average curve

Another important remark must be reported about the elastic modulus. Indeed, using the average stress-strain curve, Young modulus is determined by fitting a straight line along the elastic part (Figure 5-47), which gives $E \approx 80\,000$ MPa. This value is significantly lower than the ones usually observed in a classical tensile test (105 000 – 116 000 MPa). According to Coppieters (2012), layer compression tests are not adequate to identify Young modulus, as well as the initial yield stress, for the following reasons:

- the compliance of the adhesive if the stack is glued;
- the elasticity of the experimental device;
- a parallelism defect of the punches.

Similar observations can also be found in Maeda *et al.* (1998). The first two points can be neglected. Indeed no glue was used between the layers and the elasticity of the machine was taken into account in the computation of the strain rate. In addition, the strain field is determined by DIC. However a parallelism defect was measured between the punches of the machine. Another cause which could explain the low value of the elastic modulus is the surface roughness between the different layers of the stack.

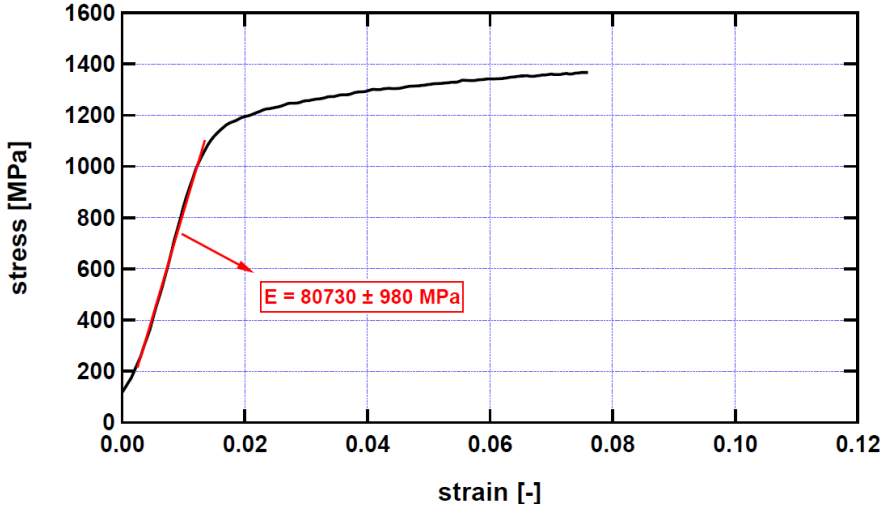

Figure 5-47 Determination of Young modulus (average stress-strain curve)

5.2.7. Results from deep-drawing tests

Figure 5-48 shows the deformed cups obtained for the different deep-drawing tests summarized in Table 4-6, while Figure 5-49 gives the corresponding force-displacement curves. It can be observed that some problems occured during the second and third tests. The deformed cup from the test 2 exhibits bumps along the wall part of the specimen. These bumps are actually due to a too large internal radius of the matrix. Concerning the specimen used for the test 3, the matrix was changed but significant failure occured during the process, making impossible the determination of the earing profile. This problem was caused by an unadapted lubricant. Indeed only oil was used for the test 3, while test 4 differs from the previous ones by the fact that Teflon was added.

Hereafter, only the tests 4 and 5 are analyzed since the lubricant as well as the dimensions of the tools, except the profile radius of the matrix, are identical.

The earing profile was determined on each quarter of the deformed cup (see Figure 5-50). Since the sheet presents an orthotropic symmetry, the four profiles should perfectly superimpose. Actually some deviations are observed and are probably due to an improper alignment of the center of the blank with the centers of the matrix and the punch during the deep-drawing process. An average earing profile was then determined from the four experimental results obtained for each quarter.

For some materials such as aluminium, the shape of the earing profile and the number of ears can be predicted by analyzing the distribution of the tensile *r*-ratios (Yoon *et al.* (2006)). Indeed, during the deformation, the flange of the cup is subjected to a tensile strain ε_1 along the radial direction and a compressive strain ε_2 acting along the circumference (Figure 5-51). In addition the latter is predominant, *i.e.* $|\varepsilon_1| < |\varepsilon_2|$. Besides, under tension, the lower the *r*-ratio is, the higher the thickness deformation of the sheet is. Since the flange is dominated by compression, its thickness tends to increase and the effect is even more significant that the *r*-ratio is small. As the volume is conserved during plastic deformations, a high increase of the thickness corresponds to a low earing, which means that the earing is minimum (resp. maximum) where the *r*-ratio is minimum (resp. maximum). Since compression occurs along the circumferential direction, the behavior of the flange in a θ-direction with respect to RD is controlled by the *r*-ratio of the material in the direction defined by $\theta + 90°$.

Test 1

Test 2

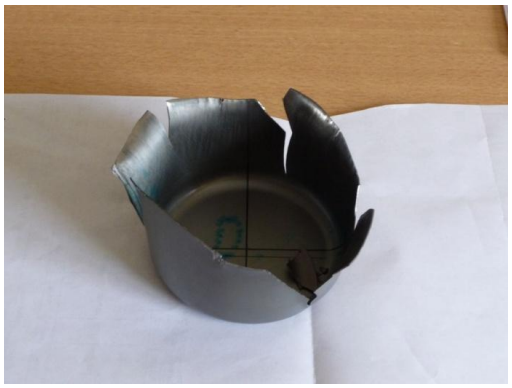

Test 3

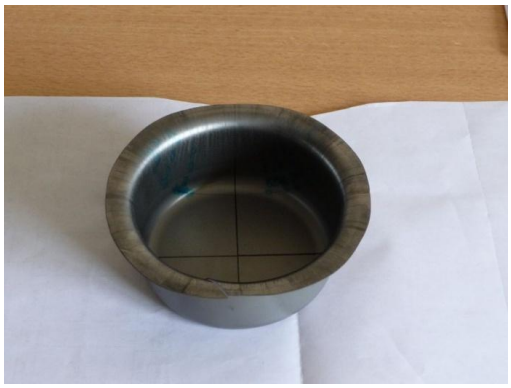

Test 4

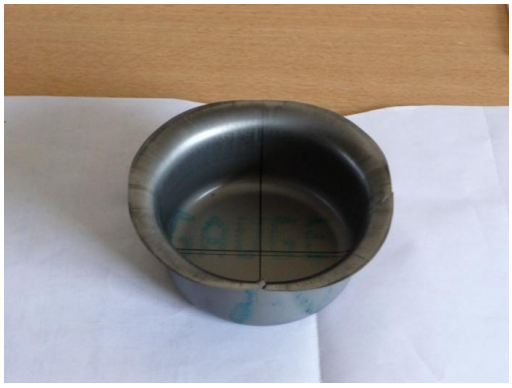

Test 5

Figure 5-48 Deformed cups resulting from deep-drawing tests

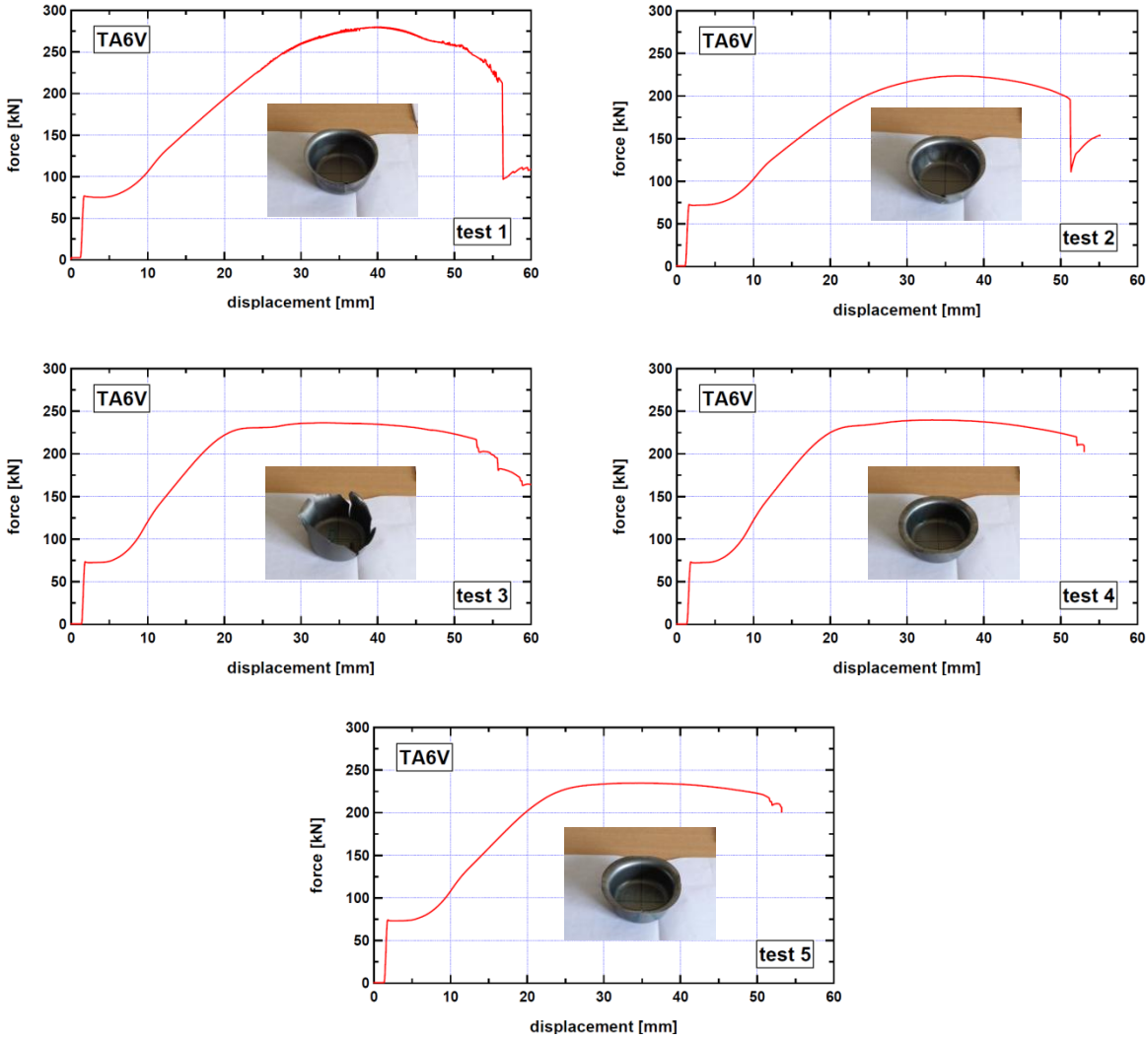

Figure 5-49 Force-displacement curves obtained for the different deep-drawing tests

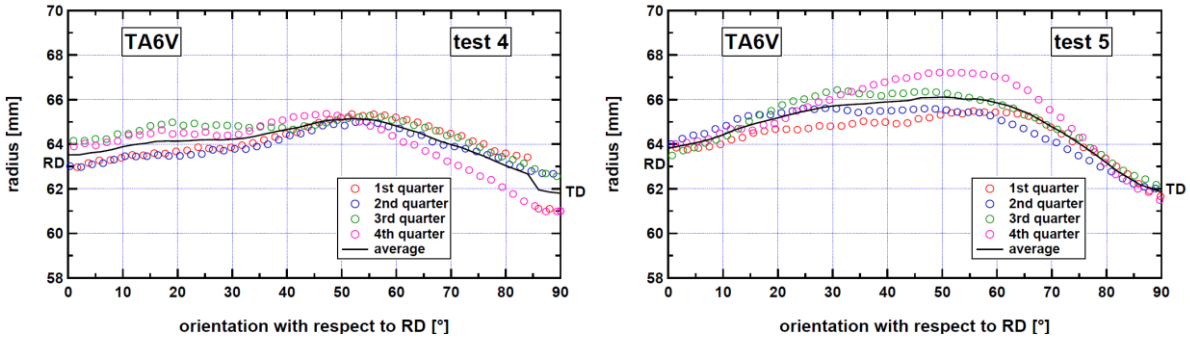

Figure 5-50 Earing profile of each quarter of the deformed cup and average profile for the tests 4 and 5

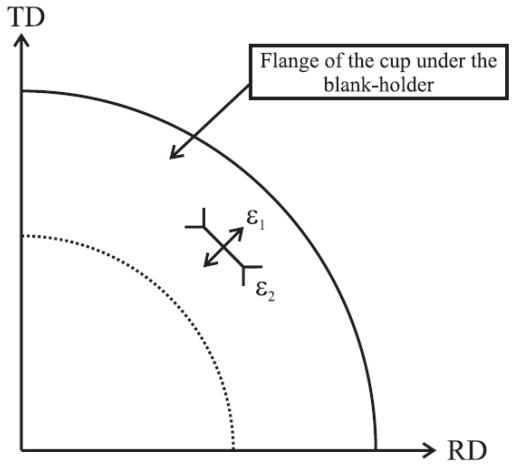

Figure 5-51 Strains along the radial and circumferential directions on the flange of the cup during the deep-drawing process

In the case of Ti6Al4V, it can be noticed that this link between the earing profile and the distribution of the *r*-ratios also exists (see Figure 5-52).

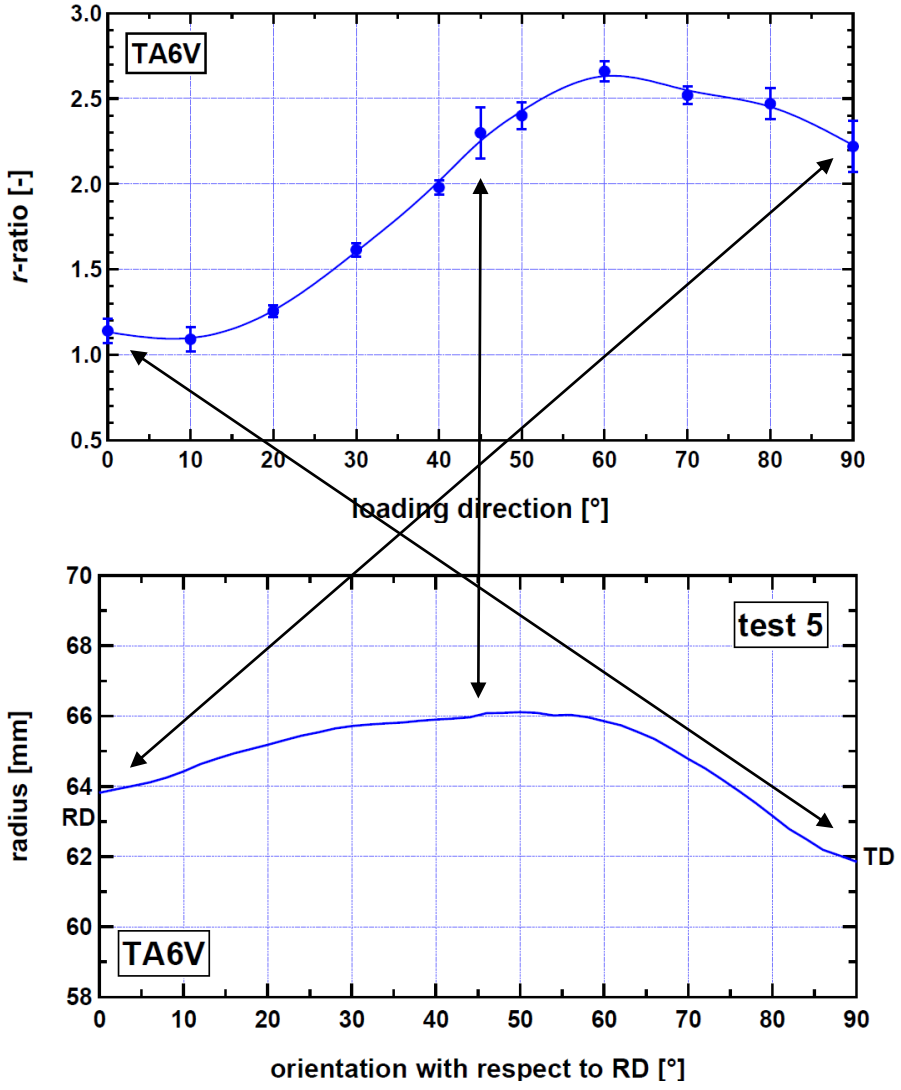

Figure 5-52 Link between the earing profile (test 5) and the distribution of the r-ratios in the case of Ti6Al4V

5.3. Study of the strain rate effect

As explained in Section 2.4.3.3, Ti6Al4V mechanical response is very sensitive to the strain ate, as shown in Figure 5-53 where the material is loaded in tension at different strain rates along RD, namely 10^{-4} s^{-1}, 10^{-3} s^{-1}, 10^{-2} s^{-1} and 10^{-1} s^{-1}. It can be noticed that the yield stress (respectively the work-hardening) increases (respectively decreases) when increasing the strain rate. It is thus required, when characterizing the material under different strain paths and identifying its initial yield locus, to perform experimental tests with same (equivalent) strain rates. Nevertheless, when different devices are used to carry out experiments, it is often difficult to reach an identical strain rate. The present study is on strain-rate effects in the low strain rate range.

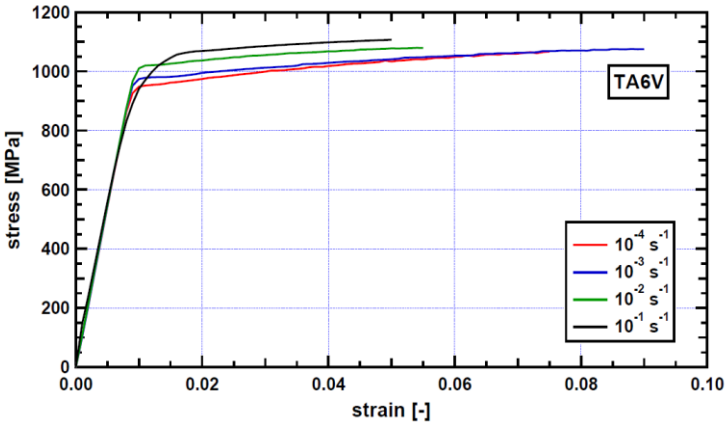

Figure 5-53 Ti6Al4V mechanical behavior in tension along RD at different strain rates

Figure 5-54 to Figure 5-57 show the evolution of different strain components with time for tensile, plane strain, simple shear and layer compression tests. It can be noticed that, in some cases, the strain rate was kept constant during the whole deformation (see Figure 5-54 and Figure 5-57), while it was only possible to maintain a constant speed in the other cases, which resulted in a different strain rate during the elastic and plastic regimes (see Figure 5-55 and Figure 5-56.

As different stress states are investigated, the equivalent strain rate has to be determined for each test. According to the work-equivalence principle, the rate of plastic work per unit of volume $\dot{W}^p$ is related to the equivalent stress and the equivalent plastic strain rate $\dot{\bar{\varepsilon}}^p$ by the following relationship:

$$\dot{W}^p = \bar{\sigma}\,\dot{\bar{\varepsilon}}^p = \sigma_{ij}\,\dot{\varepsilon}_{ij}^p \tag{5.12}$$

where σ_{ij} and $\dot{\varepsilon}_{ij}^p$ are respectively the components of the stress and plastic strain rate tensors.

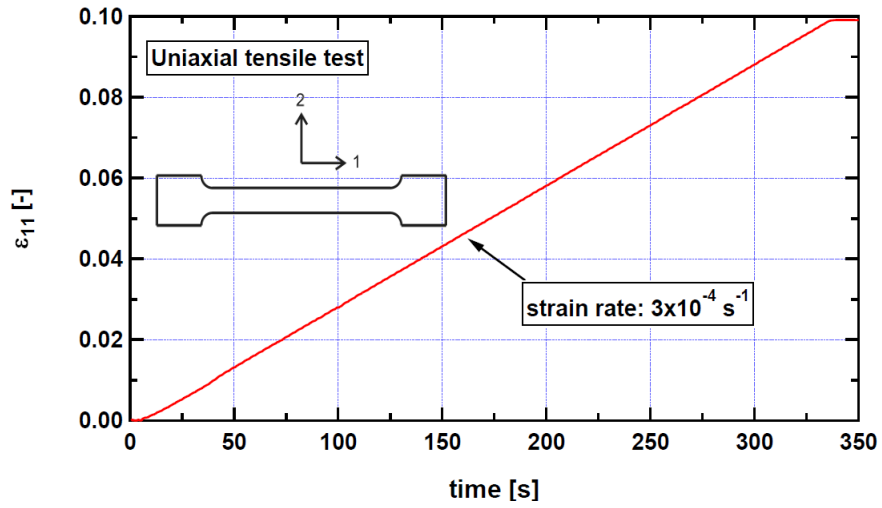

Figure 5-54 Evolution of ε_{11} with time during a tensile test (DIC measurement)

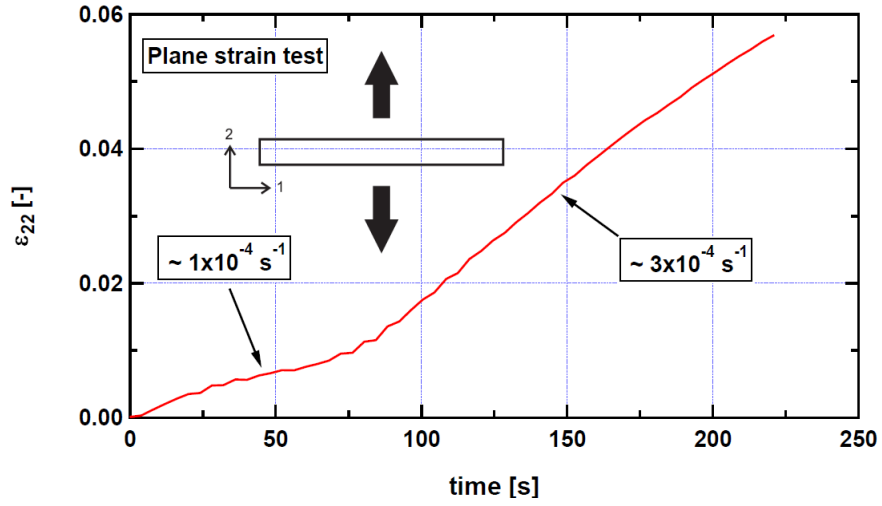

Figure 5-55 Evolution of ε_{22} with time during a plane strain test (DIC measurement)

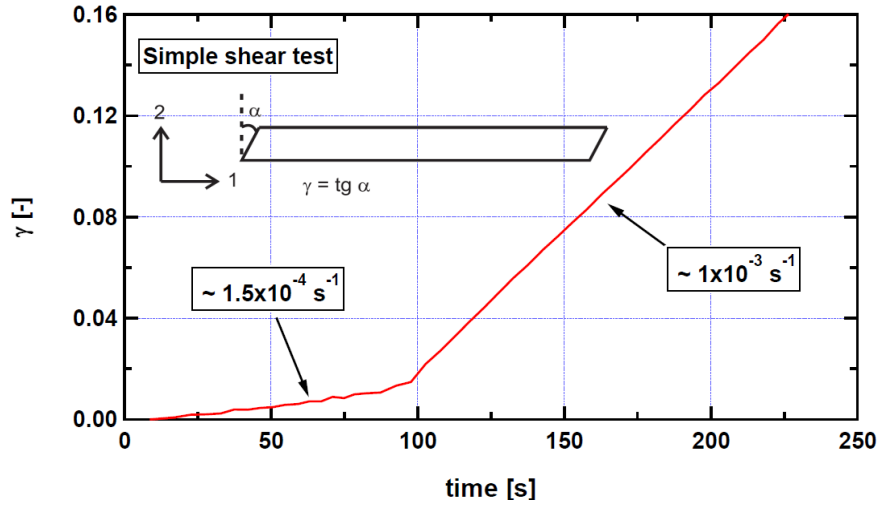

Figure 5-56 Evolution of γ with time during a plane strain test (DIC measurement)

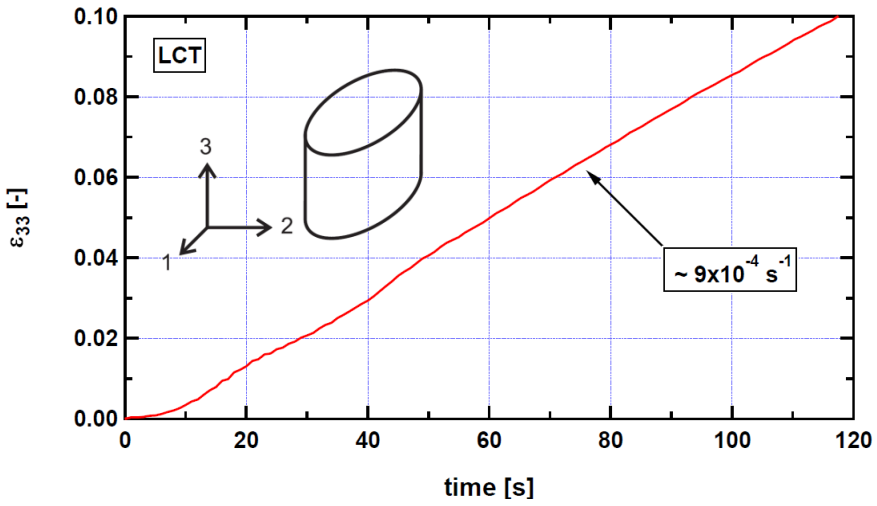

Figure 5-57 Evolution of ε_{33} with time during a layer compression test (DIC measurement)

The equivalent stress and the equivalent strain rate depend on the model used to describe the yield locus. For instance, if Von Mises criterion is considered, $\bar{\sigma}$ is given by:

$$\bar{\sigma} = \sqrt{\frac{3}{2} s_{ij} s_{ij}} \tag{5.13}$$

where s_{ij} denotes the components of the stress deviator. As for $\dot{\bar{\varepsilon}}^p$, it is determined as follows:

$$\dot{\bar{\varepsilon}}^p = \sqrt{\frac{2}{3} \dot{\varepsilon}_{ij}^p \dot{\varepsilon}_{ij}^p} \tag{5.14}$$

Since Ti6Al4V displays anisotropy and a tension-compression asymmetry, Von Mises criterion is not adapted to capture the material behavior. It is thus required to use another model able to take into account these specific features, as CPB06 (see Section 3.1.2). Nevertheless material parameters involved in anisotropic yield criteria have to be identified thanks to the experimental data. Because of this drawback, Equation (5.14) is used to assess the equivalent strain rate since it does not need any parameter.

Table 5-3 lists the different tests and the corresponding Von Mises equivalent strain rate (the reference frame used for each experiment is presented in Figure 5-54 to Figure 5-57). It has to be noted that the value determined for the simple shear tests is not accurate since the components ε_{11} and ε_{22} are not insignificant at large deformations and the used relationship assumes pure shear state. Nevertheless, for the sake of simplicity, it will be assumed that the component γ mostly contributes to the equivalent strain rate.

Tensile test	$\dot{\bar{\varepsilon}} = \dot{\varepsilon}_{11} = 3\times10^{-4}\ \text{s}^{-1}$
Plane strain test	$\dot{\bar{\varepsilon}} = \frac{2}{\sqrt{3}}\dot{\varepsilon}_{22} = \frac{2}{\sqrt{3}}\times3\times10^{-4} \approx 3.5\times10^{-4}\ \text{s}^{-1}$
Simple shear test	$\dot{\bar{\varepsilon}} = \frac{\dot{\gamma}}{\sqrt{3}} = \frac{10^{-3}}{\sqrt{3}} \approx 5.8\times10^{-4}\ \text{s}^{-1}$
Layer compression test	$\dot{\bar{\varepsilon}} = \dot{\varepsilon}_{33} = 9\times10^{-4}\ \text{s}^{-1}$

Table 5-3 Assessment of the equivalent strain rates for the different loadings

The results in Table 5-3 show that $\dot{\bar{\varepsilon}}$ is different from one test to another. It is thus essential to determine whether the experimental stress-strain curves need to be corrected. In order to answer this question, the following procedure is performed:

1. Johnson-Cook (JC) constitutive model (Equation (3.70)) is used to determine the stress-strain curves at any strain rate. The identification of JC parameters is performed using the experimental data in tension along RD at 10^{-4}, 10^{-3} and 10^{-2} s^{-1} (Figure 5-53) and assuming $T = T_{\text{room}}$ since the strain rates are low (note that this assumption is not in agreement with López (2014) research which has identified thermal effect by performing tests in air and fluid for strain rates larger than 6×10^{-4} s^{-1}). The material parameters (when choosing $\dot{\bar{\varepsilon}}_0 = 10^{-4}\ \text{s}^{-1}$) are listed in Table 5-4 while the numerical curves are compared with the experiments in Figure 5-58.

Hardening parameters			Viscous parameter (sensitivity to strain rate)
A	*B*	*n*	*C*
935.16	460.67	0.5103	0.0104

Table 5-4 Johnson-Cook hardening material parameters based on the experimental data in tension at different strain rates

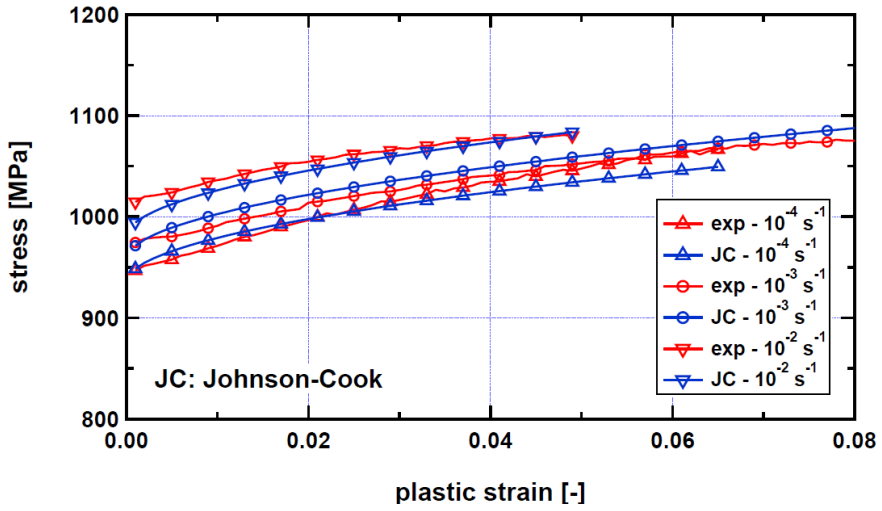

Figure 5-58 Comparison between experimental and numerical stress-plastic strain curves according to Johnson-Cook model for tensile tests

2. In the case of the plane strain, simple shear and layer compression tests, the material hardening parameters A, B and n are identified for each loading direction while the viscous parameter $C = 0.0104$ is assumed independent on the direction and the stress state. The results of the identification are given in Table 5-5 and the numerical curves are compared with the experimental data in Figure 5-59.

	$\dot{\bar{\varepsilon}}$	A	B	n	C
Plane strain RD	3.5×10^{-4} s^{-1}	745.36	597.12	0.1514	0.0104
Plane strain 45°		760.43	619.18	0.1523	
Plane strain TD		806.90	692.69	0.1953	
Simple shear RD	5.8×10^{-4} s^{-1}	801.59	578.57	0.5606	
Simple shear 45°		836.76	516.70	0.3610	
Simple shear TD		785.16	520.28	0.4483	
LCT	9.0×10^{-4} s^{-1}	916.74	773.53	0.2151	

Table 5-5 Johnson-Cook hardening material parameters based on experimental data in plane strain, simple shear and layer compression tests

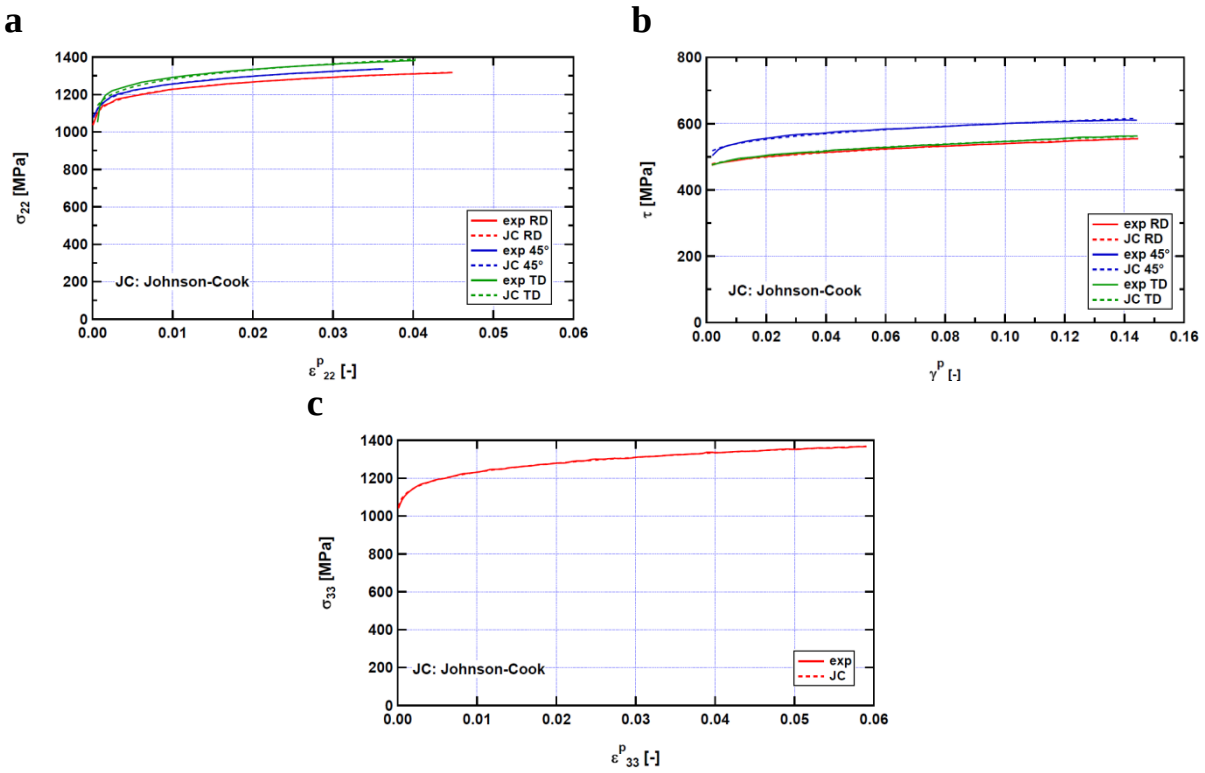

Figure 5-59 Comparison between experimental and numerical stress-plastic strain curves according to Johnson-Cook model (hardening and viscous parameters from Table 5-5): (a) plane strain tests; (b) simple shear tests; (c) layer compression tests

3. Using the Johnson-Cook model and the parameters in Table 5-5, the different stress-strain curves are corrected to be at $\dot{\bar{\varepsilon}} = 3\times10^{-4}$ s^{-1} (*i.e.* the strain rate used for the ten-

sile tests) are assessed and compared with the experimental curves performed at strain rates going from 3.5 to 9×10^{-4} s^{-1} (see Figure 5-60).

Even if there are some discrepancies in terms of equivalent strain rate from one test to another, Figure 5-60 confirms that the viscous effect within this range of values (3.5×10^{-4} to 9×10^{-4} s^{-1}) has no effect. It could be explained by the fact that the stress-strain curves in tension at 10^{-4} and 10^{-3} s^{-1} are very close (see Figure 5-53).

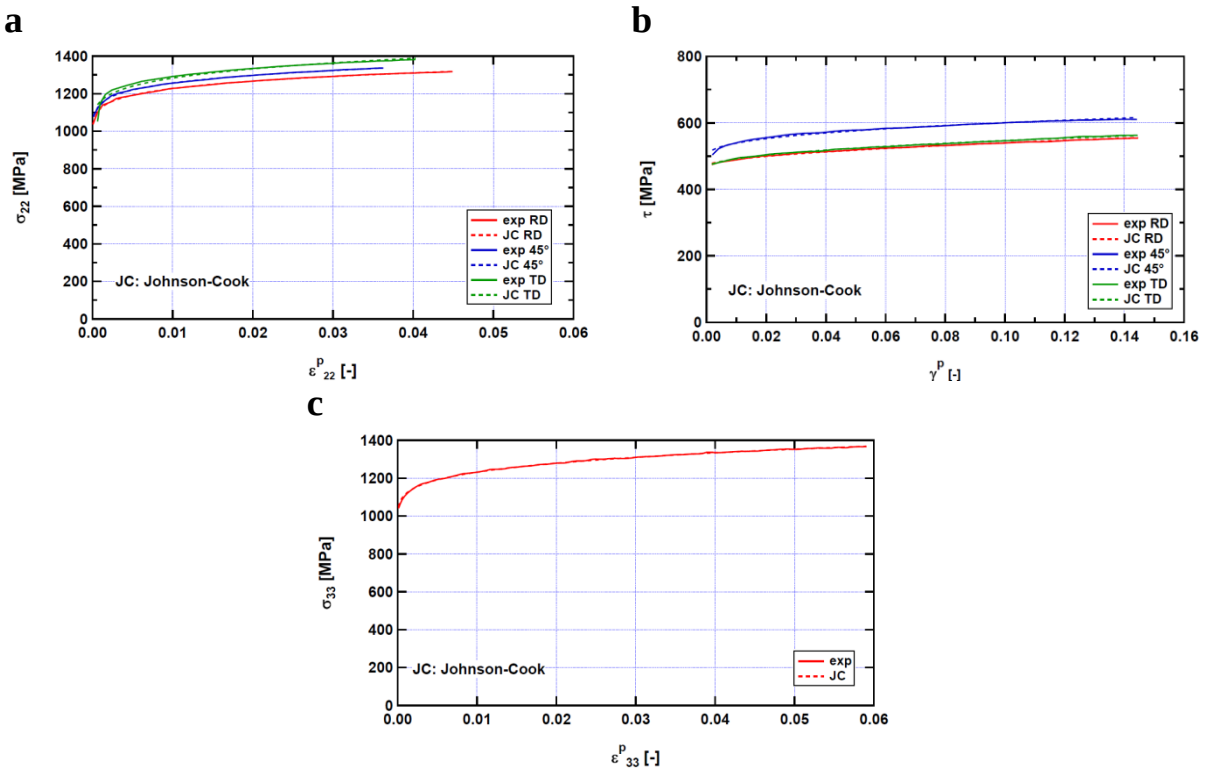

Figure 5-60 Comparison of the numerical stress-plastic strain curves according to Johnson-Cook model at $\dot{\bar{\varepsilon}} = 3\times10^{-4}\ s^{-1}$ ***with the experimental data performed at different strain rates in (a) plane strain, (b) simple shear and (c) layer compression tests***

5.4. General conclusion and discussion

This chapter described the experiments carried out on Ti6Al4V sheet under different loading conditions. It was observed that the material displays a moderate anisotropy in yield stresses, a pronounced anisotropy in *r*-ratios and a strength differential effect between tension and compression, which implies that classic plasticity models (J_2-flow theory, Hill 1948) are not able to capture the material response. For this reason, CPB06 yield criterion and its extensions are used in the following of this work to model the yield locus. About the hardening behavior, the experimental results show that the evolution of the yield locus shape must be taken into account. In addition a significant Bauschinger effect was noticed when reversing the loading direction during a simple shear test. Different hardening formulations will be proposed in the next part in order to predict with a good accuracy the material behavior.

Part III Numerical study

Chapter 6 Implementation of the CPB06 yield criterion in the finite element code LAGAMINE

The simulation of the experimental tests performed on Ti6Al4V and described in both Chapter 4 and Chapter 5 has been performed using the FE code LAGAMINE. The latter is an implicit nonlinear FE code with an updated Lagrangian formulation and is adapted to large strains and large displacements. It was developed by the ArGEnCo department (ULg) in 1984 and has been applied to numerous forming processes: rolling (Habraken *et al.* (1998)), forging (Habraken and Cescotto (1990)), continuous casting (Castagne *et al.* (2003); Castagne *et al.* (2004)), deep drawing (Duchêne *et al.* (2002)) and so on. The code uses a large element library (e.g. Cescotto and Charlier (1993); Zhu and Cescotto (1994); Zhu and Cescotto (1995); Habraken and Cescotto (1998)) and numerous constitutive laws (e.g. Habraken and Duchêne (2004)). Nevertheless, CPB06 yield criterion was not included in the code at the beginning of this work. Then the first step consisted in implementing the model into LAGAMINE in order to use it in the simulations. This chapter describes the different integration schemes which were integrated in the code.

6.1. Introduction

6.1.1. Discretization of equilibrium equations

The physical phenomenons such as equilibrium, compatibility, … are governed by partial differential equations whose solution can be determined by minimizing the total energy of the system. It can be proved that this minimization amounts to checking the virtual work principle:

$$\delta W_I = \int_V \boldsymbol{\sigma} : \delta\boldsymbol{\varepsilon}\, dV = \int_V \rho\, \mathbf{b} : \delta\mathbf{u}\, dV + \int_S \rho\, \mathbf{t} : \delta\mathbf{u}\, dS = \delta W_E \tag{6.1}$$

In Equation (6.1), δW_I and δW_E are respectively the internal and external virtual works. $\boldsymbol{\sigma}$ represents the stress tensor, $\delta\boldsymbol{\varepsilon}$ is the virtual strain tensor determined from the virtual displacement $\delta\mathbf{u}$, $\mathbf{b}$ and $\mathbf{t}$ denote the external volumetric and surface loads respectively, ρ is the density while V and S denote the current volume and surface respectively.

In finite elements, the virtual displacement field is discretized as follows:

$$\delta\mathbf{u} = \mathbf{H} : \delta\mathbf{q} \tag{6.2}$$

where $\delta\mathbf{q}$ is the vector of the nodal values while $\mathbf{H}$ is the shape function matrix.

The virtual strain field is determined by:

$$\delta\boldsymbol{\varepsilon} = \mathbf{B} : \delta\mathbf{q} \tag{6.3}$$

where $\mathbf{B}$ is the strain-displacement matrix.

By introducing Equations (6.2) and (6.3) in the virtual work principle, Equation (6.1) becomes:

$$\int_V \boldsymbol{\sigma} : \mathbf{B} : \delta\mathbf{q}\, dV = \int_V \rho\, \mathbf{b} : \mathbf{H} : \delta\mathbf{q}\, dV + \int_S \rho\, \mathbf{t} : \mathbf{H} : \delta\mathbf{q}\, dS \tag{6.4}$$

Since $\delta\mathbf{q}$ contains the virtual nodal displacements, it can be written:

$$\mathbf{F}^{\text{int}} : \delta\mathbf{q} = \mathbf{F}^{\text{ext}} : \delta\mathbf{q} \tag{6.5}$$

where $\mathbf{F}^{\text{ext}}$ denotes the nodal external force vector equivalent to the applied loadings:

$$\mathbf{F}^{\text{ext}} = \int_V \rho\, \mathbf{b} : \mathbf{H}\, dV + \int_S \rho\, \mathbf{t} : \mathbf{H}\, dS \tag{6.6}$$

and $\mathbf{F}^{\text{int}}$ denotes the nodal internal force vector equivalent to the stresses:

$$\mathbf{F}^{\text{int}} = \int_V \boldsymbol{\sigma} : \mathbf{B}\, dV \tag{6.7}$$

Since $\delta\mathbf{q}$ is arbitrary, Equation (6.5) leads to:

$$\mathbf{F}^{\text{int}} = \mathbf{F}^{\text{ext}} \tag{6.8}$$

expressing the discretized equilibrium condition in the finite element method.

6.1.2. Temporal integration

LAGAMINE enables the solving of a finite element problem by applying either explicit or implicit approach. Nevertheless implicit integration schemes are very often used since they are more stable and allow larger time increments.

Implicit methods are incremental: the loading P or the displacement U is applied step by step. $\lambda_1 P$ or $\lambda_1 U$ with $0<\lambda_1<1$ is imposed to the initial configuration. The Newton-Raphson method (see Figure 6-1) is then used to find a new balanced configuration. Next $\lambda_2 P$ or $\lambda_2 U$ with $\lambda_1<\lambda_2$ is applied to the previous configuration and the procedure is repeated until $\sum_k \lambda_k = 1$ is reached.

The equilibrium is satisfied when the nodal external forces are equal to the nodal internal forces (Equation (6.8)) or, in other words, the out-of-balance force vector $\mathbf{F}^{\mathrm{OOB}} = \mathbf{F}^{\mathrm{int}} - \mathbf{F}^{\mathrm{ext}}$ is zero. In practice, it is unrealistic to require this equality and an iterative procedure is used to reduce the norm of $\mathbf{F}^{\mathrm{OOB}}$ under a convergence tolerance. By a first-order Taylor development around the nodal position $\mathbf{x}_{i+1}$ at the $(i+1)$-th iteration, it is obtained:

$$\mathbf{F}^{\mathrm{OOB}}\left(\mathbf{x}_{i+1}\right) = \mathbf{F}^{\mathrm{OOB}}\left(\mathbf{x}_i\right) + \left(\frac{\partial \mathbf{F}^{\mathrm{OOB}}}{\partial \mathbf{x}}\right)_{\mathbf{x}=\mathbf{x}_i} \Delta\mathbf{x} \tag{6.9}$$

where $\mathbf{x}_i$ is the nodal position at the i-th iteration while $\Delta\mathbf{x}$ represents the nodal position correction. The gradient:

$$\mathbf{K} = \left(\frac{\partial \mathbf{F}^{\mathrm{OOB}}}{\partial \mathbf{x}}\right)_{\mathbf{x}=\mathbf{x}_i} \tag{6.10}$$

denotes the tangent stiffness matrix. As the goal is to cancel the out-of-balance forces, $\mathbf{F}^{\mathrm{OOB}}\left(\mathbf{x}_{i+1}\right) = \mathbf{0}$ is imposed, which gives from Equation (6.9):

$$\Delta\mathbf{x} = -\mathbf{K}^{-1}\,\mathbf{F}^{\mathrm{OOB}}\left(\mathbf{x}_i\right) \tag{6.11}$$

Finally, the nodal position at the $(i+1)$-th iteration is determined by:

$$\mathbf{x}_{i+1} = \mathbf{x}_i + \Delta\mathbf{x} \tag{6.12}$$

The previous algorithm is repeated until the following condition is satisfied:

$$\frac{\left\|\mathbf{F}^{\mathrm{OOB}}\right\|}{\left\|\mathbf{R}\right\|} < \varepsilon_f \tag{6.13}$$

where $\mathbf{R}$ is the reaction containing all force components of fixed or constrained nodes, while ε_f is the force convergence tolerance. The symbol $\|.\|$ denotes the norm of a vector. Different definitions can be used in LAGAMINE (n is the length of $\mathbf{F}$ associated to the nodal degree of freedom):

- $\left\|\mathbf{F}\right\|_1 = \frac{1}{n}\sum_{i=1}^{n}\left|F_i\right|$
- $\left\|\mathbf{F}\right\|_2 = \frac{1}{n}\sqrt{\sum_{i=1}^{n}F_i^2}$

- $\|\mathbf{F}\|_\infty = \max_{i=1...n}(|F_i|)$

Another convergence tolerance ε_u is used in the code in order to check the balance convergence and to prevent jump displacements:

$$\frac{\|\Delta\mathbf{x}\|}{\|\mathbf{x}_i - \mathbf{x}_A\|} < \varepsilon_u \tag{6.14}$$

where $\mathbf{x}_A$ denotes the nodal position at the previous balance configuration.

A summary of the LAGAMINE flowchart is given in Figure 6-2.

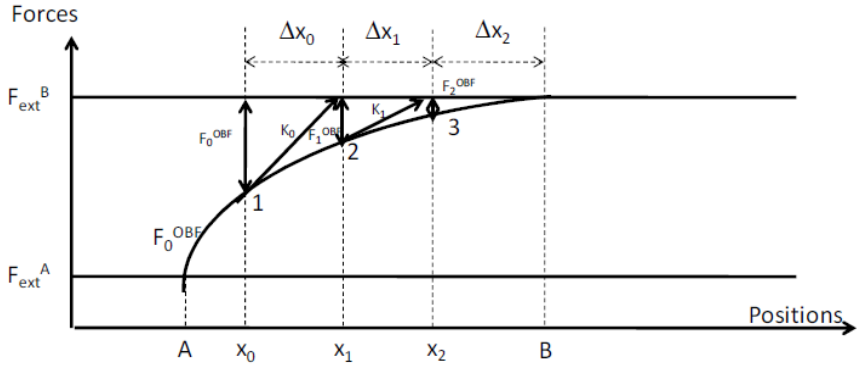

Figure 6-1 Description of the Newton-Raphson method (figure from Lequesne (2009))

Note that special cases are defined when $\|\mathbf{R}\|$ is null or very small, but this will not be described here.

6.1.3. Constitutive laws

In order to determine the stresses, it is required to use a constitutive model characterizing the material behavior and which is able to compute the stresses when the nodal coordinates and the loading history are known. LAGAMINE proposes a large library of constitutive laws. However, no model adapted to hcp metals in general and to Ti6Al4V titanium alloy in particular had been implemented when this thesis started. The following sections describe the two implementations which are proposed to model the mechanical behavior of hcp materials and have been introduced into LAGAMINE. The modifications have been performed at the level of the preprocessor (subroutine LAWPRE.F) and the finite element code (subroutine LOI2.F).

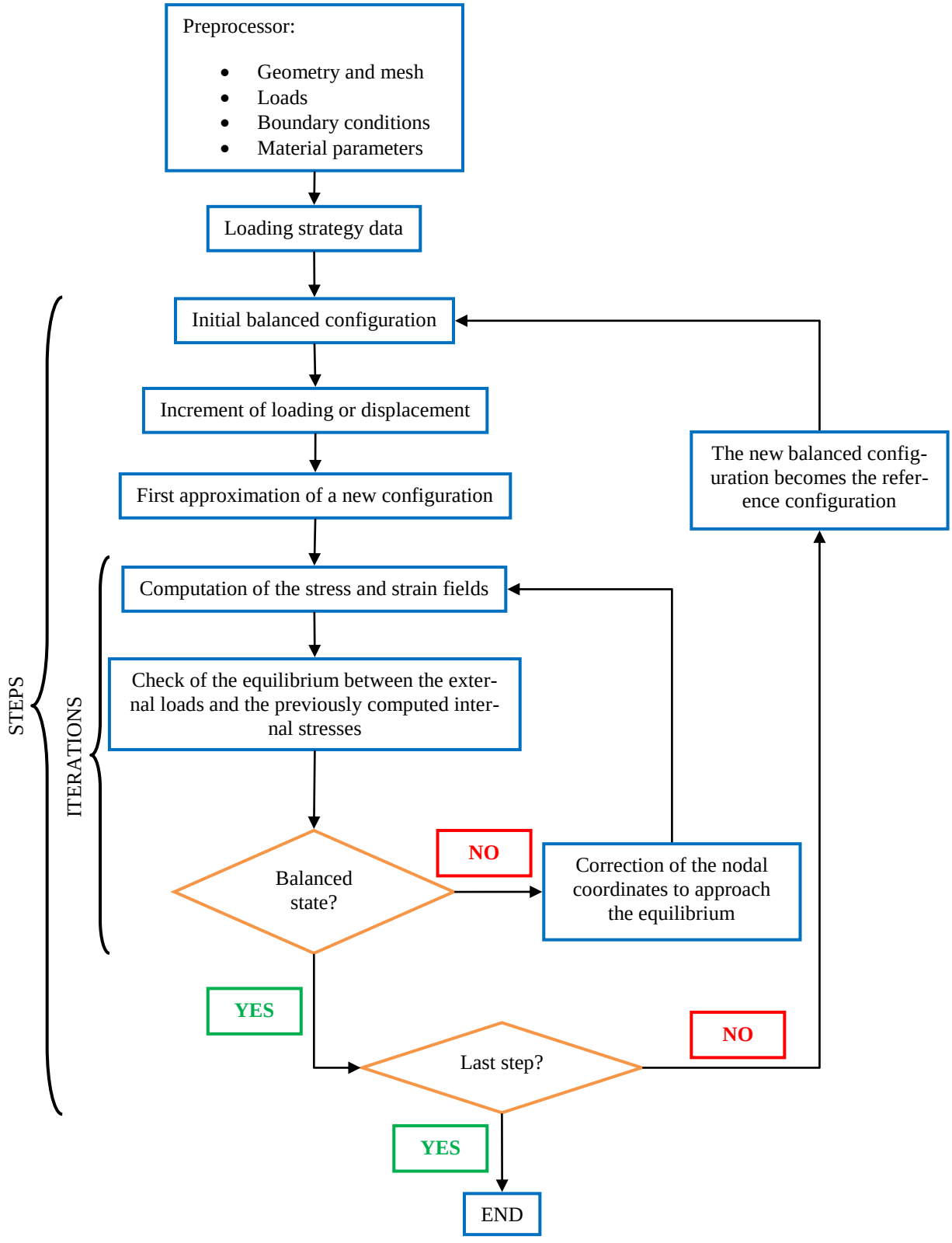

Figure 6-2 General flowchart of the LAGAMINE code

6.2. Implementation of CPB06 associated to isotropic and kinematic hardening laws

It is assumed that yielding is described as follows:

$$\varphi\left(\boldsymbol{\sigma}-\mathbf{X},\bar{\varepsilon}_p\right)=\bar{\sigma}\left(\boldsymbol{\sigma}-\mathbf{X},\bar{\varepsilon}_p\right)-Y\left(\bar{\varepsilon}_p\right) \tag{6.15}$$

This relationship is similar to Equation (3.41), excepted the equivalent stress $\bar{\sigma}$ only depend on the equivalent plastic strain $\bar{\varepsilon}^p$.

$\bar{\sigma}$ is based on the stress potential given by Equation (3.33) associated to CPB06 yield criterion, or Equation (3.36) associated to CPB06ex*n* yield criteria. If CPB06 yield criterion is considered (all the following relationships can easily be extended to CPB06ex*n* family), the equivalent stress has the form:

$$\bar{\sigma}=B\left\{\left(\left|\Sigma_1\right|-k\Sigma_1\right)^a+\left(\left|\Sigma_2\right|-k\Sigma_2\right)^a+\left(\left|\Sigma_3\right|-k\Sigma_3\right)^a\right\}^{\frac{1}{a}} \tag{6.16}$$

where B is a constant defined such that $\bar{\sigma}$ reduces to the tensile yield stress in RD, *i.e.*:

$$B=\left\{\left(\left|\Phi_1\right|-k\Phi_1\right)^a+\left(\left|\Phi_2\right|-k\Phi_2\right)^a+\left(\left|\Phi_3\right|-k\Phi_3\right)^a\right\}^{-\frac{1}{a}} \tag{6.17}$$

with

$$\begin{aligned}
\Phi_1&=\frac{2}{3}C_{11}-\frac{1}{3}C_{12}-\frac{1}{3}C_{13}\\
\Phi_2&=\frac{2}{3}C_{12}-\frac{1}{3}C_{22}-\frac{1}{3}C_{23}\\
\Phi_3&=\frac{2}{3}C_{13}-\frac{1}{3}C_{23}-\frac{1}{3}C_{33}
\end{aligned} \tag{6.18}$$

The following algorithmic aspects were adopted for the simulations. Since the elastic strains are usually much smaller than the plastic strains, it is considered an additive decomposition of the total strain rate $\dot{\boldsymbol{\varepsilon}}$ into an elastic part $\dot{\boldsymbol{\varepsilon}}^e$ and a plastic part $\dot{\boldsymbol{\varepsilon}}^p$:

$$\dot{\boldsymbol{\varepsilon}}=\dot{\boldsymbol{\varepsilon}}^e+\dot{\boldsymbol{\varepsilon}}^p \tag{6.19}$$

The elastic stress-strain relationship is expressed in a rate form to fit the incremental procedure. It is given by:

$$\overset{\nabla}{\boldsymbol{\sigma}}=\mathbf{C}^e:\dot{\boldsymbol{\varepsilon}}^e \tag{6.20}$$

where $\mathbf{C}^e$ is the fourth-order elasticity tensor. The evolution of the plastic strain is given by an associated flow rule:

$$\dot{\boldsymbol{\varepsilon}}^p = \dot{\lambda}\frac{\partial \varphi}{\partial \boldsymbol{\sigma}} \tag{6.21}$$

where $\dot{\lambda} \geq 0$ is the plastic multiplier and φ is given by Equation (6.15). Since the effective stress $\bar{\sigma}$ (Equation (6.16)) is a first order homogeneous function in stresses, the application of Euler theorem leads to:

$$\boldsymbol{\sigma} : \frac{\partial \bar{\sigma}}{\partial \boldsymbol{\sigma}} = \bar{\sigma} \tag{6.22}$$

From the work-equivalence principle, it can thus be shown that:

$$\dot{W}^p = \boldsymbol{\sigma} : \dot{\boldsymbol{\varepsilon}}^p = \dot{\lambda}\, \boldsymbol{\sigma} : \frac{\partial \bar{\sigma}}{\partial \boldsymbol{\sigma}} = \bar{\sigma}\, \dot{\lambda} = \bar{\sigma}\, \dot{\bar{\varepsilon}}^p \tag{6.23}$$

i.e.:

$$\dot{\lambda} = \dot{\bar{\varepsilon}}_p \tag{6.24}$$

where $\dot{\bar{\varepsilon}}_p$ is the equivalent plastic strain rate.

The integration scheme implemented into LAGAMINE to determine the stress state at each step is the closest point projection algorithm (see Figure 6-3). During a time step $\Delta t = t_{n+1} - t_n$, the trial state $\boldsymbol{\sigma}_{n+1}^{\text{trial}} = \boldsymbol{\sigma}_n + \mathbf{C}^e : \Delta \boldsymbol{\varepsilon}_n$ is computed. If $\varphi\left(\boldsymbol{\sigma}_{n+1}^{\text{trial}} - \mathbf{X}_n, \bar{\varepsilon}_n^p\right) \leq 0$, the stress state is elastic and then $\boldsymbol{\sigma}_{n+1} = \boldsymbol{\sigma}_{n+1}^{\text{trial}}$. If $\varphi\left(\boldsymbol{\sigma}_{n+1}^{\text{trial}} - \mathbf{X}_n, \bar{\varepsilon}_n^p\right) > 0$, there is plastic flow and the following non-linear system must be solved for $\boldsymbol{\sigma}_{n+1}$, $\mathbf{X}_{n+1}$ and $\Delta\lambda_{n+1}$:

$$\begin{cases} \boldsymbol{\sigma}_{n+1} &= \boldsymbol{\sigma}_{n+1}^{\text{trial}} - \Delta\lambda_{n+1}\mathbf{C}^e : \left(\dfrac{\partial \varphi}{\partial \boldsymbol{\sigma}}\right)_{n+1} \\ \varphi_{n+1} &= \bar{\sigma}\left(\boldsymbol{\sigma}_{n+1} - \mathbf{X}_{n+1}, \bar{\varepsilon}_{n+1}^p\right) - Y\left(\bar{\varepsilon}_{n+1}^p\right) \end{cases} \tag{6.25}$$

where $-\Delta\lambda_{n+1}\mathbf{C}^e : \left(\dfrac{\partial \varphi}{\partial \boldsymbol{\sigma}}\right)_{n+1}$ is the stress correction due to the plastic strains. If the elastic trial state is denoted as iteration $k = 0$ ($\boldsymbol{\sigma}_{n+1}^0 = \boldsymbol{\sigma}_{n+1}^{\text{trial}}$ and $\Delta\lambda_{n+1}^0 = 0$), k being the local iteration counter, the stress increment update takes the effects of the plastic strains as follows:

$$\boldsymbol{\sigma}_{n+1}^{k+1} = \boldsymbol{\sigma}_{n+1}^k + \delta\boldsymbol{\sigma}_{n+1}^{k+1} = \boldsymbol{\sigma}_{n+1}^k - \delta\lambda_{n+1}^{k+1}\mathbf{C}^e : \left(\frac{\partial \varphi}{\partial \boldsymbol{\sigma}}\right)_{n+1}^{k+1} \tag{6.26}$$

where δ denotes the variation of the variable between iterations k and $k+1$, *i.e.*:

$$\begin{cases} \delta\boldsymbol{\sigma}_{n+1}^{k+1} &= \boldsymbol{\sigma}_{n+1}^{k+1} - \boldsymbol{\sigma}_{n+1}^k \\ \delta\lambda_{n+1}^{k+1} &= \Delta\lambda_{n+1}^{k+1} - \Delta\lambda_{n+1}^k \end{cases} \tag{6.27}$$

The stress potential gradient (see Appendix E for its computation) at the updated state $\left(\frac{\partial \varphi}{\partial \boldsymbol{\sigma}}\right)_{n+1}^{k+1}$ is approximated by:

$$\left(\frac{\partial \varphi}{\partial \boldsymbol{\sigma}}\right)_{n+1}^{k+1} \simeq \left(\frac{\partial \varphi}{\partial \boldsymbol{\sigma}}\right)_{n+1}^{k} = \mathbf{Q}_{n+1}^{k} \tag{6.28}$$

and the stress correction is then given by:

$$\delta\boldsymbol{\sigma}_{n+1}^{k+1} = -\delta\lambda_{n+1}^{k+1}\mathbf{C}^{e} : \mathbf{Q}_{n+1}^{k} \tag{6.29}$$

The incremental variation of the plastic multiplier $\delta\lambda_{n+1}^{k+1}$ is obtained through a Taylor expansion of the yield criterion about the current state:

$$\begin{aligned} \varphi_{n+1}^{k+1} &= \varphi_{n+1}^{k} + \left(\frac{\partial \varphi}{\partial \boldsymbol{\sigma}}\right)_{n+1}^{k} : \delta\boldsymbol{\sigma}_{n+1}^{k+1} + \left(\frac{\partial \varphi}{\partial \mathbf{X}}\right)_{n+1}^{k} : \delta\mathbf{X}_{n+1}^{k+1} + \left(\frac{\partial \varphi}{\partial \bar{\varepsilon}^{p}}\right)_{n+1}^{k} \delta\lambda_{n+1}^{k+1} \\ &= \varphi_{n+1}^{k} - \delta\lambda_{n+1}^{k+1}\, \mathbf{Q}_{n+1}^{k} : \mathbf{C}^{e} : \mathbf{Q}_{n+1}^{k} - \mathbf{Q}_{n+1}^{k} : \delta\mathbf{X}_{n+1}^{k+1} + \left(\frac{\partial \bar{\sigma}}{\partial \bar{\varepsilon}^{p}} - \frac{\partial Y}{\partial \bar{\varepsilon}^{p}}\right)_{n+1}^{k} \delta\lambda_{n+1}^{k+1} \\ &= 0 \end{aligned} \tag{6.30}$$

where $\delta\mathbf{X}_{n+1}^{k+1} = \mathbf{X}_{n+1}^{k+1} - \mathbf{X}_{n+1}^{k}$.

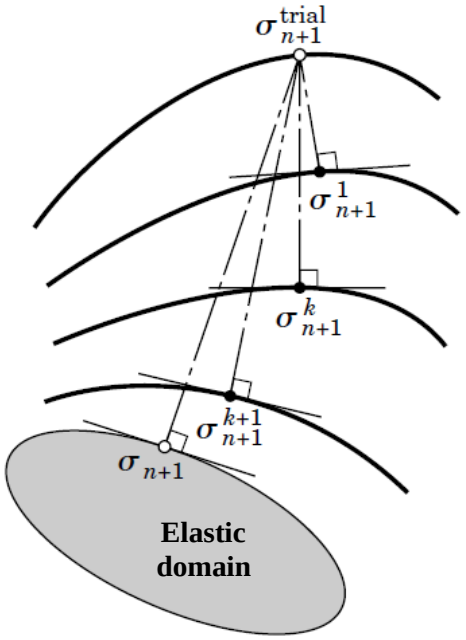

Figure 6-3 Geometric interpretation of the closest point projection algorithm: at each iteration k, the constraint is linearized to find the intersection with $\varphi = 0$; σ_{n+1}^{k+1}, located on φ_{n+1}^{k+1}, is the closest point of this surface to σ_{n+1}^{k} (Simo and Hughes (1998))

The computation of $\delta \mathbf{X}_{n+1}^{k+1}$ and $\left(\frac{\partial Y}{\partial \bar{\varepsilon}^p} \right)_{n+1}^{k}$ depends on the constitutive laws used to describe the kinematic and isotropic hardenings, respectively.

In order to describe the expansion of the yield locus with the plastic deformation as well as the Bauschinger effect revealed by Ti6Al4V (see Section 5.2.4), a combined Voce isotropic – Armstrong-Frederick kinematic hardening model (see Equations (3.45) and (3.48)) was first considered. If the equivalent stress $\bar{\sigma}$ is assumed to be independent from the equivalent plastic strain $\bar{\varepsilon}^p$, *i.e.* $\frac{\partial \bar{\sigma}}{\partial \bar{\varepsilon}^p} = 0$, Equation (6.30) combined with Equations (3.44), (3.45) and (3.48) leads to:

$$\begin{aligned} &\varphi_{n+1}^{k} - \delta\lambda_{n+1}^{k+1}\, \mathbf{Q}_{n+1}^{k} : \mathbf{C}^e : \mathbf{Q}_{n+1}^{k} \\ &\quad - \mathbf{Q}_{n+1}^{k} : \left[c_X \left(s_X \left(\delta\boldsymbol{\varepsilon}^p \right)_{n+1}^{k+1} - \mathbf{X}_{n+1}^{k}\, \delta\lambda_{n+1}^{k+1} \right) \right] - c_R \left(s_R - R_{n+1}^{k} \right) \delta\lambda_{n+1}^{k+1} = 0 \end{aligned} \tag{6.31}$$

Since

$$\left(\delta\boldsymbol{\varepsilon}^p \right)_{n+1}^{k+1} = \delta\lambda_{n+1}^{k+1} \left(\frac{\partial \varphi}{\partial \boldsymbol{\sigma}} \right)_{n+1}^{k+1} \approx \delta\lambda_{n+1}^{k+1} \left(\frac{\partial \varphi}{\partial \boldsymbol{\sigma}} \right)_{n+1}^{k} = \delta\lambda_{n+1}^{k+1}\, \mathbf{Q}_{n+1}^{k} \tag{6.32}$$

the plastic multiplier is given by:

$$\delta\lambda_{n+1}^{k+1} = \frac{\varphi_{n+1}^{k}}{\mathbf{Q}_{n+1}^{k} : \mathbf{C}^e : \mathbf{Q}_{n+1}^{k} + c_X \left(s_X\, \mathbf{Q}_{n+1}^{k} : \mathbf{Q}_{n+1}^{k} - \mathbf{Q}_{n+1}^{k} : \mathbf{X}_{n+1}^{k} \right) + c_R \left(s_R - R_{n+1}^{k} \right)} \tag{6.33}$$

The stresses, the back-stress and the plastic strains are then updated through $\delta\lambda$. The plastic corrector step is repeated until a specified tolerance η of the yield function has been obtained. Once convergence is reached, the updated stresses and strains are accepted as the current state.

The compliance matrix relates the current stress increment to the current total strain increment. It is used to predict the total strain increment for the next iteration. The derivative of the yield function gives:

$$d\varphi = \frac{\partial \varphi}{\partial \boldsymbol{\sigma}} : d\boldsymbol{\sigma} + \frac{\partial \varphi}{\partial \mathbf{X}} : d\mathbf{X} + \frac{\partial \varphi}{\partial \bar{\varepsilon}^p} d\lambda = 0 \tag{6.34}$$

Since $d\boldsymbol{\varepsilon}^e = d\boldsymbol{\varepsilon} - d\boldsymbol{\varepsilon}^p = d\boldsymbol{\varepsilon} - d\lambda\, \mathbf{Q}$, it yields $d\boldsymbol{\sigma} = \mathbf{C}^e : d\boldsymbol{\varepsilon} - d\lambda\, \mathbf{C}^e : \mathbf{Q}$ and thus:

$$d\lambda = \frac{\mathbf{Q} : \mathbf{C}^e : d\boldsymbol{\varepsilon}}{\mathbf{Q} : \mathbf{C}^e : \mathbf{Q} + c_X \left(s_X\, \mathbf{Q} : \mathbf{Q} - \mathbf{Q} : \mathbf{X} \right) + c_R \left(s_R - R \right)} \tag{6.35}$$

The compliance matrix is then given by:

$$\mathbf{C}^{ep} = \frac{d\boldsymbol{\sigma}}{d\boldsymbol{\varepsilon}} = \mathbf{C}^e - \frac{\left(\mathbf{C}^e : \mathbf{Q} \right) \otimes \left(\mathbf{C}^e : \mathbf{Q} \right)}{\mathbf{Q} : \mathbf{C}^e : \mathbf{Q} + c_X \left(s_X\, \mathbf{Q} : \mathbf{Q} - \mathbf{Q} : \mathbf{X} \right) + c_R \left(s_R - R \right)} \tag{6.36}$$

The flowchart of the integration scheme described above is given in Figure 6-4 and Figure 6-5.

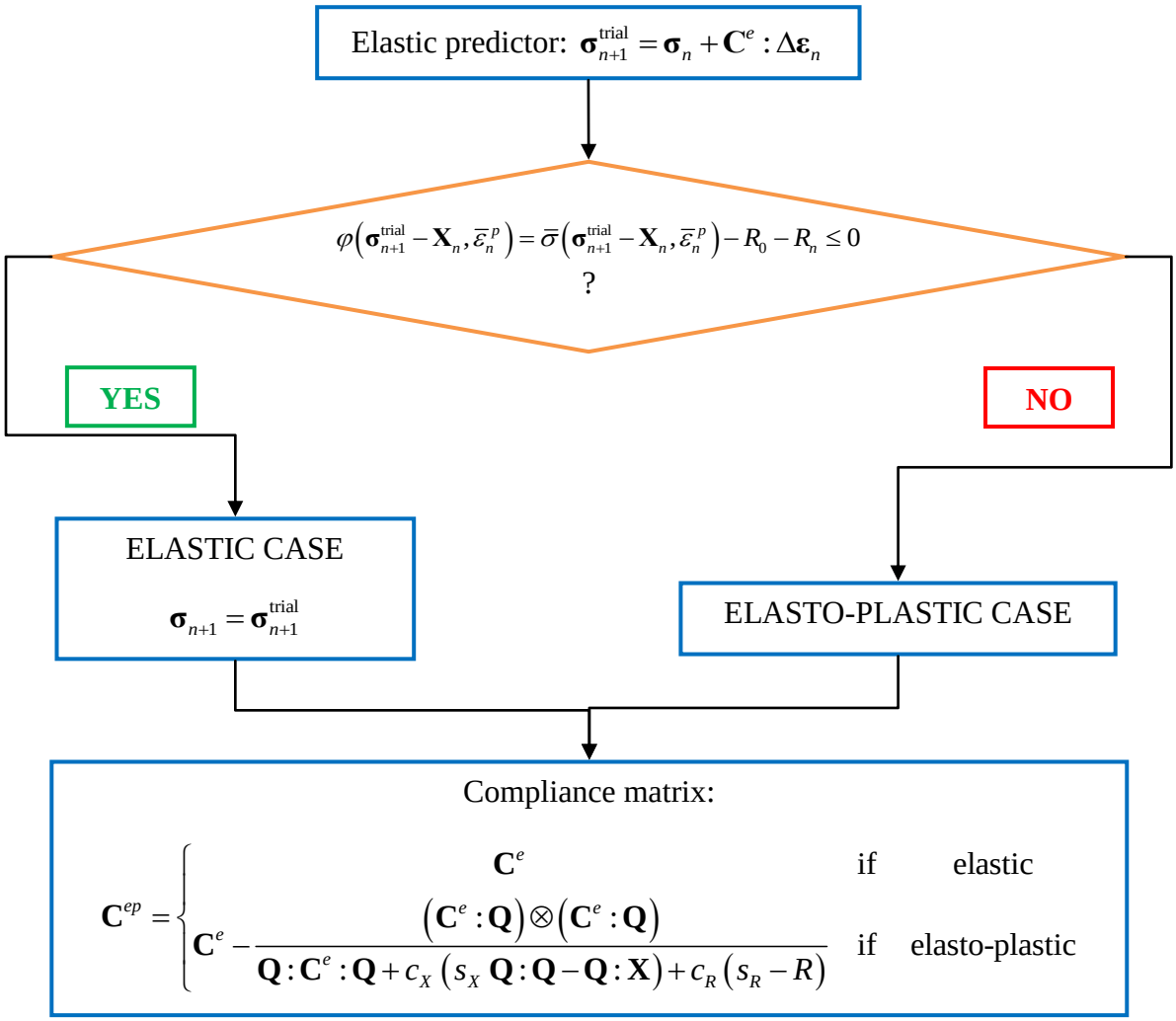

Figure 6-4 General flowchart of the integration scheme associating CPB06 yield criterion with a mixed hardening law

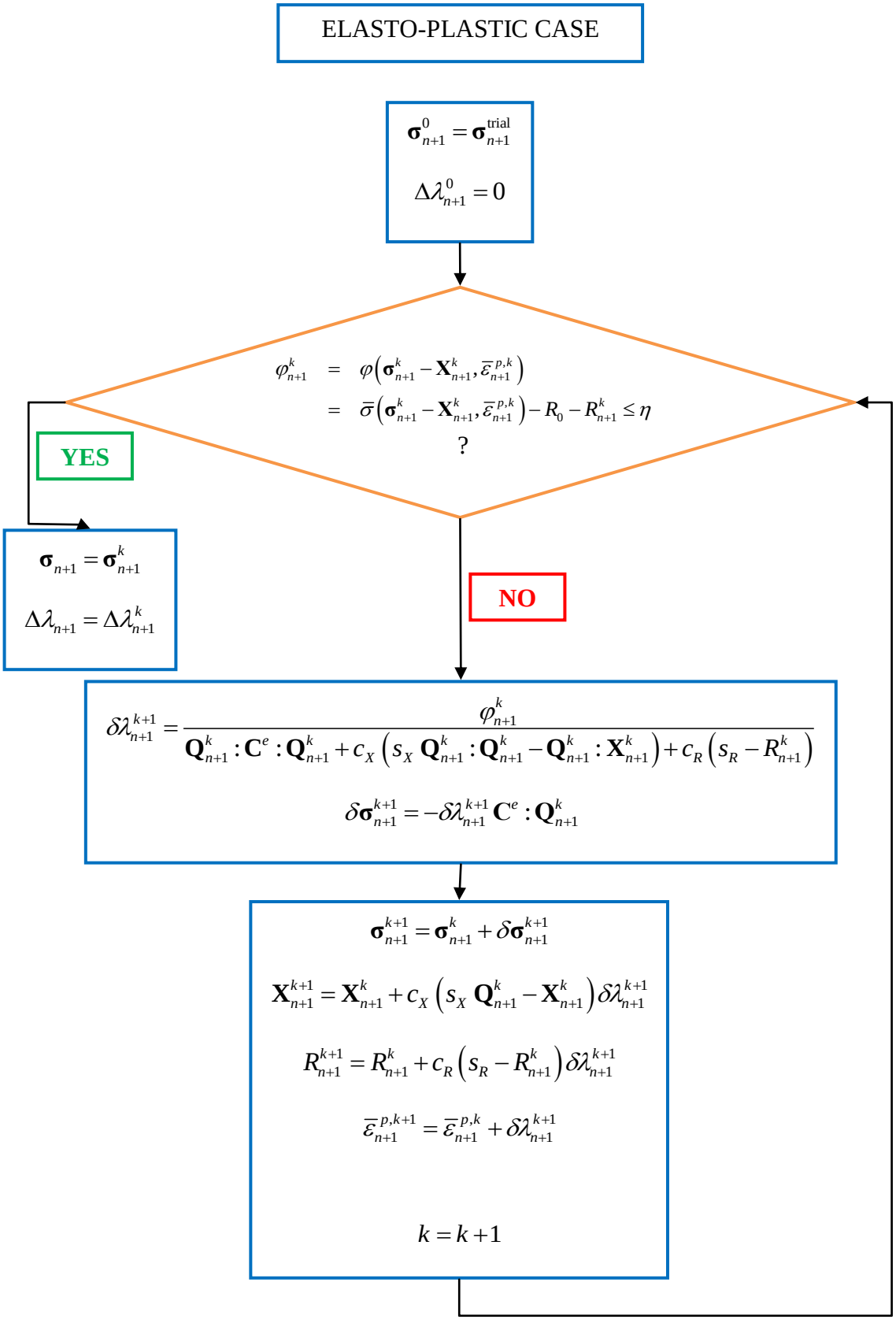

Figure 6-5 Flowchart of the integration scheme associating CPB06 yield criterion with a mixed hardening law when the material is in an elasto-plastic state

6.3. Evolution of CPB06 shape with the plastic work

For monotonic loadings, the general practice is to assume isotropic hardening and use a representative hardening curve (in the rolling or biaxial direction) as input for FE simulations. An isotropic hardening model, which implies a proportional expansion of the yield locus (see Section 3.2), is only valid if the material hardens at the same rate along every strain path. However, for hexagonal materials (see Lou *et al.* (2007); Nixon *et al.* (2010); etc.), the rate of hardening depends on the loading direction and/or its orientation even for the simplest loading paths. A methodology that allows describing directional hardening of hexagonal materials has been proposed by Plunkett *et al.* (2006). It consists in determining the anisotropy coefficients corresponding to several fixed levels of accumulated plastic deformation and then using piece-wise linear interpolation to obtain the yield surface corresponding to any level of accumulated plastic deformation. Another method that allows the description of distortional hardening occurring in proportional loading deformation through incorporation of explicit analytical laws for the variation of the anisotropy coefficients and strength differential parameters, was proposed by Ertürk *et al.* (2009) and used in conjunction with the orthotropic yield criterion of Cazacu and Barlat (2004).

In this section, the methodology of Plunkett *et al.* (2006) is used. The anisotropy coefficients and SD parameters are considered to evolve as a function of the plastic work per unit volume W^p. They are determined for several levels of W^p, *i.e.* $W^{p(1)} < \ldots < W^{p(j)} < \ldots < W^{p(m)}$, $j = 1 \ldots m$, where $W^{p(1)}$ corresponds to initial yielding and $W^{p(m)}$ corresponds to the highest level of plastic work attainable in all mechanical tests. Next, for each of the individual plastic work levels $W^{p(j)}$, $\bar{\sigma}$ is computed using Equation (6.16). To determine the yield surface corresponding to an intermediate level of plastic work ($W^{p(j)} \leq W^p \leq W^{p(j+1)}$), a linear interpolation is used:

$$\bar{\sigma} = \chi\left(W^p\right)\bar{\sigma}^{(j)} + \left(1 - \chi\left(W^p\right)\right)\bar{\sigma}^{(j+1)} \tag{6.37}$$

where χ is a weighting factor defined as:

$$\chi\left(W^p\right) = \frac{W^{p(j+1)} - W^p}{W^{p(j+1)} - W^{p(j)}} \tag{6.38}$$

such that $\chi\left(W^{p(j)}\right) = 1$ and $\chi\left(W^{p(j+1)}\right) = 0$.

If kinematic hardening is disregarded and isotropic hardening is described by Voce law (Equations (3.44) and (3.45)), the derivatives in Equation (6.30) are evaluated as follows:

$$\begin{aligned}
\mathbf{Q} &= \frac{\partial \varphi}{\partial \boldsymbol{\sigma}} = \frac{\partial \bar{\sigma}}{\partial \boldsymbol{\sigma}} = \chi\left(W^p\right)\frac{\partial \bar{\sigma}^{(j)}}{\partial \boldsymbol{\sigma}} + \left(1-\chi\left(W^p\right)\right)\frac{\partial \bar{\sigma}^{(j+1)}}{\partial \boldsymbol{\sigma}} \\
\frac{\partial \bar{\sigma}}{\partial \bar{\varepsilon}^p} &= \frac{\partial \chi}{\partial \bar{\varepsilon}^p}\bar{\sigma}^{(j)} - \frac{\partial \chi}{\partial \bar{\varepsilon}^p}\bar{\sigma}^{(j+1)} = \frac{\partial \chi}{\partial W^p}\frac{\partial W^p}{\partial \bar{\varepsilon}^p}\left(\bar{\sigma}^{(j)} - \bar{\sigma}^{(j+1)}\right) = \bar{\sigma}\frac{\bar{\sigma}^{(j+1)} - \bar{\sigma}^{(j)}}{W^{p(j+1)} - W^{p(j)}} \\
\frac{\partial Y}{\partial \bar{\varepsilon}^p} &= \frac{\partial R}{\partial \bar{\varepsilon}^p} = c_R\left(s_R - R\right)
\end{aligned} \tag{6.39}$$

If v denotes the derivative $\frac{\partial \bar{\sigma}}{\partial \bar{\varepsilon}^p}$, Equation (6.30) leads to:

$$\varphi_{n+1}^k - \delta\lambda_{n+1}^{k+1}\,\mathbf{Q}_{n+1}^k : \mathbf{C}^e : \mathbf{Q}_{n+1}^k + \left(v_{n+1}^k - c_R\left(s_R - R_{n+1}^k\right)\right)\delta\lambda_{n+1}^{k+1} = 0 \tag{6.40}$$

and thus:

$$\delta\lambda_{n+1}^{k+1} = \frac{\varphi_{n+1}^k}{\mathbf{Q}_{n+1}^k : \mathbf{C}^e : \mathbf{Q}_{n+1}^k + c_R\left(s_R - R_{n+1}^k\right) - v_{n+1}^k} \tag{6.41}$$

The compliance matrix is determined in a similar way as in the previous section and is given by:

$$\mathbf{C}^{ep} = \mathbf{C}^e - \frac{\left(\mathbf{C}^e : \mathbf{Q}\right)\otimes\left(\mathbf{C}^e : \mathbf{Q}\right)}{\mathbf{Q} : \mathbf{C}^e : \mathbf{Q} + c_R\left(s_R - R\right) - v} \tag{6.42}$$

Figure 6-6 and Figure 6-7 show the flowchart of the integration scheme described in this section.

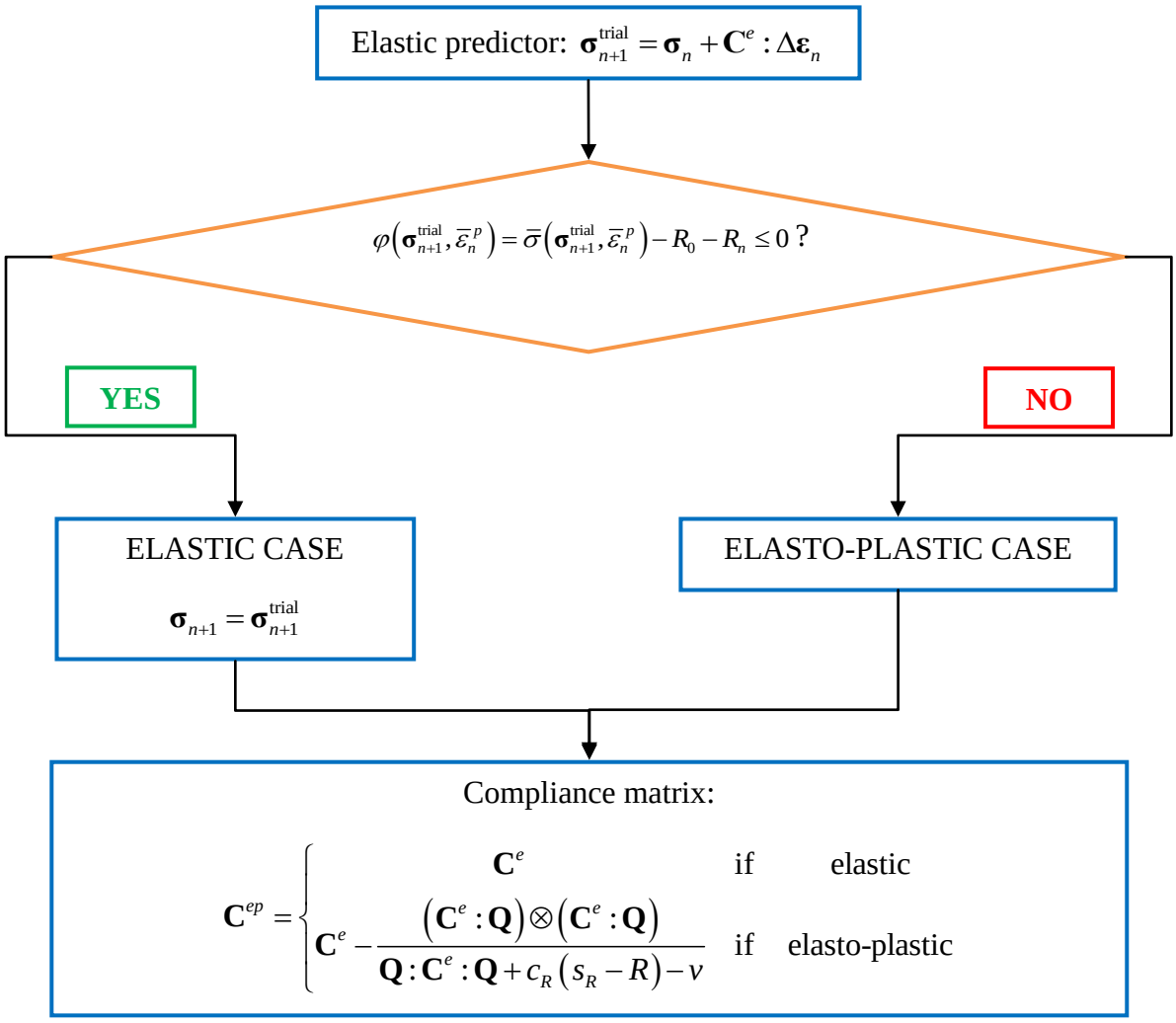

Figure 6-6 General flowchart of the integration scheme considering an evolution of the yield locus shape

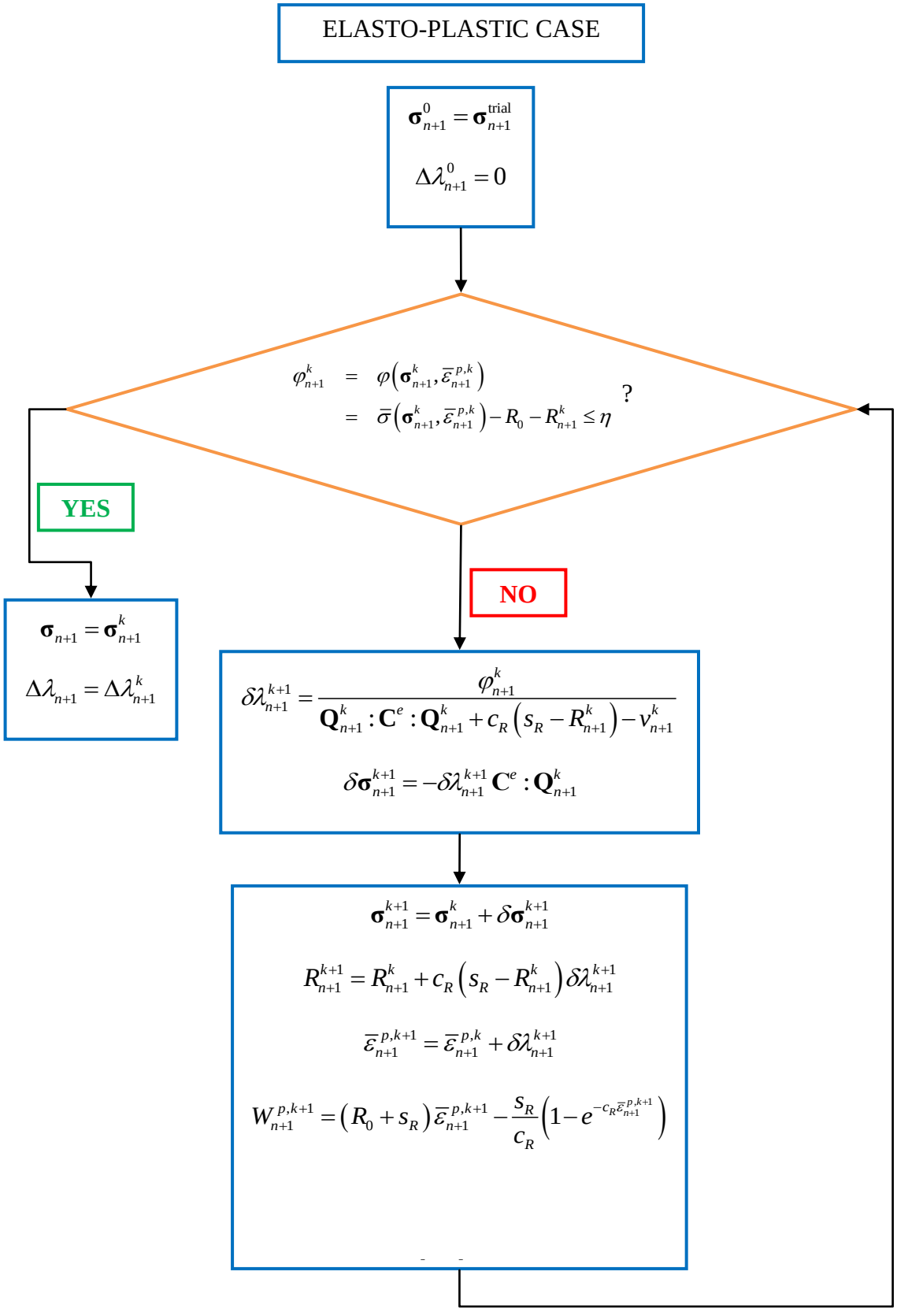

Figure 6-7 Flowchart of the integration scheme considering an evolution of the yield locus shape when the material is in an elasto-plastic state

6.4. Conclusion

The two integration schemes detailed in Sections 6.2 and 6.3 are implemented into the non-linear finite element code LAGAMINE, respectively in CAZACU2 and CAZACUW subroutines. The choice of the model is specified from an integer variable in the input file which is read by the preprocessor. This variable is fixed to 521 in the case of CPB06ex*n* yield criteria associated to a mixed Voce isotropic – Armstrong-Frederick kinematic law and 524 in the case of CPB06ex*n* associated to the formulation taking into account the evolution of the shape with the plastic work. Simulations with one element subjected to a simple strain path (tension, compression, simple shear, …) were performed in order to validate both implementations and to check the computation time and the convergence.

Chapter 7 Parameter identifications for the description of Ti6Al4V mechanical behavior

---

Chapter 5 analyses the results of the experimental tests carried out on Ti6Al4V while Chapter 6 introduces the different constitutive models chosen to describe the material behavior and implemented into the FE code LAGAMINE. The next step consists in identifying the parameters included in the different models. In this chapter, the two optimization methods used to determine these parameters, namely the classical simulated annealing algorithm and the inverse method, are first described. Then several parameter identifications are performed in order to determine which function among the CPB06ex*n* criteria family is required to represent the yield locus of the selected Ti6Al4V alloy. Finally the last section deals with the optimization of the parameters involved in three hardening modelings, namely the Voce isotropic hardening law, a mixed formulation combining Voce isotropic and kinematic hardening laws, and a formulation taking into account a shape evolution of the yield locus (distortional hardening).

7.1. Description of the optimization methods used for the parameter identifications

7.1.1. Classical simulated annealing method

7.1.1.1. Introduction

Constitutive laws may involve a lot of parameters. A significant work in the characterization of a material is to determine the set of parameters which fit at best the experimental results. In general, the parameters are identified by an optimization procedure. Classical optimization

methods are usually based on a gradient descent: gradient method, conjugate gradient, Newton, quasi Newton, Levenberg-Marquardt, … (a literature review concerning the optimization methods can be found in Kleinermann (2000)). They are very efficient when applied to optimization problems of convex objective functions. However these methods present two main drawbacks:

- They require the assessment of the objective function gradient at each iteration, which assumes the existence of the gradient and, as a consequence, the differentiability of the function.
- The convergence to the global minimum (resp. maximum) is not ensured. Indeed, the gradient is a vector field that locally indicates the direction of the highest rate of change. When the function has only one minimum (resp. maximum), gradient methods work very well. However, in the case of functions with several local minima (resp. maxima), the solution provided by the algorithm might not be the global optimum if the initial guess is wrongly chosen. The problem can be solved using several times the optimization method with different initial guesses, but this solution is not very effective in practice.

The classical simulated annealing (CSA) algorithm is an iterative global optimization method that distinguishes between different local minima (resp. maxima). This method is based on Metropolis' works (Metropolis *et al.* (1953); Hastings (1970)). At each iteration, a trial point is generated from the previous one. If this point improves the objective function to be optimized, it is automatically accepted. If it does not, it can however be accepted with a probability p defined as follows:

$$p = \exp\left(-\frac{\left|E_{n+1} - E_n\right|}{T}\right) \tag{7.1}$$

where E_i stands for the value of the objective function at step i and T is a fictious temperature. The expression (7.1) shows that upwards (resp. downwards) transitions are more likely to take place for large values of T and/or for small differences between two consecutives values of the objective function. After a fixed number of transitions at a constant temperature, the latter is decreased so that less upwards (resp. downwards) transitions are allowed as the algorithm processes, which eventually leads to the determination of the global minimum (resp. maximum). The acceptance of such a solution allows exploring a larger part of the state space and prevents to freeze the system on a local optimum (see Figure 7-1). In contrast to gradient methods, the CSA algorithm only requires the evaluation of the objective function for each trial point. In the CSA method, three major parameters can be adjusted:

- the initial temperature T_0;
- the temperature reduction rate factor α;
- the maximal number of transitions $N_t^{\max}$.

A too low initial temperature will not allow exploring the whole state space and might converge to a local optimum, whereas a too high temperature will uselessly increase the computation time. The reduction factor is usually chosen between 0.9 and 0.99. A too fast decrease might freeze the system into a local optimum. Finally, a common rule is to fix the maximal

number of transitions to at least 100 times the number of parameters. More details concerning the optimization by simulated annealing method can be found in Kirkpatrick *et al.* (1983).

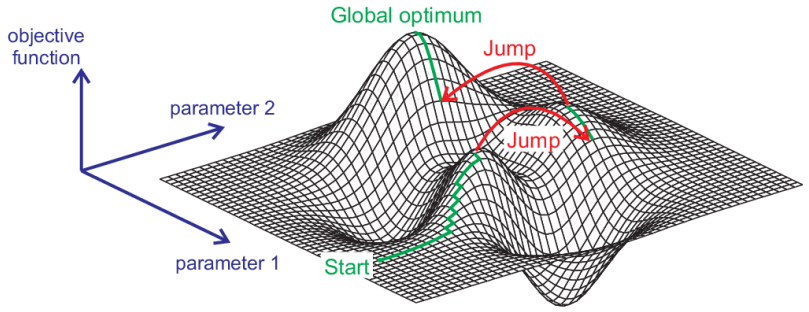

Figure 7-1 Principle of the simulated annealing method applied to the determination of the global maximum: downwards transitions are allowed in order to prevent the system from freezing into a local maximum

7.1.1.2. Definition of the error functions

Optimization methods require the definition of an *objective function* or *error function*. For the parameter identifications using the classical simulated annealing method, two functions E_1 and E_2 are considered and defined as follows:

$$E_1 = \sum_{i=1}^{N_d} \eta_i \, e_i^2 \tag{7.2}$$

$$E_2 = \sum_{i=1}^{N_d} e_i^2 \tag{7.3}$$

where:

- N_d is the number of experimental data used for the identifications;
- η_i are weight factors;
- e_i are the relative errors between the experimental data and the corresponding numerical values, *i.e.*:

$$e_i = \frac{\left(\text{experimental value}\right)_i - \left(\text{numerical value}\right)_i}{\left(\text{experimental value}\right)_i} \tag{7.4}$$

E_1 represents the error function used for each identification. However this function is not appropriate to compare the results. Indeed, since the formulation of E_1 includes weigth factors which are modified from one identification to another, the optimal values given by the algorithm actually correspond to different functions. For this reason, E_2 is simultaneously computed in order to compare and analyse the theoretical results using the same mathematical quantity.

The experimental data considered in the identifications are yield stresses and tensile *r*-ratios. The relative errors are defined as follows in the case of yield stresses:

$$e_i = \frac{\left(\sigma_\theta^S\right)^{\text{num}} - \left(\sigma_\theta^S\right)^{\text{exp}}}{\left(\sigma_\theta^S\right)^{\text{exp}}} \tag{7.5}$$

In the case of tensile *r*-ratios, they are determined as follows:

$$e_i = \frac{\left(r_\theta^T\right)^{\text{num}} - \left(r_\theta^T\right)^{\text{exp}}}{\left(r_\theta^T\right)^{\text{exp}}} \tag{7.6}$$

The superscript S in Equation (7.5) denotes the stress state ($S = T$ for tension, $S = C$ for compression, $S = PS$ for plane strain, $S = SSH$ for simple shear) while the subscript θ represents the loading direction with respect to RD. A remark has to be nevertheless underlined concerning the data in plane strain. As explained in Section 5.2.5, only one component of the stress tensor can be identified in the plane strain tests. At the onset of plasticity, it is possible to assess the other component using Hooke's law. At larger plastic strains, this component cannot be determined. However, the strain along the direction transverse to the loading direction is zero, which means that the *r*-ratio is also zero. When identifying the yield locus for these levels of large deformation, the error corresponding to the experimental data in plane strain is thus chosen as follows:

$$e_i = \left(r_\theta^{PS}\right)^{\text{num}} - \left(r_\theta^{PS}\right)^{\text{exp}} = \left(r_\theta^{PS}\right)^{\text{num}} \tag{7.7}$$

since $\left(r_\theta^{PS}\right)^{\text{exp}} = 0$.

7.1.1.3. Optimization parameters

The CSA algorithm requires the following parameters:

- the number of parameters N_p to be identified;
- the maximum number of transitions $N_t^{\max}$;
- the number of weight factors (which is identical to the number of experimental data N_d used for the identifications in this study) and their value;
- the initial temperature of the system T_0;
- the temperature reduction factor α: if i denotes the *i*-th iteration, the temperature T_{i+1} at the iteration $i+1$ is given by $T_{i+1} = \alpha T_i$;
- the error tolerance ε for termination: if the final function values from the last four temperatures differ from the corresponding value at the current temperature by less than ε and the final function value at the current temperature differs from the current optimal function value by less than ε, the execution is stopped;
- the lower and upper bounds for the allowable solution parameters;
- the initial guess for the parameters to be optimized;

For each identification presented in the following sections, $N_t^{\max}$, N_d, T_0, α and ε are kept constant. Their values are given in Table 7-1. Concerning the other parameters, the latter will gradually be defined.

$N_t^{\max}$	2.0×10^9
N_d	31
T_0	2.0×10^9
α	0.99
ε	10^{-4}

Table 7-1 Constant CSA parameters used for the identifications

7.1.2. Inverse method (OPTIM)

7.1.2.1. Introduction

The inverse method consists in determining several parameters of a complex material law with the help of a finite element code. The principle of this method is the following one: a set of experimental tests whose results are sensitive to the material parameters to fit are selected. These tests are then simulated using an initial guess which can arbitrarily be chosen. Nevertheless it has to be noted that the optimization process will be faster if the initial guess is close to the solution. The numerical results are compared with the experimental curves and, if the accuracy defined by the user is not achieved, the parameters are iteratively adjusted with an optimization algorithm (Figure 7-2). The advantage of this method is that complex tests with heterogeneous stress and strain states can be chosen to identify the parameters.

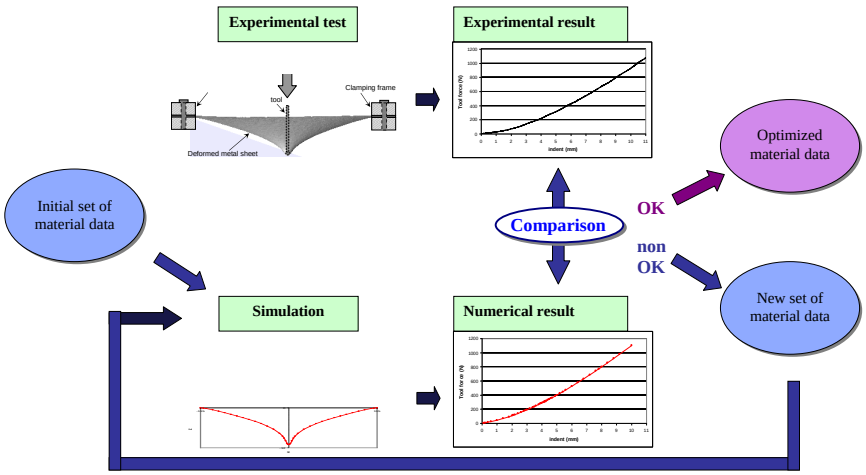

Figure 7-2 Parameter identification by inverse method (scheme from the oral presentation of Bouffioux et al. (2008))

A home-made code called OPTIM and developed by V. Mathonet based on the main Levenberg-Marquardt algorithm (Mathonet (2003)) will be used in this work to identify the hardening parameters in Voce isotropic law and Armstrong-Frederick kinematic law. This optimization code is coupled with the finite element code LAGAMINE and has already been

applied in various investigations (Florès (2005), Henrard (2008), Lequesne (2009), Bouffioux *et al.* (2011)).

7.1.2.2. Error computation

A first definition of the error function could be the following one:

$$E = \sqrt{\sum_{i=1}^{n_{\text{tot}}} \left(u_i^{\text{EF}} - u_i^{\text{REF}} \right)^2} \tag{7.8}$$

where:

- i denotes a point among the n_{tot} points belonging to the reference curve;
- u_i^{REF} and u_i^{EF} are respectively the *y*-coordinates of the reference and numerical curves associated to the n_{tot} points (see Figure 7-3).

The function E represents the square root of the sum of the squared deviations. In the case of a single curve, this definition is sufficient to be used for the optimization. When several curves with different orders of magnitude are taken into account, it is required to normalize the data in order to prevent the disruption of the optimization. Then the error function becomes:

$$\begin{aligned} E &= \sqrt{\sum_{i=1}^{n_{\text{tot}}} \left(\frac{u_i^{\text{EF}} - u_i^{\text{REF}}}{u_i^{\text{REF}}} \right)^2} \quad \text{if} \quad \left| u_i^{\text{REF}} \right| > \text{tolerance} \\ E &= \sqrt{\sum_{i=1}^{n_{\text{tot}}} \left(u_i^{\text{EF}} - u_i^{\text{REF}} \right)^2} \quad \text{if} \quad \left| u_i^{\text{REF}} \right| < \text{tolerance} \end{aligned} \tag{7.9}$$

where a tolerance is defined by the user.

Since the finite element code does not exactly compute the numerical curve u^{EF} at the same points defining the reference curve, OPTIM determines the common domain of the two curves $\left[x_{\min}, x_{\max} \right]$ which is divided into n_{tot} points regularly distributed (Figure 7-3). For each value x_i, u_i^{REF} and u_i^{EF} are then obtained by linear interpolation.

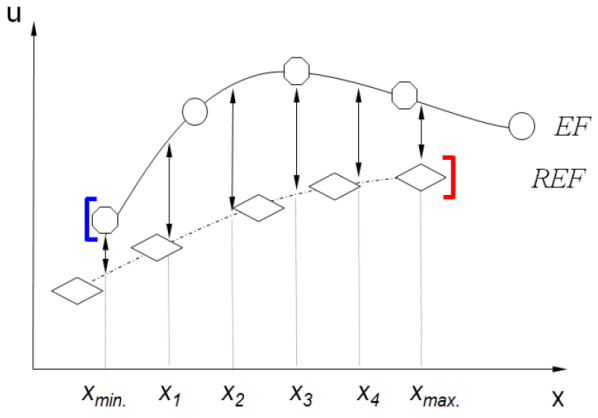

Figure 7-3 Comparison between the finite element (EF) and reference (REF) curves and determination of the common domain

7.1.2.3. Sensitivity analysis

One of the most important parts in the inverse method consists in determining the sensitivity matrix. The latter represents the sensitivity of the results to the different parameters. The sensitivity S of u with respect to the parameter p_i is defined by:

$$S_{p_i} = \frac{u_{p_i+dp_i} - u_{p_i-dp_i}}{2.dp_i} \tag{7.10}$$

with $dp_i = p_i.\eta$ the absolute value of the perturbation and η a perturbation factor. For each step of the simulation, the results are computed with the initial parameters $(p_1,\ldots, p_i,\ldots, p_k)$ and, for each parameter p_i, with $(p_1,\ldots, p_i + dp_i,\ldots, p_k)$ and $(p_1,\ldots, p_i - dp_i,\ldots, p_k)$.

7.2. Identification of the initial Ti6Al4V yield locus using the classical simulated annealing method

7.2.1. Identifications of the parameters in CPB06 yield criterion

The equivalent stress $\bar{\sigma}$ associated to the CPB06 yield criterion (see Equation (6.16)) involves 11 parameters, namely the degree of homogeneity a, the strength differential parameter k and the anisotropy coefficients C_{11}, C_{12}, C_{13}, C_{22}, C_{23}, C_{33}, C_{44}, C_{55}, C_{66}. As $\bar{\sigma}$ is homogeneous of degree one in its arguments, the coefficients C_{ij} can be replaced by βC_{ij}, β being any positive number, without changing the expression of the yield function. Hence, the anisotropy coefficients can be scaled by C_{11}, or in other words C_{11} can be fixed to 1. In addition, as the studied material is a "thin" sheet, it is only possible to easily determine one of the shear coefficients (*i.e.* C_{44}, C_{55}, C_{66}) and it is thus assumed in the identifications that $C_{44} = C_{55} = C_{66}$. Finally, it has to be noted that the degree of homogeneity is fixed to 2 because of the nearly elliptical shape of the initial yield locus for Ti6Al4V (see Figure 5-27). The number of parameters to be optimized is reduced in this way to 7, namely k, C_{12}, C_{13}, C_{22}, C_{23}, C_{33} and C_{66}. In order to identify them, it is required to use seven experimental data, at least. Generally, the yield stresses and/or *r*-ratios in tension along RD, 45° and TD are considered. However, data in compression are also needed in the case of hcp materials since they display the asymmetry between tension and compression.As a lot of results were obtained with the tests carried out on Ti6Al4V, several parameter optimizations using different experimental data sets are performed with the aim to study the effect of these different selections on the accuracy of the results. The complete list of the identifications and the data which are associated is given in Table 7-2: a green (respectively red) symbol means that the experimental value is (respectively is not) taken into account for the optimization, in other words $\eta_i = 1$ (respectively $\eta_i = 0$).

		IDENTIFICATION NUMBER															
		IDENT1	IDENT2	IDENT3	IDENT4	IDENT5	IDENT6	IDENT7	IDENT8	IDENT9	IDENT10	IDENT11	IDENT12	IDENT13	IDENT14	IDENT15	IDENT16
EXPERIMENTAL DATA	σ_0^T	✓	✓	✓	✓	✓	✓	✓	✓	✓	✓	✓	✓	✓	✓	✓	✓
	σ_{10}^T	✗	✗	✗	✗	✓	✓	✓	✓	✗	✗	✗	✗	✓	✓	✓	✓
	σ_{20}^T	✗	✗	✗	✗	✓	✓	✓	✓	✗	✗	✗	✗	✓	✓	✓	✓
	σ_{30}^T	✗	✗	✗	✗	✓	✓	✓	✓	✗	✗	✗	✗	✓	✓	✓	✓
	σ_{40}^T	✗	✗	✗	✗	✓	✓	✓	✓	✗	✗	✗	✗	✓	✓	✓	✓
	σ_{45}^T	✓	✓	✓	✓	✓	✓	✓	✓	✓	✓	✓	✓	✓	✓	✓	✓
	σ_{50}^T	✗	✗	✗	✗	✓	✓	✓	✓	✗	✗	✗	✗	✓	✓	✓	✓
	σ_{60}^T	✗	✗	✗	✗	✓	✓	✓	✓	✗	✗	✗	✗	✓	✓	✓	✓
	σ_{70}^T	✗	✗	✗	✗	✓	✓	✓	✓	✗	✗	✗	✗	✓	✓	✓	✓
	σ_{80}^T	✗	✗	✗	✗	✓	✓	✓	✓	✗	✗	✗	✗	✓	✓	✓	✓
	σ_{90}^T	✓	✓	✓	✓	✓	✓	✓	✓	✓	✓	✓	✓	✓	✓	✓	✓
	r_0^T	✓	✓	✓	✓	✓	✓	✓	✓	✓	✓	✓	✓	✓	✓	✓	✓
	r_{10}^T	✗	✗	✗	✗	✗	✗	✗	✗	✓	✓	✓	✓	✓	✓	✓	✓
	r_{20}^T	✗	✗	✗	✗	✗	✗	✗	✗	✓	✓	✓	✓	✓	✓	✓	✓
	r_{30}^T	✗	✗	✗	✗	✗	✗	✗	✗	✓	✓	✓	✓	✓	✓	✓	✓
	r_{40}^T	✗	✗	✗	✗	✗	✗	✗	✗	✓	✓	✓	✓	✓	✓	✓	✓
	r_{45}^T	✓	✓	✓	✓	✓	✓	✓	✓	✓	✓	✓	✓	✓	✓	✓	✓
	r_{50}^T	✗	✗	✗	✗	✗	✗	✗	✗	✓	✓	✓	✓	✓	✓	✓	✓
	r_{60}^T	✗	✗	✗	✗	✗	✗	✗	✗	✓	✓	✓	✓	✓	✓	✓	✓
	r_{70}^T	✗	✗	✗	✗	✗	✗	✗	✗	✓	✓	✓	✓	✓	✓	✓	✓
	r_{80}^T	✗	✗	✗	✗	✗	✗	✗	✗	✓	✓	✓	✓	✓	✓	✓	✓
	r_{90}^T	✓	✓	✓	✓	✓	✓	✓	✓	✓	✓	✓	✓	✓	✓	✓	✓
	σ_0^C	✓	✓	✓	✓	✓	✓	✓	✓	✓	✓	✓	✓	✓	✓	✓	✓
	σ_{45}^C	✓	✓	✓	✓	✓	✓	✓	✓	✓	✓	✓	✓	✓	✓	✓	✓
	σ_{90}^C	✓	✓	✓	✓	✓	✓	✓	✓	✓	✓	✓	✓	✓	✓	✓	✓
	σ_0^{PS}	✗	✓	✗	✓	✗	✓	✗	✓	✗	✓	✗	✓	✗	✓	✗	✓
	σ_{45}^{PS}	✗	✓	✗	✓	✗	✓	✗	✓	✗	✓	✗	✓	✗	✓	✗	✓
	σ_{90}^{PS}	✗	✓	✗	✓	✗	✓	✗	✓	✗	✓	✗	✓	✗	✓	✗	✓
	σ_0^{SSH}	✗	✗	✓	✓	✗	✗	✓	✓	✗	✗	✓	✓	✗	✗	✓	✓
	σ_{45}^{SSH}	✗	✗	✓	✓	✗	✗	✓	✓	✗	✗	✓	✓	✗	✗	✓	✓
	σ_{90}^{SSH}	✗	✗	✓	✓	✗	✗	✓	✓	✗	✗	✓	✓	✗	✗	✓	✓

Table 7-2 List of the experimental data used in the different identifications performed to identify the initial Ti6Al4V yield locus described by the CPB06 yield criterion: a green symbol means that the weight factor is fixed to 1 while a red symbol corresponds to a weight factor equal to zero.

It can be observed from Table 7-2 that the tensile yield stresses, tensile *r*-ratios and compressive yield stresses along RD, 45°-direction and TD are used for all the optimizations. In addition, four groups of identifications can be highlighted:

- A first group (from **IDENT1** to **IDENT4**) for which only the data in tension along RD, 45°-direction and TD (3 yield stresses and 3 *r*-ratios) are taken into account.
- A second group (from **IDENT5** to **IDENT8**) for which all the yield stresses in tension and the *r*-ratios along RD, 45°-direction and TD (11 yield stresses and 3 *r*-ratios) are taken into account.
- A third group (from **IDENT9** to **IDENT12**) for which the yield stresses in tension along RD, 45°-direction and TD, and all the *r*-ratios (3 yield stresses and 11 *r*-ratios) are taken into account.
- The last group (from **IDENT13** to **IDENT 16**) for which all the data in tension (11 yield stresses and 11 *r*-ratios) are taken into account.

It has to be noted that the identifications within a group differ from one another in that the yield stresses in plane strain and/or in simple shear are considered or not.

For all these identifications, the initial guess and the bounds of the parameters are fixed as shown in Table 7-3. It has to be noticed that:

- The initial guess for the anisotropy coefficients correspond to the values associated to the isotropic case.
- The strength differential parameter k was assessed as follows: by means of Equation (3.16) and Equation (3.17) which are only valid for the isotropic formulation of CPB06 (see Section 3.1.1, Equations (3.15) to (3.17)), three different values denoted k_{RD}, k_{45} and k_{TD} were determined using the experimental data in tension and compression along RD, 45° and TD, respectively. The initial guess was then chosen as the average of these values, *i.e.* $(1/3).(k_{RD}+k_{45}+k_{TD})$. As for the bounds, they were fixed to keep $k<0$ since the yield stresses in compression are higher than the ones in tension.

	k	C_{12}	C_{13}	C_{22}	C_{23}	C_{33}	C_{66}
Lower bound	-1.0	-5.0	-5.0	-5.0	-5.0	-5.0	-5.0
Upper bound	-0.001	5.0	5.0	5.0	5.0	5.0	5.0
Initial guess	-0.08	0.0	0.0	1.0	0.0	1.0	1.0

Table 7-3 Initial guess and bounds used for the parameter identifications associated to CPB06 yield criterion

Table 7-4 gives the values of the error functions E_1 and E_2 with respect to the identification number. As mentioned before, E_1 does not represent a good indicator to analyze the accuracy of the different optimizations since the function depends on weight factors, which is not the case using E_2.

Identification number	E_1	E_2
IDENT1	1.35×10^{-2}	17.0×10^{-2}
IDENT2	1.76×10^{-2}	16.1×10^{-2}
IDENT3	1.65×10^{-2}	14.1×10^{-2}
IDENT4	2.61×10^{-2}	14.0×10^{-2}
IDENT5	2.12×10^{-2}	17.4×10^{-2}
IDENT6	2.38×10^{-2}	17.2×10^{-2}
IDENT7	2.85×10^{-2}	7.26×10^{-2}
IDENT8	2.81×10^{-2}	17.6×10^{-2}
IDENT9	3.84×10^{-2}	6.69×10^{-2}
IDENT10	8.61×10^{-2}	15.7×10^{-2}
IDENT11	4.99×10^{-2}	5.44×10^{-2}
IDENT12	4.23×10^{-2}	4.54×10^{-2}
IDENT13	4.72×10^{-2}	5.35×10^{-2}
IDENT14	4.84×10^{-2}	5.54×10^{-2}
IDENT15	4.17×10^{-2}	4.47×10^{-2}
IDENT16	5.42×10^{-2}	5.42×10^{-2}

Table 7-4 Values of the error functions E_1 and E_2 for each identification

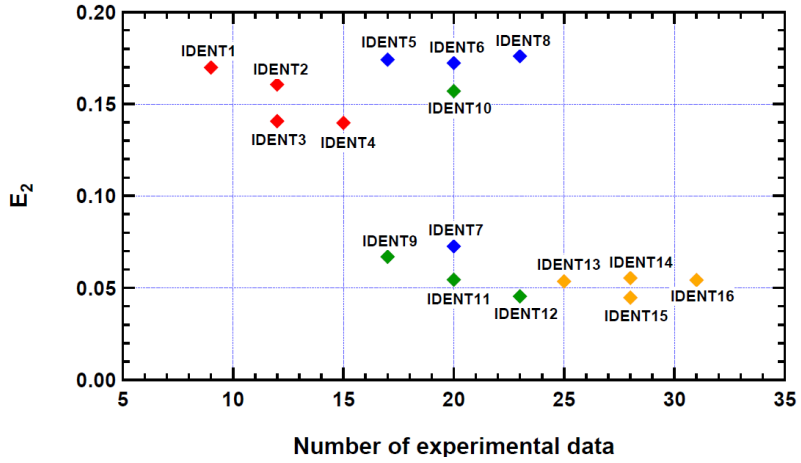

Figure 7-4 Error function E_2 according to the number of experimental used in each identification

Figure 7-4 compares the identifications in terms of the E_2-error function value and the number of experimental data used for the optimization. By observing the graph, it can be concluded that:

- Even if seven experimental results are theoretically enough to identify the strength differential parameter and the anisotropy coefficients, adding more data can overall improve the quality of the optimization. This can be observed in Figure 7-5 where the theoretical results according to IDENT15 (corresponding to the lower E_2-error) and IDENT3 (taking into account the data in simple shear as IDENT15) are compared with the experimental data.

- Excepted for IDENT7 and IDENT10, the points associated to a same group of identifications are quite close to each other. In addition, it can be observed that taking into account the complete distribution of the *r*-ratios in the identification provides better results.

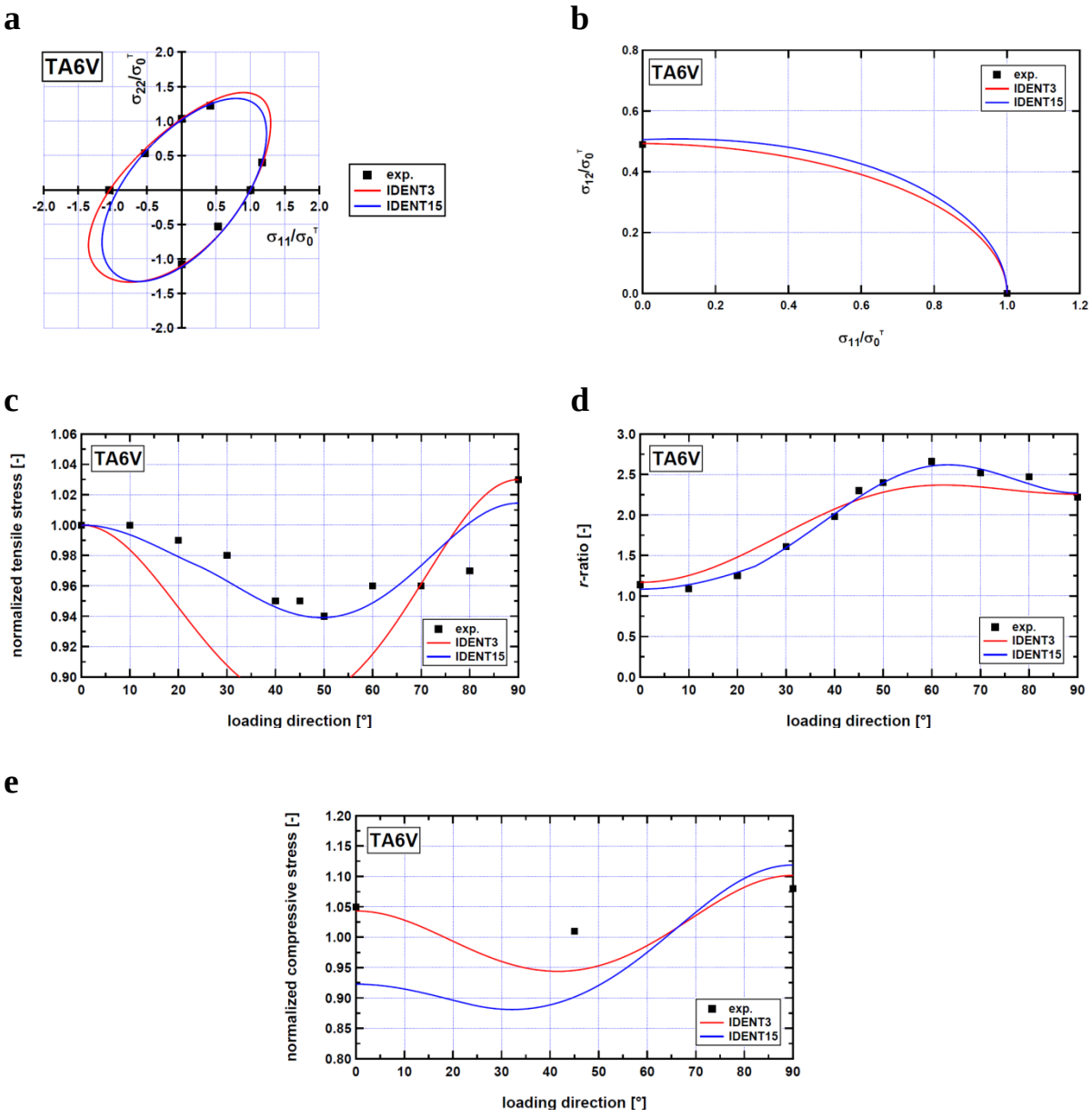

Figure 7-5 Comparison of the theoretical results according to IDENT3 and IDENT15 with the experimental data: (a) yield locus in the biaxial plane ($\sigma_{12}=0$); (b) yield locus in the plane $\sigma_{11}-\sigma_{12}$ ($\sigma_{22}=0$); (c) anisotropy in tensile yield stresses; (d) anisotropy in tensile r-ratios; (e) anisotropy in compressive yield stresses.

Figure 7-6 shows the theoretical results according to IDENT13, IDENT14, IDENT15 and IDENT16 compared with the experimental data. The associated parameters are given in Table 7-5. It can be noticed that the theoretical curves essentially differ from each other in terms of the yield locus shape in the third quadrant of the biaxial plane and in terms of the anisotropy in tensile and compressive yield stresses. The differences are explained by the low quantity of data in compression (yield stresses along three loading directions) compared to what is available in tension (eleven yield stresses and *r*-ratios along eleven loading directions). In order to fix the shape of the yield locus in the third quadrant, it will thus be necessary in future inves-

tigations to characterize the material under strain paths allowing the determination of other points in this zone, for instance uniaxial compression along more than three directions with respect to RD, compressive plane strain or equibiaxial compression. In the case of a sheet as the studied material, the first suggestion is the easier to conduct, in particular using the experimental device described in Section 4.1.1.2. It can also be noted that the CPB06 criterion is not able to capture the tension-compression asymmetry displayed by Ti6Al4V (see Figure 7-6(c) and Figure 7-6(e)), which means that additional parameters are needed to improve the modeling of the yield locus. The next section is dedicated to the identification of the parameters involved in three extensions of the CPB06 criterion (namely CPB06ex2, CPB06ex3 and CPB06ex4) and to determine the best compromise in terms of accuracy and computation time.

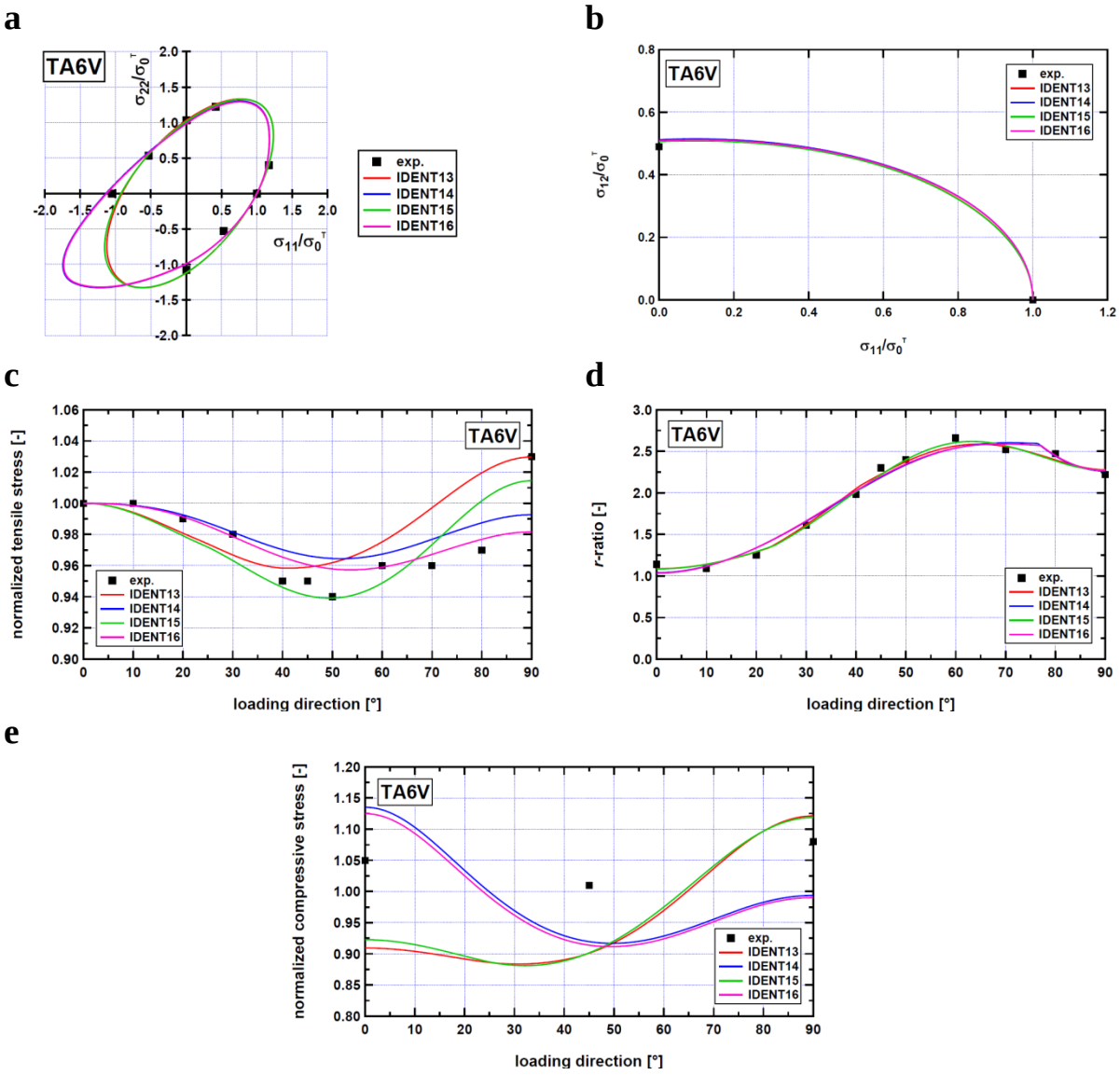

Figure 7-6 Comparison of the theoretical results according to IDENT13, IDENT14, IDENT15 and IDENT16 with the experimental data: (a) yield locus in the biaxial plane ($\sigma_{12}=0$); (b) yield locus in the plane $\sigma_{11}-\sigma_{12}$ ($\sigma_{22}=0$); (c) anisotropy in tensile yield stresses; (d) anisotropy in tensile r-ratios; (e) anisotropy in compressive yield stresses.

	k	C_{12}	C_{13}	C_{22}	C_{23}	C_{33}	C_{66}
IDENT13	-0.0475	1.9098	1.8740	2.3730	3.5427	2.3499	1.5284
IDENT14	-0.2502	-1.4038	1.5750	1.8384	-0.3233	-1.9125	-3.4915
IDENT15	-0.0550	1.5898	3.2530	4.3248	2.6166	2.0370	-2.2656
IDENT16	-0.2501	-2.3785	1.8377	2.2736	-0.8232	-3.0901	4.9610
$a=2$, $C_{11}=1.0$							

Table 7-5 Yield function CPB06 coefficients for IDENT13, IDENT14, IDENT15 and IDENT16 based on the experimental data given in Table 7-2

7.2.2. Identifications of the parameters in CPB06ex2, CPB06ex3 and CPB06ex4 yield criteria

As explained in the previous section, the CPB06 model is not convenient for the representation of the Ti6Al4V yield locus. Nevertheless the latter can be improved by introducing additional linear transformations in the criterion (see Section 3.1.2). Several identifications were performed in order to determine the parameters involved in the CPB06ex2, CPB06ex3 and CPB06ex4 yield criteria using the experimental data given in Table 7-6.

		IDENTIFICATION NUMBER						**IDENTIFICATION NUMBER**			
		IDENT1ex2 IDENT1ex3 IDENT1ex4	**IDENT2ex2 IDENT2ex3 IDENT2ex4**	**IDENT3ex2 IDENT3ex3 IDENT3ex4**	**IDENT4ex2 IDENT4ex3 IDENT4ex4**			**IDENT1ex2 IDENT1ex3 IDENT1ex4**	**IDENT2ex2 IDENT2ex3 IDENT2ex4**	**IDENT3ex2 IDENT3ex3 IDENT3ex4**	**IDENT4ex2 IDENT4ex3 IDENT4ex4**
		①	②	③	④			①	②	③	④
EXPERIMENTAL DATA	σ_0^T	✓	✓	✓	✓	**EXPERIMENTAL DATA**	r_{45}^T	✓	✓	✓	✓
	σ_{10}^T	✓	✓	✓	✓		r_{50}^T	✓	✓	✓	✓
	σ_{20}^T	✓	✓	✓	✓		r_{60}^T	✓	✓	✓	✓
	σ_{30}^T	✓	✓	✓	✓		r_{70}^T	✓	✓	✓	✓
	σ_{40}^T	✓	✓	✓	✓		r_{80}^T	✓	✓	✓	✓
	σ_{45}^T	✓	✓	✓	✓		r_{90}^T	✓	✓	✓	✓
	σ_{50}^T	✓	✓	✓	✓		σ_0^C	✓	✓	✓	✓
	σ_{60}^T	✓	✓	✓	✓		σ_{45}^C	✓	✓	✓	✓
	σ_{70}^T	✓	✓	✓	✓		σ_{90}^C	✓	✓	✓	✓
	σ_{80}^T	✓	✓	✓	✓		σ_0^{PS}	×	✓	×	✓
	σ_{90}^T	✓	✓	✓	✓		σ_{45}^{PS}	×	✓	×	✓
	r_0^T	✓	✓	✓	✓		σ_{90}^{PS}	×	✓	×	✓
	r_{10}^T	✓	✓	✓	✓		σ_0^{SSH}	×	×	✓	✓
	r_{20}^T	✓	✓	✓	✓		σ_{45}^{SSH}	×	×	✓	✓
	r_{30}^T	✓	✓	✓	✓		σ_{90}^{SSH}	×	×	✓	✓
	r_{40}^T	✓	✓	✓	✓						

Table 7-6 List of the experimental data used in the four different identifications performed to identify the initial Ti6Al4V yield locus described by the CPB06ex2, CPB06ex3 and CPB06ex4 yield criteria: a green symbol means that the weight factor is fixed to 1 while a red symbol corresponds to a weight factor equal to zero.

Every identification is labeled by a number which has the following structure: IDENT*i*ex*n*, where *n* reminds the number of linear transformations included in the associated criterion while *i* is used as an identifier.

All the identifications were completed using the initial guess and the bounds given in Table 7-7. It has to be noted that the strength differential parameters (k, k', k'', k''') and their sign cannot be assessed as in Section 7.2.1 when more than one linear transformation are considered, which explains the changes for the upper bound and the initial guess compared to Table 7-3.

	k, k', k'', k'''	C_{12}, C'_{12}, C''_{12}, C'''_{12}	C_{13}, C'_{13}, C''_{13}, C'''_{13}	C_{22}, C'_{22}, C''_{22}, C'''_{22}	C_{23}, C'_{23}, C''_{23}, C'''_{23}	C_{33}, C'_{33}, C''_{33}, C'''_{33}	C_{66}, C'_{66}, C''_{66}, C'''_{66}
Lower bound	-1.0	-5.0	-5.0	-5.0	-5.0	-5.0	-5.0
Upper bound	1.0	5.0	5.0	5.0	5.0	5.0	5.0
Initial guess	0.0	0.0	0.0	1.0	0.0	1.0	1.0

Table 7-7 Initial guess and bounds used for the parameter identifications associated to CPB06ex2, CPB06ex3 and CPB06ex4 yield criteria

Table 7-8 to Table 7-10 list the identification results, namely the values of the material parameters for Ti6Al4V using CPB06ex2, CPB06ex3 and CPB06ex4 yield criteria, respectively. Figure 7-7 to Figure 7-9 show the associated biaxial plane projections $\sigma_{11}-\sigma_{22}$ and $\sigma_{11}-\sigma_{12}$ (elements a and b, respectively) of the yield loci, the anisotropy of the tensile and compressive yield stresses (elements c and e, respectively) and the anisotropy of the tensile *r*-ratios (element d) as described by the different parameter sets in comparison with the experimental data.

IDENT1ex2						
k	C_{12}	C_{13}	C_{22}	C_{23}	C_{33}	C_{66}
-0.5144	-1.0648	2.2381	4.9699	0.9547	-1.3450	-2.2168
k'	C'_{12}	C'_{13}	C'_{22}	C'_{23}	C'_{33}	C'_{66}
0.9577	-0.5316	-1.7240	0.3416	2.1204	0.3450	4.9141
IDENT2ex2						
k	C_{12}	C_{13}	C_{22}	C_{23}	C_{33}	C_{66}
0.4922	1.5173	-0.3369	-3.3689	-1.5588	3.6233	-4.7836
k'	C'_{12}	C'_{13}	C'_{22}	C'_{23}	C'_{33}	C'_{66}
0.9957	-3.3008	-1.2519	1.6440	0.7412	-3.0051	-4.6907
IDENT3ex2						
k	C_{12}	C_{13}	C_{22}	C_{23}	C_{33}	C_{66}
0.7671	4.3357	2.3790	0.8118	2.9526	1.8643	1.0719
k'	C'_{12}	C'_{13}	C'_{22}	C'_{23}	C'_{33}	C'_{66}
0.6671	-0.4930	-0.5604	0.0669	0.1352	2.6429	4.0709
IDENT4ex2						
k	C_{12}	C_{13}	C_{22}	C_{23}	C_{33}	C_{66}
-0.1361	4.9247	2.3313	0.3820	-0.1369	4.5720	0.8832
k'	C'_{12}	C'_{13}	C'_{22}	C'_{23}	C'_{33}	C'_{66}
0.5478	0.9354	2.1177	0.2993	-0.1927	1.3701	4.7385
$a=2$, $C_{11}=C'_{11}=1.0$						

Table 7-8 Yield function CPB06ex2 coefficients for four identifications of CPB06ex2 based on the experimental data given in Table 7-6

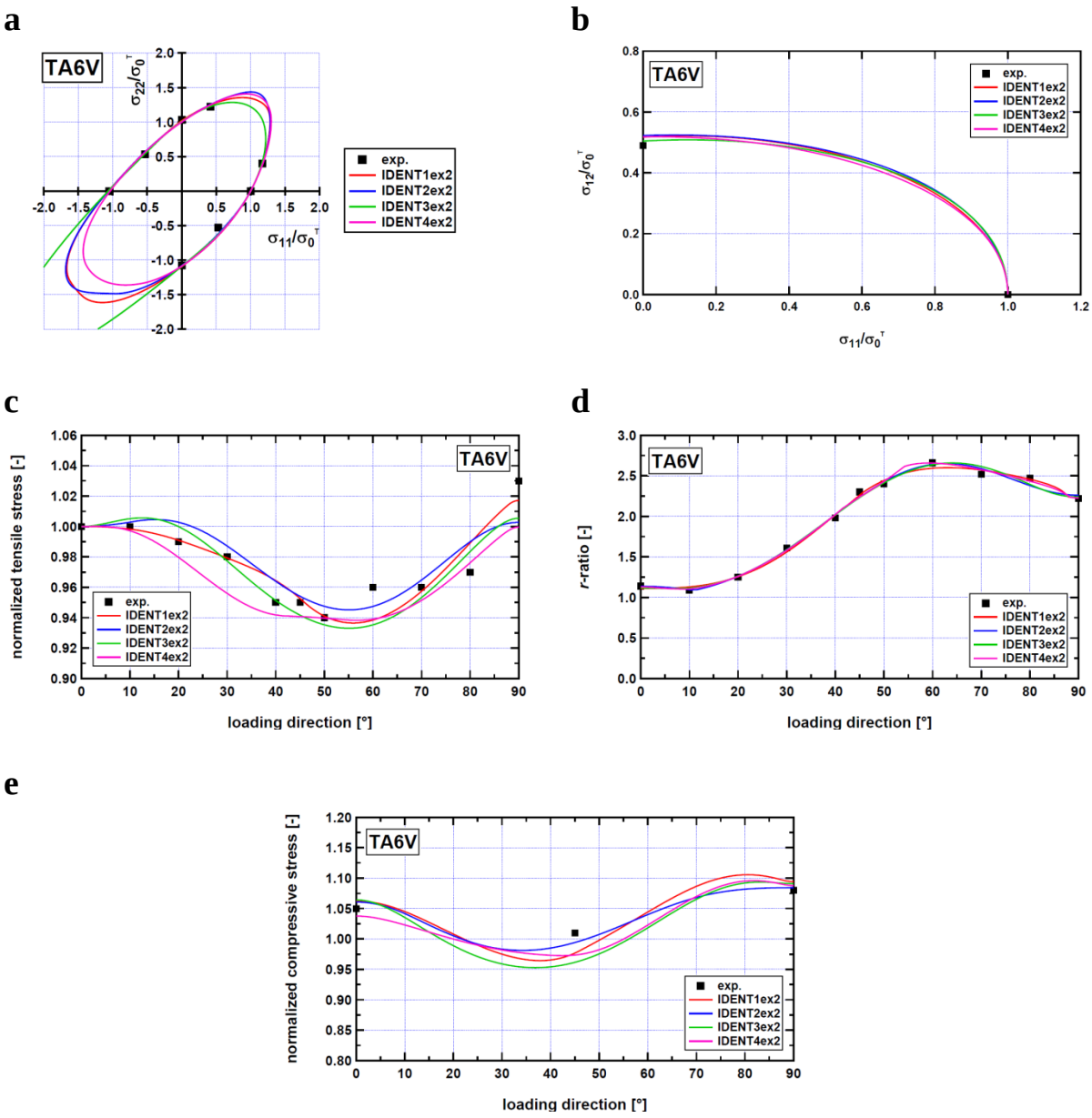

Figure 7-7 Comparison of the theoretical results according to the four different identifications of CPB06ex2 with the experimental data: (a) yield locus in the biaxial plane ($\sigma_{12}=0$); (b) yield locus in the plane $\sigma_{11}-\sigma_{12}$ ($\sigma_{22}=0$); (c) anisotropy in tensile yield stresses; (d) anisotropy in tensile r-ratios; (e) anisotropy in compressive yield stresses.

IDENT1ex3						
k	C_{12}	C_{13}	C_{22}	C_{23}	C_{33}	C_{66}
0.3889	1.5770	1.7583	-0.2465	-1.5721	2.2579	3.6770
k'	C'_{12}	C'_{13}	C'_{22}	C'_{23}	C'_{33}	C'_{66}
0.4231	-2.3458	-0.0661	3.0287	2.5279	-2.4311	-1.0463
k''	C''_{12}	C''_{13}	C''_{22}	C''_{23}	C''_{33}	C''_{66}
0.6559	1.3013	3.1259	-0.0781	0.1609	0.8711	-4.8500
IDENT2ex3						
k	C_{12}	C_{13}	C_{22}	C_{23}	C_{33}	C_{66}
0.6591	-1.3348	0.4665	2.7780	2.8894	-1.6051	3.4600
k'	C'_{12}	C'_{13}	C'_{22}	C'_{23}	C'_{33}	C'_{66}
0.4877	-3.3954	0.2286	-1.1044	-1.1218	-3.9788	3.0752
k''	C''_{12}	C''_{13}	C''_{22}	C''_{23}	C''_{33}	C''_{66}
-0.3406	0.7469	2.2770	4.7344	3.5580	0.9388	-4.6070
IDENT3ex3						
k	C_{12}	C_{13}	C_{22}	C_{23}	C_{33}	C_{66}
-0.5620	2.0154	0.8296	2.1989	0.4410	-4.3967	-4.1235
k'	C'_{12}	C'_{13}	C'_{22}	C'_{23}	C'_{33}	C'_{66}
0.7363	-4.7242	-1.7058	1.6037	-0.9136	-2.2133	4.7862
k''	C''_{12}	C''_{13}	C''_{22}	C''_{23}	C''_{33}	C''_{66}
0.8973	2.2403	-0.7692	-1.3438	-0.1391	-1.1843	3.9812
IDENT4ex3						
k	C_{12}	C_{13}	C_{22}	C_{23}	C_{33}	C_{66}
0.6128	0.4954	1.9668	0.2163	2.0640	3.6799	4.4709
k'	C'_{12}	C'_{13}	C'_{22}	C'_{23}	C'_{33}	C'_{66}
0.6480	-4.8810	-1.1894	1.8702	-0.8121	0.8803	4.3005
k''	C''_{12}	C''_{13}	C''_{22}	C''_{23}	C''_{33}	C''_{66}
0.9433	2.4919	-0.9502	-1.3865	-0.5440	2.5894	4.3253
$a = 2$, $C_{11} = C'_{11} = C''_{11} = 1.0$						

Table 7-9 Yield function CPB06ex3 coefficients for IDENT1ex3, IDENT2ex3, IDENT3ex3 and IDENT4ex3 based on the experimental data given in Table 7-6

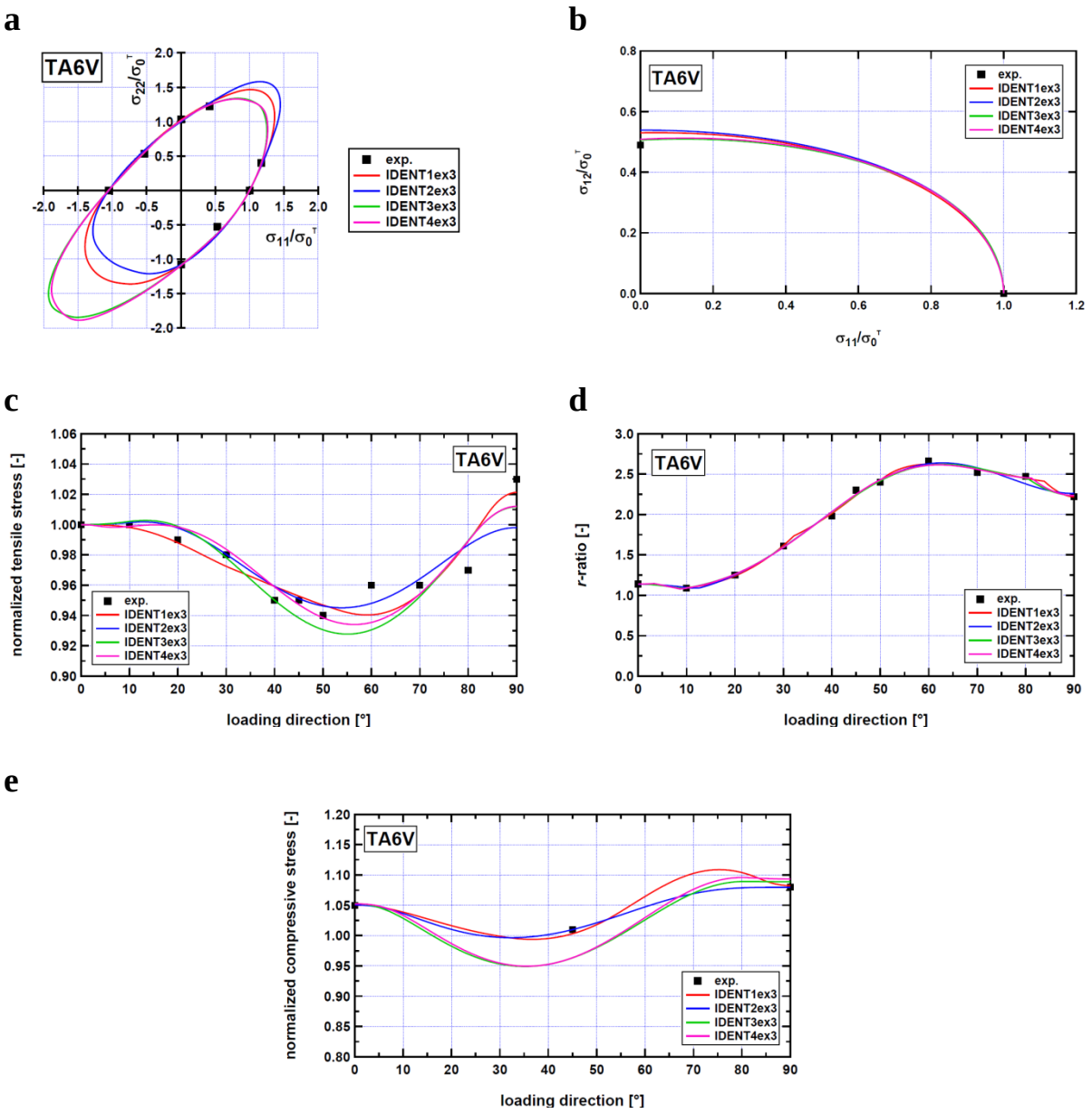

Figure 7-8 Comparison of the theoretical results according to the four different identifications of CPB06ex3 with the experimental data: (a) yield locus in the biaxial plane ($\sigma_{12}=0$); (b) yield locus in the plane $\sigma_{11}-\sigma_{12}$ ($\sigma_{22}=0$); (c) anisotropy in tensile yield stresses; (d) anisotropy in tensile r-ratios; (e) anisotropy in compressive yield stresses.

IDENT1ex4						
k	C_{12}	C_{13}	C_{22}	C_{23}	C_{33}	C_{66}
0.9954	-0.2897	-0.9986	-0.8508	0.5514	-2.2320	-3.9711
k'	C'_{12}	C'_{13}	C'_{22}	C'_{23}	C'_{33}	C'_{66}
-0.2488	-0.9431	0.9499	-1.8127	-4.6369	-2.6824	-2.1974
k''	C''_{12}	C''_{13}	C''_{22}	C''_{23}	C''_{33}	C''_{66}
-0.9503	-2.5504	-1.4569	-3.5544	-1.7540	-4.4660	-2.9842
k'''	C'''_{12}	C'''_{13}	C'''_{22}	C'''_{23}	C'''_{33}	C'''_{66}
0.9255	-3.7355	-0.9408	-3.6656	-3.2894	-2.0736	-3.2087
IDENT2ex4						
k	C_{12}	C_{13}	C_{22}	C_{23}	C_{33}	C_{66}
0.9146	0.1751	1.5247	-0.2624	1.4799	1.6501	-4.3104
k'	C'_{12}	C'_{13}	C'_{22}	C'_{23}	C'_{33}	C'_{66}
0.7037	3.1608	-0.3728	-2.8319	1.9159	-2.3678	-4.0804
k''	C''_{12}	C''_{13}	C''_{22}	C''_{23}	C''_{33}	C''_{66}
0.1581	-1.6456	-3.3395	1.7315	1.2470	1.9015	-2.7864
k'''	C'''_{12}	C'''_{13}	C'''_{22}	C'''_{23}	C'''_{33}	C'''_{66}
0.9692	4.6099	4.1275	4.5432	3.0852	1.9517	-2.4132
IDENT3ex4						
k	C_{12}	C_{13}	C_{22}	C_{23}	C_{33}	C_{66}
0.9578	3.7704	0.1765	-1.4160	2.0269	0.6110	-2.8704
k'	C'_{12}	C'_{13}	C'_{22}	C'_{23}	C'_{33}	C'_{66}
-0.8955	2.8999	3.0461	0.6647	2.2946	-1.3543	-4.1208
k''	C''_{12}	C''_{13}	C''_{22}	C''_{23}	C''_{33}	C''_{66}
-0.7489	-3.8795	-3.1481	-1.3474	-1.9742	-1.2101	2.6718
k'''	C'''_{12}	C'''_{13}	C'''_{22}	C'''_{23}	C'''_{33}	C'''_{66}
0.8289	0.2186	1.7608	-0.7999	0.0453	0.4559	-4.3066
IDENT4ex4						
k	C_{12}	C_{13}	C_{22}	C_{23}	C_{33}	C_{66}
0.3019	-0.6652	-0.5020	4.3297	3.3647	1.7893	-2.1117
k'	C'_{12}	C'_{13}	C'_{22}	C'_{23}	C'_{33}	C'_{66}
0.6168	2.1702	-0.9903	0.8459	-0.1423	0.0576	-3.8785
k''	C''_{12}	C''_{13}	C''_{22}	C''_{23}	C''_{33}	C''_{66}
-0.8862	-2.5649	0.2133	2.9518	-0.3164	0.5723	3.3717
k'''	C'''_{12}	C'''_{13}	C'''_{22}	C'''_{23}	C'''_{33}	C'''_{66}
-0.7339	2.3232	1.1536	2.2379	0.4598	-3.1825	4.7262
$a = 2$, $C_{11} = C'_{11} = C''_{11} = C'''_{11} = 1.0$						

Table 7-10 Yield function CPB06ex4 coefficients for IDENT1ex4, IDENT2ex4, IDENT3ex4 and IDENT4ex4 based on the experimental data given in Table 7-6

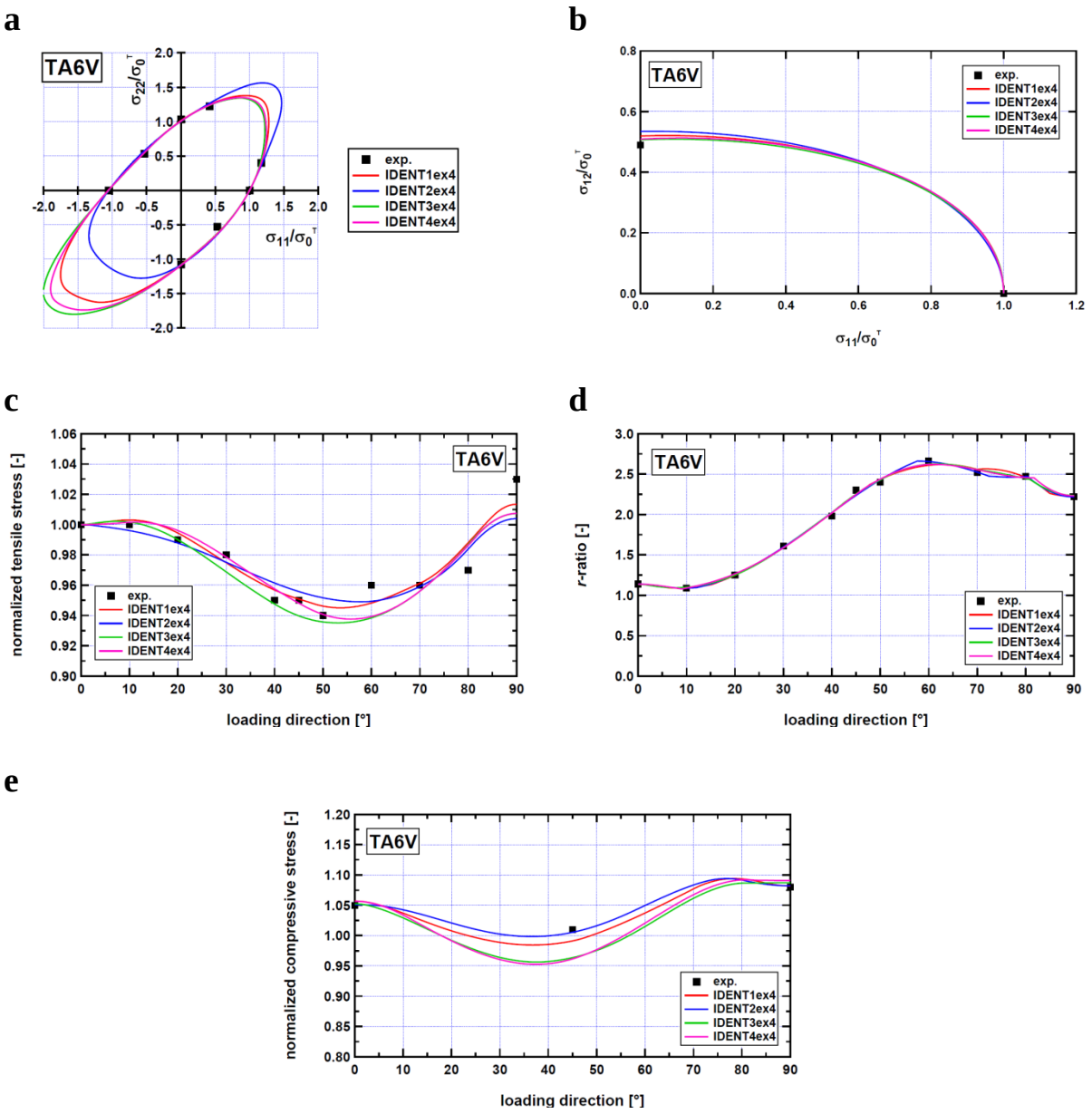

Figure 7-9 Comparison of the theoretical results according to the four different identifications of CPB06ex4 with the experimental data: (a) yield locus in the biaxial plane ($\sigma_{12}=0$); (b) yield locus in the plane $\sigma_{11}-\sigma_{12}$ ($\sigma_{22}=0$); (c) anisotropy in tensile yield stresses; (d) anisotropy in tensile r-ratios; (e) anisotropy in compressive yield stresses.

The simple observation and comparison of the different graphs do not allow the determination of the best parameter set(s). In order to fix it, the error functions E_1 and E_2 as defined in Section 7.1.1.2 as well as the number of transitions N_t performed during the optimizations were computed and reported in Table 7-11 for each identification (the results obtained for IDENT13 to IDENT16 are also recalled). Figure 7-10 summarizes the data of the last two columns. For the sake of clarity, it has to be noted that N_t was divided by a reference number $N_{t,0}$ corresponding to the average of the values associated to IDENT13, IDENT14, IDENT15 and IDENT16, *i.e.*:

$$N_{t,0} = \frac{1}{4}\left(N_t^{\text{IDENT13}} + N_t^{\text{IDENT14}} + N_t^{\text{IDENT15}} + N_t^{\text{IDENT16}}\right) = 2\ 156\ 001 \qquad (7.11)$$

In addition, a specified color was associated to each identification depending on the number of parameters used to model the yield locus, namely:

- **Blue symbols for IDENT13 to IDENT16** corresponding to the identifications of the 7 parameters involved in CPB06;
- **Red symbols for IDENT1ex2 to IDENT4ex2** corresponding to the identifications of the 14 parameters involved in CPB06ex2;
- **Green symbols for IDENT1ex3 to IDENT4ex3** corresponding to the identifications of the 21 parameters involved in CPB06ex3;
- **Orange symbols for IDENT1ex4 to IDENT4ex4** corresponding to the identifications of the 28 parameters involved in CPB06ex4.

Identification number	E_1	E_2	N_t
IDENT13	4.72×10^{-2}	5.35×10^{-2}	2 169 301
IDENT14	4.84×10^{-2}	5.54×10^{-2}	2 177 701
IDENT15	4.17×10^{-2}	4.47×10^{-2}	2 153 201
IDENT16	5.42×10^{-2}	5.42×10^{-2}	2 123 801
IDENT1ex2	0.78×10^{-2}	1.64×10^{-2}	4 369 401
IDENT2ex2	0.73×10^{-2}	1.77×10^{-2}	4 400 201
IDENT3ex2	1.13×10^{-2}	1.45×10^{-2}	4 449 201
IDENT4ex2	1.62×10^{-2}	1.62×10^{-2}	4 435 201
IDENT1ex3	0.31×10^{-2}	1.97×10^{-2}	6 699 001
IDENT2ex3	0.62×10^{-2}	2.89×10^{-2}	6 617 101
IDENT3ex3	0.92×10^{-2}	1.21×10^{-2}	6 709 501
IDENT4ex3	1.14×10^{-2}	1.14×10^{-2}	6 575 101
IDENT1ex4	0.33×10^{-2}	1.26×10^{-2}	8 912 401
IDENT2ex4	0.34×10^{-2}	2.21×10^{-2}	8 929 201
IDENT3ex4	0.82×10^{-2}	1.13×10^{-2}	9 032 801
IDENT4ex4	1.13×10^{-2}	1.13×10^{-2}	8 876 001

Table 7-11 Values of the error functions and number of transitions for the different identifications associated to CPB06, CPB06ex2, CPB06ex3 and CPB06ex4

From Figure 7-10, it can be observed that:

- Higher the number of parameters to be optimized is, higher the computation time directly linked to $N_t/N_{t,0}$ is;
- The value of the error function is reduced when two linear transformations are taken into account to describe the yield surface. On the other hand, when adding more linear transformations, two alternatives may arise: (1) a gain in accuracy is achieved, but it is rather low compared to the one obtained when CPB06ex2 is used instead of CPB06; (2) the value of the error function is higher, meaning that the parameter set is less appropriate.

From an accuracy-computation time ratio point of view, it can be concluded that the CPB06ex2 yield criterion is necessary and sufficient to model the yield locus of Ti6Al4V.

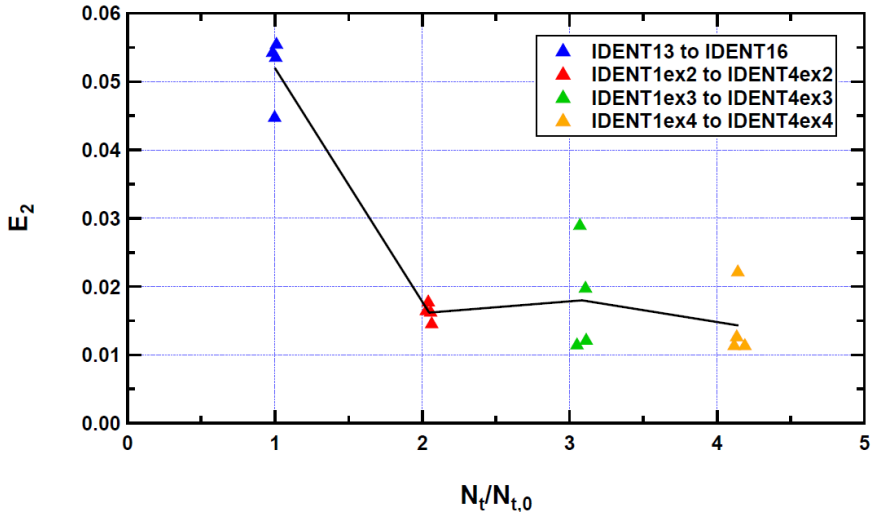

Figure 7-10 Error function E_2 with respect to the number of transitions performed for the identifications IDENT13 to IDENT16 (blue symbols), IDENT1ex2 to IDENT4ex2 (red symbols), IDENT1ex3 to IDENT4ex3 (green symbols) and IDENT1ex4 to IDENT4ex4 (orange symbols).

Among the identifications IDENT1ex2, IDENT2ex2, IDENT3ex2 and IDENT4ex2, it is still possible to exclude one of them. Indeed it can be noticed in Figure 7-7 (a) that the theoretical yield loci in the biaxial plane $\sigma_{11}-\sigma_{22}$ display different shapes in the first and third quadrants. In order to determine which ones are the most adapted for modeling, the yield stress in equibiaxial tension was assessed using the work-equivalence principle and the experimental curve obtained from the layer compression tests (see Section 5.2.6 and Figure 5-46). As reported by Coppieters (2012), this result is underestimated, which means that it can be used as a lower boundary. When adding the associated point in the biaxial plane and comparing with the theoretical yield loci shown in Figure 7-7 (a), it can be observed that the parameter set given by IDENT3ex2 is unadapted to describe the yield locus of Ti6Al4V (see Figure 7-11).

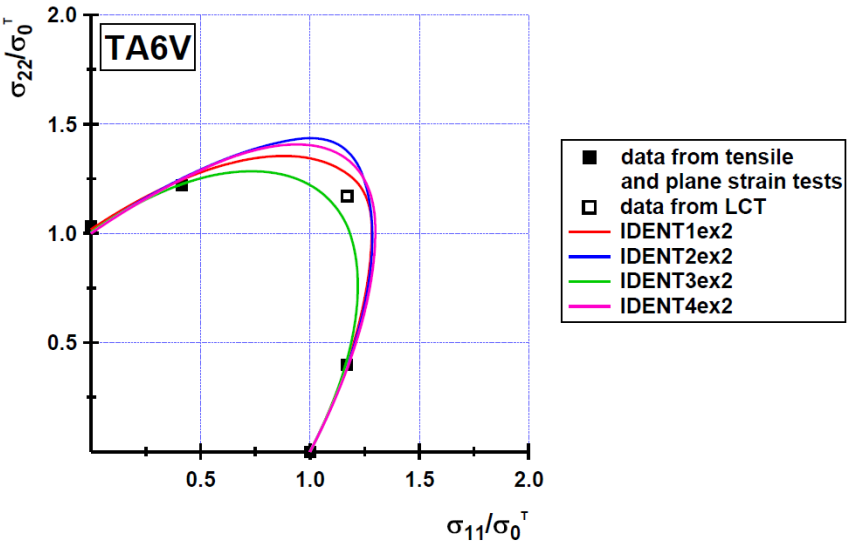

Figure 7-11 Comparison of the theoretical yield loci according to IDENT1ex2, IDENT2ex2, IDENT3ex2 and IDENT4ex2 with the experimental data from the tensile, plane strain and layer compression tests

7.2.3. Conclusion

In Section 7.2, different parameter identifications were performed in order to determine which criterion from the family proposed by Plunkett *et al.* (2008) was appropriate to describe the initial yield locus of Ti6Al4V. The analysis of the error function given by Equations (7.3) to (7.6) with respect to the number of linear transformations used in the criterion showed that CPB06ex2 is required to obtain a good accuracy with a minimum computation time. The results given by the identifications **IDENT1ex2**, **IDENT2ex2** and **IDENT4ex2**, were finally selected as the most reliable parameters sets. The next section is devoted to identify the parameters in different formulations for the description of the hardening behavior.

7.3. Hardening parameter identifications

7.3.1. CPB06ex2 associated to Voce isotropic hardening law

The parameters included in Voce isotropic hardening model (Equations (3.44) and (3.45)) are first identified by inverse method using the stress-strain curve in tension along RD only. The optimized parameter set, which will be denoted by "Voce_1", is given in Table 7-12.

R_0 [MPa]	s_R [MPa]	c_R [-]
964.24	190.17	15.35

Table 7-12 Voce isotropic hardening parameters obtained after the first identification (set "Voce_1")

The different experimental tests in tension, compression, plane strain and simple shear detailed in Chapter 4 are simulated with the FE code LAGAMINE using one BWD3D element. The latter is an 8-node 3D brick element with a mixed formulation and one integration point.

It is based on the nonlinear three-field (stress, strain and displacement) Hu-Washizu variational principle (Belytschko and Bindeman (1991)). BWD3D element is characterized by a new shear locking treatment based on the Wang-Wagoner method (Wang and Wagoner (2004)) which consists in identifying the hourglass modes causing the shear locking and removing them. The two bending hourglass modes as well as the warp hourglass mode are eliminated, while the volumetric locking is also treated by removing inconvenient hourglass modes. This method is very efficient in FE analyses owing to its deep physical roots. A second feature of BWD3D element is its use of a co-rotational reference system in which the formulation of the kinematics is expressed in order to identify the hourglass modes. This co-rotational reference system is closely linked to the element coordinates: its origin is the center of the element and its reference axes are aligned with element edges as much as possible, depending on the element shape. Thanks to this co-rotational system, the hourglass stress objectivity can be treated in a simple and accurate way by using initial and final time step rotation. BWD3D element has proved its efficiency in various simulations such as deep drawing, incremental forming and large strain torsion (Duchêne *et al.* (2007)). More details about BWD3D element can be found in Duchene *et al.* (2005) and Duchêne *et al.* (2008).

The simulations of the tensile, compression, plane strain and simple shear tests are performed using the parameter sets IDENT1ex2, IDENT2ex2 and IDENT4ex2 associated to the hardening parameters in Table 7-12. Figure 7-12 and Figure 7-13 compare the experimental stress-strain curves with the FE predictions. It can be observed a good agreement between the experiments and the numerical curves, excepted in compression along RD, in plane strain and in simple shear for which the flow stress is overestimated.

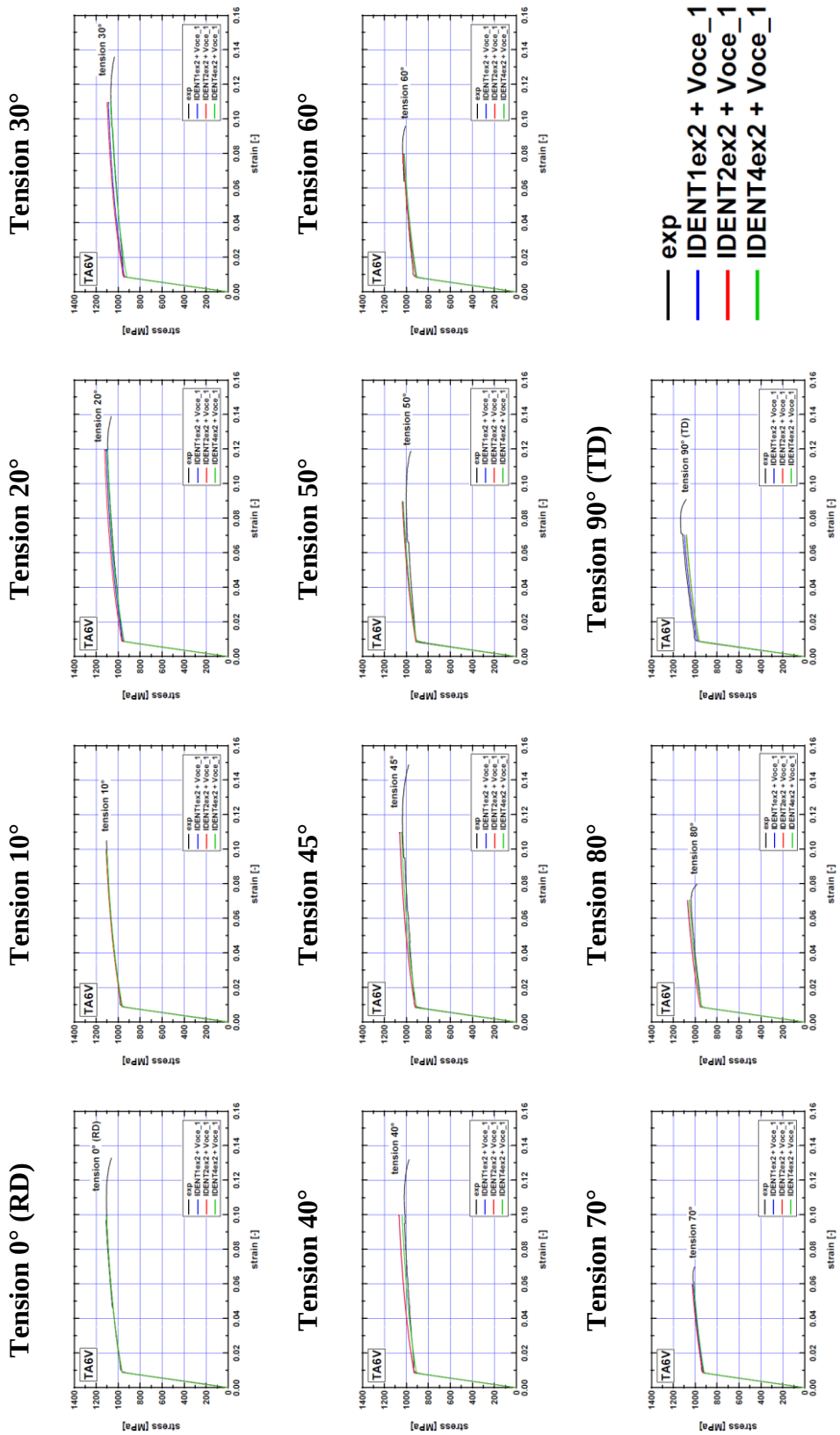

Figure 7-12 Experimental stress-strain curves in tension compared to the numerical predictions according to IDENT1ex2 + Voce_1, IDENT2ex2 + Voce_1 and IDENT4ex2 + Voce_1

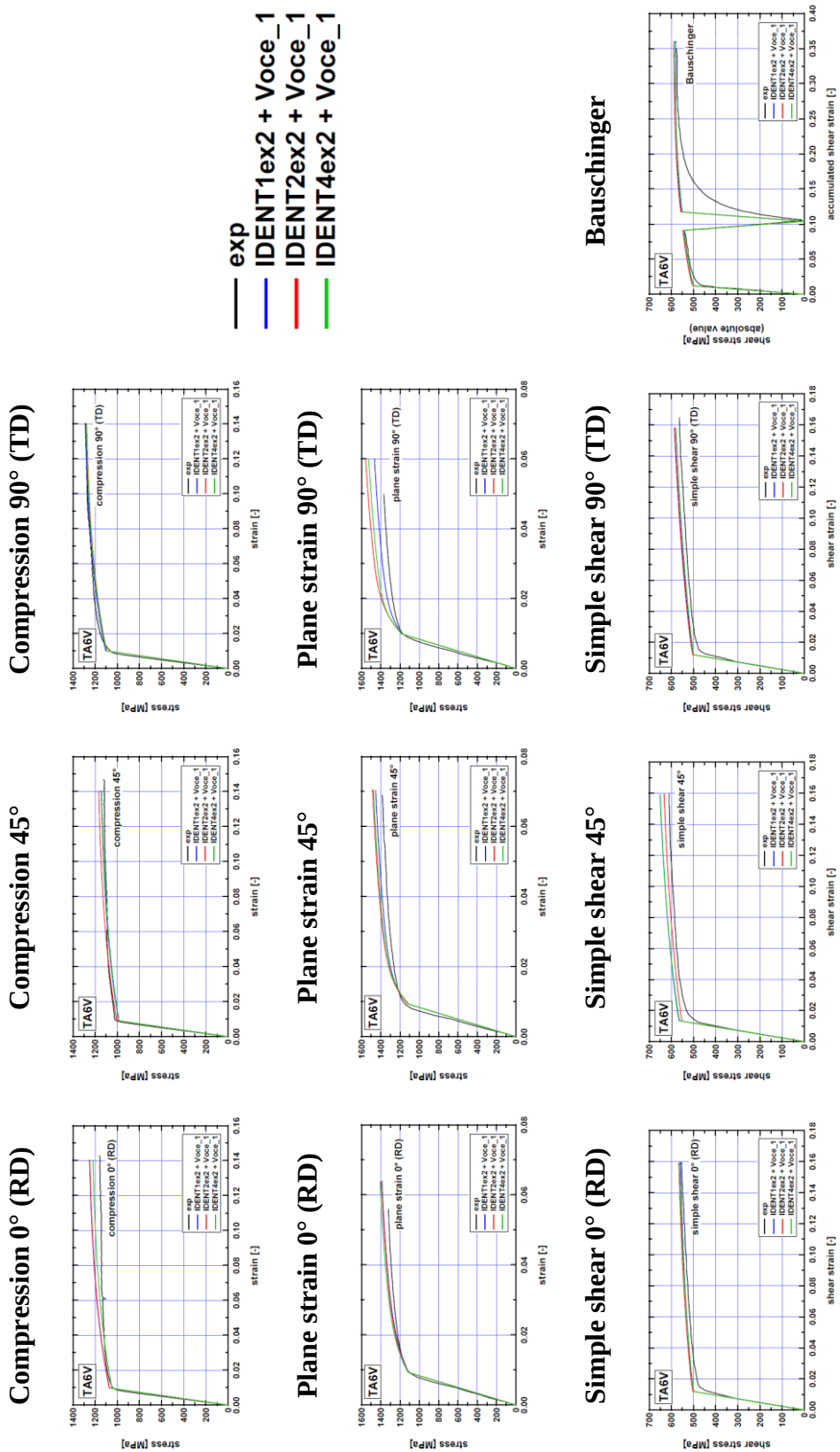

Figure 7-13 Experimental stress-strain curves in compression, plane strain and simple shear compared to the numerical predictions according to IDENT1ex2 + Voce_1, IDENT2ex2 + Voce_1 and IDENT4ex2 + Voce_1

In order to improve the FE results, OPTIM is used a second time to identify the Voce hardening parameters, but using all the experimental curves as data, choosing the parameter set "Voce_1" as initial guess and fixing the value of R_0 (R_0 = 964.24 MPa, see Table 7-12). Since each experiment is taken into account, the optimization results will depend on the parameters in CPB06ex2 characterizing the initial yield locus. Table 7-13 gives the optimized hardening parameter sets denoted by "Voce_21", Voce_22", "Voce_23", and respectively associated to IDENT1ex2, IDENT2ex2, IDENT4ex2. The corresponding FE stress-strain curves in tension, compression, plane strain and simple shear are compared with the experimental results in Figure 7-14 and Figure 7-15.

Set name	Associated yield locus parameter set	R_0 [MPa]	s_R [MPa]	c_R [-]
Voce_21	IDENT1ex2	964.24	214.73	8.41
Voce_22	IDENT2ex2	964.24	386.06	3.59
Voce_23	IDENT4ex2	964.24	341.04	5.05

Table 7-13 Voce isotropic hardening parameters obtained after the second identifications

In order to compare the accuracy of the different identifications performed in this section, an error function based on Equation (7.9) (see Section 7.1.2.2) was computed from the experimental and finite element stress-strain curves as follows:

$$E' = \sqrt{\sum_{i=1}^{n_{\text{exp}}} \sum_{j=1}^{n_{\text{points}}} \left(\frac{\sigma_{i,j}^{\text{EF}} - \sigma_{i,j}^{\text{EXP}}}{\sigma_{i,j}^{\text{EXP}}} \right)^2} \tag{7.12}$$

where:

- i denotes a point belonging to the experimental curve referred by the index j;
- $\sigma_{i,j}^{\text{EXP}}$ and $\sigma_{i,j}^{\text{EF}}$ are respectively the stresses of the experimental and finite element curves associated to the n_{points} points and n_{exp} tests.

The errors associated to the different identifications in Table 7-12 and Table 7-13 are reported in Figure 7-16. It can be observed that the lowest errors are obtained with the Voce_1 parameter set. In addition, E' is minimal in the case of **IDENT2ex2 combined with Voce_1**.

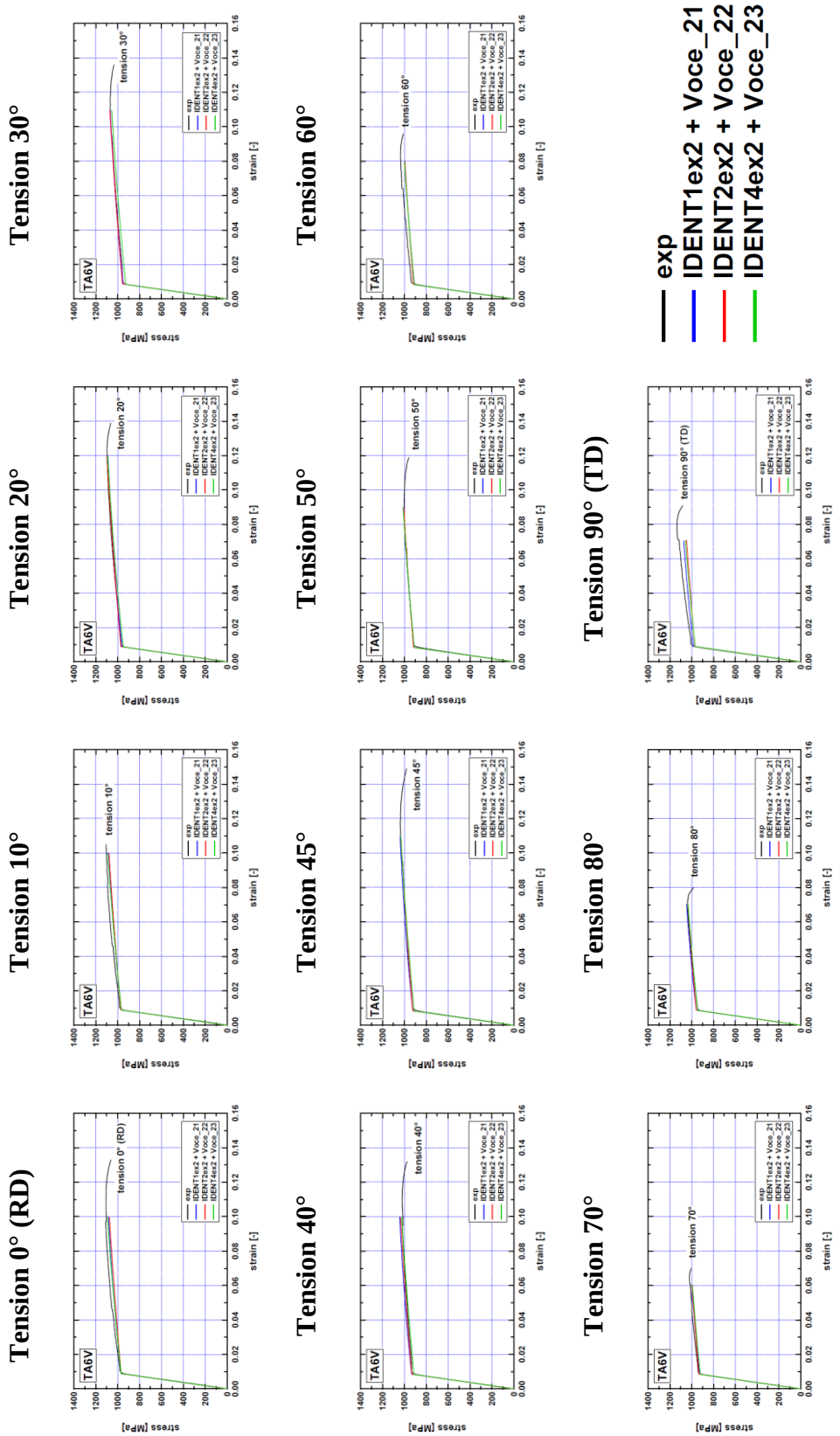

Figure 7-14 Experimental stress-strain curves in tension compared to the numerical predictions according to IDENT1ex2 + Voce_21, IDENT2ex2 + Voce_22 and IDENT4ex2 + Voce_23

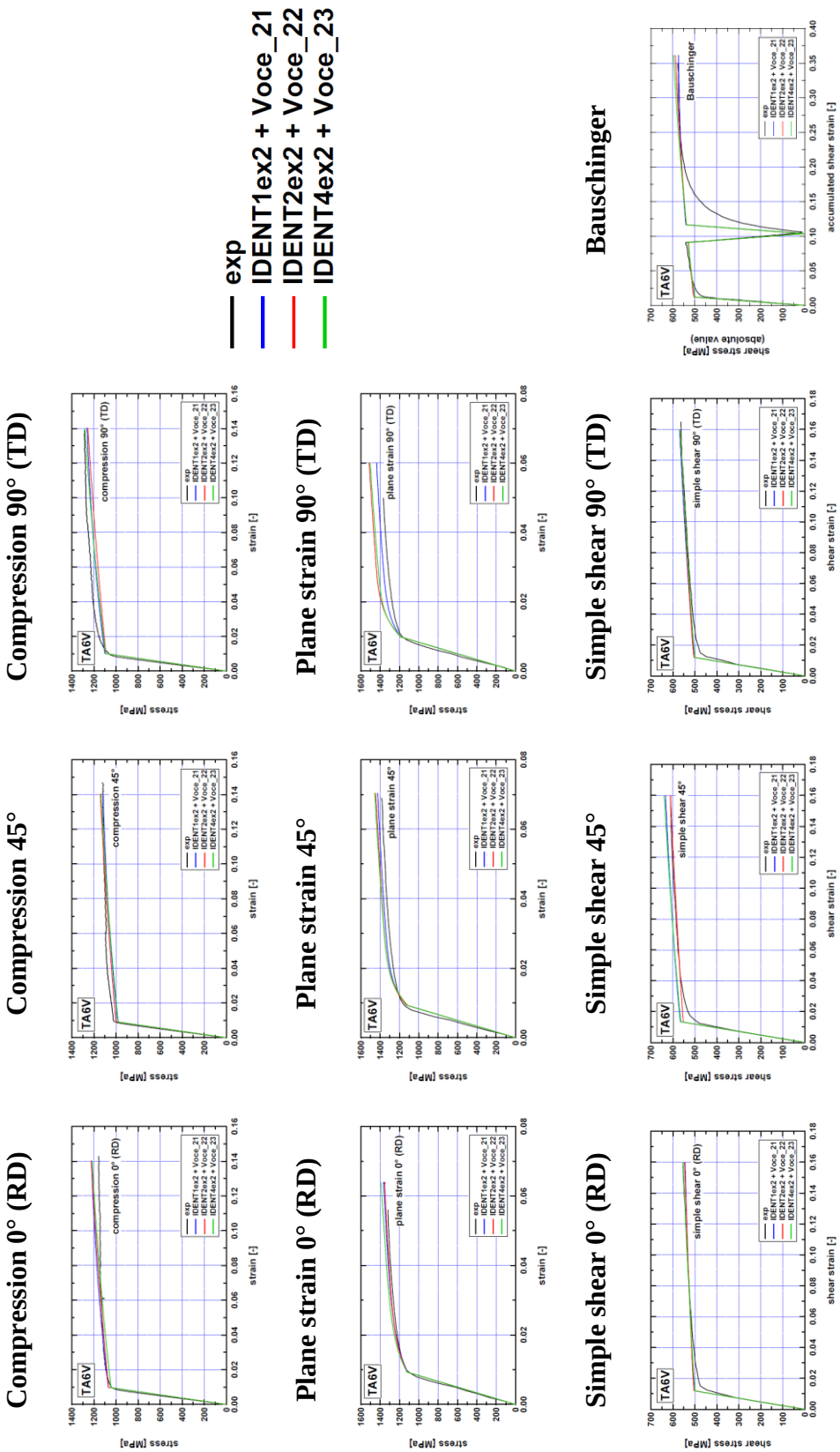

Figure 7-15 Experimental stress-strain curves in compression, plane strain and simple shear compared to the numerical predictions according to IDENT1ex2 + Voce_21, IDENT2ex2 + Voce_22 and IDENT4ex2 + Voce_23

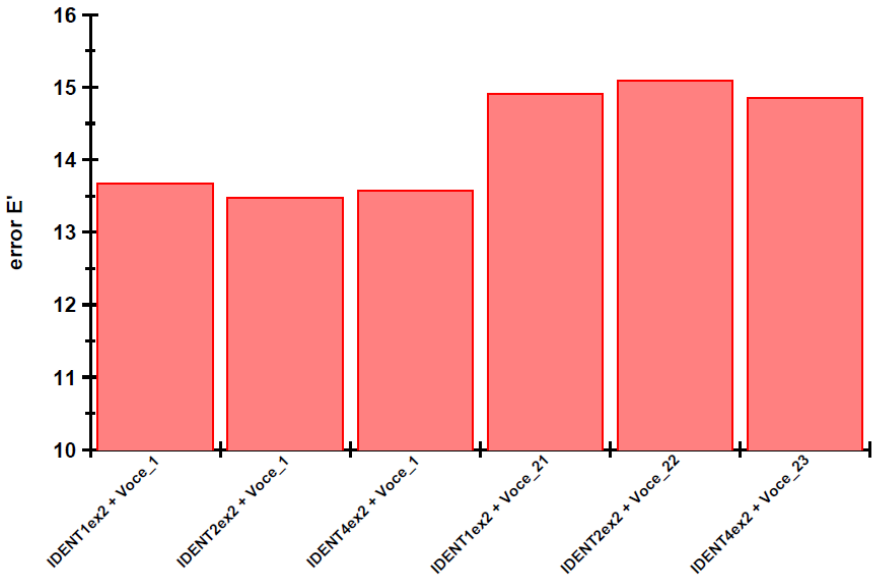

Figure 7-16 Error function E' with respect to the different identifications associated to Voce isotropic hardening law

7.3.2. CPB06ex2 associated to a mixed hardening law (Voce + Armstrong-Frederick)

As explained in Section 5.2.4, Ti6Al4V reveals a significant Bauschinger effect. It can also be observed by comparing the experimental stress-strain curve obtained for the Bauschinger tests with the FE results when using the CPB06ex2 yield criterion associated to Voce hardening law only (see Figure 7-17 and Figure 7-18). In order to take into account the Bauschinger effect, Armstrong-Frederick kinematic hardening model was added in the implementation of the constitutive law in LAGAMINE (see Section 6.2).

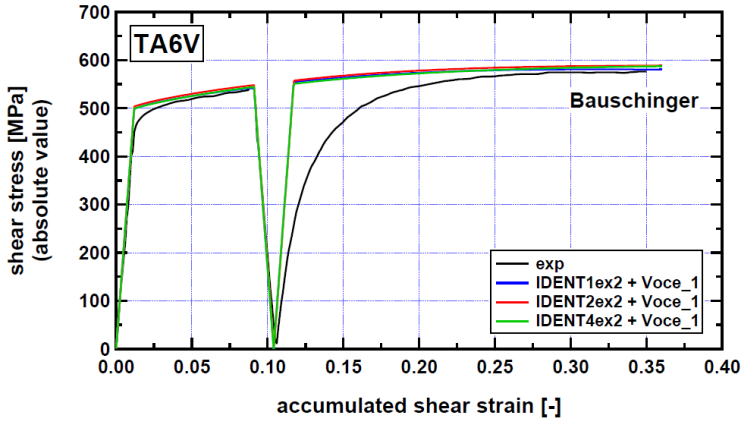

Figure 7-17 Experimental stress-strain curves in cyclic simple shear (Bauschinger) compared to the numerical predictions according to IDENT1ex2 + Voce_1, IDENT2ex2 + Voce_1 and IDENT4ex2 + Voce_1

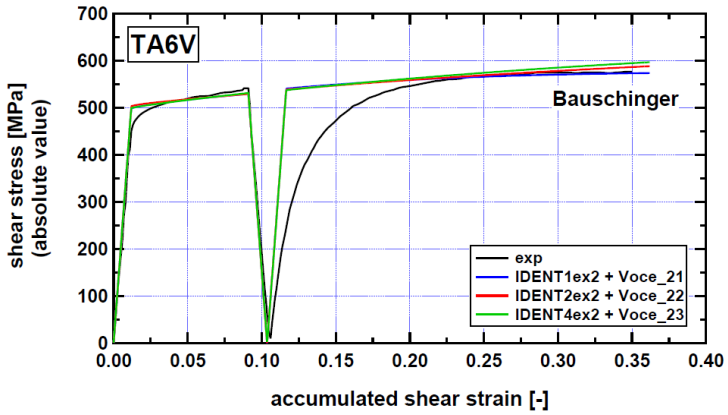

Figure 7-18 Experimental stress-strain curves in cyclic simple shear (Bauschinger) compared to the numerical predictions according to IDENT1ex2 + Voce_21, IDENT2ex2 + Voce_22 and IDENT4ex2 + Voce_23

Similarly to the previous section, two optimization steps using the inverse method are performed to determine the parameters included in Voce and Armstrong-Frederick laws. The first one consists in identifying s_R, c_R, s_X and c_X from the experimental curves in tension along RD and in cyclic simple shear. The optimized parameter sets are given in Table 7-14 with respect to the different yield locus identifications selected in Section 7.2. The comparison between the experimental and FE stress-strain curves is shown in Figure 7-19 and Figure 7-20.

Set name	Associated yield locus parameter set	R_0 [MPa]	s_R [MPa]	c_R [-]	s_X [MPa]	c_X [-]
Voce_AF_11	IDENT1ex2	964.24	97.03	15.63	38.17	25.32
Voce_AF_12	IDENT2ex2	964.24	107.01	13.14	37.51	23.55
Voce_AF_13	IDENT4ex2	964.24	95.34	15.86	37.68	25.48

Table 7-14 Voce and Armstrong-Frederick hardening parameters obtained after the first identifications

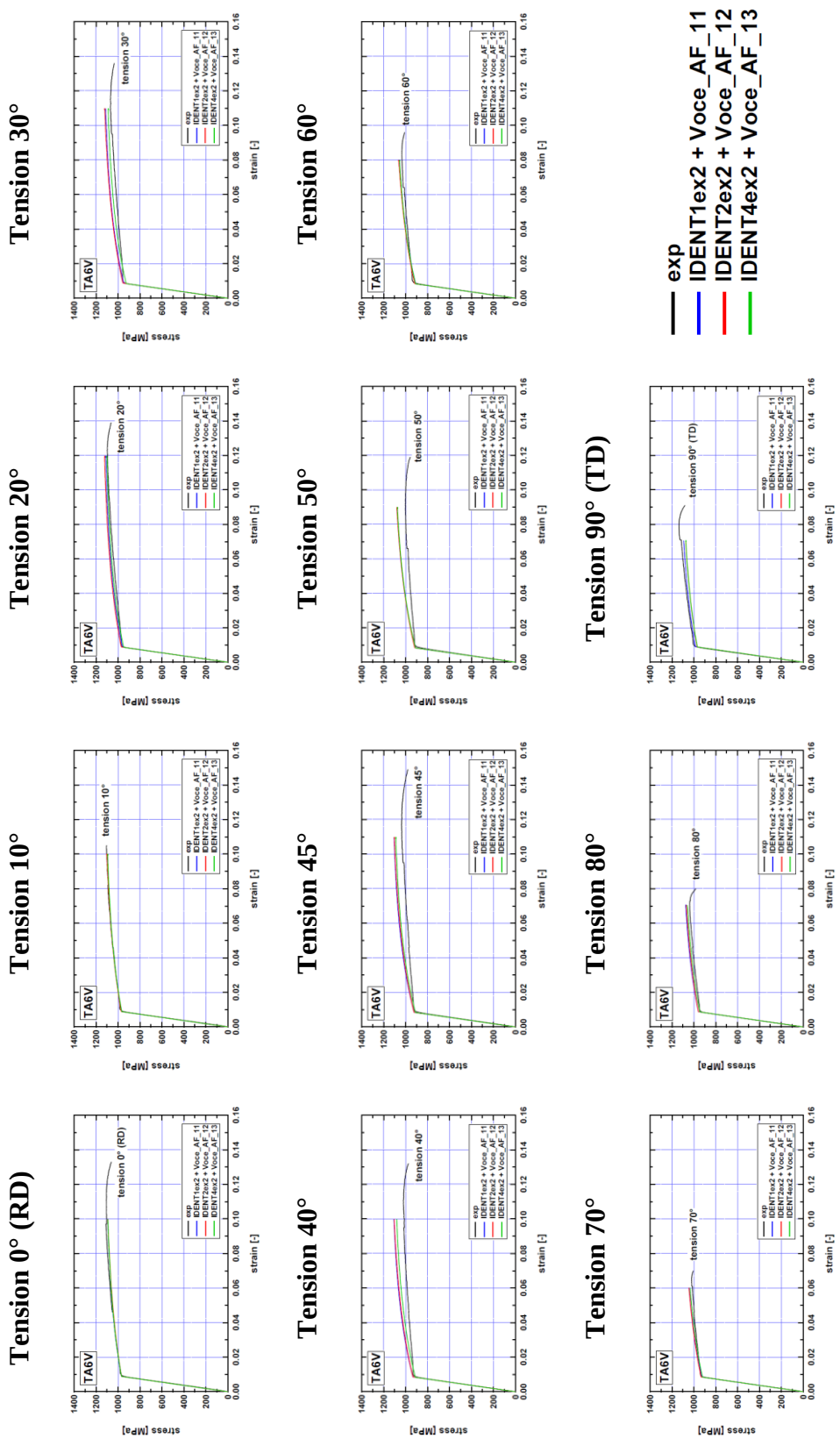

Figure 7-19 Experimental stress-strain curves in tension compared to the numerical predictions according to IDENT1ex2 + Voce_AF_11, IDENT2ex2 + Voce_AF_12 and IDENT4ex2 + Voce_AF_13

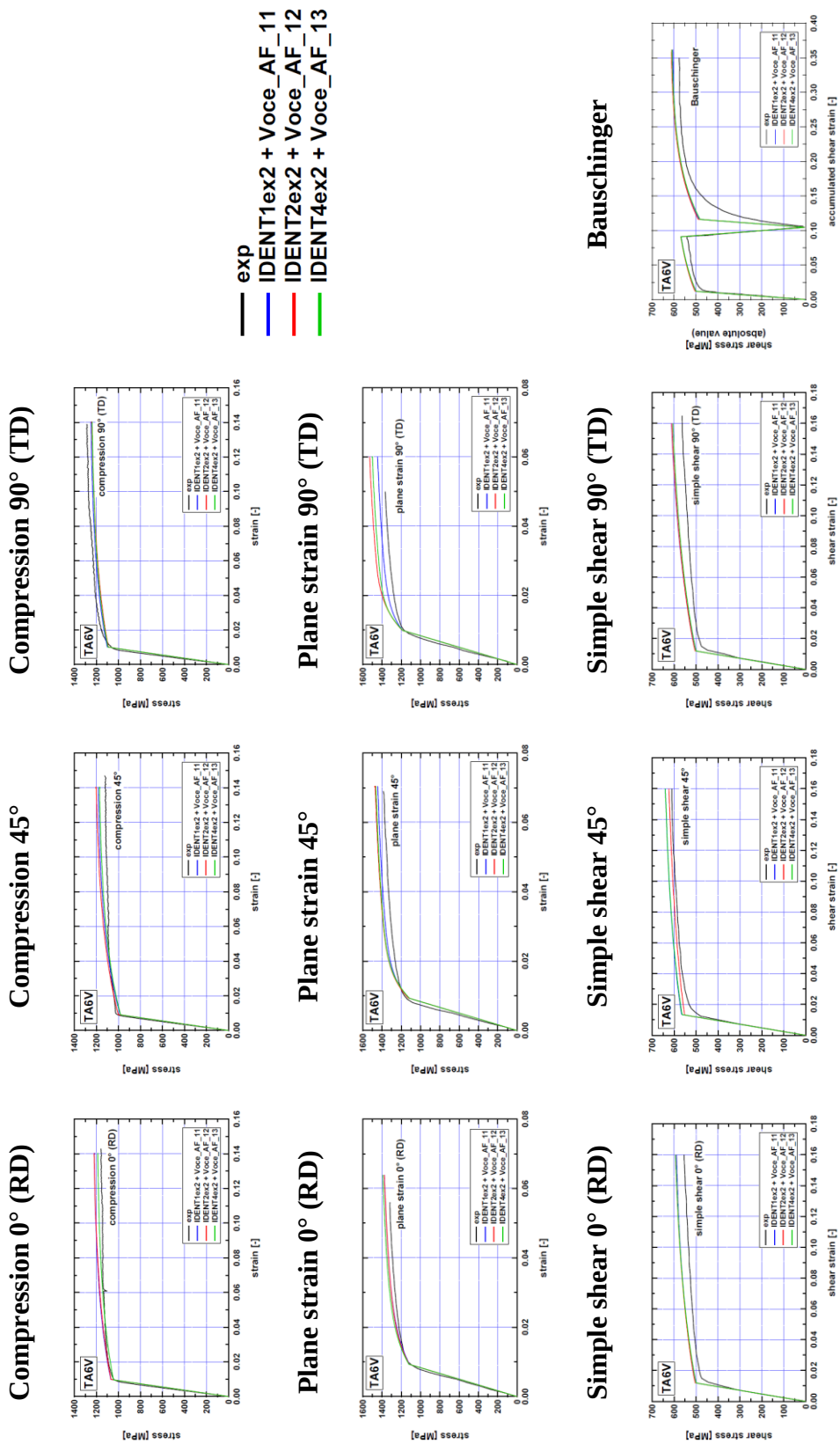

Figure 7-20 Experimental stress-strain curves in compression, plane strain, simple shear and cyclic simple shear (Bauschinger) compared to the numerical predictions according to IDENT1ex2 + Voce_AF_11, IDENT2ex2 + Voce_AF_12 and IDENT4ex2 + Voce_AF_13

It can be observed from these graphs that, for several strain paths, the flow stress predicted by the different models is overestimated. In order to reduce these discrepancies, a second set of identifications is performed by including all the experimental stress-strain curves in the optimization as it was achived for the Voce hardening parameters in Section 7.3.1. The optimized parameters are given in Table 7-15 and the corresponding FE results are compared with the experiments in Figure 7-21 and Figure 7-22 in which it can be noticed an improvement of the numerical predictions in the case of the monotonic strain paths (tension, compression, plane strain, simple shear). Nevertheless, it has to be noted that the Bauschinger effect is not represented with a good accuracy either for the first or the second identifications. Other optimizations by inverse method were performed in order to find a parameter set which could better fit the experimental behavior of Ti6Al4V, but without success. The reason for which Armstrong-Frederick kinematic hardening law fails to predict the Bauschinger effect displayed by Ti6Al4V is due to the fact that this model is too simple from a phenomenological point of view. It would be required to develop an approach based on the microstructure evolution, as the formulation proposed by Teodosiu and Hu (1995) for bcc mono-crystals and then applied to other materials (IF steel sheets, dual phase steels, aluminium).

Set name	Associated yield locus parameter set	R_0 [MPa]	s_R [MPa]	c_R [-]	s_X [MPa]	c_X [-]
Voce_AF_21	IDENT1ex2	964.24	136.24	10.95	20.90	9.75
Voce_AF_22	IDENT2ex2	964.24	136.24	7.99	24.48	9.75
Voce_AF_23	IDENT4ex2	964.24	138.67	8.49	32.97	11.49

Table 7-15 Voce and Armstrong-Frederick hardening parameters obtained after the second identifications

Equation (7.12) was used to compute the error E' corresponding to the different identifications in Table 7-14 and Table 7-15. The results are given in Figure 7-23 and show that the lowest error is obtained in the case of **IDENT4ex2 associated to Voce_AF_13**.

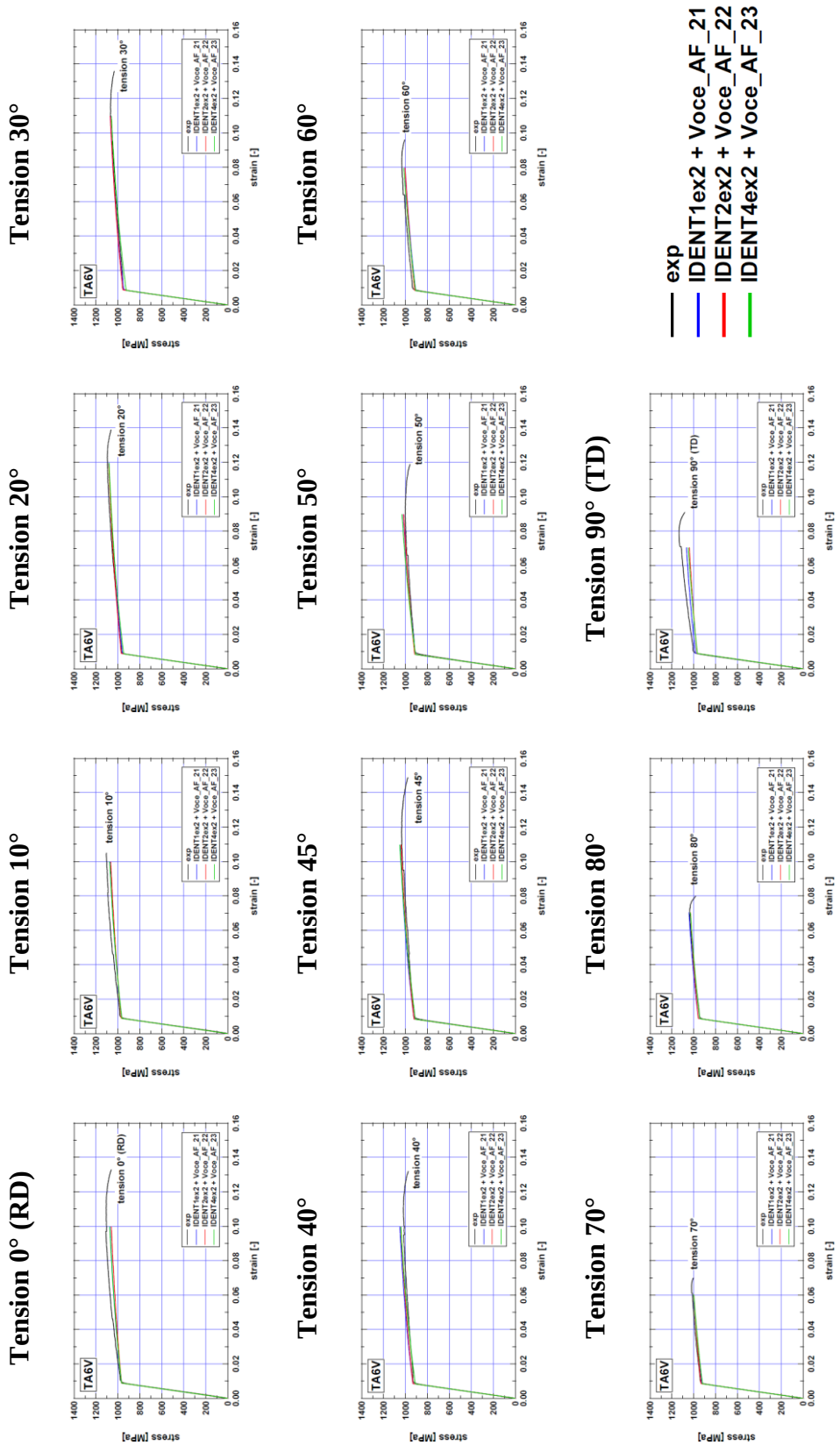

Figure 7-21 Experimental stress-strain curves in tension compared to the numerical predictions according to IDENT1ex2 + Voce_AF_21, IDENT2ex2 + Voce_AF_22 and IDENT4ex2 + Voce_AF_23

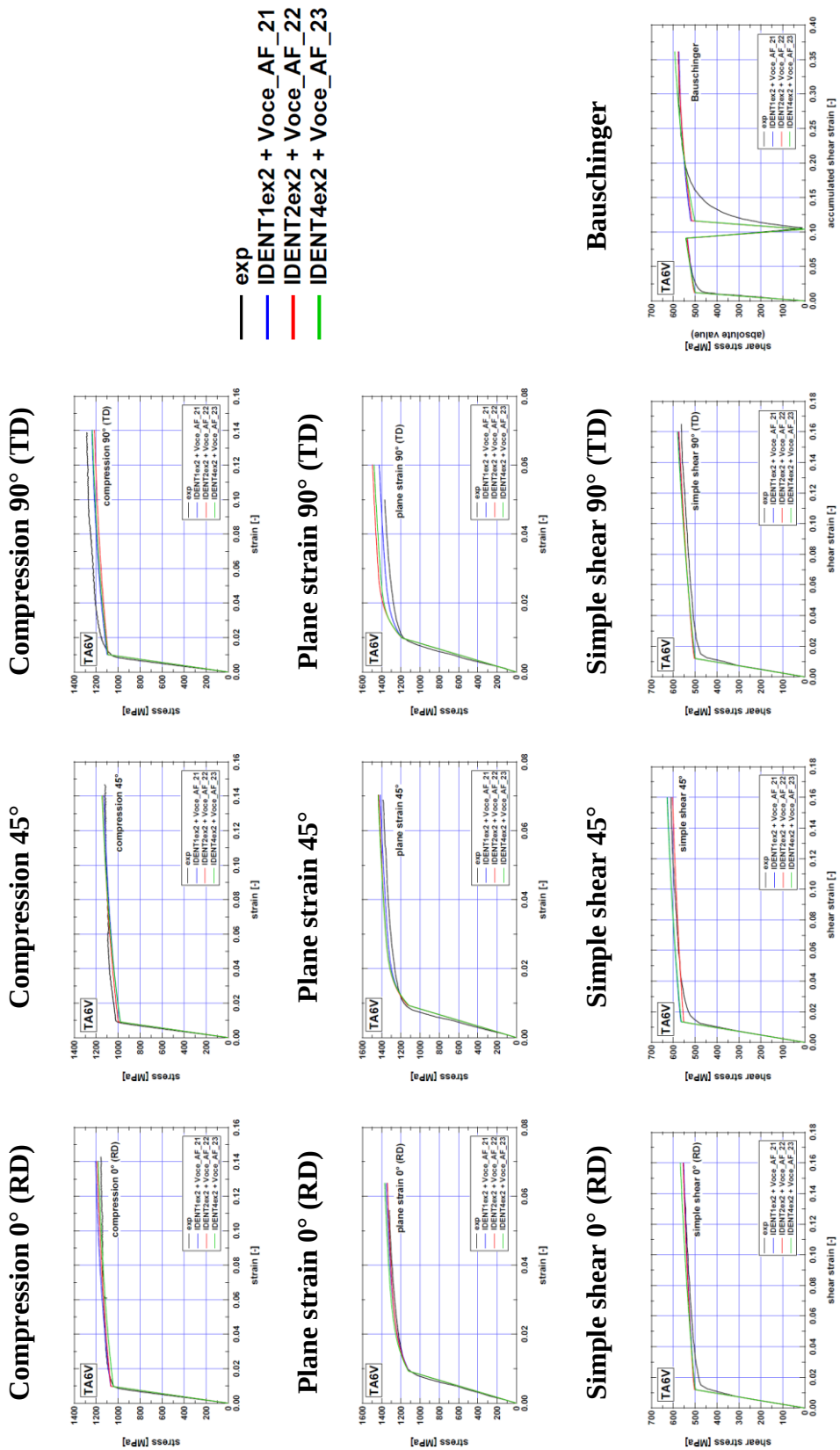

Figure 7-22 Experimental stress-strain curves in compression, plane strain, simple shear and reversed simple shear (Bauschinger) compared to the numerical predictions according to IDENT1ex2 + Voce_AF_21, IDENT2ex2 + Voce_AF_22 and IDENT4ex2 + Voce_AF_23

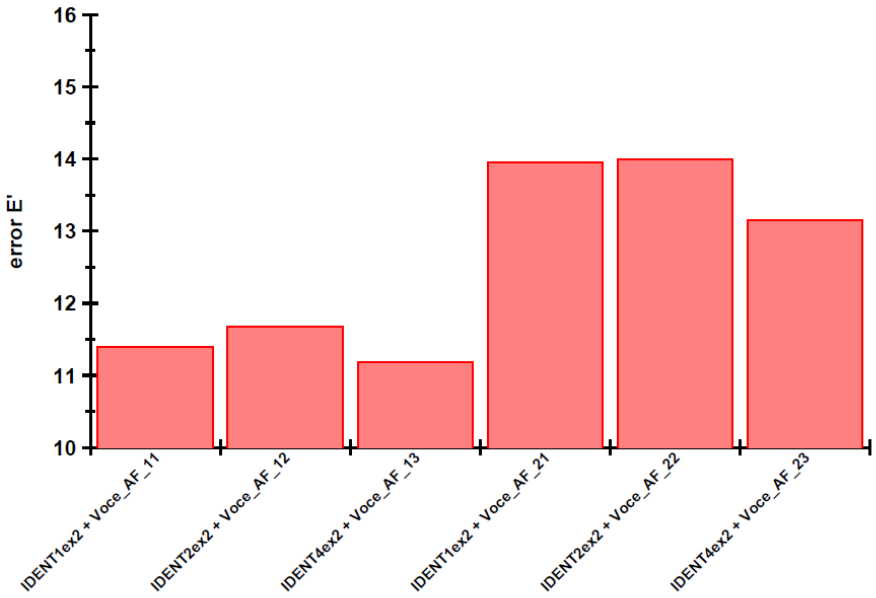

Figure 7-23 Error function E' with respect to the different identifications associated to the mixed hardening law

7.3.3. Evolution of the parameters involved in CPB06ex2 with the plastic work

The analysis of the mechanical tests on Ti6Al4V revealed a shape evolution of the yield locus with the plastic deformation (see Section 5.2.5). For this reason, a constitutive model taking into account the distortional hardening of the material was also implemented into LAGAMINE (see Section 6.3).

In Section 5.2.5, the yield locus of Ti6Al4V is displayed for four levels of plastic work per unit of volume. From these experimental data, it is possible to identify the CPB06ex2 parameters for each level using the CSA algorithm. The identification of the initial yield locus (corresponding to the first plastic work level $W_{p,1} =$ 2.0 J/cm³) having been achieved and discussed previously, the following results will mainly be focused on the higher levels, namely $W_{p,2} =$ 9.8 J/cm³, $W_{p,3} =$ .19.9 J/cm³ and $W_{p,4} =$ 51.3 J/cm³. For these levels, the SD parameters and the anisotropy coefficients involved in CPB06ex2 yield criterion are optimized using the experimental data in tension, compression and plane strain. It has to be noted that the data in simple shear are not included in these identifications since the complete stress state cannot experimentally be determined. In addition, for the plane strain tests, it has to be recalled that the axial stress can be computed from the experiments while the transversal stress is unknown. Due to this, dashed lines are used in the biaxial plane $\sigma_{11} - \sigma_{22}$ to represent the corresponding data.

Three sets of optimizations are performed, each one starting respectively with the identifications IDENT1ex2, IDENT2ex2 and IDENT4ex2 for the description of the initial yield locus. For each set, the CPB06ex2 parameters for the plastic work level $W_{p,i}$ $(i = 2,3,4)$ are deter-

mined using the solution obtained for the previous level $W_{p,i-1}$ as initial guess. Besides the error functions E_1 and E_2 described by Equations (7.2) to (7.6) are modified for these identifications. Indeed, as explained in Section 7.1.1.2, Equation (7.7) is used to take into account the data in plane strain at large plastic strains. In addition the experimental stresses in simple shear cannot be included in the optimization since the complete stress state is unknown at these levels of plastic work. Considering these remarks, the modified error functions are formulated as follows:

$$E_1' = \sum_{i=1}^{N_d'} \eta_i \, e_i^2 \tag{7.13}$$

$$E_2' = \sum_{i=1}^{N_d'} e_i^2 \tag{7.14}$$

where N_d' is the total number of experimental values in tension, compression and plane strain. e_i is defined by Equation (7.5) for the flow stresses in tension and compression, by Equation (7.6) for the tensile *r*-ratios, and by Equation (7.7) for the plane strain tests. It has to be noted that the weight factors in Equation (7.13) associated to the data in plane strain and the ones in tension and compression were fixed to 0.01 and 1.0 respectively. Indeed when all these factors are kept to 1.0, it was noticed that the yield loci corresponding to the different plastic work levels can cross each other, which does not cause any problem of convergence but can result in a negative hardening rate in some finite element stress-strain curves relative to the different experimental tests. For this reason, it was decided to reduce the weight of the errors linked with the plane strain states in order to prevent the overlapping of the yield surfaces. However this approach can affect the ability of the modeling to describe the material behavior under this strain path.

It has also to be noted that the identification of the yield locus at the different levels of plastic work is based on experimental data for which the texture differs from a test to another. Indeed the texture evolution strongly depends on the strain path in the case of the investigated Ti6Al4V sheet, which means that the yield loci determined according to the proposed approach does not correspond to the same material. It would be required to use a microscopic model able to take into account the texture evolution of hcp materials in order to obtain reliable information concerning the evolution of the yield locus shape with the plastic deformation.

The optimized parameter sets, denoted EVOL_1, EVOL_2 and EVOL_3 respectively, are given in Table 7-16, Table 7-17 and Table 7-18, while Figure 7-24, Figure 7-25 and Figure 7-26 show the biaxial projections in the planes $\sigma_{11}-\sigma_{22}$ and $\sigma_{11}-\sigma_{12}$ as well as the anisotropy in terms of tensile and compressive yield stresses as described by the different parameter sets in comparison with the experimental data. It can be observed that, even if the same experimental data and error functions are used during the optimizations, the shape of the yield loci is different from a set to another, which implies that a local minimum is likely reached. This is confirmed by the analysis of E_2' in Figure 7-27 which shows that the errors associated to the different parameter sets are not identical for a same level of plastic work.

Parameter set "EVOL_1"						
$W_{p,1}$ **= 2.0 J/cm³ (IDENT1ex2)**						
k	C_{12}	C_{13}	C_{22}	C_{23}	C_{33}	C_{66}
-0.5144	-1.0648	2.2381	4.9699	0.9547	-1.3450	-2.2168
k'	C'_{12}	C'_{13}	C'_{22}	C'_{23}	C'_{33}	C'_{66}
0.9577	-0.5316	-1.7240	0.3416	2.1204	0.3450	4.9141
$W_{p,2}$ **= 9.8 J/cm³**						
k	C_{12}	C_{13}	C_{22}	C_{23}	C_{33}	C_{66}
-0.8119	-0.6360	1.6816	3.8171	0.7765	-0.8374	-1.6891
k'	C'_{12}	C'_{13}	C'_{22}	C'_{23}	C'_{33}	C'_{66}
0.7256	-0.6331	-1.8494	0.2706	2.2217	0.2808	4.9684
$W_{p,3}$ **= 19.9 J/cm³**						
k	C_{12}	C_{13}	C_{22}	C_{23}	C_{33}	C_{66}
-0.9835	-0.7964	1.2230	3.1054	0.5405	-1.1919	-1.4359
k'	C'_{12}	C'_{13}	C'_{22}	C'_{23}	C'_{33}	C'_{66}
0.7586	-0.5132	-1.6590	0.3408	1.9545	0.3062	-4.6871
$W_{p,4}$ **= 51.3 J/cm³**						
k	C_{12}	C_{13}	C_{22}	C_{23}	C_{33}	C_{66}
-0.9214	-0.7298	1.1837	3.0301	0.5890	-1.2072	-1.0728
k'	C'_{12}	C'_{13}	C'_{22}	C'_{23}	C'_{33}	C'_{66}
0.7265	-0.5435	-1.6698	0.2926	1.7774	0.1337	-4.6037
$a = 2$, $C_{11} = C'_{11} = 1.0$						

Table 7-16 Yield function CPB06ex2 coefficients for Ti6Al4V based on the experimental data in tension, compression and plane strain corresponding to four levels of plastic work per unit volume (first parameter set denoted "EVOL_1")

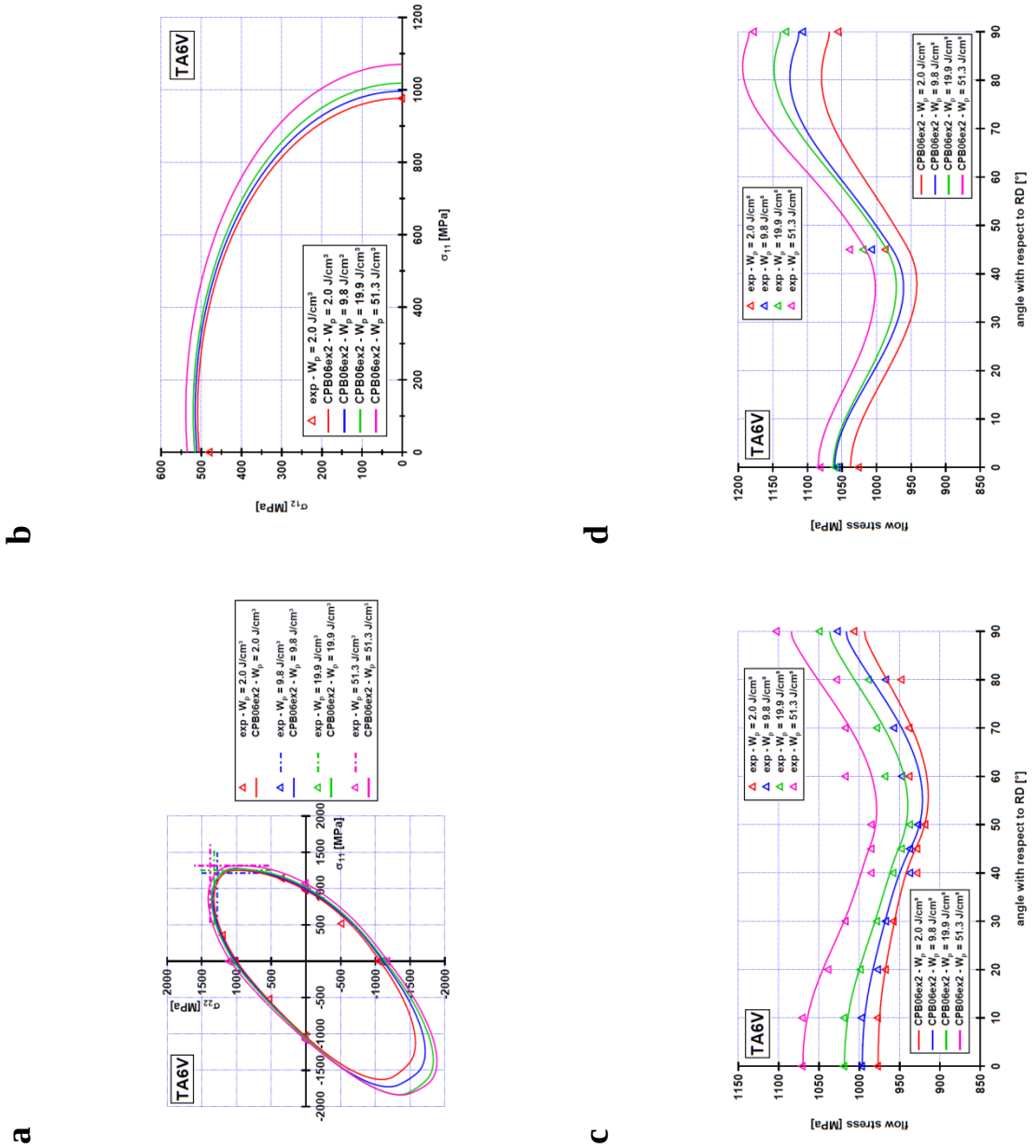

Figure 7-24 Comparison of the theoretical results according to EVOL_1 with the experimental data: (a) yield loci in the biaxial plane $\sigma_{11}-\sigma_{22}$ ($\sigma_{12}=0$); (b) yield loci in the plane $\sigma_{11}-\sigma_{12}$ ($\sigma_{22}=0$); (c) anisotropy in tensile yield stresses; (d) anisotropy in compressive yield stresses

Parameter set "EVOL_2"						
$W_{p,1}$ **= 2.0 J/cm³ (IDENT2ex2)**						
k	C_{12}	C_{13}	C_{22}	C_{23}	C_{33}	C_{66}
0.4922	1.5173	-0.3369	-3.3689	-1.5588	3.6233	-4.7836
k'	C'_{12}	C'_{13}	C'_{22}	C'_{23}	C'_{33}	C'_{66}
0.9957	-3.3008	-1.2519	1.6440	0.7412	-3.0051	-4.6907
$W_{p,2}$ **= 9.8 J/cm³**						
k	C_{12}	C_{13}	C_{22}	C_{23}	C_{33}	C_{66}
0.5942	1.3572	-0.0140	-2.3859	-0.9174	3.5940	-3.8546
k'	C'_{12}	C'_{13}	C'_{22}	C'_{23}	C'_{33}	C'_{66}
0.9734	-3.2890	-1.3854	1.3840	0.4266	-2.8489	-4.6990
$W_{p,3}$ **= 19.9 J/cm³**						
k	C_{12}	C_{13}	C_{22}	C_{23}	C_{33}	C_{66}
0.7149	1.2272	0.1440	-1.8735	-0.4184	3.7459	-3.3207
k'	C'_{12}	C'_{13}	C'_{22}	C'_{23}	C'_{33}	C'_{66}
0.8889	-3.5693	-1.7670	1.2366	-0.0325	-3.1277	-4.9233
$W_{p,4}$ **= 51.3 J/cm³**						
k	C_{12}	C_{13}	C_{22}	C_{23}	C_{33}	C_{66}
0.7207	1.1270	0.2575	-1.4406	-0.5273	3.6505	-3.0666
k'	C'_{12}	C'_{13}	C'_{22}	C'_{23}	C'_{33}	C'_{66}
0.8584	-3.6664	-1.9373	1.0124	-0.1384	-3.3712	4.9443
$a = 2$, $C_{11} = C'_{11} = 1.0$						

Table 7-17 Yield function CPB06ex2 coefficients for Ti6Al4V based on the experimental data in tension, compression and plane strain corresponding to four levels of plastic work per unit volume (second parameter set denoted "EVOL_2")

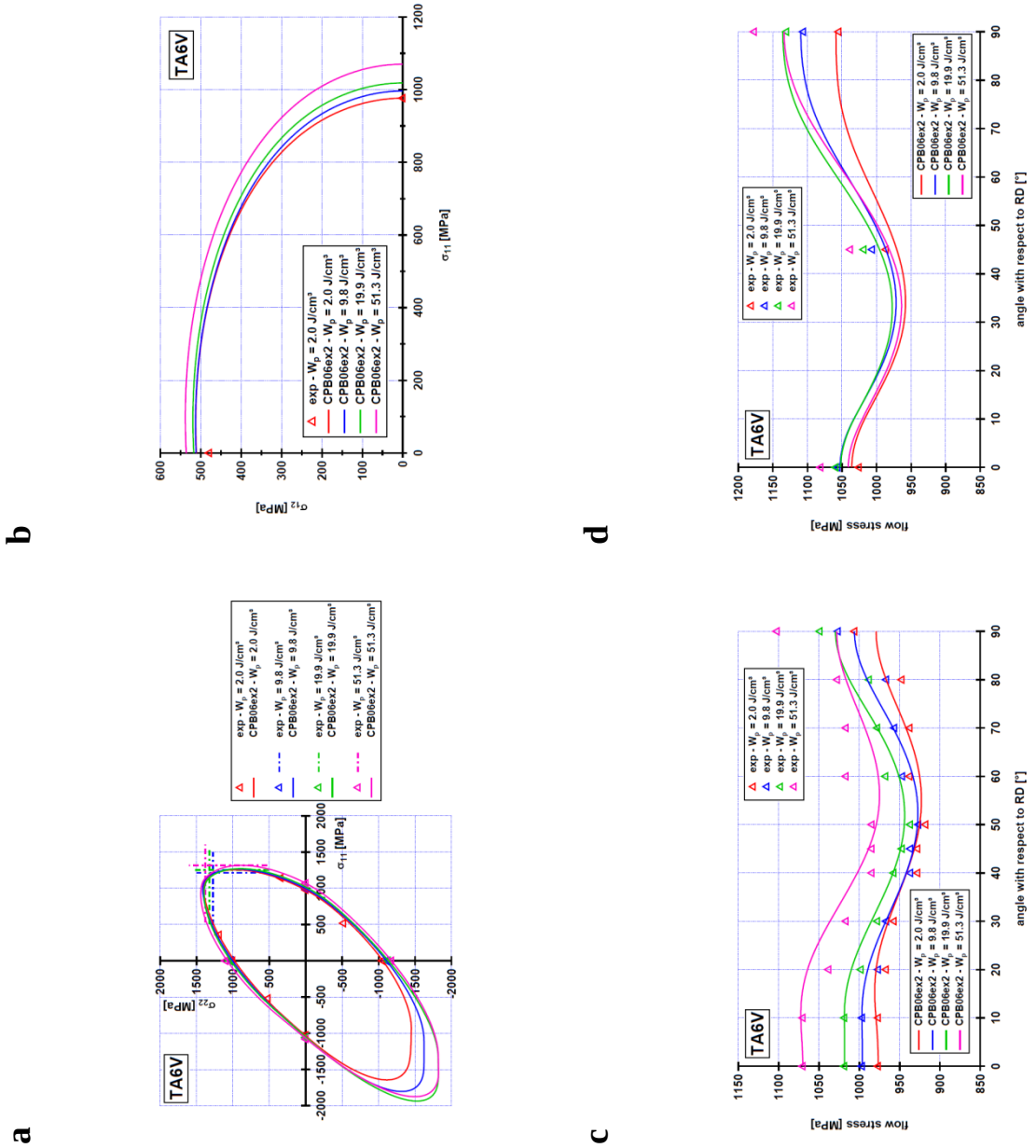

Figure 7-25 Comparison of the theoretical results according to EVOL_2 with the experimental data: (a) yield loci in the biaxial plane $\sigma_{11}-\sigma_{22}$ ($\sigma_{12}=0$); (b) yield loci in the plane $\sigma_{11}-\sigma_{12}$ ($\sigma_{22}=0$); (c) anisotropy in tensile yield stresses; (d) anisotropy in compressive yield stresses

Parameter set "EVOL_3"						
$W_{p,1}$ **= 2.0 J/cm³ (IDENT4ex2)**						
k	C_{12}	C_{13}	C_{22}	C_{23}	C_{33}	C_{66}
-0.1361	4.9247	2.3313	0.3820	-0.1369	4.5720	0.8832
k'	C'_{12}	C'_{13}	C'_{22}	C'_{23}	C'_{33}	C'_{66}
0.5478	0.9354	2.1177	0.2993	-0.1927	1.3701	4.7385
$W_{p,2}$ **= 9.8 J/cm³**						
k	C_{12}	C_{13}	C_{22}	C_{23}	C_{33}	C_{66}
-0.1346	4.9809	2.1131	0.2258	-0.2719	4.2821	1.0543
k'	C'_{12}	C'_{13}	C'_{22}	C'_{23}	C'_{33}	C'_{66}
0.7388	0.8988	1.9805	0.4205	-0.0069	1.3114	4.4020
$W_{p,3}$ **= 19.9 J/cm³**						
k	C_{12}	C_{13}	C_{22}	C_{23}	C_{33}	C_{66}
-0.1232	4.9959	2.0671	0.1307	-0.3957	4.3071	1.1063
k'	C'_{12}	C'_{13}	C'_{22}	C'_{23}	C'_{33}	C'_{66}
0.7752	0.9057	1.9559	0.4015	-0.0142	1.2322	4.4098
$W_{p,4}$ **= 51.3 J/cm³**						
k	C_{12}	C_{13}	C_{22}	C_{23}	C_{33}	C_{66}
-0.0927	4.9366	2.0173	0.1984	-0.5160	4.2106	1.1415
k'	C'_{12}	C'_{13}	C'_{22}	C'_{23}	C'_{33}	C'_{66}
0.8289	0.9467	1.8255	0.4072	0.0398	1.1093	4.2377
$a = 2$, $C_{11} = C'_{11} = 1.0$						

Table 7-18 Yield function CPB06ex2 coefficients for Ti6Al4V based on the experimental data in tension, compression and plane strain corresponding to four levels of plastic work per unit volume (second parameter set denoted "EVOL_3")

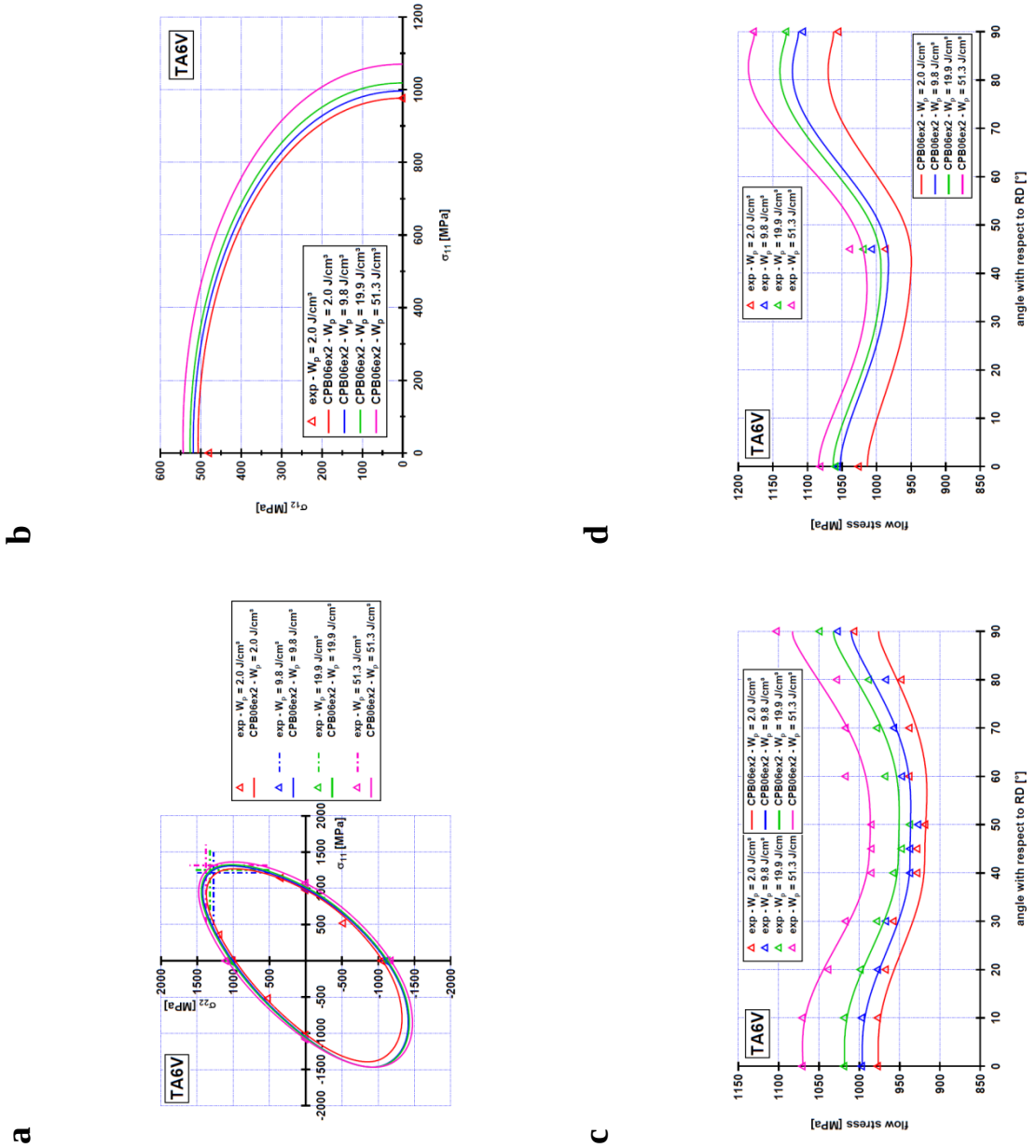

Figure 7-26 Comparison of the theoretical results according to EVOL_3 with the experimental data: (a) yield loci in the biaxial plane $\sigma_{11}-\sigma_{22}$ ($\sigma_{12}=0$); (b) yield loci in the plane $\sigma_{11}-\sigma_{12}$ ($\sigma_{22}=0$); (c) anisotropy in tensile yield stresses; (d) anisotropy in compressive yield stresses

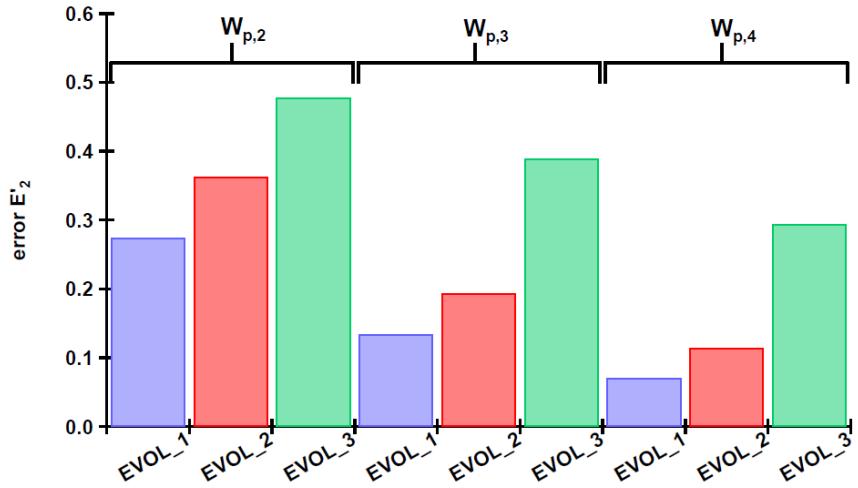

Figure 7-27 Error function E_2' with respect to the identifications EVOL_1, EVOL_2 and EVOL_3 at the levels of plastic work $W_{p,2}$ to $W_{p,4}$

Figure 7-28 and Figure 7-29 compare the experimental stress-strain curves in tension, compression, plane strain, simple shear and cyclic simple shear with the FE results according to EVOL_1, EVOL_2 and EVOL_3. The following observations can be formulated:

- for any parameter set, a very good agreement is obtained between the experimental and numerical results in tension and compression;
- the flow stress in plane strain along RD and 45°-direction is very well predicted by EVOL_1 and EVOL_2 while it is overestimated by EVOL_3. Concerning the behavior along TD, EVOL_1 provides the best result.
- there is a good agreement between the experiments and the FE predictions in simple shear along RD and TD whatever the parameter set. On the other hand, the flow stress along 45°-direction is overestimated by all models, EVOL_2 being the closest to the experimental curve.
- concerning the Bauschinger effect, this one is captured by none of the parameter sets since it is not taken into account in the constitutive law describing the yield locus of the material at different plastic work levels.

In light of these observations and the analysis of the error E_2', it can be concluded that the parameter set **EVOL_1** constitutes the best choice to model the shape evolution of the Ti6Al4V yield locus.

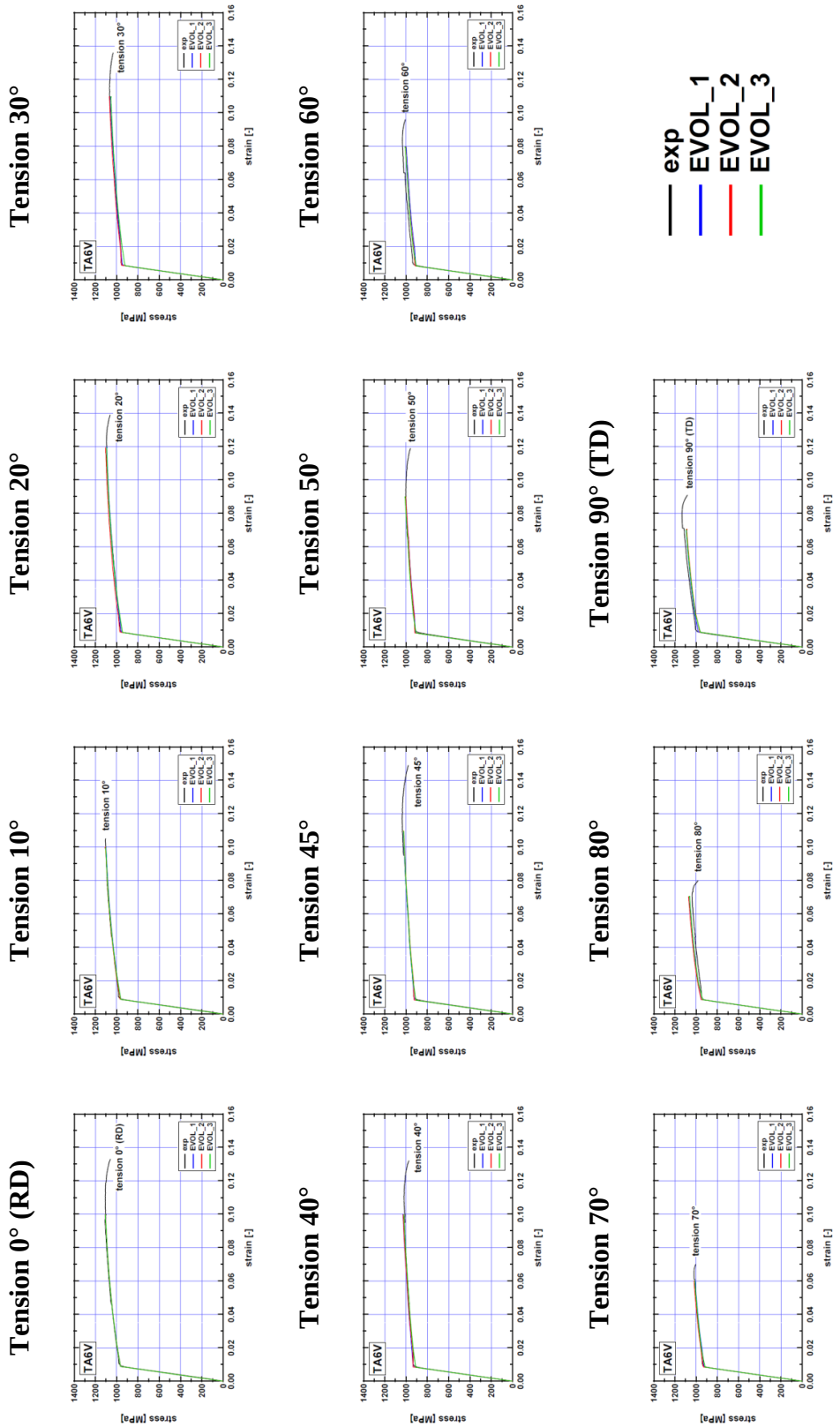

Figure 7-28 Experimental stress-strain curves in tension compared to the numerical predictions according to EVOL_1, EVOL_2 and EVOL_3

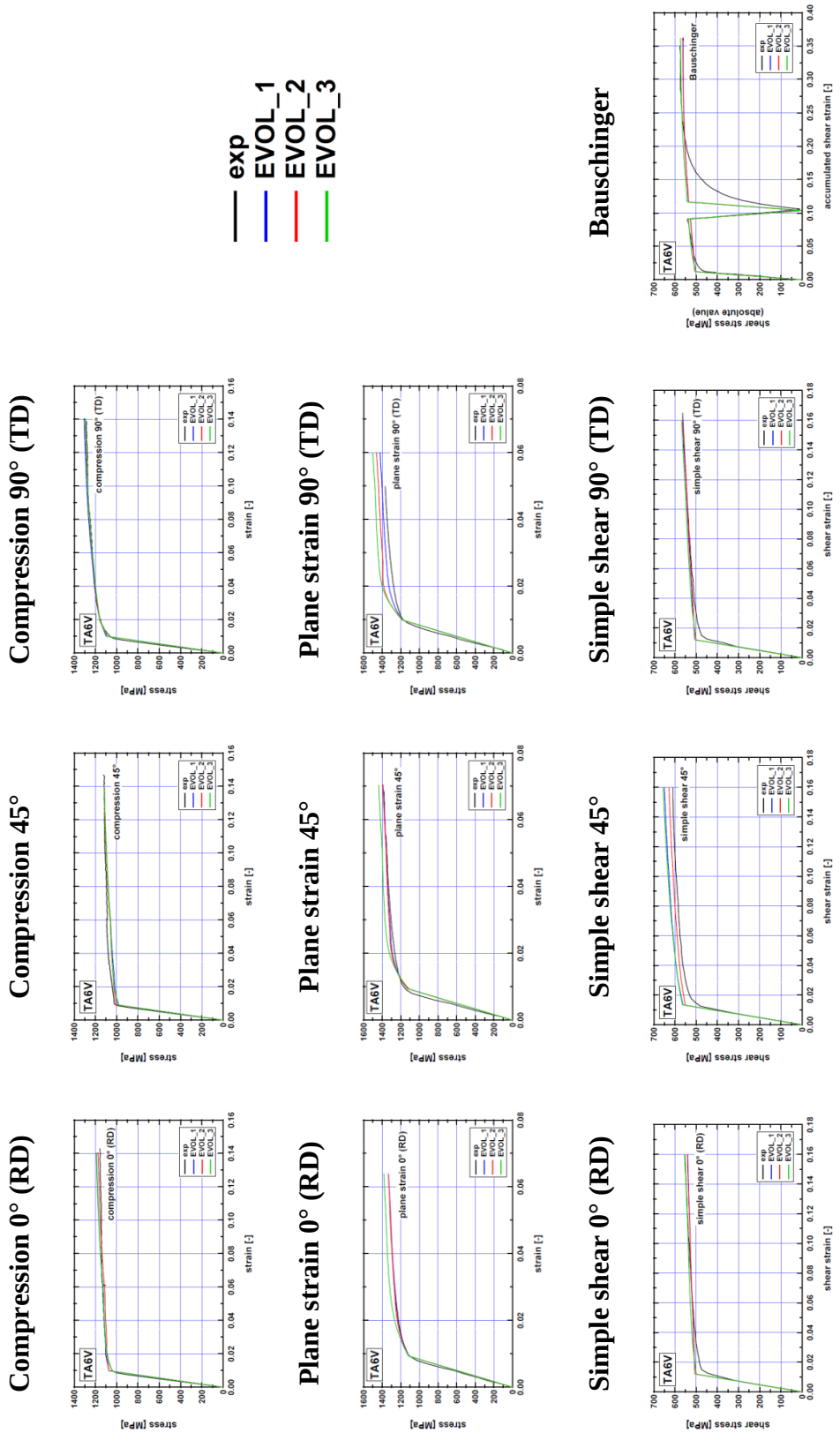

Figure 7-29 Experimental stress-strain curves in compression, plane strain, simple shear and reversed simple shear (Bauschinger) compared to the numerical predictions according to EVOL_1, EVOL_2 and EVOL_3

7.4. Summary and conclusions

In this chapter, one significant conclusion has to be highlighted, namely the fact that the CPB06ex2 criterion is necessary to model the yield locus of Ti6Al4V, but is also sufficient since the accuracy gain obtained when adding more linear transformations (and so more parameters) is very low. Concerning the description of the hardening behavior, the choice of the best modeling is more difficult since the different formulations considered in this study (CPB06ex2 associated to Voce isotropic hardening law, CPB06ex2 associated to Voce isotropic and Armstrong-Frederick kinematic hardening models, evolution of the yield locus shape with the plastic deformation) are generally in good agreement with the experimental data. In the next part of this investigation, three of these formulations will be used to study their ability to predict the mechanical response of Ti6Al4V in the case of the layer compression tests as well as the deep-drawing process, namely:

- yield locus described by **IDENT2ex2 associated to Voce_1** parameter set;
- yield locus described by **IDENT4ex2 associated to Voce_AF_13** parameter set;
- **EVOL_1**.

The choice of these formulations is based on the errors computed in the different identifications.

IV Validation

Chapter 8 Validation for complex strain paths

This chapter deals with the ability of the models identified in Chapter 7 to describe the mechanical behavior of Ti6Al4V under processes with complex strain paths. The layer compression and the deep-drawing tests are simulated using the finite element code LAGAMINE and the experimental data are compared with the numerical results according to the different modelings.

8.1. Layer compression test

8.1.1. Description of the simulations

As it can be seen in Figure 8-1, the symmetry of the problem is taken into account to reduce the size of the simulations and then the computation time. One eighth of the specimen is modeled using adapted boundary conditions (the nodes in the planes $x=0$, $y=0$ and $z=0$ are fixed along the directions x, y and z, respectively) and 2865 BWD3D brick elements with one integration point. The contact between the punch (represented by one undeformable triangular foundation element) and the specimen is considered by adding 191 CFI3D elements on the surface $z=h/2$ where h is the height of the specimen. It has to be noted that the initial size of the elements BWD3D is progressively reduced when coming closer to the contact surface in order to enable the barreling effect occuring during the deformation. For the sake of simplification, the different layers forming the specimens are not modeled and the stack is assumed as a single body.

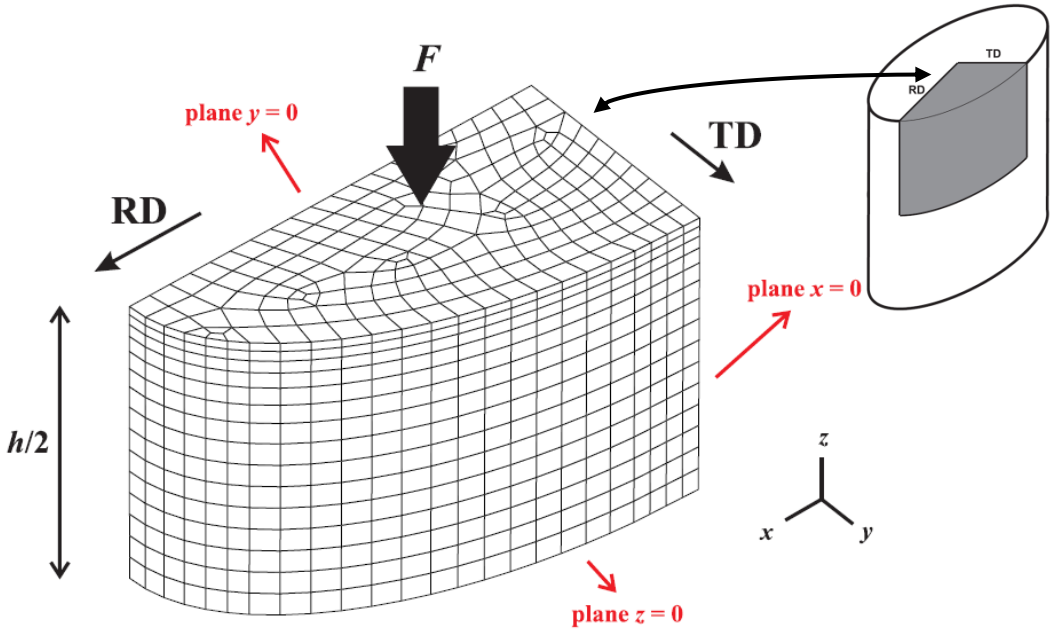

Figure 8-1 Mesh used for the simulations of the layer compression tests

The material behavior is described by one of the parameter sets determined in Chapter 7 (IDENT2ex2 + Voce_1, IDENT4ex2 + Voce_AF_13, EVOL_1) while a Coulomb law is used to model the contact between the tool and the sample. However the punch-specimen friction coefficient is unknown and its identification needs the help of finite element simulations. The effect of friction on the numerical results is the object of the next section.

8.1.2. Effect of friction

In order to investigate the influence of the friction coefficient μ on the finite element results in terms of geometry, strains and stresses, several simulations were achieved using the IDENT2ex2 + Voce_1 model with low and high values of μ (0.0, 0.02, 0.04, 0.2, 0.4).

Figure 8-2 and Figure 8-3 show the evolution of the middle cross-section area and the major to minor axes ratio with the average axial strain according to the different simulations and compared to the experimental data. Two stages can be noticed in the growth rate of the middle cross-section. A low rate is observed during the first stage which is related to the elastic deformation of the material. During the second stage, the specimen undergoes plastic deformations and the growth rate of the area increases. However, the numerical results predict a change in the slope occuring earlier than the one experimentally observed. This difference can be explained by the fact that the specimen was modeled as a single structure, assuming that the layers of the stack are perfectly piled. Actually some defects exist between the different layers, which affects the elastic part of the stress-strain curves as explained in Section 5.2.6 (see Figure 5-45). The slope of the experimental curves in Figure 8-2 changes at an average axial strain level between 2% and 3%, which should be linked to the elastic-plastic transition in the stress-strain curves. In the numerical simulations, as the defects are not taken into account, the elastic part of the stress-strain curve is a straight line and the elastic-plastic transition occurs at a strain level of ~1.1%. For these reasons, the finite element curves are not in good agreement with the experimental results. Nevertheless it can be observed that the growth rate of the middle cross-section is better predicted for high values of the friction coefficient ($\mu = 0.2$ and $\mu = 0.4$).

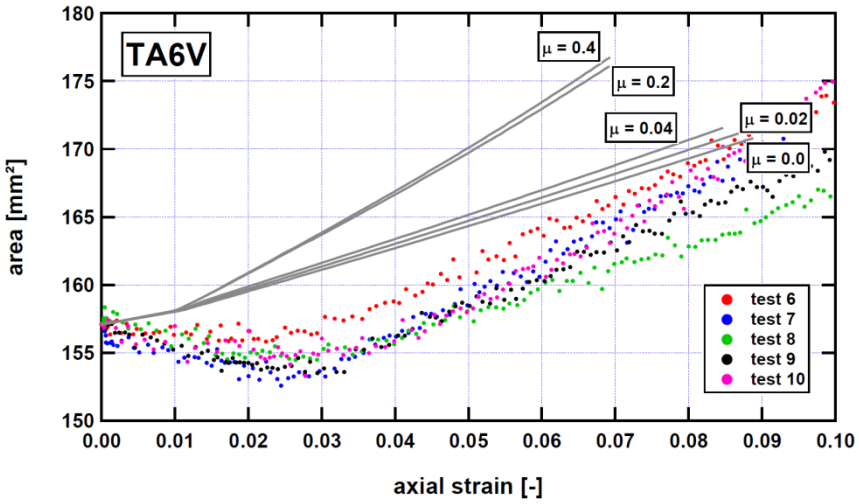

Figure 8-2 Area of the middle cross-section with respect to the average axial strain: comparison between the experimental data and the numerical results for different friction coefficients

The numerical results in Figure 8-3 again show an elastic-plastic transition when the average axial strain reaches ~1.1%. Two cases can also be noticed depending on the value of the friction coefficient: the major axis increases faster than the minor axis when μ is low while the opposite is observed for high values of μ. However it is difficult to determine which friction coefficient is adapted to describe the evolution of the ratio a/b since the experimental data are not reproducible from one test to another.

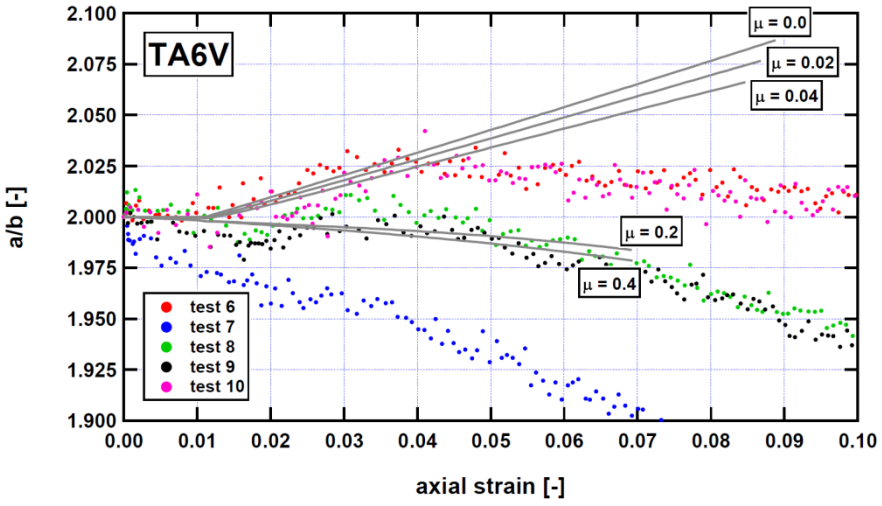

Figure 8-3 Evolution of the major to minor axes ratio with the average axial strain: comparison between the experimental data and the numerical results for different friction coefficients

Figure 8-4 compares the experimental curvature of the specimen in RD with the finite element results for the different friction coefficient values when the average axial strain reaches 7%. Since the barreling effect observed during the experiments is not significant, the curvature is better predicted with low coefficients (0.0, 0.02 and 0.04).

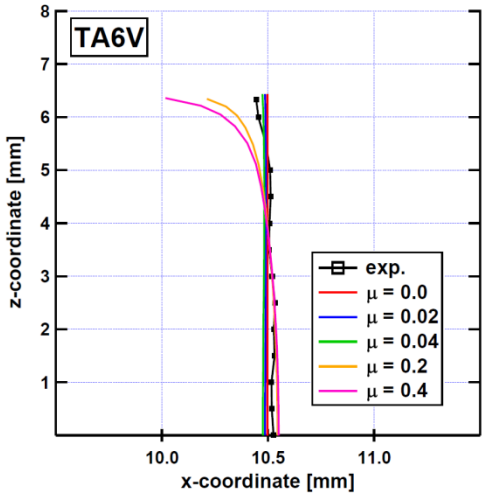

Figure 8-4 Curvature of the specimen lateral surface in RD at an average strain level of 7%: comparison between the experimental data (average) and the numerical results for different friction coefficients

Figure 8-5 shows the axial strain field along the surface of middle cross-section at an average strain level of 7% according to the different experimental tests and numerical simulations. As previously, it can be noticed that low values of μ seem more adapted to fit the distribution of the axial strain. The same observations can be made when comparing the experimental and finite element stress-plastic strain curves (see Figure 8-6). The numerical curve is assessed by the ratio of the predicted axial reaction and the actual middle section area.

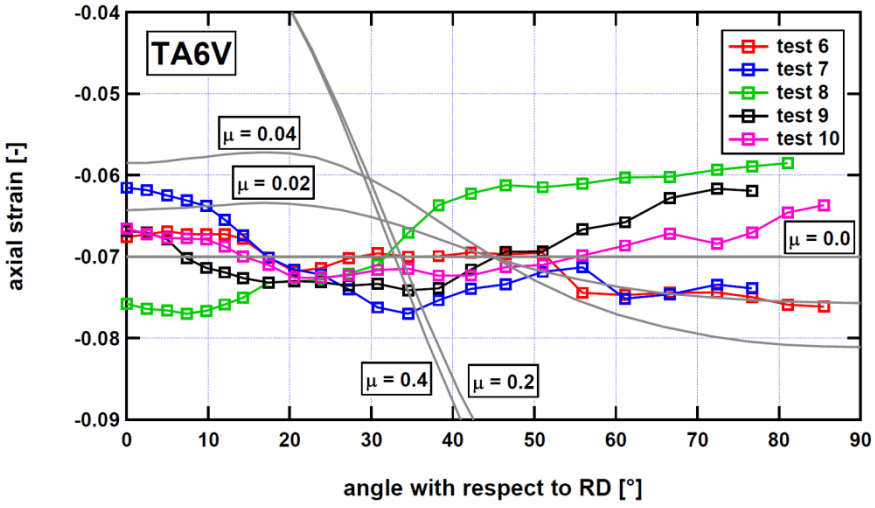

Figure 8-5 Distribution of the axial strain along the surface of the middle cross-section at an average strain level of 7%: comparison between the experimental data and the numerical results for different friction coefficients

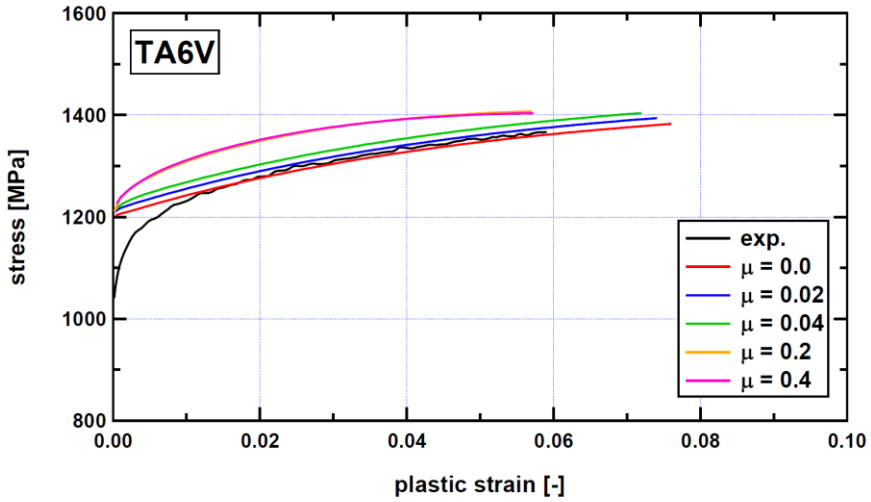

Figure 8-6 Stress-plastic strains curves: comparison between the experimental data (average) and the numerical results for different friction coefficients

8.1.3. Effect of the modeling

The results of the previous section support the conclusion that it is difficult to fix the value of the coefficient μ as the area measurements suggest high values while force and strain measurements identify lower values. For this reason, the ability of the models, denoted IDENT2ex2 + Voce_1, IDENT4ex2 + Voce_AF_13 and EVOL_1 respectively, to predict the mechanical behavior of Ti6Al4V in a layer compression test is investigated by assuming for each model a low and a high values ($\mu = 0.02$ and $\mu = 0.2$ respectively) of the friction coefficient.

Figure 8-7 to Figure 8-11 compare the experimental curves mentioned above with the finite element results according to the different modelings. As in Section 8.1.2, it can be noticed that a low friction coefficient is more adapted to describe the response of the material in some cases (see curvature in Figure 8-9 or axial strain field in Figure 8-10) while the predictions obtained using a higher value of μ are in better agreement with other data (see growth rate of the middle cross-section in Figure 8-7). However it can also be observed that the model can significantly affect the results, especially when an evolution of the yield locus shape is taken into account (EVOL_1). Indeed the variation of the major to minor axes ratio a/b with the deformation according to EVOL_1 (Figure 8-8 (c)) is very different from the finite element curves associated to the other models (Figure 8-8 (a) and (b)). In addition, for $\mu = 0.2$, the barreling effect is less strong and the difference between the maximal and minimal values in the axial strain distribution is reduced when considering that the parameters involved in CPB06ex2 change with the deformation (see Figure 8-9 and Figure 8-10).

In conclusion, although the agreement between the experimental and finite element results is not entirely fulfilled for any modeling, the simulations show that an hardening law taking into account the evolution of the yield locus shape is *qualitatively* more adapted to represent the mechanical behavior of the material than an isotropic hardening formulation, combined or not with a kinematic hardening formulation. However the comparison of the experimental data with the numerical curves also suggest that the friction model assuming a constant coefficient μ is not appropriate, which implies that further investigations are required.

a

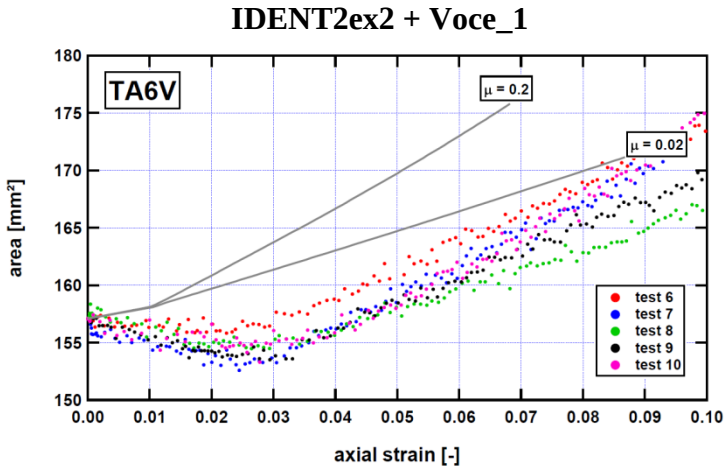

b

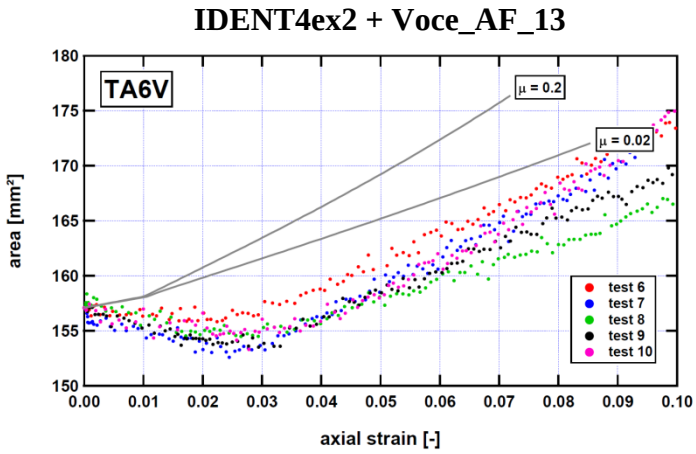

c

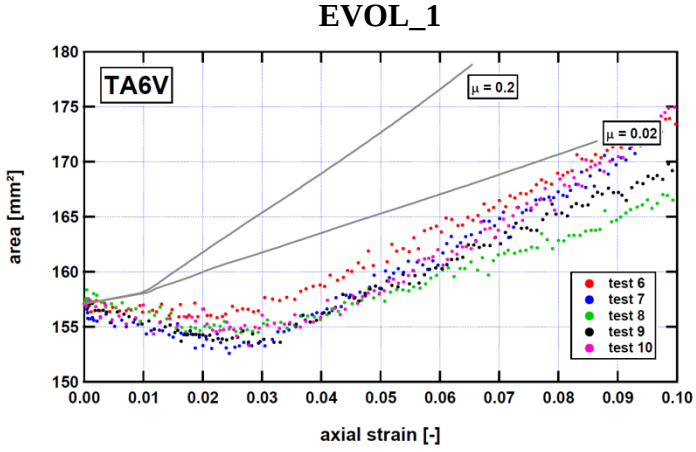

Figure 8-7 Area of the middle cross-section with respect to the average axial strain: comparison between the experimental data and the numerical results according to (a) IDENT2ex2 + Voce_1, (b) IDENT4ex2 + Voce_AF_13, (c) EVOL_1 when $\mu = 0.02$ ***and*** $\mu = 0.2$

a

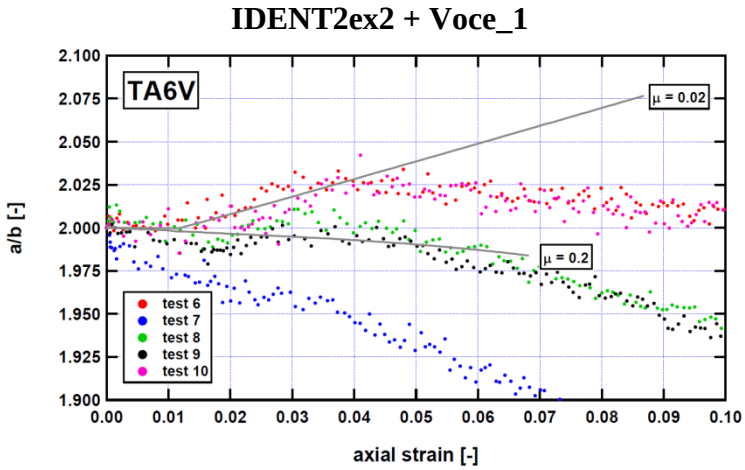

b

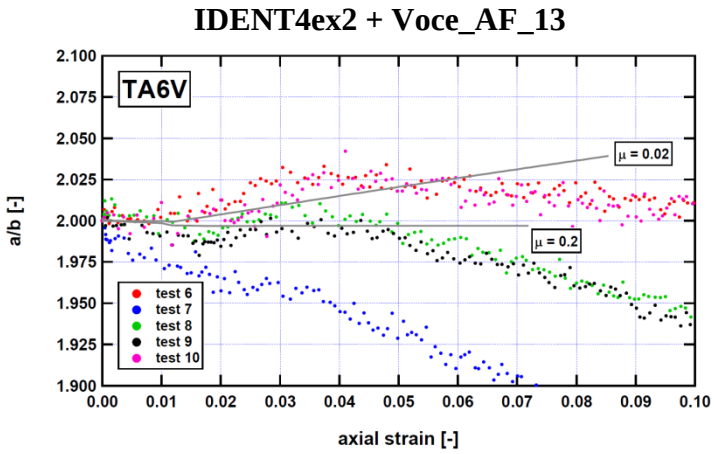

c

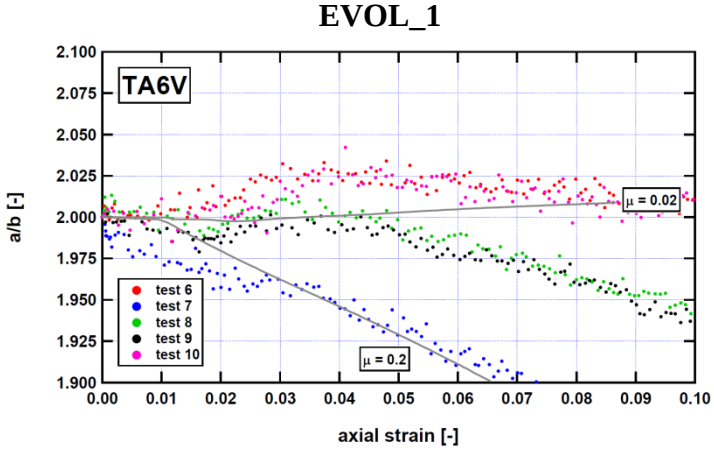

Figure 8-8 Evolution of the major to minor axes ratio with the average axial strain: comparison between the experimental data and the numerical results according to (a) IDENT2ex2 + Voce_1, (b) IDENT4ex2 + Voce_AF_13, (c) EVOL_1 when $\mu = 0.02$ ***and*** $\mu = 0.2$

a

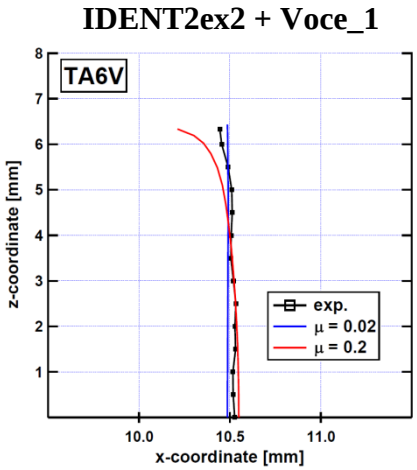

b

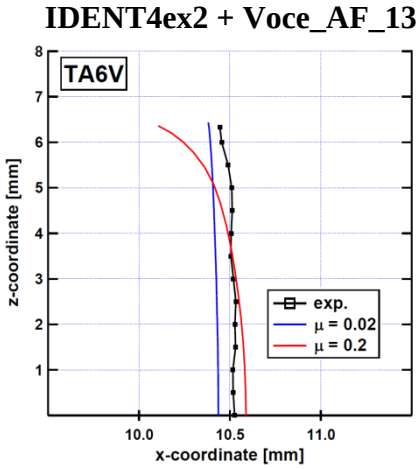

c

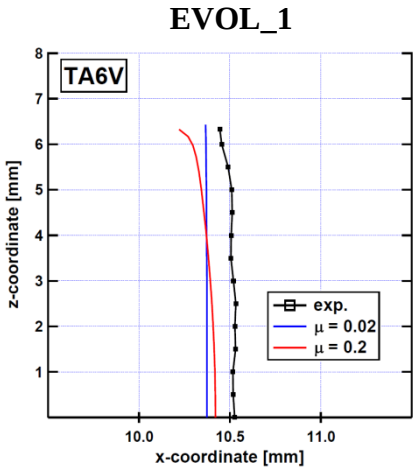

Figure 8-9 Curvature of the specimen lateral surface in RD at an average strain level of 7%: comparison between the experimental data (average) and the numerical results according to (a) IDENT2ex2 + Voce_1, (b) IDENT4ex2 + Voce_AF_13, (c) EVOL_1 when $\mu = 0.02$ ***and*** $\mu = 0.2$

a

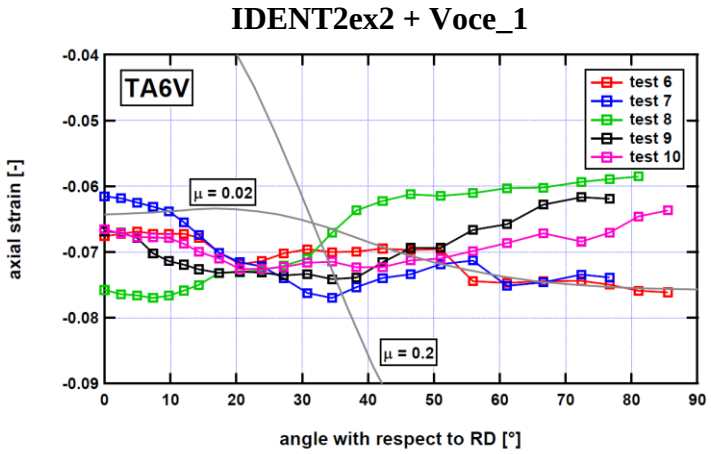

b

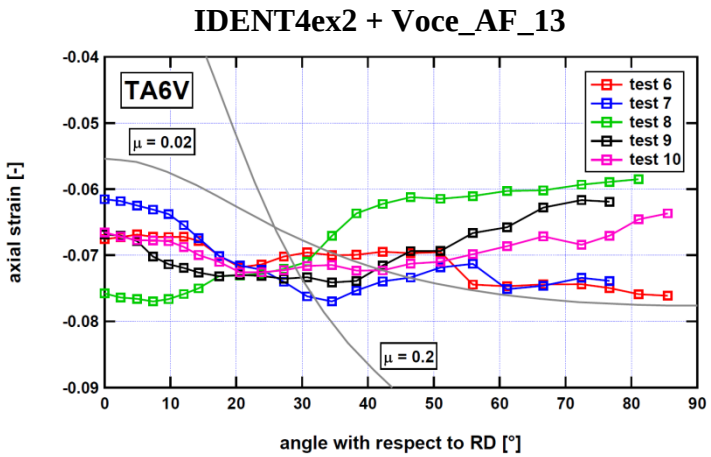

c

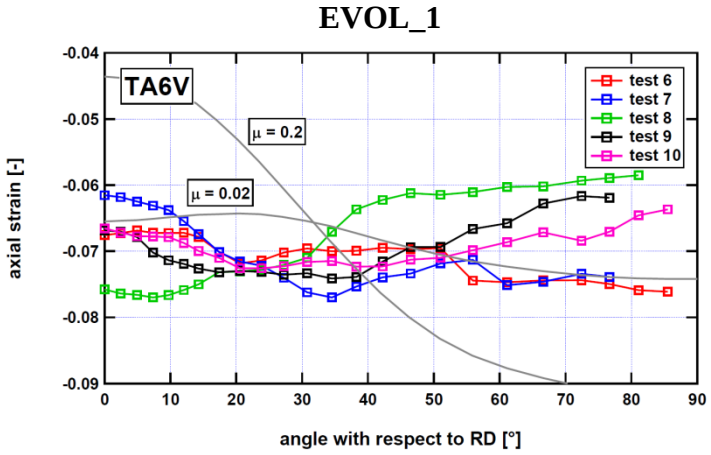

Figure 8-10 Distribution of the axial strain along the middle cross-section at an average strain level of 7%: comparison between the experimental data and the numerical results according to (a) IDENT2ex2 + Voce_1, (b) IDENT4ex2 + Voce_AF_13, (c) EVOL_1 when $\mu = 0.02$ ***and*** $\mu = 0.2$

a

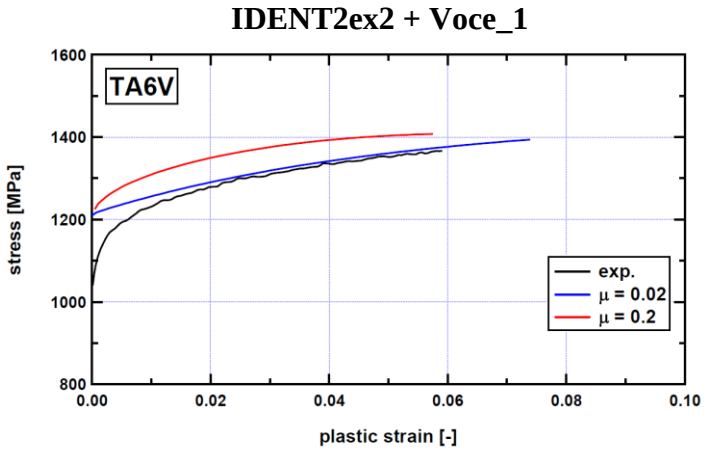

b

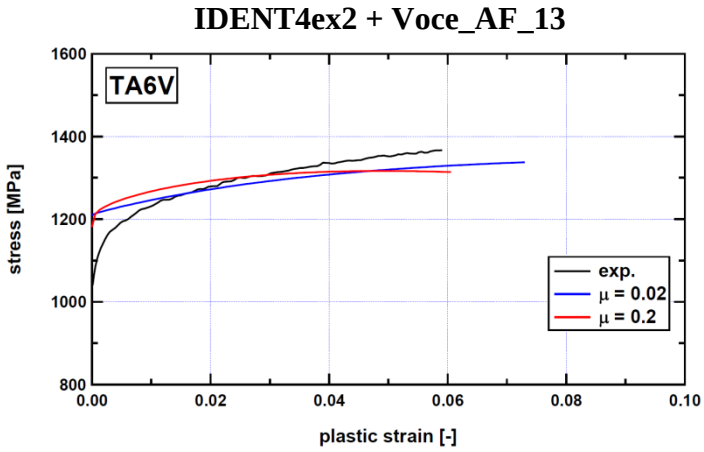

c

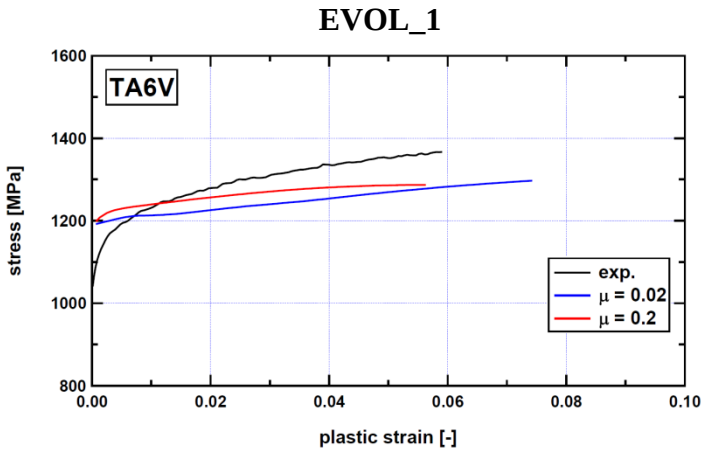

Figure 8-11 Stress-plastic strains curves: comparison between the experimental data (average) and the numerical results according to (a) IDENT2ex2 + Voce_1, (b) IDENT4ex2 + Voce_AF_13, (c) EVOL_1 when $\mu = 0.02$ ***and*** $\mu = 0.2$

8.2. Deep-drawing process

8.2.1. Description of the simulations

As explained in Section 5.2.7, only the data from the tests 4 and 5 are taken into account since some problems (bumps along the wall of the deformed specimen, huge damage) occurred during the other experiments. The deep-drawing process is simulated using the mesh shown in Figure 8-12 (split view) and Figure 8-13 (initial configuration). The dimensions of the blank and the tools are identical for both tests, except for the profile radius r_M of the matrix which is 8 mm in the case of the test 4 and 12 mm in the case of the test 5 (see Table 4-6 and Figure 8-14). In order to reduce the computation time, the symmetry of the blank and the tools is taken into account to model only a quarter of the structure with adapted boundary conditions.

The tools are meshed with undeformable triangular foundation elements. The punch, the blank-holder and the matrix contain 792, 48 and 672 elements respectively. A pilot node is associated to each tool to control its displacement. The blank is built using 6576 BWD3D elements with one integration point divided in three layers. 6864 CFI3D elements are added in order to take into account the contact between the blank and the different tools.

The simulations are performed in four phases:

- The first step consists in applying the blank-holder force while the punch and the matrix are fixed;
- During the second phase, the punch is moved in the *z*-direction (see Figure 8-13) at a speed of 1 mm/s, causing the deformation of the blank;
- At the end of the deep-drawing process, the punch is first removed (third phase) and the matrix is next taken away from the deformed cup (fourth phase).

The third and fourth phases are required since the elastic strains are significant when observing, for example, the different stress-strain curves obtained during the tensile tests carried out on Ti-6Al-4V (see Figure 5-7). A large springback can then occur, which is confirmed by comparing the earing profile of the deformed specimens at the end of the second and fourth phases, respectively (Figure 8-15 and Figure 8-16), where the maximal difference is about 0.73 mm. It has to be noted that it was very difficult to remove the deformed specimens from the matrix after the experimental tests, which attests to a sizeable springback effect.

Different simulations of the deep-drawing tests 4 and 5 were launched using the parameter sets IDENT2ex2 + Voce_1, IDENT4ex2 + Voce_AF_13 and EVOL_1 to describe the mechanical behavior of the Ti-6Al-4V blank, while the contact between the tools and the sheet was modeled by a Coulomb law with a friction coefficient of 0.04 (Teflon was added on both sides of the blank in order to reduce the friction). The penalty coefficients were 500 in the case of the punch-blank contact and 2000 in the other cases (blank-matrix or blank-holder).

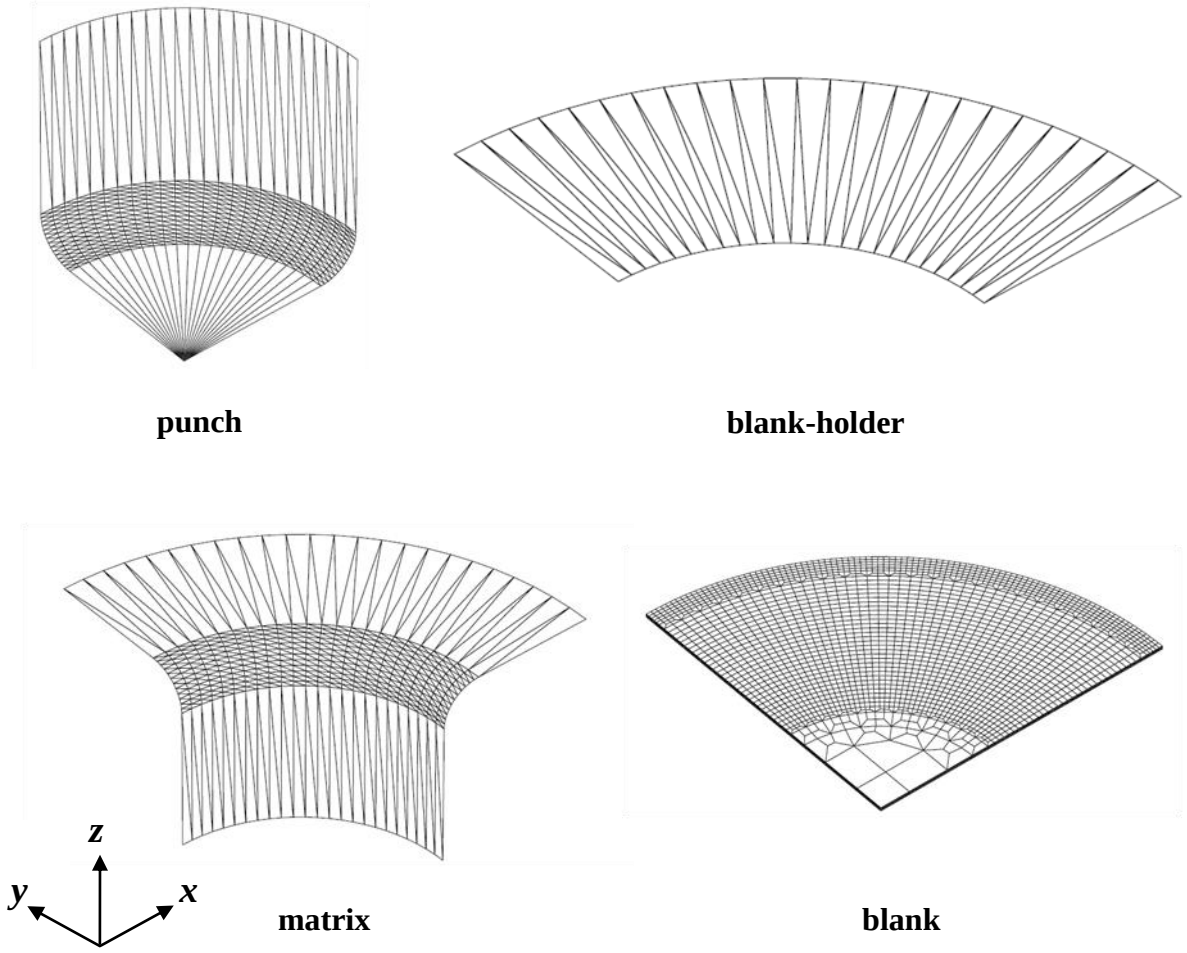

Figure 8-12 Mesh of the blank and the tools (punch, blank-holder, matrix) in split view – configuration corresponding to test 5

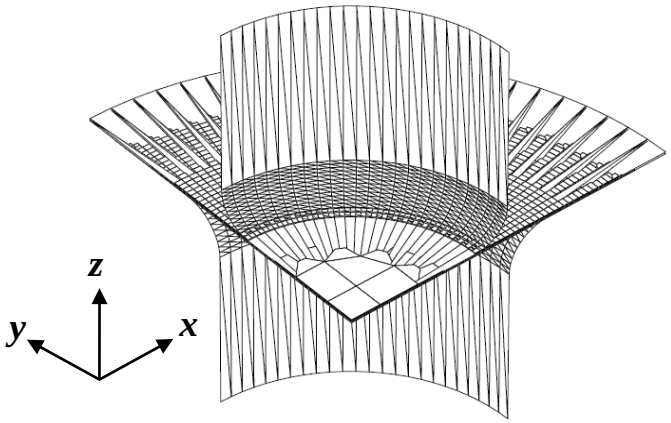

Figure 8-13 Position of the blank and the tools at the beginning of the simulation associated to test 5

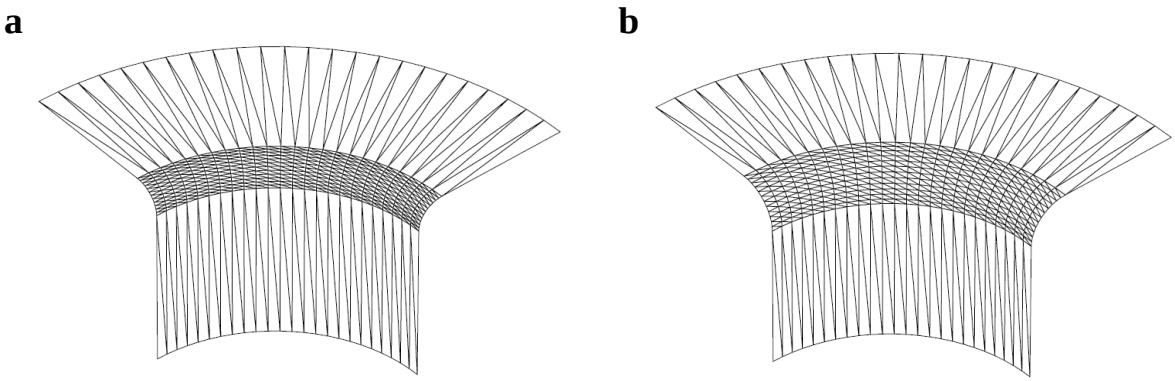

Figure 8-14 Mesh of the matrices: (a) r_M = 8 mm (test 4), (b) r_M = 12 mm (test 5)

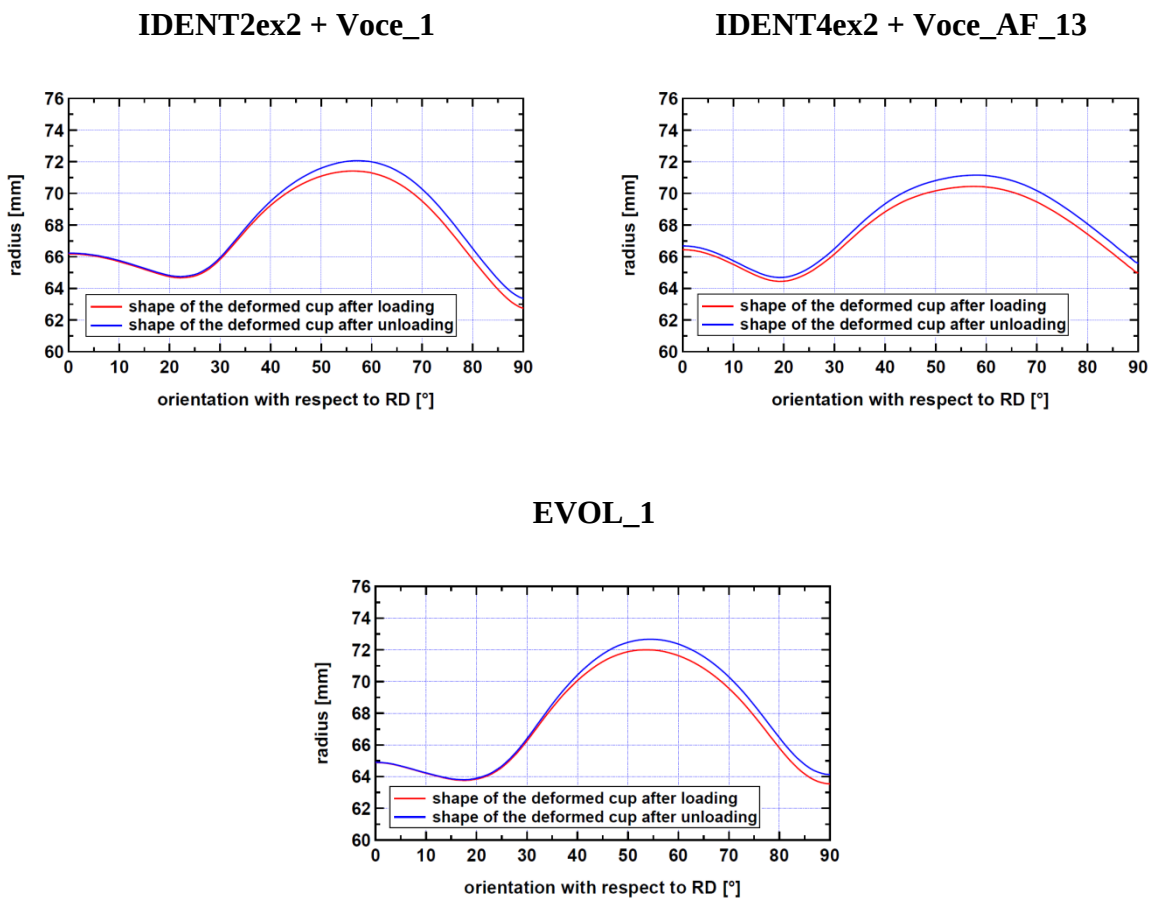

Figure 8-15 Earing profile of the deformed specimen after loading (phase 2 of the simulation) and unloading (phase 4 of the simulation) - results corresponding to test 4

IDENT2ex2 + Voce_1

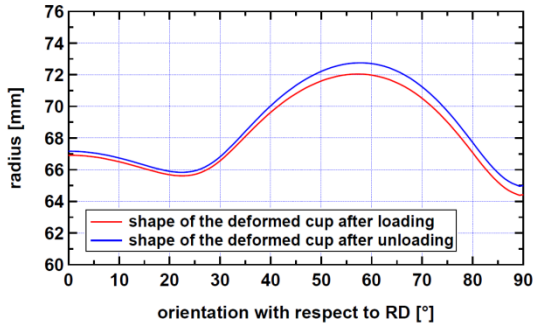

IDENT4ex2 + Voce_AF_13

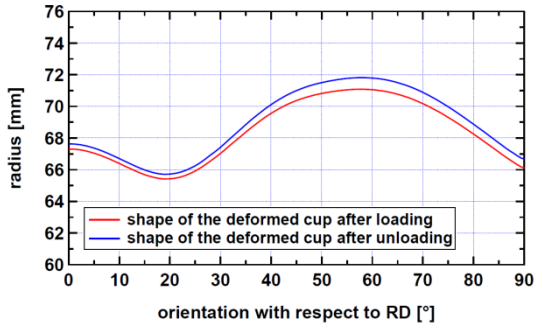

EVOL_1

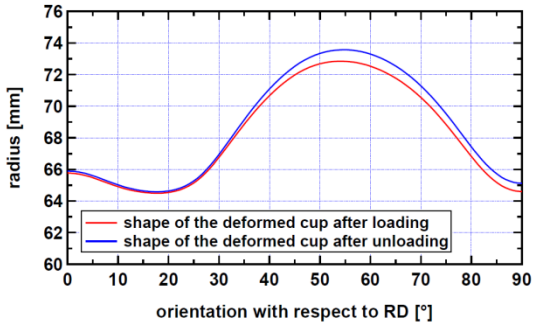

Figure 8-16 Earing profile of the deformed specimen after loading (phase 2 of the simulation) and unloading (phase 4 of the simulation) - results corresponding to test 5

8.2.2. Results

Figure 8-17 compares the experimental force-displacement curves and the earing profiles from the tests 4 and 5 with the simulation results. It can be observed that, as explained in Section 5.2.7, the shape of the earing profile and the number of ears is linked to the distribution of the tensile *r*-ratios. Although the different models capture with great accuracy the *r*-values variation (see Figure 7-7), the agreement between the experimental and theoretical results in cup drawing is less satisfactory. Further experimental tests need to be conducted to assess the effects of friction/tooling on the profile. It can also be noticed some oscillations on the numerical force-displacement curves, especially in test 5. They are caused by the passing of the finite elements on the matrix shoulder where bending occurs (Duchêne (2003)).

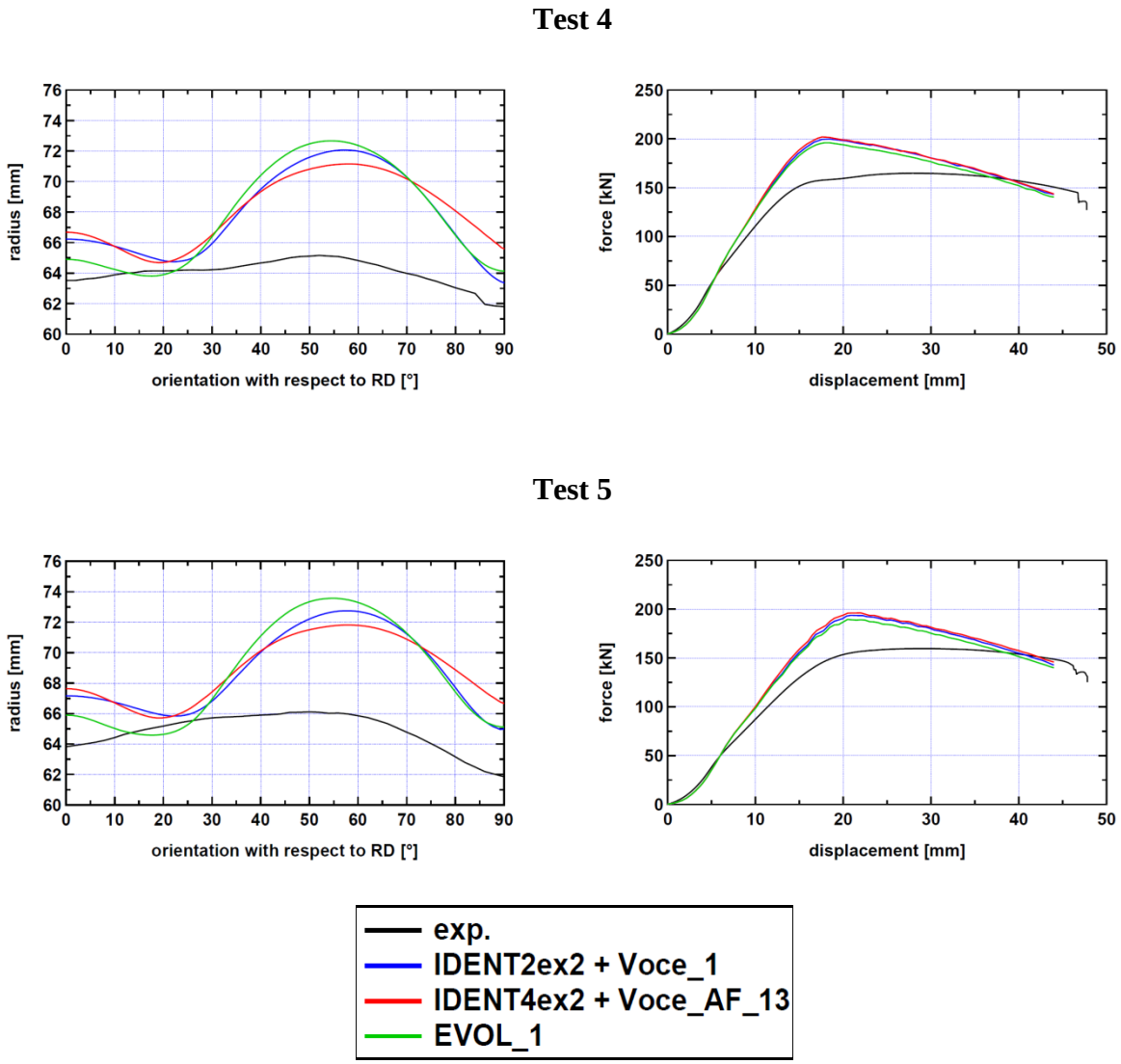

Figure 8-17 Experimental earing profiles and force-displacement curves associated to deep-drawing tests 4 and 5 in comparison with the predictions according to IDENT2ex2 + Voce_1, IDENT4ex2 + Voce_AF_13 and EVOL_1

Table 8-1 gives the maximal absolute errors and the average errors between the experimental data obtained from the deep-drawing tests (earing profile and force-displacement curves) and the associated finite element predictions. The results reveal that:

- the maximal absolute error on the earing profile is minimal in the case of IDENT4ex2 + Voce_AF_13, while the average error is the lowest when IDENT2ex2 + Voce_1 and EVOL_1 are used as model;
- the errors (maximal and average values) on the force are minimal in the case of EVOL_1.

These observations suggest that, as in Section 8.1, the modeling taking into account the evolution of the parameters in the CPB06ex2 yield criterion with the deformation is the best choice to describe the behavior of Ti6Al4V.

Test number	Model	Earing profile		Force	
		Maximal absolute error [mm]	Average error [mm]	Maximal absolute error [kN]	Average error [kN]
Test 4	IDENT2ex2 + Voce_1	7.18	3.86	42.0	16.8
	IDENT4ex2 + Voce_AF_13	6.38	4.02	44.0	17.5
	EVOL_1	7.58	3.88	38.0	15.0
Test 5	IDENT2ex2 + Voce_1	6.85	3.93	39.0	16.3
	IDENT4ex2 + Voce_AF_13	6.11	4.03	41.0	17.9
	EVOL_1	7.55	3.94	35.0	14.3

Table 8-1 Maximal absolute errors and average errors between finite element results and experimental data associated to deep-drawing tests (see Figure 8-17)

8.3. Conclusion

The comparison of the experimental data from the layer compression tests and the deep-drawing processes with the numerical predictions according to IDENT2ex2 + Voce_1, IDENT4ex2 + Voce_AF_13 and EVOL_1 shows that further studies are required to develop a model able to describe the mechanical behavior of Ti6Al4V. Nevertheless, it was shown that the finite element results given by EVOL_1 are in better agreements with the experiments than the other models. In addition, it has to be noted that the formulations proposed in this thesis are more adapted to Ti6Al4V than the classical ones. Figure 8-18 compares the curves given in Figure 8-17 (test 4) with the finite element results obtained when the material behavior is modeled using Hill'48 yield criterion and Voce isotropic hardening law. The Hill'48 parameters were determined from the tensile *r*-ratios in RD, 45°-direction and TD (see Figure 5-15), while the hardening parameters in Table 7-12 (Voce_1 set) were used. It can be noticed that Hill'48 predicts a symmetric earing profile with a maximal value at 45° while the experiment and the finite element results associated to CPB06ex2 show an asymmetric profile with a maximal value between 50° and 60°. These observations confirm that CPB06ex2 criterion is required to model the yield locus of Ti6Al4V.

The results of this chapter especially suggest to investigate the material response under different strain paths in compression in order to collect more data concerning the shape of the yield locus in the third quadrant. Indeed the experimental campaign described in Chapter 4 and Chapter 5 is mainly focused on monotonic tests enabling a good identification of the yield surface in the first quadrant. However, in light of the strength asymmetry of Ti6Al4V between tension and compression, it is necessary to fill the lack of data concerning the mechanical behavior of the alloy under compression. In addition, friction also plays a significant part on

the results, which accounts for the sake to conduct additional studies in order to obtain more accurate information about its effect on the layer compression and deep-drawing experiments.

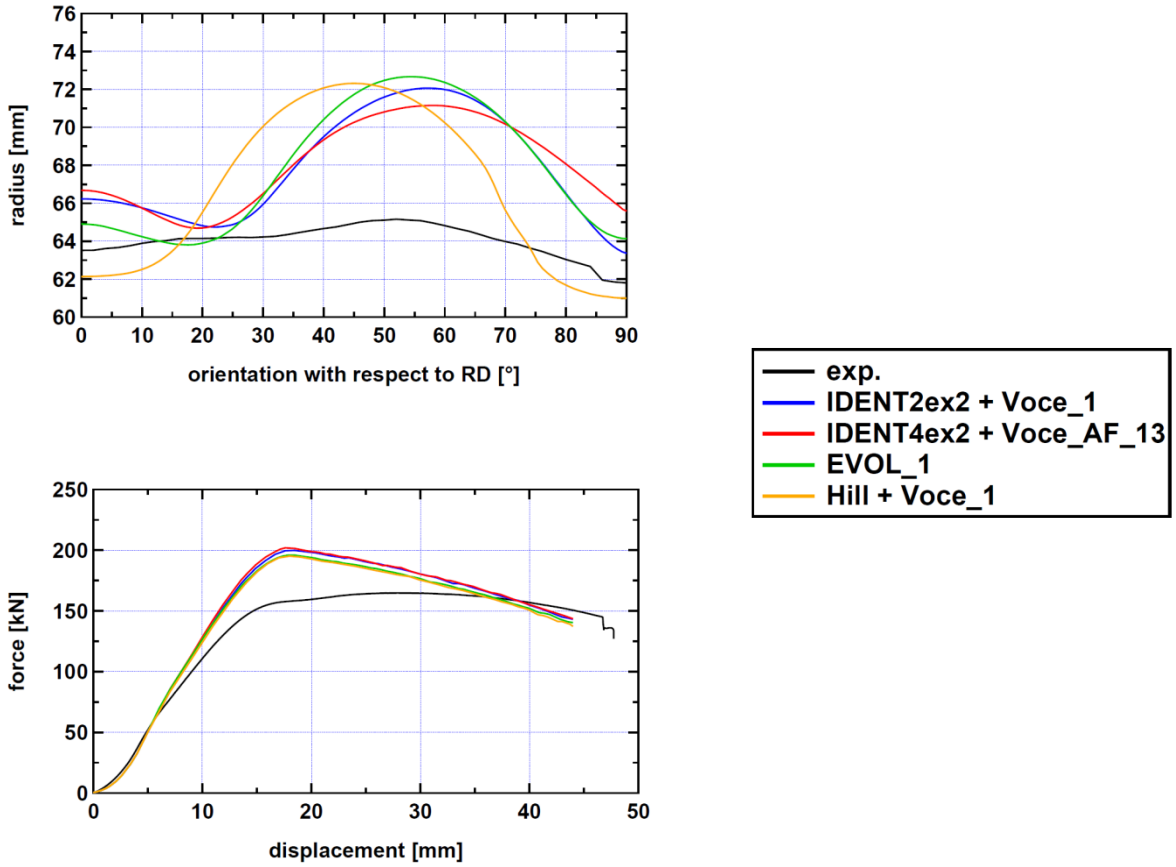

Figure 8-18 Experimental earing profiles and force-displacement curves associated to deep-drawing tests 4 in comparison with the predictions according to IDENT2ex2 + Voce_1, IDENT4ex2 + Voce_AF_13, EVOL_1 and Hill + Voce_1

Chapter 9 General conclusion

The quasi-static mechanical behavior of a 0.6 mm thick Ti6Al4V sheet at room temperature was experimentally investigated under different loading conditions. Monotonic tests (tension, compression, plane strain, simple shear) revealed the anisotropy and the tension-compression asymmetry displayed by the material.

The CP06ex*n* criteria were chosen to model the yield locus of the material since they are able to take into account both the anisotropy and the strength differential effect exhibited by hcp metals. Concerning the hardening modeling, two formulations were considered and associated to CPB06ex*n*: (1) Voce isotropic hardening law coupled with Armstrong-Frederick kinematic hardening law; (2) an evolution of the yield locus shape with the plastic work. The two phenomenological models were implemented into LAGAMINE finite element code.

The identification of the anisotropy coefficients and strength differential parameters involved in the yield criteria was achieved using the classical simulated annealing algorithm and the results from the monotonic tests. It was shown that CPB06ex2 criterion is required to represent the yield surface of Ti6Al4V with a good accuracy. Then three sets of hardening parameters were identified, each one corresponding to the following cases respectively: (1) hardening described by Voce isotropic law; (2) hardening described by a mixed Voce isotropic – Armstrong-Frederick kinematic law; (3) hardening described by a law taking into account the evolution of the parameters in CPB06ex2 with the plastic work.

The ability of the three phenomenological models proposed in this investigation to describe the material response was tested in the finite element simulation of a layer compression test and a deep-drawing process. The comparison of the numerical predictions with the experimental results shows that better results are obtained when the evolution of the yield locus shape with the deformation is regarded, although the agreement between experimental and finite element curves is not entirely satisfactory.

The original contributions of this thesis are:

- the production of a large set of experimental data on the mechanical behavior of Ti6Al4V in sheet form;
- the implementation of the CPB06ex*n* yield criteria in association with a hardening model able to take into account the evolution of the yield locus shape into LAGAMINE;
- the development of numerical tools for the parameter identification based on the simulated annealing algorithm.

Note that these contributions have already helped in other studies (see for instance Tuninetti *et al.* (2015)).

Future investigations will be required to improve the modeling of the Ti6Al4V mechanical behavior and to simultaneously predict the strength differential effect displayed by the material, its anisotropy and its response in complex processes. A first step would be to perform additional tests in compression in order to fix the shape of the yield locus in the third quadrant of the biaxial plane $\sigma_{11}-\sigma_{22}$. It could be planned to conduct uniaxial compression experiments in more directions than the three usual ones (RD, 45°, TD) and to determine both the yield stresses and *r*-ratios since it was shown that the latter can improve the parameter identification. Another suggestion would be to develop a device which would be able to submit specimens to a compressive plane strain state. A second step would be to determine the equibiaxial point on the yield locus using an experimental device adapted to Ti6Al4V since the tests conducted by Prof. Kuwabara at TUAT (equibiaxial tests on cruciform specimens) and by Prof. Thuillier at Université de Bretagne-Sud (bulge tests) encountered problems of failure occurring in parts of the specimens other than the gage zones.

It has to be recalled that the yield locus of Ti6Al4V was identified at several levels of plastic work from different monotonic tests and therefore each surface gathers data associated to different states of the material. However it is not possible to avoid this problem when determining the yield locus from experimental tests only. For this reason, it could be interesting to use a reliable microscopic model which would be able to take into account the evolution of the texture in hcp metals and to combine the model predictions with the experimental data in order to obtain a better knowledge on the evolution of the yield locus shape with the plastic deformation. In addition, the microscopic model could generate additional data (for instance yield stresses relative to strain paths which are not possible to experimentally achieve) which would be included in the identification of the anisotropy coefficients and the strength differential parameters involved in CPB06ex*n* yield criteria.

Finally, this thesis is focused on the quasi-static behavior of Ti6Al4V, but the material is also very sensitive to the strain rate and the temperature. As explained in the first chapter, several investigations have already been conducted on the alloy at high strain rates and high temperatures. However the proposed models usually neglect the tension-compression asymmetry and the distortional hardening exhibited by Ti6Al4V, even its anisotropy. Nevertheless recent studies such as the work of Tuninetti (2014) provide some suggestions of phenomenological modelings adapted to hcp materials and taking into account its dependence to strain rate and temperature. Peirs (2012) proposed a characterization and a modeling of the dynamic behavior of Ti6Al4V, while López (2014) used the VPSC model to capture the anisotropy of the alloy for a wide range of strain rate and temperature conditions. Another challenge concerning the modeling of hcp metals is the damage evolution. Cazacu and Stewart (2009) and Revil-Baudard *et al.* (2012) recently presented a new constitutive model for voided polycrystals that incorporates the effects of the tension-compression asymmetry of the incompressible matrix on the overall dilatational plastic behavior. In conclusion, it can be noticed that the Ti6Al4V mechanical response is studied under various facets, but it would be needed to share and gather all these data in order to improve the modeling of the material behavior.

Appendix A Convexity of the isotropic and anisotropic yield functions proposed by Cazacu *et al.* (2006)

The isotropic yield function is written as:

$$\varphi_{\text{iso}} = \left(|s_1| - ks_1\right)^a + \left(|s_2| - ks_2\right)^a + \left(|s_3| - ks_3\right)^a \tag{A.1}$$

φ_{iso} is convex if its Hessian matrix $\mathbf{H}$ is positive semi-definite, *i.e.*:

$$\boldsymbol{\sigma}^T \, \mathbf{H} \, \boldsymbol{\sigma} = \sigma_i \, H_{ij} \, \sigma_j = \sigma_i \, \frac{\partial^2 \varphi_{\text{iso}}}{\partial \sigma_i \partial \sigma_j} \, \sigma_j \geq 0 \qquad \forall \boldsymbol{\sigma} \tag{A.2}$$

where $\boldsymbol{\sigma}$ is the vector containing the principal stresses σ_i ($i = 1 \ldots 3$). Since the eigenvalues s_i ($i = 1 \ldots 3$) of the stress deviator are given by:

$$\mathbf{s} = \begin{pmatrix} s_1 \\ s_2 \\ s_3 \end{pmatrix} = \begin{bmatrix} 2/3 & -1/3 & -1/3 \\ -1/3 & 2/3 & -1/3 \\ -1/3 & -1/3 & 2/3 \end{bmatrix} \begin{pmatrix} \sigma_1 \\ \sigma_2 \\ \sigma_3 \end{pmatrix} = \mathbf{L} \, \boldsymbol{\sigma} \tag{A.3}$$

the Hessian matrix can be rewritten as follows:

$$H_{ij} = \frac{\partial^2 \varphi_{\text{iso}}}{\partial \sigma_i \partial \sigma_j} = L_{ki} \, \frac{\partial^2 \varphi_{\text{iso}}}{\partial s_k \partial s_l} \, L_{lj} = L_{ki} \, \bar{H}_{kl} \, L_{lj} \tag{A.4}$$

where $\bar{H}_{ij} = \dfrac{\partial^2 \varphi_{\text{iso}}}{\partial s_i \partial s_j}$. It can be noticed that Equation (A.2) combined with Equation (A.4) leads to:

$$\sigma_i \, H_{ij} \, \sigma_j = \sigma_i \, L_{ki} \, \bar{H}_{kl} \, L_{lj} \, \sigma_j = s_k \, \bar{H}_{kl} \, s_l \tag{A.5}$$

In addition, the matrix $\bar{\mathbf{H}}$ is diagonal:

$$\bar{\mathbf{H}} = \begin{bmatrix} \bar{H}_1 & 0 & 0 \\ 0 & \bar{H}_2 & 0 \\ 0 & 0 & \bar{H}_3 \end{bmatrix} \tag{A.6}$$

where the components $\bar{H}_i$ $(i = 1 \ldots 3)$ are given by:

$$\bar{H}_i = a(a-1)\left[\operatorname{sign}(s_i) - k\right]^a s_i^{a-2} \tag{A.7}$$

Therefore convexity is satisfied if $s_i \, \bar{H}_{ij} \, s_j \geq 0 \;\; \forall \mathbf{s}$, *i.e.* $\bar{H}_i \geq 0 \;\; \forall i$. It implies that the following conditions are required:

- $a \geq 1$;
- if $s_i \geq 0$, $\bar{H}_i = a(a-1)(1-k)^a s_i^{a-2}$ and so $k \leq 1$;
- if $s_i \leq 0$, $\bar{H}_i = a(a-1)(-1)^a (1+k)^a s_i^{a-2}$ and so $k \geq -1$.

The convexity of the anisotropic yield function can be proved in a similar way. Indeed, the function is written as follows:

$$\varphi_{\text{ani}} = \left(|\Sigma_1| - k\Sigma_1\right)^a + \left(|\Sigma_2| - k\Sigma_2\right)^a + \left(|\Sigma_3| - k\Sigma_3\right)^a \tag{A.8}$$

where:

$$\boldsymbol{\Sigma} = \begin{pmatrix} \Sigma_1 \\ \Sigma_2 \\ \Sigma_3 \end{pmatrix} = \begin{bmatrix} C_{11} & C_{12} & C_{13} \\ C_{12} & C_{22} & C_{23} \\ C_{13} & C_{23} & C_{33} \end{bmatrix} \begin{bmatrix} 2/3 & -1/3 & -1/3 \\ -1/3 & 2/3 & -1/3 \\ -1/3 & -1/3 & 2/3 \end{bmatrix} \begin{pmatrix} \sigma_1 \\ \sigma_2 \\ \sigma_3 \end{pmatrix} = \mathbf{C}\,\mathbf{L}\,\boldsymbol{\sigma} = \tilde{\mathbf{C}}\,\boldsymbol{\sigma} \tag{A.9}$$

Since

$$\sigma_i \, H_{ij} \, \sigma_j = \sigma_i \, \frac{\partial^2 \varphi_{\text{ani}}}{\partial \sigma_i \partial \sigma_j} \, \sigma_j = \sigma_i \, \tilde{C}_{ki} \, \frac{\partial^2 \varphi_{\text{ani}}}{\partial \Sigma_k \partial \Sigma_l} \, \tilde{C}_{lj} \, \sigma_j = \Sigma_k \, \tilde{H}_{kl} \, \Sigma_l \tag{A.10}$$

where

$$\tilde{H}_{ij} = \frac{\partial^2 \varphi_{\text{ani}}}{\partial \Sigma_i \partial \Sigma_j} \tag{A.11}$$

and the matrix $\tilde{\mathbf{H}}$ is also diagonal:

$$\tilde{\mathbf{H}} = \begin{bmatrix} \tilde{H}_1 & 0 & 0 \\ 0 & \tilde{H}_2 & 0 \\ 0 & 0 & \tilde{H}_3 \end{bmatrix} \tag{A.12}$$

with

$$\tilde{H}_i = a(a-1)\left[\text{sign}(\Sigma_i) - k\right]^a \Sigma_i^{a-2}, \quad i = 1\ldots 3 \tag{A.13}$$

the Hessian matrix will be positive semi-definite when $\tilde{H}_i \geq 0 \quad \forall i$. The same conclusions ensuring that the yield function is convex are obtained as previously, namely $a \geq 1$ and $-1 \leq k \leq 1$.

It has to be mentioned that the proof of convexity was done in Cazacu *et al.* (2006).

Appendix B Insensitivity of CPB06 yield function to hydrostatic pressure

The CPB06 orthotropic yield criterion is:

$$\varphi = \left(\left|\Sigma_1\right| - k\Sigma_1\right)^a + \left(\left|\Sigma_2\right| - k\Sigma_2\right)^a + \left(\left|\Sigma_3\right| - k\Sigma_3\right)^a \tag{B.1}$$

where Σ_i $(i = 1\ldots3)$ are the eigenvalues of the transformed stress tensor $\boldsymbol{\Sigma}$ defined as:

$$\boldsymbol{\Sigma} = \mathbf{C} : \mathbf{s} \tag{B.2}$$

$\mathbf{s}$ is the stress deviator while $\mathbf{C}$ is a constant 4th-order tensor. Let $p = \sigma_{ii}$ denote the mean stress. The yield function f will be said insensitive to hydrostatic pressure when:

$$\frac{\partial \varphi}{\partial p} = \frac{\partial \varphi}{\partial \Sigma_k} \frac{\partial \Sigma_k}{\partial \Sigma_{ij}} \frac{\partial \Sigma_{ij}}{\partial p} = 0 \tag{B.3}$$

If $\frac{\partial \Sigma_{ij}}{\partial p} = 0$ is proved, the condition of plastic incompressibility will be satisfied.

Since

$$\boldsymbol{\Sigma} = \mathbf{C} : \mathbf{s} = \mathbf{C} : \left(\mathbf{L} : \boldsymbol{\sigma}\right) = \tilde{\mathbf{C}} : \boldsymbol{\sigma} \tag{B.4}$$

where

$$\tilde{\mathbf{C}} = \mathbf{C} : \mathbf{L} \tag{B.5}$$

and $\mathbf{L}$ is the 4th-order deviatoric projection transforming a 2nd-order tensor in its deviator, it results in:

$$\frac{\partial \Sigma_{ij}}{\partial p} = \frac{\partial \left(\tilde{C}_{ijkl}\ \sigma_{kl}\right)}{\partial \sigma_{mm}} = \tilde{C}_{ijkl}\ \delta_{kl} = \tilde{C}_{ijkk} \tag{B.6}$$

In the orthotropy axes, the tensors $\mathbf{C}$ and $\mathbf{L}$ are respectively represented by:

$$\mathbf{C} = \begin{bmatrix} C_{11} & C_{12} & C_{13} & 0 & 0 & 0 \\ C_{12} & C_{22} & C_{23} & 0 & 0 & 0 \\ C_{13} & C_{23} & C_{33} & 0 & 0 & 0 \\ 0 & 0 & 0 & C_{44} & 0 & 0 \\ 0 & 0 & 0 & 0 & C_{55} & 0 \\ 0 & 0 & 0 & 0 & 0 & C_{66} \end{bmatrix} \tag{B.7}$$

$$\mathbf{L} = \begin{bmatrix} 2/3 & -1/3 & -1/3 & 0 & 0 & 0 \\ -1/3 & 2/3 & -1/3 & 0 & 0 & 0 \\ -1/3 & -1/3 & 2/3 & 0 & 0 & 0 \\ 0 & 0 & 0 & 1 & 0 & 0 \\ 0 & 0 & 0 & 0 & 1 & 0 \\ 0 & 0 & 0 & 0 & 0 & 1 \end{bmatrix} \tag{B.8}$$

where the simplified contracted indices convention of Voigt ($C_{1111} \leftrightarrow C_{11}$, $C_{1122} \leftrightarrow C_{12}$, $C_{1133} \leftrightarrow C_{13}$, …) is used. Since the non-zero components of $\tilde{\mathbf{C}}$ are:

$$\begin{aligned}
\tilde{C}_{11} &= \frac{2}{3}C_{11} - \frac{1}{3}C_{12} - \frac{1}{3}C_{13} \\
\tilde{C}_{12} &= -\frac{1}{3}C_{11} + \frac{2}{3}C_{12} - \frac{1}{3}C_{13} \\
\tilde{C}_{13} &= -\frac{1}{3}C_{11} - \frac{1}{3}C_{12} + \frac{2}{3}C_{13} \\
\tilde{C}_{21} &= \frac{2}{3}C_{12} - \frac{1}{3}C_{22} - \frac{1}{3}C_{23} \\
\tilde{C}_{22} &= -\frac{1}{3}C_{12} + \frac{2}{3}C_{22} - \frac{1}{3}C_{23} \\
\tilde{C}_{23} &= -\frac{1}{3}C_{12} - \frac{1}{3}C_{22} + \frac{2}{3}C_{23} \\
\tilde{C}_{31} &= \frac{2}{3}C_{13} - \frac{1}{3}C_{23} - \frac{1}{3}C_{33} \\
\tilde{C}_{32} &= -\frac{1}{3}C_{13} + \frac{2}{3}C_{23} - \frac{1}{3}C_{33} \\
\tilde{C}_{33} &= -\frac{1}{3}C_{13} - \frac{1}{3}C_{23} + \frac{2}{3}C_{33}
\end{aligned} \tag{B.9}$$

it is obtained:

$$\begin{cases} \tilde{C}_{11} + \tilde{C}_{12} + \tilde{C}_{13} = 0 \\ \tilde{C}_{21} + \tilde{C}_{22} + \tilde{C}_{23} = 0 \\ \tilde{C}_{31} + \tilde{C}_{32} + \tilde{C}_{33} = 0 \end{cases} \tag{B.10}$$

and so $\dfrac{\partial \Sigma_{ij}}{\partial p} = 0$. It has to be noted that this appendix exactly includes the proof of the insensitivity of the CPB06 yield function to the hydrostatic pressure given in Cazacu *et al.* (2006).

Appendix C Numerical analysis of the homogeneous zone evolution and stress computation in plane strain tests

Plane strain tests on Ti6Al4V show a strain field distribution characterized by a homogeneous zone at the center of the specimen and a heterogeneous zone at the edges (see Section 4.2.3.1). In order to take into account the edge effects in the stress computation, a numerical investigation using finite elements is performed with the aim of expressing the actual stress in the specimen's plane strain state zone along the loading direction in terms of the available experimental data.

Given the symmetry of the problem, only a quarter of the gage zone is modeled with 3D solid elements BWD3D (see Figure C-1). A displacement along x_1-direction is applied to the upper nodes while they are fixed along x_2-direction. The nodes on the left (respectively bottom) side are fixed along x_2-direction (respectively x_1-direction).

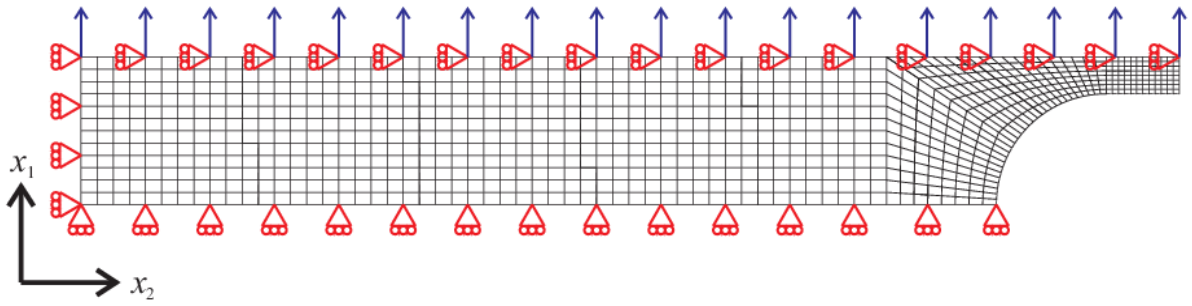

Figure C-1 Mesh and boundary conditions for the simulation of plane strain tests

CPB06 yield criterion associated to Voce isotropic hardening model is used as constitutive law. Several simulations are run using different sets of material parameters (see Table C-1). The first one (MAT A) considers an isotropic yield surface. The sets from MAT B to MAT D differ in the strength differential parameters and the anisotropy coefficients, determined by the classical simulated annealing method using different initial guesses and the experimental data in tension and compression for Ti6Al4V in RD, 45°-direction and TD. Finally, regarding the sets from MAT E to MAT G, they differ from MAT B in the hardening constants.

	k	C_{12}	C_{13}	C_{22}	C_{23}	C_{33}	C_{66}	s_R	c_R
MAT A	0.0	0.0	0.0	1.0	0.0	1.0	1.0	211.65	12.57
MAT B	-0.1948	-1.4863	1.2348	1.3724	-0.4480	-2.1227	3.3588	211.65	12.57
MAT C	-0.1101	4.9139	2.1494	1.5700	0.8506	4.2660	4.4153	211.65	12.57
MAT D	-0.1100	-1.6860	-2.6221	0.7767	0.9460	-2.9217	-4.0709	211.65	12.57
MAT E	-0.1948	-1.4863	1.2348	1.3724	-0.4480	-2.1227	3.3588	400.00	12.57
MAT F	-0.1948	-1.4863	1.2348	1.3724	-0.4480	-2.1227	3.3588	211.65	30.0
MAT G	-0.1948	-1.4863	1.2348	1.3724	-0.4480	-2.1227	3.3588	400.00	30.0
$a=2$, $C_{11}=1.0$, $C_{44}=C_{55}=C_{66}$, $R_0=971.24$ MPa									

Table C-1 Material parameters used for finite element simulations of the plane strain test

The simulation data enable to compute the load F_H acting on the homogeneous strain field zone. For each simulation, the relationship between the ratios F_H / F_T and W_H / W_T, where F_T is the total force applied to the specimen while W_H and W_T are respectively the total width of the gage zone and the homogeneous zone width, is plotted. The results are given in Figure C-2. As in Florès *et al.* (2010), it can be observed a linear trend between the two ratios which is similar for every simulation. Then, if α and β are constants, it can be written:

$$\frac{F_H}{F_T} = \alpha \frac{W_H}{W_T} + \beta \tag{C.1}$$

Assuming that $W_H = W_T$ and $F_H = F_T$ at the beginning of the deformation, it leads to $\alpha + \beta = 1$ and Equation (C.1) can be rewritten as:

$$\frac{F_H}{F_T} = \alpha \frac{W_H}{W_T} + (1-\alpha) \tag{C.2}$$

The stress component σ_{11} along the loading direction is then given by:

$$\sigma_{11} = \frac{F_H}{A_H} = \alpha \frac{F_T}{W_T t_H} + (1-\alpha) \frac{F_T}{W_H t_H} \tag{C.3}$$

The coefficient α is determined by linear regression thanks to the software Igor Pro 6.22A. The results give $\alpha = 1.0154$ (see Figure C-2).

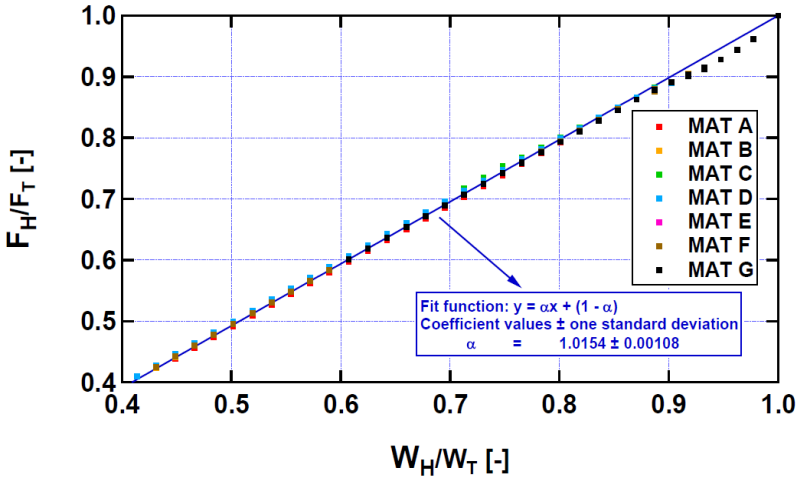

Figure C-2 Linear trend between the ratios W_H / W_T and F_H / F_T for the different parameter sets.

Equation (C.3) is used to compute the stress-strain curves in RD, 45°-direction and TD for Ti6Al4V in plane strain state (Figure C-3). Two different values of the constant α are considered:

- $\alpha = 1$, which involves considering that the strain field is homogeneous along the total width of the gage zone during all the deformation of the specimen;
- $\alpha = 1.0154$, value which was previously determined.

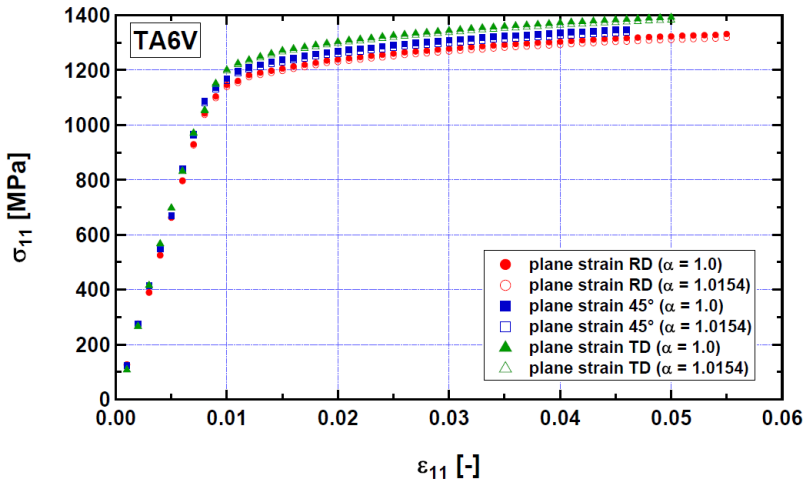

Figure C-3 Stress-strain curves in RD, 45°-direction and TD for Ti6Al4V in plane strain state, determined by Equation (C.3) when considering $\alpha = 1$ ***and*** $\alpha = 1.0154$

It can be noticed that, although sizeable edge effects occur, the discrepancies between the curves computed with both values of α are not significant. It can thus be maintained that, in the case of plane strain tests on Ti6Al4V specimens with the geometry given in Figure 4-23, assuming a homogeneous strain field along the total width of the gage zone enables the determination of the axial stress with a quite good accuracy.

Appendix D Determination of the yield stress for different strain paths

In order to characterize the initial yield locus, it is required to determine the yield stress for several strain paths and loading direction. In the framework of this investigation, the following procedure was performed to identify different points on the yield locus:

1. An experiment, usually tension in RD, is first defined as reference. The yield stress is determined by the offset method. The choice of the offset is fixed to a plastic strain value ε_0^p, usually 0.2% (see Figure 5-11).
2. The yield stress for the other loading directions in tension or the other stress states are determined using the work-equivalence principle (see Figure 5-12).

The above procedure requires the computation of the plastic work per unit of volume W^p which is given by:

$$dW^p = \sigma_{ij}\, d\varepsilon_{ij}^p \tag{D.1}$$

where σ_{ij} and ε_{ij}^p are the components of the stress and plastic strain tensors, respectively. Here are given some examples for specific strain paths which are dealt with in this study:

- **Uniaxial tension/compression.** The only non-zero stress component in the local axes is σ_{11} (see Sections 4.2.2.1 and 4.2.2.2). Equation (D.1) is then written as:

$$dW^p = \sigma_{11}\, d\varepsilon_{11}^p \tag{D.2}$$

- **Plane strain.** In plane strain state, two stress components, σ_{11} and σ_{22}, occur (see Section 4.2.3) and the plastic work is determined as follows:

$$dW^p = \sigma_{11}\, d\varepsilon_{11}^p + \sigma_{22}\, d\varepsilon_{22}^p \tag{D.3}$$

  Nevertheless, since the transversal strain ε_{22}^p is zero, it leads to:

$$dW^p = \sigma_{11}\, d\varepsilon_{11}^p \tag{D.4}$$

- **Simple shear.** In simple shear, Equation (D.1) is written as:

$$dW^p = \sigma_{11}\, d\varepsilon_{11}^p + \sigma_{22}\, d\varepsilon_{22}^p + 2\,\sigma_{12}\, d\varepsilon_{12}^p \tag{D.5}$$

At the onset of plasticity, since the components σ_{11} and σ_{22} are low with respect to σ_{12}, Equation (D.5) can be simplified as follows:

$$dW^p \simeq 2\,\sigma_{12}\, d\varepsilon_{12}^p = \tau\, d\gamma^p \tag{D.6}$$

where it is set $\tau = \sigma_{12}$ and $d\gamma^p = 2\, d\varepsilon_{12}^p$.

As it can be noticed for the above mentioned strain paths, the computation of W^p needs to know only one component of the stress state and one component of the plastic strain state (see Equations (D.2), (D.4) and (D.6)). In this specific case, denoting by σ and ε^p the stress and plastic strain components respectively, the plastic work per unit of volume is given by:

$$W^p\left(\varepsilon^p\right) = \int_0^{\varepsilon^p} \sigma\, d\lambda \tag{D.7}$$

The determination of the yield stresses using the work-equivalence principle thus consists in identifying the stress for a particular value of W^p, denoted W_0^p. This value is obtained by integrating Equation (D.2) since it is assumed that the tensile yield stress in RD is given by the offset method:

$$W_0^p = \int_0^{\varepsilon_0^p} \sigma_{11}\, d\varepsilon_{11}^p \tag{D.8}$$

where $\varepsilon_0^p = 0.2\%$. For the other stress states, a Newton-Raphson iterative process is used to find the root of the function $W^p - W_0^p$ and then to determine the stress value associated to W_0^p. Starting with ε_0^p as initial guess and denoting ε_n^p the current approximation, the next approximation ε_{n+1}^p is given by:

$$\varepsilon_{n+1}^p = \varepsilon_n^p - \frac{W_n^p - W_0^p}{\left.\dfrac{dW^p}{d\varepsilon^p}\right|_n} = \varepsilon_n^p - \frac{W_n^p - W_0^p}{\sigma_n} \tag{D.9}$$

until $\left|W_{n+1}^p - W_0^p\right|$ is lower than a definite value. When the strain ε^p corresponding to W_0^p is known, the stress σ can be determined using the stress-plastic strain curve. It has to be noted that the process described above can be used to identify the yield locus for other levels of plastic work.

Appendix E Computation of stress potential gradient

The integration algorithm requires the computation of the stress potential gradient (see Equation (6.30)). If CPB06 yield criterion is considered, the derivative $\frac{\partial \varphi}{\partial \boldsymbol{\sigma}}$ can be decomposed as follows:

$$\frac{\partial \varphi}{\partial \boldsymbol{\sigma}} = \frac{\partial \varphi}{\partial \Sigma_1}\frac{\partial \Sigma_1}{\partial \boldsymbol{\Sigma}}\frac{\partial \boldsymbol{\Sigma}}{\partial \boldsymbol{\sigma}} + \frac{\partial \varphi}{\partial \Sigma_2}\frac{\partial \Sigma_2}{\partial \boldsymbol{\Sigma}}\frac{\partial \boldsymbol{\Sigma}}{\partial \boldsymbol{\sigma}} + \frac{\partial \varphi}{\partial \Sigma_3}\frac{\partial \Sigma_3}{\partial \boldsymbol{\Sigma}}\frac{\partial \boldsymbol{\Sigma}}{\partial \boldsymbol{\sigma}} \tag{E.1}$$

where $\varphi = \bar{\sigma} - Y$ with $\bar{\sigma}$ defined in Equation (6.16).

The components $\frac{\partial \varphi}{\partial \Sigma_i}$ $(i = 1\ldots3)$ are given by:

$$\frac{\partial \varphi}{\partial \Sigma_i} = B\left\{\left(|\Sigma_1| - k\Sigma_1\right)^a + \left(|\Sigma_2| - k\Sigma_2\right)^a + \left(|\Sigma_3| - k\Sigma_3\right)^a\right\}^{\frac{1-a}{a}} \left(|\Sigma_i| - k\Sigma_i\right)^{a-1}\left\{\mathrm{sgn}\left(\Sigma_i\right) - k\right\} \tag{E.2}$$

The computation of the components $\frac{\partial \Sigma_i}{\partial \boldsymbol{\Sigma}}$ $(i = 1\ldots3)$ is based on the characteristic polynomial:

$$\Sigma_i^3 - I_1\Sigma_i^2 + I_2\Sigma_i - I_3 = 0 \tag{E.3}$$

where I_1, I_2, I_3 are respectively the first, second and third invariants of tensor $\boldsymbol{\Sigma}$ defined as follows:

$$I_1 = \mathrm{tr}\left(\boldsymbol{\Sigma}\right) = \Sigma_{ii} \tag{E.4}$$

$$I_2 = \frac{1}{2}\left(\Sigma_{ii}\Sigma_{jj} - \Sigma_{ij}\Sigma_{ji}\right) \tag{E.5}$$

$$I_3 = \det\left(\boldsymbol{\Sigma}\right) = e_{ijk}\Sigma_{1i}\Sigma_{2j}\Sigma_{3k} \tag{E.6}$$

where e_{ijk} is the Levi-Civita symbol.

If Λ denotes any eigenvalue of $\boldsymbol{\Sigma}$, Equation (E.3) can be rewritten as:

$$\Lambda^3 - I_1\Lambda^2 + I_2\Lambda - I_3 = 0 \tag{E.7}$$

and the differentiation with respect to Λ leads to:

$$\left(3\Lambda^2 - 2I_1\Lambda + I_2\right)\frac{\partial\Lambda}{\partial\boldsymbol{\Sigma}} - \left(\Lambda^2\frac{\partial I_1}{\partial\boldsymbol{\Sigma}} - \Lambda\frac{\partial I_2}{\partial\boldsymbol{\Sigma}} + \frac{\partial I_3}{\partial\boldsymbol{\Sigma}}\right) = 0 \tag{E.8}$$

i.e.:

$$\frac{\partial\Lambda}{\partial\boldsymbol{\Sigma}} = \frac{1}{3\Lambda^2 - 2I_1\Lambda + I_2}\left(\Lambda^2\frac{\partial I_1}{\partial\boldsymbol{\Sigma}} - \Lambda\frac{\partial I_2}{\partial\boldsymbol{\Sigma}} + \frac{\partial I_3}{\partial\boldsymbol{\Sigma}}\right) \tag{E.9}$$

where, δ_{ij} being the Kronecker delta,

$$\begin{aligned}
\frac{\partial I_1}{\partial\Sigma_{ij}} &= \delta_{ij} \\
\frac{\partial I_2}{\partial\Sigma_{ij}} &= I_1\delta_{ij} - \Sigma_{ij} \\
\frac{\partial I_3}{\partial\Sigma_{ij}} &= e_{jkl}\left(\delta_{1i}\Sigma_{2k}\Sigma_{3l} + \delta_{2i}\Sigma_{3k}\Sigma_{1l} + \delta_{3i}\Sigma_{1k}\Sigma_{2l}\right)
\end{aligned} \tag{E.10}$$

It is worth noting that the previous mathematical development is correct insomuch as $3\Lambda^2 - 2I_1\Lambda + I_2 \neq 0$. If this condition is not fulfilled, namely if $I_2 = 2I_1\Lambda - 3\Lambda^2$, Equation (E.7) gives:

$$2\Lambda^3 - I_1\Lambda^2 + I_3 = 0 \tag{E.11}$$

and thus:

$$\frac{\partial\Lambda}{\partial\boldsymbol{\Sigma}} = \frac{1}{6\Lambda^2 - 2I_1\Lambda}\left(\Lambda^2\frac{\partial I_1}{\partial\boldsymbol{\Sigma}} - \frac{\partial I_3}{\partial\boldsymbol{\Sigma}}\right) \tag{E.12}$$

The last components $\dfrac{\partial\boldsymbol{\Sigma}}{\partial\boldsymbol{\sigma}}$ are given by:

$$\frac{\partial\boldsymbol{\Sigma}}{\partial\boldsymbol{\sigma}} = \mathbf{C} : \mathbf{K} \tag{E.13}$$

where $\mathbf{C}$ is the fourth-order symmetric and orthotropic tensor defined in CPB06 and $\mathbf{K}$ is the fourth-order symmetric deviatoric unit tensor ($K_{ijkl} = \frac{1}{2}\left(\delta_{ik}\delta_{jl} + \delta_{il}\delta_{jk}\right) - \frac{1}{3}\delta_{ij}\delta_{kl}$) while $\left(\mathbf{C} : \mathbf{K}\right)_{ijkl} = C_{ijmn}K_{mnkl}$.

Note that all these relationships can readily be extended to CPB06ex*n* yield criteria.

References

Altenhof W., Raczy A., Laframboise M., Loscher J. and Alpas A. (2004). *Numerical simulation of AM50A magnesium alloy under large deformation*. International Journal of Impact Engineering, 30:117-142.

An Y.G., Vegter H. and Elliott L. (2004). *A novel and simple method for the measurement of plane strain work hardening*. Journal of Materials Processing Technology, 155-156:1616-1622.

Armstrong P.J. and Frederick C.O. (1966). *A mathematical representation of the multiaxial Bauschinger effect.* Report RD/B/N731, CEGB, Central Electricity Generating Board, Berkeley, UK.

Barlat F., Lege D.J. and Brem J.C. (1991). *A six-component yield function for anisotropic materials*. International Journal of Plasticity, 7:693-712.

Belytschko T. and Bindeman L.P. (1991). *Assumed strain stabilization of the 4-node quadrilateral with 1-point quadrature for nonlinear problems*. Computer Methods in Applied Mechanics and Engineering, 88:311-340.

Bouffioux C., Henrard C., Eyckens P., Aerens R., Van Bael A., Sol H., Duflou J.R. and Habraken A.M. (2008). *Comparison of the tests chosen for material parameter identification to predict single point incremental forming forces*. In: Proceedings of International Deep Drawing Research Group IDDRG 2008, Olofström, Sweden.

Bouffioux C., Lequesne C., Vanhove H., Duflou J.R., Pouteau P., Duchêne L. and Habraken A.M. (2011). *Experimental and numerical study of an AlMgSc sheet formed by an incremental process*. Journal of Materials Processing Technology, 211:1684-1693.

Bouvier S., Teodosiu C., Haddadi H. and Tabacaru V. (2002). *Anisotropic Behaviour of Structural Steel and Aluminium Alloys at Large Strains*. In: Proceedings of 6th European

Mechanics of Materials Conference on Non-linear Mechanics of Anisotropic Materials, Liège, Belgium, 215-222.

Bouvier S., Haddadi H., Levée P. and Teodosiu C. (2006). *Simple shear tests: Experimental techniques and characterization of the plastic anisotropy of rolled sheets at large strains*. Journal of Materials Processing Technology, 172:96-103.

Boyer R., Collings E.W. and Welsch G. (1994). *Materials Properties Handbook: Titanium Alloys*. ASM International, USA.

Bridier F., Villechaise P. and Mendez J. (2005). *Analysis of the different slip systems activated by tension in a α/β titanium alloy in relation with local crystallographic orientation*. Acta Materialia, 53:555-567.

Bruno G. and Dunn B.D. (1997). *The precise measurement of Ti6Al4V microscopic elastic constants by means of neutron diffraction* Measurement Science and Technology, 8:1244-1249.

Castagne S., Remy M. and Habraken A.M. (2003). *Development of a mesoscopic cell modeling the damage process in steel at elevated temperature*. Key Engineering Materials, 233-236:145-150.

Castagne S., Pascon F., Blès G. and Habraken A.M. (2004). *Developments in finite element simulations of continuous casting*. Journal de Physique IV, 120:447-455.

Cazacu O. and Barlat F. (2001). *Generalization of Drucker's Yield Criterion to Orthotropy*. Mathematics and Mechanics of Solids, 6:613-630.

Cazacu O. and Barlat F. (2003). *Application of the theory of representation to describe yielding of anisotropic aluminum alloys*. International Journal of Engineering Science, 41:1367-1385.

Cazacu O. and Barlat F. (2004). *A criterion for description of anisotropy and yield differential effects in pressure-insensitive metals*. International Journal of Plasticity, 20:2027-2045.

Cazacu O., Plunkett B. and Barlat F. (2006). *Orthotropic yield criterion for hexagonal closed packed metals*. International Journal of Plasticity, 22:1171-1194.

Cazacu O. and Stewart J.B. (2009). *Analytic plastic potential for porous aggregates with matrix exhibiting tension–compression asymmetry*. Journal of the Mechanics and Physics of Solids, 57:325-341.

Cazacu O., Ionescu I.R. and Yoon J.W. (2010). *Orthotropic strain rate potential for the description of anisotropy in tension and compression of metals*. International Journal of Plasticity, 26:887-904.

Cescotto S. and Charlier R. (1993). *Frictional contact finite element based on mixed variational principles*. International Journal for Numerical Methods in Engineering, 36:1681-1701.

Coghe F., Tirry W., Rabet L., Schryvers D. and Van Houtte P. (2012). *Importance of twinning in static and dynamic compression of a Ti–6Al–4V titanium alloy with an equiaxed microstructure*. Materials Science and Engineering: A, 537:1-10.

Coppieters S. (2012). *Experimental and numerical study of clinched connections*. PhD Thesis, Katholieke Universiteit Leuven.

Delannay L., Logé R.E., Chastel Y. and Van Houtte P. (2002). *Prediction of intergranular strains in cubic metals using a multisite elastic-plastic model*. Acta Materialia, 50:5127-5138.

Drucker D.C. (1949). *Relation of experiments to mathematical theories of plasticity*. Journal of Applied Mechanics, 16:349-357.

Drucker D.C. (1950). *Some Implications of Work Hardening and Ideal Plasticity*. Quarterly of Applied Mathematics, 7:411-418.

Duc-Toan N., Jin-Gee P. and Young-Suk K. (2010). *Combined kinematic/isotropic hardening behavior study for magnesium alloy sheets to predict ductile fracture of rotational incremental forming*. In: Proceedings of 13th International ESAFORM Conference on Material Forming (ESAFORM 2010), Brescia, Italy.

Duchene L., Montleau P.d., Houdaigui F.E., Bouvier S. and Habraken A.M. (2005). *Analysis of Texture Evolution and Hardening Behavior during Deep Drawing with an Improved Mixed Type FEM Element*. AIP Conference Proceedings, 778:409-414.

Duchêne L., Godinas A., Cescotto S. and Habraken A.M. (2002). *Texture evolution during deep-drawing processes*. Journal of Materials Processing Technology, 125-126:110-118.

Duchêne L. (2003). *FEM Study of Metal Sheets with a Texture based, Local Description of the Yield Locus*. PhD Thesis, Université de Liège.

Duchêne L., El Houdaigui F. and Habraken A.M. (2007). *Length changes and texture prediction during free end torsion test of copper bars with FEM and remeshing techniques*. International Journal of Plasticity, 23:1417-1438.

Duchêne L., Lelotte T., Florès P., Bouvier S. and Habraken A.M. (2008). *Rotation of axes for anisotropic metal in FEM simulations*. International Journal of Plasticity, 24:397-427.

Duflou J.R., Verbert J., Belkassem B., Gu J., Sol H., Henrard C. and Habraken A.M. (2008). *Process window enhancement for single point incremental forming through multi-step toolpaths*. CIRP Annals - Manufacturing Technology, 57:253-256.

Ertürk S., Steglich D., Bohlen J., Letzig D. and Brocks W. (2009). *Thermo-mechanical modelling of indirect extrusion process for magnesium alloys*. In: Proceedings of 12th International ESAFORM Conference on Material Forming (ESAFORM 2009), Twente, The Netherlands.

Ferron G., Makkouk R. and Morreale J. (1994). *A parametric description of orthotropic plasticity in metal sheets*. International Journal of Plasticity, 10:431-449.

Florès P. (2003). *Experimental and Theoretical Development of Tensile-Shear Test on Metal Sheets*. DEA, Université de Liège.

Florès P. (2005). *Development of Experimental Equipment and Identification Procedures for Sheet Metal Constitutive Laws*. PhD Thesis, University of Liège.

Florès P., Duchêne L., Bouffioux C., Lelotte T., Henrard C., Pernin N., Van Bael A., He S., Duflou J. and Habraken A.M. (2007). *Model identification and FE simulations: Effect of different yield loci and hardening laws in sheet forming*. International Journal of Plasticity, 23:420-449.

Florès P., Tuninetti V., Gilles G., Gonry P., Duchêne L. and Habraken A.M. (2010). *Accurate stress computation in plane strain tensile tests for sheet metal using experimental data*. Journal of Materials Processing Technology, 210:1772-1779.

Follansbee P.S. and Gray G.T. (1989). *An analysis of the low-temperature, low and high strain-rate deformation of Ti-6Al-4V*. Metallurgical Transactions A, 20:863-874.

Fukuhara M. and Sanpei A. (1993). *Elastic moduli and internal frictions of Inconel 718 and Ti-6Al-4V as a function of temperature*. Journal of Materials Science Letters, 12:1122-1124.

Fundenberger J.J., Philippe M.J., Wagner F. and Esling C. (1997). *Modelling and prediction of mechanical properties for materials with hexagonal symmetry (zinc, titanium and zirconium alloys)*. Acta Materialia, 45:4041-4055.

Ghaffari Tari D., Worswick M.J., Ali U. and Gharghouri M.A. (2014). *Mechanical response of AZ31B magnesium alloy: Experimental characterization and material modeling considering proportional loading at room temperature*. International Journal of Plasticity, 55:247-267.

Gil Sevillano J., van Houtte P. and Aernoudt E. (1980). *Large strain work hardening and textures*. Progress in Materials Science, 25:69-134.

Gilles G., Hammami W., Libertiaux V., Cazacu O., Yoon J.H., Kuwabara T., Habraken A.M. and Duchêne L. (2011). *Experimental characterization and elasto-plastic modeling of the quasi-static mechanical response of TA-6 V at room temperature*. International Journal of Solids and Structures, 48:1277-1289.

GOM (2001). *ARAMIS, Deformation Measurement using the Grating Method.* V4.7. GOM mbh. Braunschweig.

Graff S., Brocks W. and Steglich D. (2007). *Yielding of magnesium: From single crystal to polycrystalline aggregates*. International Journal of Plasticity, 23:1957-1978.

Habraken A.M. and Cescotto S. (1990). *An automatic remeshing technique for finite element simulation of forming processes*. International Journal for Numerical Methods in Engineering, 30:1503-1525.

Habraken A.M. and Cescotto S. (1998). *Contact between deformable solids: The fully coupled approach*. Mathematical and Computer Modelling, 28:153-169.

Habraken A.M., Charles J.F., Wegria J. and Cescotto S. (1998). *Dynamic Recrystallization during Zinc Rolling*. International Journal of Forming Processes, 1:1-20.

Habraken A.M. and Duchêne L. (2004). *Anisotropic elasto-plastic finite element analysis using a stress-strain interpolation method based on a polycrystalline model*. International Journal of Plasticity, 20:1525-1560.

Haddadi H., Bouvier S., Banu M., Maier C. and Teodosiu C. (2006). *Towards an accurate description of the anisotropic behaviour of sheet metals under large plastic deformations: Modelling, numerical analysis and identification*. International Journal of Plasticity, 22:2226-2271.

Halir R. and Flusser J. (1998). *Numerically Stable Least Squares Fitting of Ellipses*. In: Proceedings of 6th International Conference in Central Europe on Computer Graphics and Visualization (WSCG 98), Plzen, Czech Republic, 125-132.

Hastings W.K. (1970). *Monte Carlo sampling methods using Markov chains and their applications*. Biometrika, 57:97-109.

Henrard C. (2008). *Numerical Simulations of the Single Point Incremental Forming Process*. PhD Thesis, Université de Liège.

Hill R. (1948). *A theory of the yielding and plastic flow of anisotropic materials*. Proceedings of the Royal Society of London A, 193:281-297.

Hill R. (1987). *Constitutive dual potentials in classical plasticity*. Journal of the Mechanics and Physics of Solids, 35:23-33.

Hill R. and Hutchinson J.W. (1992). *Differential Hardening in Sheet Metal Under Biaxial Loading: A Theoretical Framework*. Journal of Applied Mechanics, 59:S1-S9.

Hill R., Hecker S.S. and Stout M.G. (1994). *An investigation of plastic flow and differential work hardening in orthotropic brass tubes under fluid pressure and axial load*. International Journal of Solids and Structures, 31:2999-3021.

Hoferlin E. (2001). *Incorporation of an Accurate Model of Texture and Strain-path Induced Anisotropy in Simulations of Sheet Metal Forming*. PhD Thesis, Katholieke Universiteit Leuven.

Hogström P., Ringsberg J.W. and Johnson E. (2009). *An experimental and numerical study of the effects of length scale and strain state on the necking and fracture behaviours in sheet metals*. International Journal of Impact Engineering, 36:1194-1203.

Hosford W.F. (1972). *A generalized isotropic yield criterion*. Journal of Applied Mechanics-Transactions of the ASME, 39:607-609.

Hosford W.F. (1993). *The mechanics of crystals and textured polycrystals*. Oxford University Press, New York.

Hu Z. (1992). *Lois de Comportement des Métaux en Grandes Transformations tenant Compte de l'Evolution de la Microstructure*. PhD Thesis, Institut National Polytechnique de Grenoble.

Jeunechamps P.P. (2008). *Simulation numérique, à l'aide d'algorithmes thermomécaniques implicites, de matériaux endommageables pouvant subir de grandes vitesses de déformation.*

Application aux structures aéronautiques soumises à impact. PhD Thesis, Université de Liège.

Johnson G.R. and Cook W.H. (1983). *A consitutive model and data for metals subjected to large strains, high strain rates and high temperatures*. In: Proceedings of 7th International Symposium on Ballistic, The Hague, The Netherlands, 541-547.

Jones I.P. and Hutchinson W.B. (1981). *Stress-state dependence of slip in Titanium-6Al-4V and other H.C.P. metals*. Acta Metallurgica, 29:951-968.

Karafillis A.P. and Boyce M.C. (1993). *A general anisotropic yield criterion using bounds and a transformation weighting tensor*. Journal of the Mechanics and Physics of Solids, 41:1859-1886.

Khan A.S., Sung Suh Y. and Kazmi R. (2004). *Quasi-static and dynamic loading responses and constitutive modeling of titanium alloys*. International Journal of Plasticity, 20:2233-2248.

Khan A.S., Kazmi R. and Farrokh B. (2007). *Multiaxial and non-proportional loading responses, anisotropy and modeling of Ti-6Al-4V titanium alloy over wide ranges of strain rates and temperatures*. International Journal of Plasticity, 23:931-950.

Kim J., Ryou H., Kim D., Kim D., Lee W., Hong S.-H. and Chung K. (2008). *Constitutive law for AZ31B Mg alloy sheets and finite element simulation for three-point bending*. International Journal of Mechanical Sciences, 50:1510-1518.

Kirkpatrick S., Gelatt C.D. and Vecchi M.P. (1983). *Optimization by Simulated Annealing*. Science, 220:671-680.

Kleinermann J.P. (2000). *Identification paramétrique et optimisation des procédés de mise à forme par problèmes inverses*. PhD Thesis, Université de Liège.

Knockaert R. (2001). *Numerical and experimental study of the strain localization during sheet forming operations*. PhD Thesis, Ecole Nationale Supérieure des Mines de Paris.

Kuwabara T., Katami C., Kikuchi M., Shindo T. and Ohwue T. (2001). *Cup drawing of pure titanium sheet - finite element analysis and experimental validation*. In: Proceedings of 7th International Conference on Numerical Methods in Industrial Forming Processes, Toyohashi, Japan, 781-787.

Kuwabara T. (2007). *Advances in experiments on metal sheets and tubes in support of constitutive modeling and forming simulations*. International Journal of Plasticity, 23:385-419.

Kuwabara T., Kumano Y., Ziegelheim J. and Kurosaki I. (2009). *Tension-compression asymmetry of phosphor bronze for electronic parts and its effect on bending behavior*. International Journal of Plasticity, 25:1759-1776.

Lăzărescu L., Comşa D.S. and Banabic D. (2011). *Determination of Stress-Strain Curves of Sheet Metals by Hydraulic Bulge Test*. In: Proceedings of 14th International ESAFORM Conference on Material Forming (ESAFORM 2011), Belfast, UK.

Lecompte D., Sol H., Vantomme J. and Habraken A.M. (2006). *Analysis of speckle patterns for deformation measurements by DIC*. In: Proceedings of SPIE, Nimes, France, E1-E6.

Lee D. and Backofen W.A. (1966). *An Experimental Determination of the Yield Locus for Titanium and Titanium-Alloy Sheet*. Transactions of the Metallurgical Society of AIME, 236:1077-1084.

Lee M.-G., Wagoner R.H., Lee J.K., Chung K. and Kim H.Y. (2008). *Constitutive modeling for anisotropic/asymmetric hardening behavior of magnesium alloy sheets*. International Journal of Plasticity, 24:545-582.

Lee W.-S. and Lin C.-F. (1998a). *High-temperature deformation behaviour of Ti6Al4V alloy evaluated by high strain-rate compression tests*. Journal of Materials Processing Technology, 75:127-136.

Lee W.-S. and Lin C.-F. (1998b). *Plastic deformation and fracture behaviour of Ti–6Al–4V alloy loaded with high strain rate under various temperatures*. Materials Science and Engineering: A, 241:48-59.

Lemaitre J., Chaboche J.L., Benallal A. and Desmorat R. (2009). *Mécanique des matériaux solides*. Dunod.

Lemoine X., Iancu A. and Ferron G. (2011). *Flow Curve Determination at Large Plastic Strain Levels: Limitations of the Membrane Theory in the Analysis of the Hydraulic Bulge Test*. In: Proceedings of 14th International ESAFORM Conference on Material Forming (ESAFORM 2011), Belfast, UK.

Lequesne C. (2009). *Modeling of fracture in heavy steel welded beam-to-column connection submitted to cyclic loading by finite elements*. PhD Thesis, Université de Liège.

Li S., Hoferlin E., Bael A.V., Houtte P.V. and Teodosiu C. (2003). *Finite element modeling of plastic anisotropy induced by texture and strain-path change*. International Journal of Plasticity, 19:647-674.

Libertiaux V., Pascon F. and Cescotto S. (2011). *Experimental verification of brain tissue incompressibility using digital image correlation*. Journal of the Mechanical Behavior of Biomedical Materials, 4:1177-1185.

López J.G. (2014). *Crystal plasticity based modelling of the strain rate dependent mechanical behaviour of Ti-6Al-4V*. PhD Thesis, Universiteit Gent.

Lou X.Y., Li M., Boger R.K., Agnew S.R. and Wagoner R.H. (2007). *Hardening evolution of AZ31B Mg sheet*. International Journal of Plasticity, 23:44-86.

Lou Y., Huh H. and Yoon J.W. (2013). *Consideration of strength differential effect in sheet metals with symmetric yield functions*. International Journal of Mechanical Sciences, 66:214-223.

Lowden M.A.W. and Hutchinson W.B. (1975). *Texture strengthening and strength differential in titanium-6Al-4V*. Metallurgical and Materials Transactions A, 6:441-448.

Lütjering G. and Williams J.C. (2007). *Titanium*. Springer, Berlin, Deutschland, 2nd edition.

Macdougall D.A.S. and Harding J. (1999). *A constitutive relation and failure criterion for Ti6Al4V alloy at impact rates of strain*. Journal of the Mechanics and Physics of Solids, 47:1157-1185.

Maeda Y., Yanagawa M., Barlat F., Chung K., Hayashida Y., Hattori S., Matsui K., Brem J.C., Lege D.J., Murtha S.J. and Ishikawa T. (1998). *Experimental analysis of aluminum yield surface for binary Al-Mg alloy sheet samples*. International Journal of Plasticity, 14:301-318.

Majorell A., Srivatsa S. and Picu R.C. (2002). *Mechanical behavior of Ti-6Al-4V at high and moderate temperatures--Part I: Experimental results*. Materials Science and Engineering A, 326:297-305.

Marketz W.T., Fischer F.D. and Clemens H. (2003). *Deformation mechanisms in TiAl intermetallics--experiments and modeling*. International Journal of Plasticity, 19:281-321.

Mathonet V. (2003). *Manuel d'Utilisation du Programme d'Identification Paramétrique Optim.* Projet Région Wallone : Caractérisation Rationnelle des Propriétés à Chaud des Matériaux Métalliques. Université de Liège.

Medina Perilla J.A. and Gil Sevillano J. (1995). *Two-dimensional sections of the yield locus of a Ti-6%Al-4%V alloy with a strong transverse-type crystallographic α-texture*. Materials Science and Engineering A, 201:103-110.

Merklein M. and Kuppert A. (2009). *A method for the layer compression test considering the anisotropic material behavior*. In: Proceedings of 12th International ESAFORM Conference on Material Forming (ESAFORM 2009), Twente, The Netherlands.

Metropolis N., Rosenbluth A.W., Rosenbluth M.N., Teller A.H. and Teller E. (1953). *Equation of State Calculations by Fast Computing Machines*. The Journal of Chemical Physics, 21:1087-1092.

Meyer Jr H.W. and Kleponis D.S. (2001). *Modeling the high strain rate behavior of titanium undergoing ballistic impact and penetration*. International Journal of Impact Engineering, 26:509-521.

Milani A.S., Dabboussi W., Nemes J.A. and Abeyaratne R.C. (2009). *An improved multi-objective identification of Johnson–Cook material parameters*. International Journal of Impact Engineering, 36:294-302.

Nebebe M., Bohlen J., Steglich D. and Letzig D. (2009). *Mechanical characterisation of Mg alloys and model parameter identification for sheet forming simulations*. In: Proceedings of 12th International ESAFORM Conference on Material Forming (ESAFORM 2009), Twente, The Netherlands.

Nemat-Nasser S., Guo W.-G., Nesterenko V.F., Indrakanti S.S. and Gu Y.-B. (2001). *Dynamic response of conventional and hot isostatically pressed Ti-6Al-4V alloys: experiments and modeling*. Mechanics of Materials, 33:425-439.

Nixon M.E., Cazacu O. and Lebensohn R.A. (2010). *Anisotropic response of high-purity α-titanium: Experimental characterization and constitutive modeling*. International Journal of Plasticity, 26:516-532.

Noman M., Clausmeyer T., Barthel C., Svendsen B., Huétink J. and van Riel M. (2010). *Experimental characterization and modeling of the hardening behavior of the sheet steel LH800*. Materials Science and Engineering: A, 527:2515-2526.

Peirs J. (2012). *Experimental Characterisation and Modelling of the Dynamic Behaviour of the Titanium Alloy Ti6Al4V*. PhD Thesis, Universiteit Gent.

Philippe M.J., Serghat M., Van Houtte P. and Esling C. (1995). *Modelling of texture evolution for materials of hexagonal symmetry--II. application to zirconium and titanium α or near α alloys*. Acta Metallurgica et Materialia, 43:1619-1630.

Picu R.C. and Majorell A. (2002). *Mechanical behavior of Ti-6Al-4V at high and moderate temperatures--Part II: constitutive modeling*. Materials Science and Engineering A, 326:306-316.

Pijlman H. (2002). *Sheet material characterisation by multi-axial experiments*. PhD Thesis, University of Twente.

Plunkett B., Lebensohn R.A., Cazacu O. and Barlat F. (2006). *Anisotropic yield function of hexagonal materials taking into account texture development and anisotropic hardening*. Acta Materialia, 54:4159-4169.

Plunkett B., Cazacu O. and Barlat F. (2008). *Orthotropic yield criteria for description of the anisotropy in tension and compression of sheet metals*. International Journal of Plasticity, 24:847-866.

Prager W. (1955). *The theory of plasticity: a survey of recent achievements*. Proceedings of the Institution of Mechanical Engineers, 169:41-57.

Rabahallah M., Balan T. and Barlat F. (2009). *Anisotropic strain-rate potential based on multiple linear transformations*. In: Proceedings of 12th International ESAFORM Conference on Material Forming (ESAFORM 2009), Twente, The Netherlands.

Revil-Baudard B., Yoon J., Stewart J.B. and Cazacu O. (2012). *On the influence of damage evolution in an incompressible material with matrix displaying tension-compression asymmetry*. Procedia IUTAM, 3:331-349.

Sachs G. (1928). *Zur Ableitung einer Fließbedingung*. Zeitschrift des Vereines Deutscher Ingenieure, 72:734-736.

Salem A.A. and Semiatin S.L. (2009). *Anisotropy of the hot plastic deformation of Ti-6Al-4V single-colony samples*. Materials Science and Engineering: A, 508:114-120.

Seo S., Min O. and Yang H. (2005). *Constitutive equation for Ti-6Al-4V at high temperatures measured using the SHPB technique*. International Journal of Impact Engineering, 31:735-754.

Simo J.C. and Hughes T.J.R. (1998). *Computational Ineslaticity*. Springer, New York.

Swift H.W. (1952). *Plastic instability under plane stress*. Journal of the Mechanics and Physics of Solids, 1:1-18.

Taylor G.I. (1938). *Plastic strain in metals*. Journal of the Institute of Metals, 62:307-324.

Teodosiu C. and Hu Z. (1995), *Evolution of the intragranular microstructure at moderate and large strains: Modelling and computational significance*. In: Shen S.F. and Dawson P.R. (Eds.), Proceedings of the 5th International Conference on Numerical Methods in Industrial Forming Processes (NUMIFORM 95). Balkema, Rotterdam, pp. 173-182.

Thuillier S. (2008). *Caractérisation et prédiction du comportement mécanique des tôles métalliques et des élastomères*. HDR, Université de Bretagne-Sud.

Tirry W., Coghe F., Bouvier S., Gasperini M., Rabet L. and Schryvers D. (2010). *A multi-scale characterization of deformation twins in Ti6Al4V sheet material deformed by simple shear*. Materials Science and Engineering: A, 527:4136-4145.

Tuninetti V. and Habraken A.M. (2011). *LIMESS DIC for compression test*. Report RWI 15, University of Liège.

Tuninetti V., Milis O. and Habraken A.M. (2011). *Compression test procedure for constant strain rate*. Report RWI 14, University of Liège.

Tuninetti V., Gilles G., Péron-Lührs V. and Habraken A.M. (2012). *Compression Test for Metal Characterization using Digital Image Correlation and Inverse Modeling*. Procedia IUTAM, 4:206-214.

Tuninetti V. (2014). *Experimental and numerical study of the quasi-static behavior of Ti-6Al-4V*. PhD Thesis, Université de Liège.

Tuninetti V. and Habraken A.M. (2014). *Impact of anisotropy and viscosity to model the mechanical behavior of Ti–6Al–4V alloy*. Materials Science and Engineering: A, 605:39-50.

Tuninetti V., Gilles G., Milis O., Pardoen T. and Habraken A.M. (2015). *Anisotropy and tension–compression asymmetry modeling of the room temperature plastic response of Ti–6Al–4V*. International Journal of Plasticity, 67:53-68.

Turkmen H.S., Dawson P.R. and Miller M.P. (2002). *The evolution of crystalline stresses of a polycrystalline metal during cyclic loading*. International Journal of Plasticity, 18:941-969.

Ulacia I., Salisbury C.P., Hurtado I. and Worswick M.J. (2011). *Tensile characterization and constitutive modeling of AZ31B magnesium alloy sheet over wide range of strain rates and temperatures*. Journal of Materials Processing Technology, 211:830-839.

Van Houtte P., Li S., Seefeldt M. and Delannay L. (2005). *Deformation texture prediction: from the Taylor model to the advanced Lamel model*. International Journal of Plasticity, 21:589-624.

Van Houtte P., Gawad J., Eyckens P., Van Bael B., Samaey G. and Roose D. (2011). *A full-field strategy to take texture-induced anisotropy into account during FE simulations of metal forming processes*. JOM, 63:37-43.

Voce E. (1948). *The relationship between stress and strain for homogeneous deformation*. Journal of the Institute of Metals, 74:537-562.

Wang J. and Wagoner R.H. (2004). *A New Hexahedral Solid Element for 3D FEM Simulation of Sheet Metal Forming*. AIP Conference Proceedings, 712:2181-2186.

Wang J., Levkovitch V., Reusch F., Svendsen B., Huétink J. and van Riel M. (2008). *On the modeling of hardening in metals during non-proportional loading*. International Journal of Plasticity, 24:1039-1070.

Yoon J., Cazacu O. and Mishra R.K. (2013). *Constitutive modeling of AZ31 sheet alloy with application to axial crushing*. Materials Science and Engineering: A, 565:203-212.

Yoon J.H., Cazacu O., Yoon J.W. and Dick R.E. (2011). *New distortional hardening model capable of predicting eight ears for textured aluminum sheet*. In: Proceedings of 14th International ESAFORM Conference on Material Forming (ESAFORM 2011), Belfast, UK.

Yoon J.W., Barlat F., Dick R.E. and Karabin M.E. (2006). *Prediction of six or eight ears in a drawn cup based on a new anisotropic yield function*. International Journal of Plasticity, 22:174-193.

Zerilli F.J. and Armstrong R.W. (1987). *Dislocation-mechanics-based constitutive relations for material dynamics calculations*. Journal of Applied Physics, 61:1816-1825.

Zhu Y.Y. and Cescotto S. (1994). *Transient thermal and thermomechanical analysis by FEM*. Computers and Structures, 53:275-304.

Zhu Y.Y. and Cescotto S. (1995). *Unified and mixed formulation of the 4-node quadrilateral elements by assumed strain method: application to thermomechanical problems*. International Journal for Numerical Methods in Engineering, 38:685-716.

Ziegler H. (1959). *A modification of Prager's hardening rule*. Quarterly of Applied Mathematics, 17:55-65.

Ziegler H. (1983). *An Introduction to Thermomechanics*. North-Holland.